Syn- to post-intrusive deformation in the Chromitiferous Harzburgite Unit of the Uitkomst Complex, Nkomati Mine, Mpumalanga Province.

Pieter Lourens Joubert

(2002032155)

Dissertation submitted in accordance with the

requirements for the degree of

MASTER OF SCIENCE

In the faculty of Agricultural and Natural Sciences

Department of Geology

University of the Free State

Bloemfontein

June 2013

Supervised by Prof. C.D.K. Gauert

Abstract

The mafic to ultra-mafic, intrusive Uitkomst Complex, situated some 20km northeast from the town of Badplaas in the Mpumalanga province of South Africa, contains a Chromitiferous Harzburgite unit that host a layer of massive chromitites at the top. The massive chromitites crop out, as three hills on the farm Uitkomst 541 JT and is exploited by South Africa's only primary Nickel mine, the Nkomati Mine.

The main research criteria of this project are the involvement of syn- and post-magmatic deformation in the petrogenesis of the Massive Chromitite Layer of the Uitkomst Complex. On chromitite hill no.1 (open pit no.3) the layer of massive chromitites consist of five smaller chromitite sub-layers with an average, individual thickness of between 1 to 3 meters. These sub-layers and lenses are stacked on top of each other and separated by layers of talc-carbonate schist, to form a massive chromitite zone with a combined thickness of up to 30m.

The project consists of four interlinked investigations:

1. A geological mapping exercise in open pit three of the Nkomati Mine. This investigation forms the basis of the project and focuses on the general geological and geometrical properties of the chromitite layers. The investigation suggests that chromitite lenses MC4 and MC5 that occurs at the base of the Massive Chromitite Layer, in the study area, were deposited as a result of continuous crystallization as they are inter grown through a large gradational contact. The fractured nature and movement indicators along the bottom contacts of chromitite lenses MC1, MC2 and MC3 higher up in the layer suggest post-intrusive duplication through thrust faulting.

2. An investigation of the geological structures in the study area once again emphasized the similarities and continuity in chromitite lenses MC4 to MC5 and supports a continuous depositional event. The jointing in chromitite lenses MC1, MC2 and MC3 are not affected by the movement along the bottom contacts of the chromitite layers but get terminated at the gradational top contacts. This suggests that the fracturing along the bottom contacts might represent syn-intrusive deformation and that these three chromitite

layers were rather deposited individually through magmatic processes and rules out the possibility of structural duplication.

3. A petrographic investigation revealed that each chromitite lens experienced a unique degree of crystal deformation, this syn-intrusive deformation suggests that the chromitite was already in the solid phase during transportation. Furthermore each chromitite lens has a unique chromite to matrix ratio that suggests unique physical conditions during the crystallization phase of each chromitite lens. This indicates that the chromitite lenses were deposited as rafts of semi-solid chromitite and further suggests that the rafts were initiated by various pulses of magma replenishment into the primary magma chamber, supplying the conduit system.

4. The mineral chemical investigations of the chromite crystals reveal a normal fractionating trend for chromitite lenses MC4 and MC5. This further supports that they were deposited during a continuous crystallization event. An irregular variation pattern in the Cr number and Mg number in relation to the depositional sequence of the three upper chromitite lenses support that their crystallization were initiated by various pulses of magma replenishment.

The former two investigations mainly suggest the involvement of post-magmatic deformational processes, whereas the latter two investigations reveal that the geomorphology of the Massive Chromitite Layer is mostly influenced by syn-magmatic processes that occurred in both the primary magma chamber further down from the study area and the conduit system in the vicinity of the study area.

Index

List of figures

Chapter 1

Chapter 3

Chapter 4

Chapter 5

Chapter 6

Chapter 7

Chapter 8

List of tables

Chapter 1

Chapter 4

Chapter 5

Chapter 6

List of abbreviations

Chemical elements

Co	-	Cobalt
Cr	-	Chromium
Cu	-	Copper
Fe	-	Iron
Mn	-	Manganese
Ni	-	Nickel
O	-	Oxygen
Si	-	Silicon
Zn	-	Zinc
PGe's	-	Platinum group elements

Crystal fracturing

cc	-	Euhedral to subhedral crystals
cf	-	Crystal fragments
ch	-	Chromite chips
fc	-	Fractured crystals
rc	-	Rounded crystals

General

EMPA	-	Electron-microprobe analyses
g/t	-	Grams per ton
GPa	-	Giga Pascal
Ma	-	Million years

OVB	-	Over burden
PXT	-	Pyroxenite
µm	-	Micrometers

Geochemistry

Cr#	-	Chrome number
Cr-Al	-	Chrome / aluminium ratio
Cr-Fe	-	Chrome / iron ratio
Mg#	-	Magnesium number

Uitkomst Complex

MC 1-5	-	Chromitite lenses of the Massive Chromitite Layer
MCHR	-	Massif Chromitite layer of the Uitkomst Complex
MMZ	-	Main mineralized zone of the Uitkomst Complex
PCR	-	Chromitiferous Harzburgite of the Uitkomst Complex

Chapter 1: Introduction

1.1 The objectives of the project

The main objective of this project is to investigate the emplacement mechanisms of the Massive Chromitite Layer of the Uitkomst Complex as exposed on benches 17 to 19 in open pit 3 and its deformational history by using open-pit mapping and mineral geochemical data of the chromite. The massive chromitite unit is thickened in three separate, areas forming three weathering-resistant chromitite hills of which two have already been removed by mining. The investigation focuses on the upper benches of the western hill that hosts open-pit number 3 (fig. 1.4). The massive chromitite unit is obviously deformed, however it is not clear if syn- or post intrusive deformation prevailed in a semi-solid or solid state respectively *(Joubert, and Gauert, 2006)*. A late stage magmatic volume increase involving the hydration of Mg-rich minerals by deuteric fluids from meteoric to groundwater could also contribute to the deformation.

In order to achieve this, the following aspects will be investigated.

- The type and orientation of the deformational structures in the massive chromitite unit: These structures represent the nature and the chronological sequences of deformation of the rock unit in the specific areas which can give information on the post-intrusive deformation of the lower central part of the complex. Findings will have to be discussed in the light of Hornsey's (1999) results.

- The textural variability within the Massive Chromitite Layer and the upper PCR unit: The textures will provide some insight into the mineral fracturing that occurred inside the Massive Chromitite Layer.

- The correlation between the chromite mineral chemistry and the deformation of the chromitite layers: The mineral chemistry could give an indication whether the deformation of the chromite of the Massive Chromitite Layer and other parts of the PCR is syn-intrusive or of a post-intrusive nature.

1.2 Background of project

The interest in the Massive Chromitite Layer is mainly derived from its enlarged thickness in the study area (Open pit 3). From the rock sections that are exposed in open-pit 3 it is clear that this layer consists of a series of smaller chromitite lenses. The Massive Chromitite Layer has a maximum thickness of up to twelve meters as exposed by the mining operation in 2006 and 2007.

The first part of this study addresses syn- to post-magmatic tectonic deformation processes that could enhance the thickness of the Massive Chromitite Layer. This includes processes such as layer-parallel shearing and duplication which result in an increase of the thickness of rock units. Hornsey (1999) has identified and discussed the impact of large layer-parallel shears in the lower parts of the Complex (Fig.1.7) and therefore much attention will be allocated to investigating the effect of this shearing on the Massive Chromitite Layer higher up in the stratigraphy of the complex. It is therefore important to identify and interpret the similar geological structures within the study area. Geological structures reflect the nature and intensity of the different stresses that were active in the area. Consequently a structural investigation of the study will assist in the distinction between the effects of post-intrusive tectonic deformation and syn-intrusive depositional possesses on the thickness of the Massive Chromitite Layer.

The second part of the research focuses on the petrographic study and the mineral geochemistry of the chromite. The petrographic properties of the chromite crystals, such as crystal size and crystal fracturing, should provide some insight into the mechanical dynamics of the magma during the deposition of the chromite. The mineral chemistry on the other hand should reveal if the Cr/Fe ratio can be used to identify progressing differentiation of the chrome minerals. Because the Uitkomst Complex is interpreted to represent a replenished open conduit system *(Gauert et al., 1995)*, several episodes of chromitite deposition are assumed, which could contribute to the thickness of the Massive Chromitite Layer.

1.3 Regional geology and setting of the Uitkomst Complex

The Uitkomst Complex is a mafic to ultra-mafic intrusive complex. It is 2044Ma old (*De Waal et al., 2001)* and intruded into the Malmani Subgroup (2400Ma) and the Timeball Hill Formation (2281Ma) of the Transvaal Supergroup (fig. 1.1).

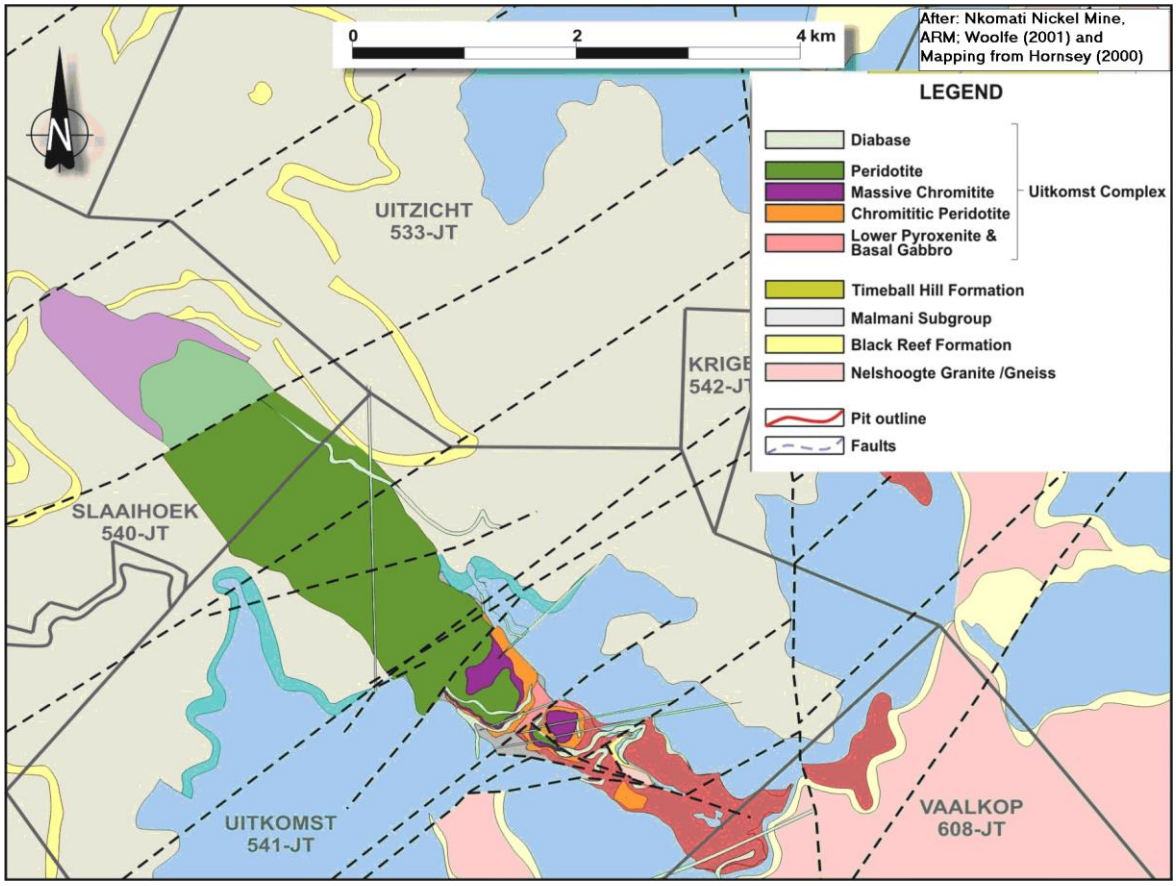

Figure 1.2: Geological map of the area around the Uitkomst Complex outcrop.

In the area surrounding the Uitkomst Complex the Black Reef Quartzite at the base mainly consists of grit and pebble conglomerate, followed by quartzite at the top. The Oaktree Formation consists of coarse-grained quartzite, followed by the Malmani Dolomite which is about 150 m thick. The subsequent Rooihoogte Formation consists of chert and the Bevets Conglomerate. This is overlain by about 1200m the Timeball Hill Shale (*Li et al., 2002; Maier et al., 2004).*

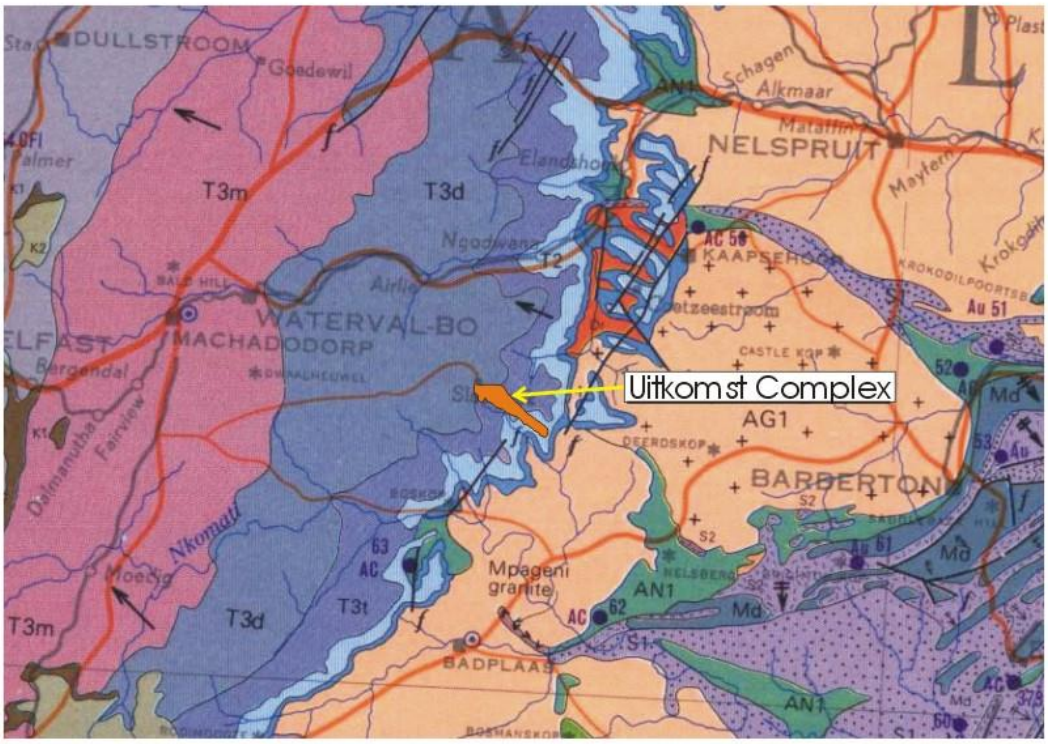

T3s	Quartzite, shale, hornfels, limestone, andesite, tuff, conglomerate	Smelterskop Stage	Pretoria Series
T3m	Quartzite, shale, hornfels, lava, pyroclasts, jaspilite, banded ironstone, chert, limestone	Magaliesberg Stage	
T3d	Quartzite, shale, tillite, andesite chert, jaspilite, limestone	Daspoort Stage	
T3t	Quartzite, shale, conglomerate	Timeball Hill Stage	
T2	Dolomite, banded ironstone, chert, shale, quartzite, conglomerate, tillite		Dolomite Series
T1	Quartzite, shale, conglomerate, andesite		Black Reef Series

TRANSVAAL SYSTEM

Dr	Conglomerate, quartzite, shale, phyllite, limestone, tillite, lava	DOMINION REEF SYSTEM (including Soetlief, Godwan and Uitkyk beds)
AG1	Granite, granodiorite	Kaap Valley and Rooiwater granites
AN1	Ultrabasic and basic intrusives and their metamorphosed derivatives	Jamestown and Rooiwater Igneous Complexes; other similar intrusives probably of various ages
Md	Conglomerate, quartzite, shale, limestone, lava	MOODIES SYSTEM
S2	Greywacke, shale, banded ironstone, volcanic	Fig Tree Series
S1	Basic and acid volcanics; sediments	Onverwag Series
S	Metamorphosed sediments, volcanics and intrusives, probably of various ages	KHEIS AND SWAZILAND SYSTEMS (including the Kraaipan, Messina, Mfongosi and Nondweni beds)

SWAZILAND SYSTEM

Figure 1.1: The geographical and geological setting of the Uitkomst Complex.

(European Commission. Joint Research Center, 1995)

The Uitkomst Complex is a layered intrusion with an elongated trough or boat like shape. The complex is enriched with Ni, Cu and PGE minerals and minor volumes of Co and Au *(Kenyon et al., 1986; Gauert et al., 1995; Gauert 2001; Theart & de Nooy 2001; Li et al., 2002; Maier et al., 2004)*. The Complex is exposed for about 9 km on the farms Slaaihoek 534-JT, Uitkomst 541-JT and Vaalkop 608-JT (fig. 1.2). These farms are situated about 20km north-northeast from Badplaas in the Mpumalanga province of South Africa (fig. 1.1). The complex has an average width ranging between 650m and 1600m, a thickness of 750 meters and dips at low (4° - 5°) angle towards the north-west.

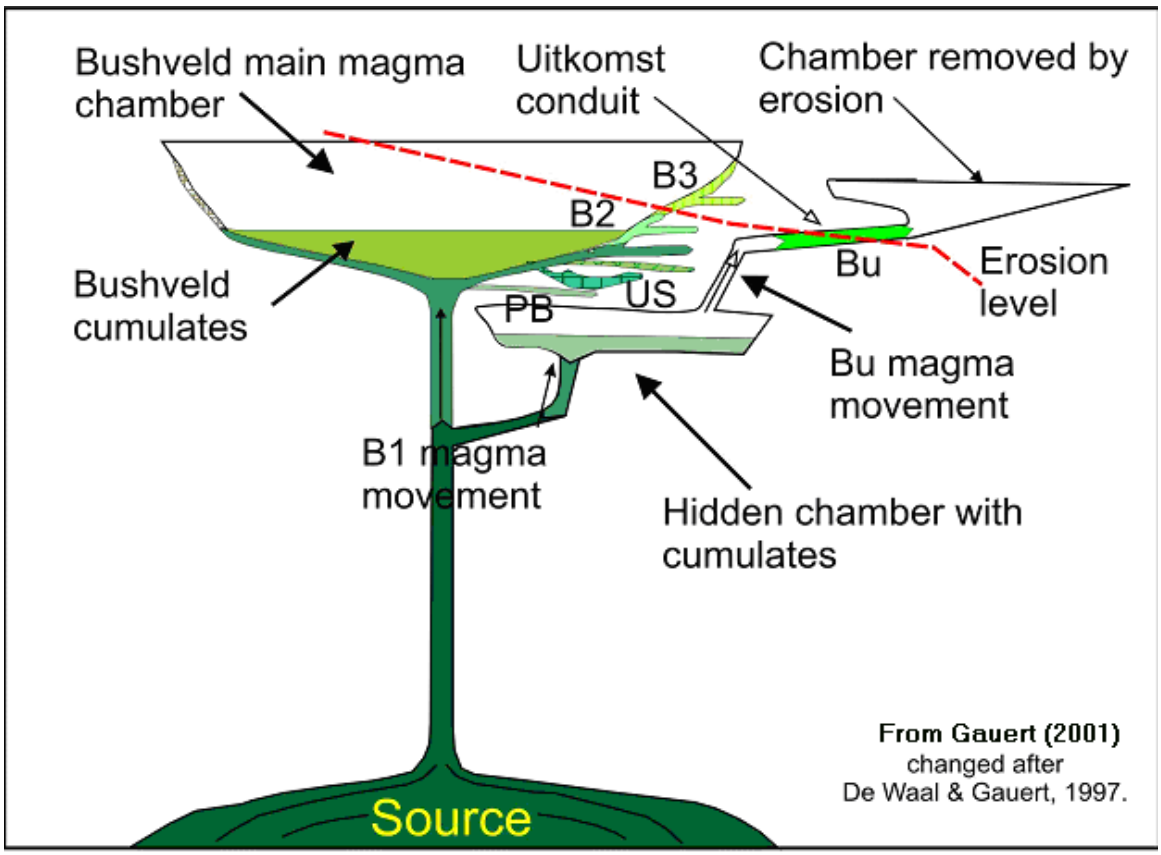

Figure 1.3: A conduit model suggested for the formation of the Uitkomst Complex.

Geochemical modeling of the magmatic processes, revealing a fractionated sequence with associated sulfide mineralization and the geochemical affinity suggests a genetic link to the assumed Bl - B2 parental magma compositions of the Bushveld Complex. A conduit model has been proposed to explain this link. (fig. 1.3) *(De Waal and Gauert, 1997; Gauert, 1998; De Waal et al., 2001; Gauert, 2001)*. Based on the abundance of xenoliths in the Lower Harzburgite and part of the chromitiferous

Harzburgite units, the primitive B1 heaves were significantly contaminated, increasing the volatile content of the magma. This culminated with the precipiation of the massive chromitite at the top of the PCR, which had their greatest thickness on the farm Uitkomst, forming prominent chromitite hills after erosion *(Gauert, 1998)*.

1.4 Local geological setting

The Uitkomst Complex is composed out of the following six lithological units from bottom to top (Fig1.5): Basal Gabbro, Lower Harzburgite, Chromitiferous Harzburgite, Main Harzburgite, Upper Pyroxenite and Gabbronorite *(Gauert et al., 1995; de Waal et al., 2001; Gauert, 2001)*.

The following rock types are present in the study area (open-pit3) (fig. 1.4):
a) Serpentine-talc-carbonate schist that is highly foliated; b) Serpentinized to uralitizised chromitiferous harzburgite; c) Rigidly-behaving brittle layers of massive chromitites; d) Gently folded, oxidized massive to semi-massive chromitite and e) Saussuritisized diabase sills.

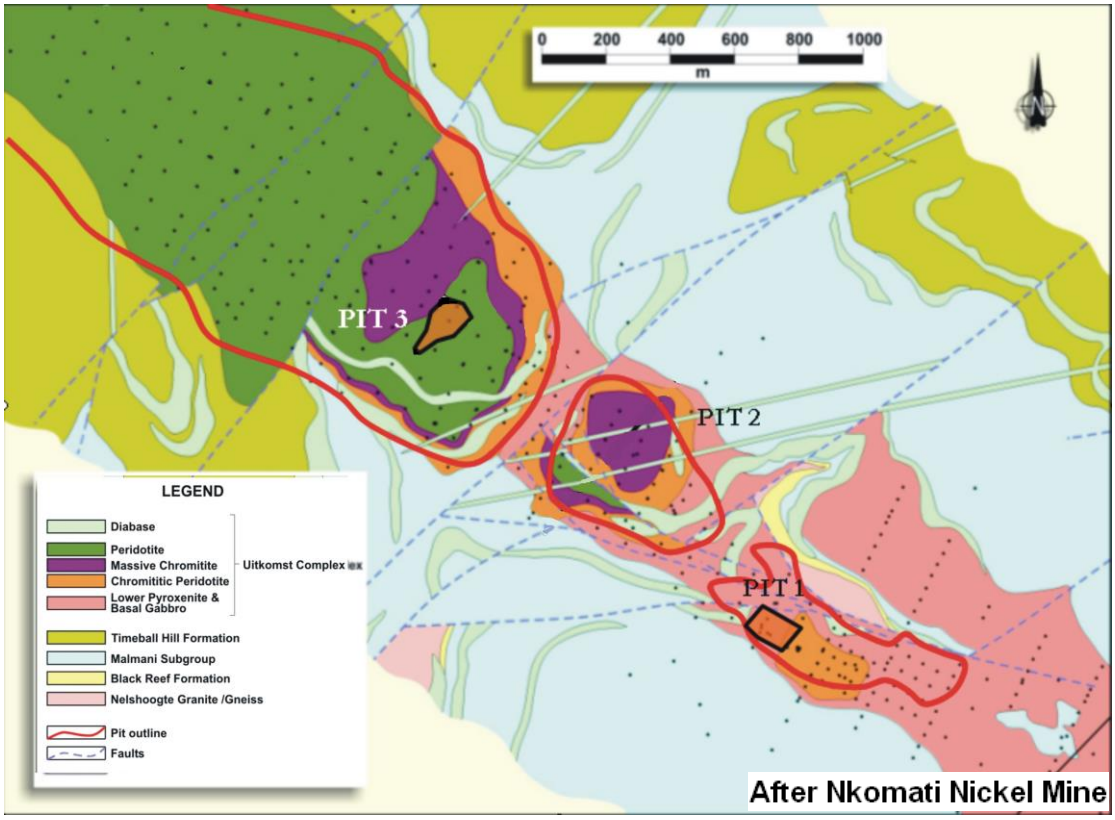

Figure 1.4: Geological map of the Uitkomst Complex with planned mining operations.

Two types of rock alteration are present in the study area: Firstly, late-magmatic to hydrothermal ‘deuteric’ alteration that occurred as a result of the influx of country rock formation water in the cooling phase of the intrusive rocks after emplacement. This alteration gave rise to a considerable volume increase resulting in strong shearing as expressed in the formation of talc-carbonate schist. Secondly, more recent surface weathering occurred after uplift of the cratonic basement and exposure to erosion.

Major structural contacts occur within the chromitiferous harzburgite unit (PCR), and steep dipping, north-west trending normal faults with vertical displacement of several kilometers are frequently observed. A number of north-east / south-west running normal faults, possibly displacing the lower three rock units of the complex for some tens of meters, which effect the north-western limit and the easternmost part of open pit 3 (fig. 1.4). A late episode of strike-slip faults oriented 050-060°TN, is related to the Gondwana break-up, and cause minor displacement of the complex. Post-intrusive diabase dikes and sills, exploiting sub-horizontal shear zones, displace the rock units vertically (fig. 1.5) *(Gauert, 1998)*. The chromitiferous harzburgite unit (PCR), which is below the Massive Chromitite Layer (fig. 1.5), commonly is a highly folded and sheared rock unit *(Gauert, 1998; Hornsey, 1999)*.

Two pairs of north-west / south-east trending contact rocks (marginal quartzite or 'rheomorphic breccia') are situated on either side of the Uitkomst lower trough and ore body, probably exploiting an extended pre-intrusive lineament parallel to the Uitkomst lineament *(Gauert et al., 1995)*. This theory has later been refuted by Hornsey (1999) who however agrees in the finding of partially molten and vertically tilted country rocks as stated by Gauert et al. (1995). Subsequent to its emplacement the Uitkomst Complex has been object to diabase sill intrusion and layer-parallel thrust-faulting *(*Gauert et al, 1995; *Hornsey, 1999)*.

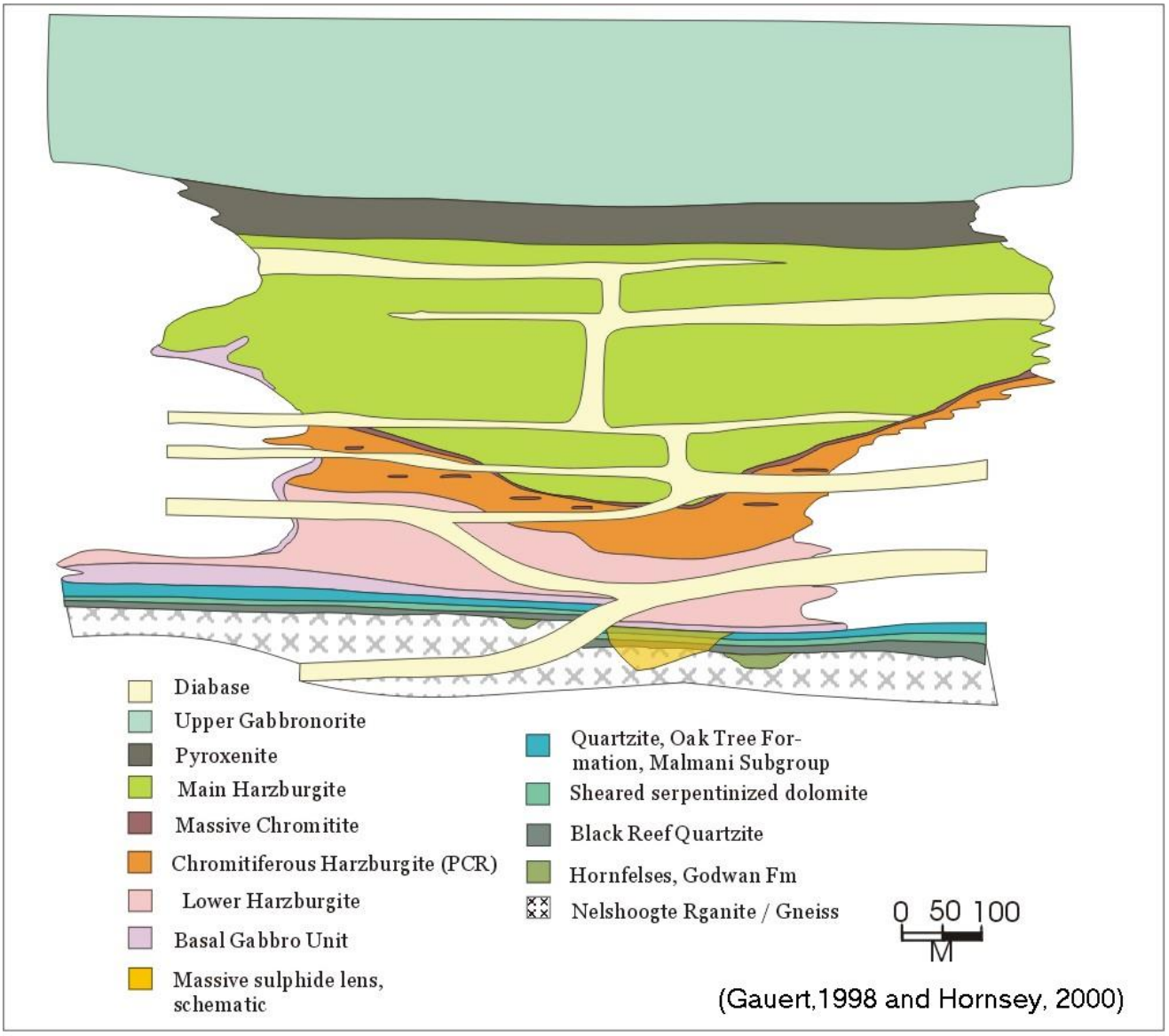

Figure 1.5: Generalized cross section of the Uitkomst Complex.

As emplacement mechanism for the Uitkomst intrusion, Gauert (1998) and De Waal et al, (2001) suggest the exploitation of a dilational jog by magma pulses of the replenished magmatic system. Hornsey (1999) elaborates on the emplacement mechanism by suggesting upwards propagation into the shale hanging wall during the later magma pulses of the intrusion 'chamber phase' following tensional fractures formed during the 'sill-phase' (fig. 1.6 from Hornsey, 1999).

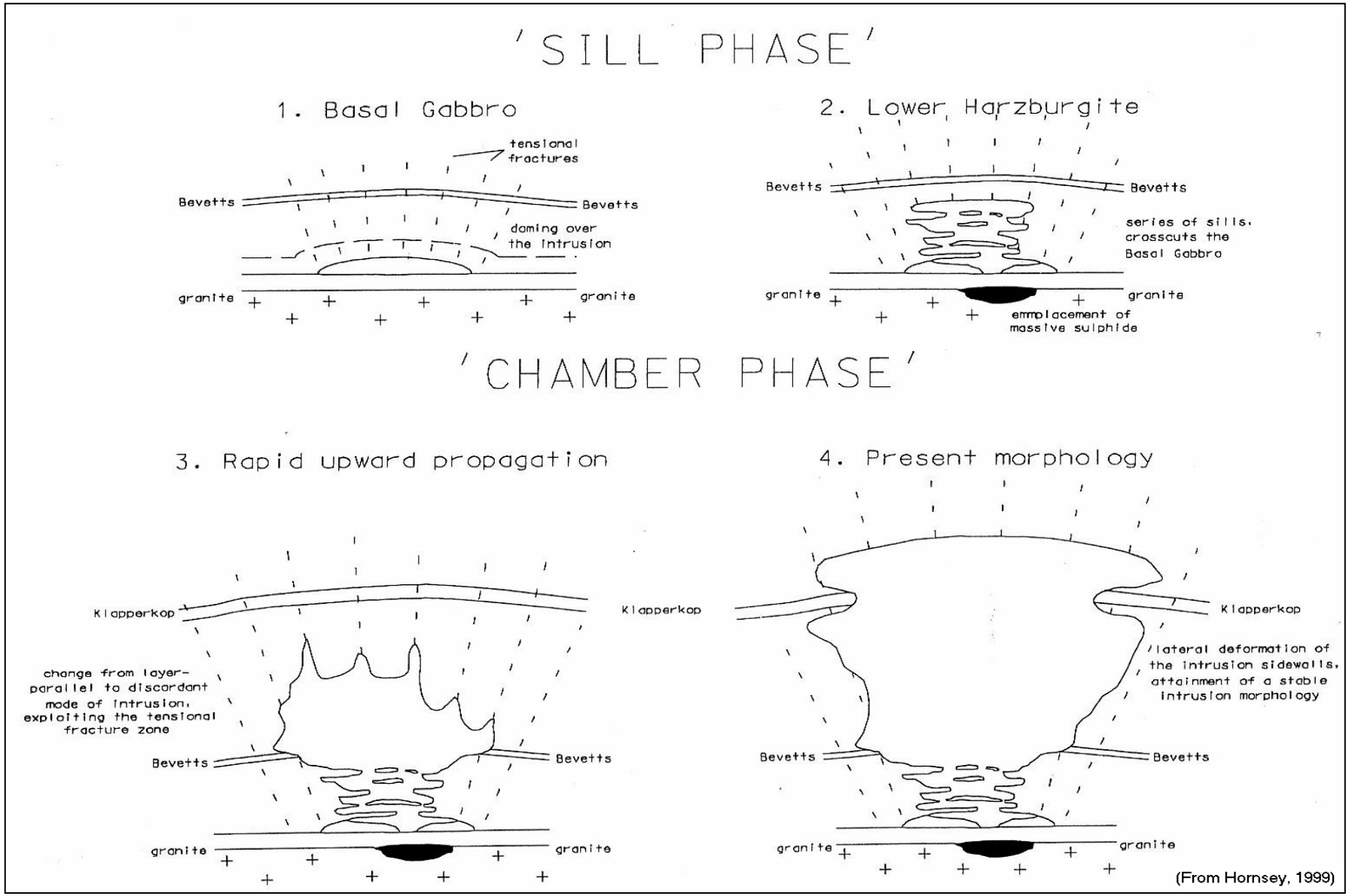

Figure 1.6: Sequence of the intrusion of the Uitkomst Complex (from Hornsey, 1999).

The major deformational event that influenced the Uitkomst Complex during the Bushveld age is layer-parallel shearing at various elevations throughout the complex *(Harley & Charlesworth, 1991, 1995; Boer et al., 1995; Hornsey, 1999)*. Figure 1.7, a long section of the Uitkomst Complex on the farm Slaaihoek after Hornsey (1999), clearly illustrates how these layer-parallel shearing deforms the complex and more specifically the Chromitiferous Harzburgite Layer (PCR) and the massive chromitites which is the top layer of the PCR. Figure 1.7 also illustrates that shearing took place below and above the PCR unit, and partly within it. This deformation style is considered to continue also on the farm Uitkomst to the south-east and will be discussed in the course of chapter 4.

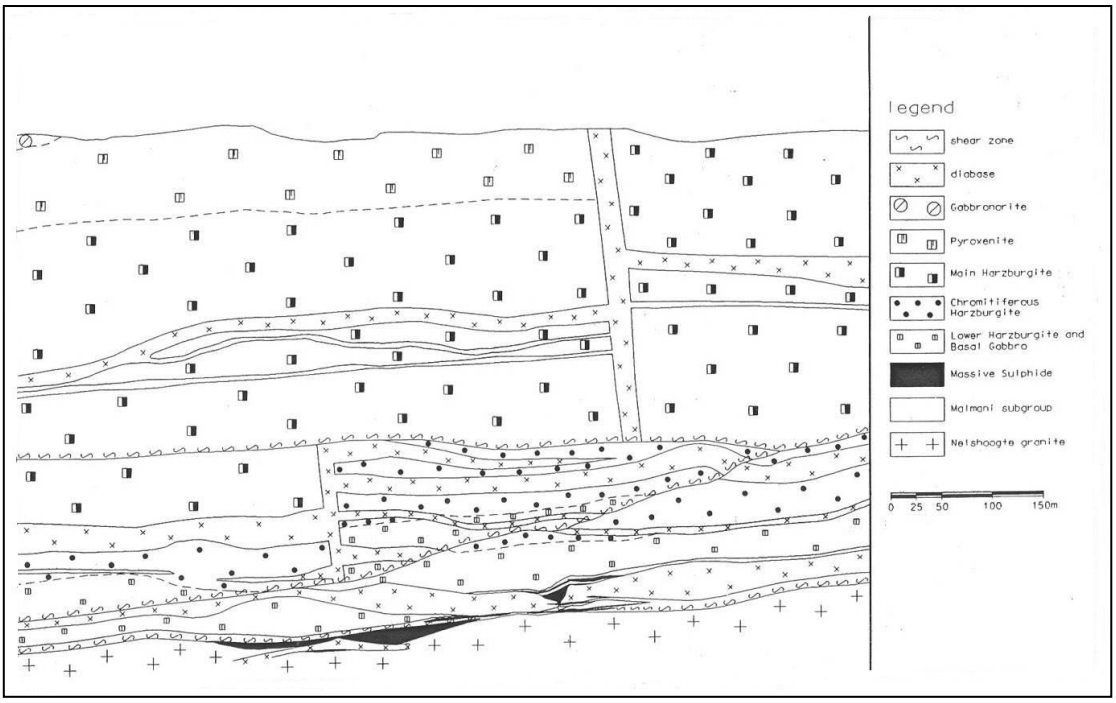

Figure 1.7: Long section of a portion the Uitkomst Complex on the farm Slaaihoek looking north-east. (Hornsey, 1999).

Figure 1.8 presents a portion of the long section of the Uitkomst Complex after Theart et al. in Gauert 1998, in the vicinity of the study area. In this figure the layer parallel shearing only occurs in the basal area of the complex and not in the Chromititic Peridotite Unite or as revered to in this study, the Chromitiferous Harzburgite Layer (PCR). Therefore it is possible that the Bushveld-age layer-parallel shearing might not be present in the study area.

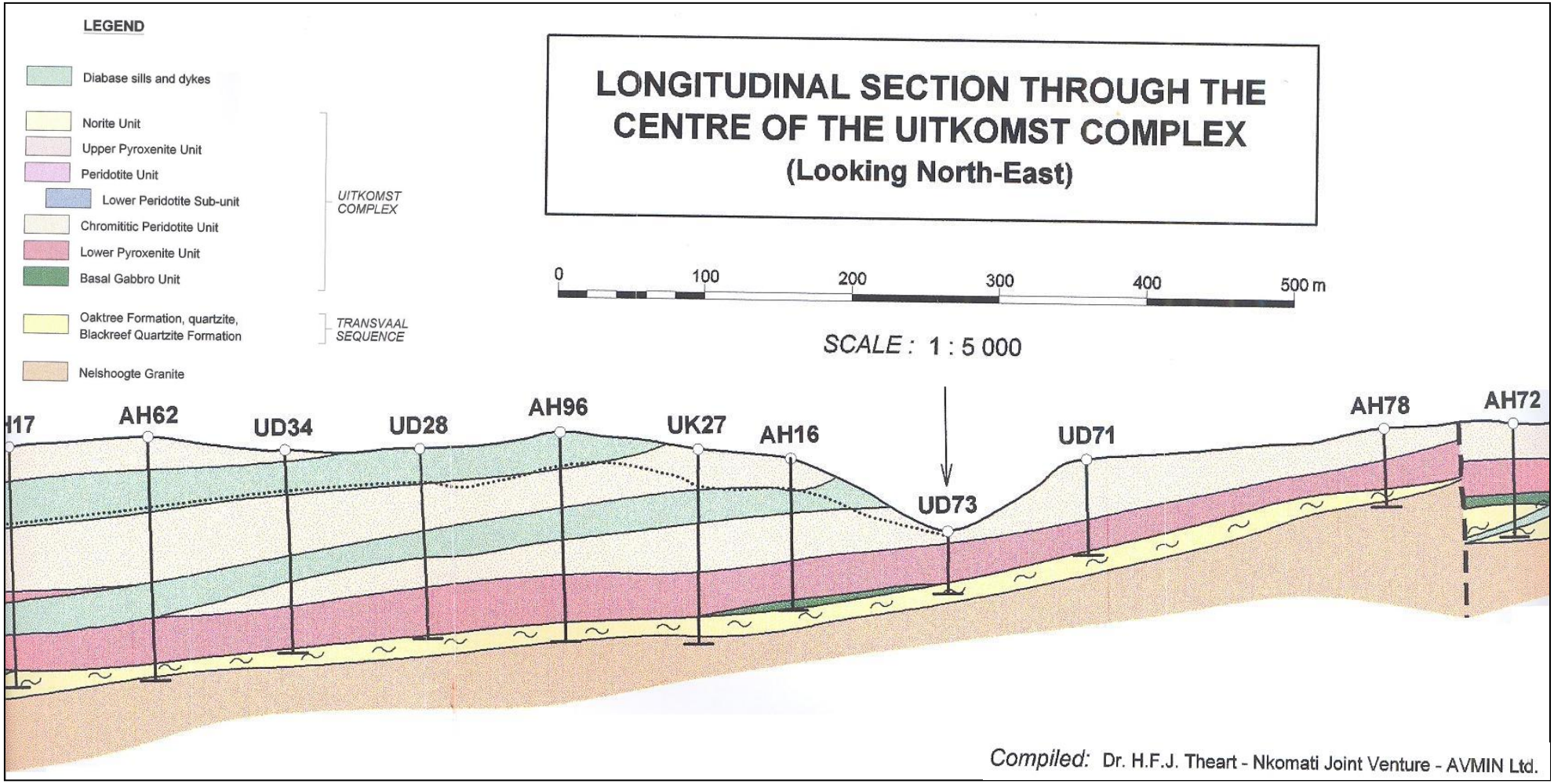

Figure 1.8: Long section of the Uitkomst complex indicating the layer parallel shearing at the location of the study area (from Gauert, 1998).

Age	Structural/Intrusive event	Reference
Mesozoic	NW/SE faulting, fracture set. NNE/SSW aligned strike slip faulting. N/S dykes.	This study. Hartzer 1995, Rozendaal *et al.* 1986. This study.
Bushveld	Layer-parallel thrust faulting. Cleavage in TBH shale.	Harley & Charlesworth 1991,1995, Boer *et al.*1995. This study. This study.
Pre Bushveld	Diabase sill intrusion, possibly associated with NNE dykes. Development of NW/SE and NE/SW interference folding, intrusion of Uitkomst Complex.	Sharpe and Snyman 1978, This study. Hartzer 1995, Rozendaal *et al.*1986, Bumby 1997, This study
Transvaal	Uplift & erosion of Chuniespoort Group. Syn depositional step faulting of Black Reef Formation and Chuniespoort Group.	Button 1973, 1986. Menell *et al.* 1986.
Post Godwan	Faulting/folding of Godwan Formation.	Laubscher 1986.
Godwan	Deposition controlled by NE/SW, NW/SE and E/W aligned structures.	Eriksson and Reczko 1995.
Pongola	Intrusion of NW/SE dyke swarm.	Visser 1957, Uken and Watkeys 1997
Archaean	Evolution and stabilisation of Barberton Granite/Greenstone terrain.	Anhaeusser *et al.* 1979. Corner 1991.

Table 1.1: Summary of structural history of the Uitkomst Complex (from Hornsey, 1999).

The structural evolution of the Uitkomst Complex is summarized by Hornsey (1999) in his summary of structural history (see table 1.1 in Hornsey, 1999). This summary will be used to understand the different stages of deformation in the study area. The Bushveld age layer-parallel thrust faulting was already earlier recognized in the region, Hornsey (1999) provides a detailed discussion of the impact of layer-parallel shearing on the basal units of the Complex, specifically the massive sulphide lenses, the Basal gabbros and Lower Pyroxenite units. This model will be discussed in conjunction with the structures in the study area.

Table 1.1 summarizes the deformational history of the Uitkomst area after Hornsey (1999); the effects of these phases on the complex will be discussed in detail in chapter 4 and the discussion, chapter. However, the complex is only affected by Bushveld-age and Mesozoic deformation, while the country rocks show deformation of the first four phases, Transvaal to Mesozoic ages.

1.5 Mining background

The complex hosts a massive sulfide body at the base, which is being mined by Nkomati Nickel Mine from 1996 to 2007. Continued underground mining of disseminated ore, containing a resource of 5.6 million tons grading 2.04% Ni, 1.13% Cu, and 6.97 g/t combined Pt, Pd, Rh, and Au was defined *(Anon, 1997)*.

In 2004 the life of mine was extend for at least 15 years by adding an estimated 139 million tons of nickel ore to the reserves at a grade of 0.49% Ni. Situated on the farms Uitkomst 541 JT and Slaaihoek 540JT (fig. 1.2), in total an estimated 680,000 tons of nickel metal *(LionOre, 2005)* were to be mined. Africa Rainbow Minerals (ARM) in a joint venture with Norilsk Nickel of South Africa are mining the main part of the disseminated ore from the three lowermost rock units namely: Basal Gabbro, Lower Harzburgite, and Chromitiferous Harzburgite Units (fig. 1.5). Three open-pit operations and considerable new underground structure will be developed (fig. 1.4). Beneficiation initially was planned to be using the high-pressure Activox hydrometallurgical leach process, however currently a 12% Ni containing FeS concentrate is shipped for conventional and pyrometallurgical processes to overseas.

The massive and disseminated chromitite is being mined in open-pit 3 (fig.1.4) for its chrome content. The layers of massive chromitite are overlying a sulfide-enriched zone and have been stripped in the south-eastern part of the pit and the metal sulfides from the MMZ are currently being recovered. The final size of open pit 3 is planned at about 2.5km X 850m X 140m to 360m.

Chapter 2: Methodology

This chapter will explain the and aim the application technique of each process that was used during the course of the research.

The research is divided into four principal subjects:

1. General geology of the chromitite lenses. By means of open-pit mapping.
2. Geological structures. By means of open-pit mapping.
3. Petrography of the chromitite. By means of reflected microscopy.
4. Mineral geochemistry of the chromite. By means of EMPA

2.1 Investigation of the chromitite lens geology

The investigation of the general geology of the chromitite lenses represents the first phase of the research. The purpose of this investigation was mainly to get acquainted with the geometry of the Massive Chromitite Layer. Some of the ground work for the other phases was also done during this investigation *(Joubert and Gauert, 2006).*

This investigation mainly involved the mapping of the rock sections generated by the mining operation in open pit 3. The method that was used for mapping the sections is normal grid mapping and the grid was created by a horizontal and vertical measuring tape. The size of the grid is 5m X 5m, except for the areas where the complexity of the geology required a smaller grid. The geological mappings were plotted on A3 graph paper at a scale of 1:100. These mappings were digitized in Corel Draw 9-software by means of copying the essential points from the mapping to the exact point on a grid. All geological units were digitized as polygons and filled according to the color coding in the legend.

The survey measurements of the outlines of open pit 3 were optioned from the survey department of Nkomati Mine. This survey plan (fig. 3.1.8) was combined with the measurements taken during the mapping of the geological sections to generate a simplified outline plan of the open pit indicating the position and orientation of each geological section (fig. 3.1.9).

All the geological structures that were encountered during the mapping exercise were recorded on the geological profiles. The orientation of most of the structures was measured by means of a Brunton geological compass. These orientations are reported on the sections in the strike-dip notation.

During the mapping of the sections the general geological properties of each geological unit were described and illustrated. These properties include obvious rock type, mineralogy, color and hardness of minerals. The geological units were also sampled by means of random grab sampling. The position of each sample was recorded and is reported on the respective geological profiles. These samples became the basis for the textural and mineral chemical investigations.

2.2 Geological structures

The structural investigation coincided with the investigation of the geometry and composition of the chromitite lenses, by identifying, describing and recording all the geological structures in the study area. The aim of this investigation is to determine if there were any syn- to post-intrusive deformational events that contributed to the enhanced thickness of the Massive Chromitite Layer *(Joubert and Gauert, 2007).*

The structural investigation mainly involves correlating the orientation of the structures with one another, in order to determine the preferred stress orientations. The orientation of the structures is further correlated with the general intrusion orientation of the Uitkomst Complex, in order to investigate the force and influence of the flowing magma on the deformation of already solidifying geological units. All the orientations are statistically interpreted and correlated by means of stereonet diagrams and rose diagrams.

2.3 Petrography of the chromitite

The main focus of petrography is to investigate the shape, size and deformation of the chromite crystals, as well as the chromite to matrix-ratio inside the Massive Chromitite

Layer. This will shed some light on the crystallization, deposition, entrainment into crystal cumulate pile and deformation of the chromite crystals in the magmatic conduit system.

In order to perform the petrographic investigation, microscopic images were captured from polished thin sections from selected chromitite samples. The grab samples from the open-pit as well as the samples from the drill core of borehole UK33 were used in the petrographic investigation. The images were captured with a digital camera that is mounted on top of a petrographic microscope. Images were captured at using both 40 times and 100 times magnification.

The second part of this investigation involved point-counts of minerals in the thin sections. This was done in order to calculate the percentage of each crystal shape within the chromitite samples. The counts were conducted with a swift automatic point counter. The counting was performed on a grid of 2μm by 2mm. A total of 2000 points were counted per sample. Apart from the different chromite crystals that were counted, the counts also included the amount of altered silicate minerals and hydrated iron oxides. The sum of these two minerals adds up to an amount that represents the total amount of matrix material. The chromite counts, excluding the matrix minerals, were re-calculated into percentages for the different chromite crystal shapes.

The results from the point counts were further used to calculate the percentage of crystal fracturing that occurred within each of the chromitite lenses. This was achieved by assigning a weight to each crystal shape and calculating the weighted average for each lens. The weighting represents the intensity of the fracturing that the specific crystal shape was exposed to.

2.4 Mineral chemistry of the chromite

By investigating the mineral composition of the chromite crystals inside the Massive Chromitite Layer, it provides the opportunity to understand changes in the chemical composition of the magma from which the chromite were deposited. It will also show if

in-situ re-equilibration of chromite crystals with residential melt took place to reset the initial composition trends caused by magma differentiations. Hopefully core-rim compositional zonation patterns will create a better understanding of these re-equilibration processes. This forms a crucial part of the research.

In order to carry out the geochemical investigation a total of almost 400 electron-microprobe analyses were done from 38 chromitite samples. Once again the samples were prepared into polished thin sections and coated with a thin layer of carbon by using a sputtering machine. All the analyses were re-calculated into molecular percentages and plotted on scattered diagrams for investigation. The following chemical element-oxides were measured during the analyses: SiO_2, Al_2O_3, FeO, MnO, MgO, CaO, ZnO, TiO_2, Cr_2O_3 and NiO.

From the molecular percentages the following ratios were calculated and used for correlating between the different chromitite lenses: Chrome number (Cr#), Magnesium number (Mg#), Chrome iron ratio (Cr-Fe) and the Chrome aluminium ratio (Cr-Al). These ratios are calculated as follow:

$Cr\# = Cr / (Cr + X\ Fe^{3+} + Al)$

$Mg\# = Mg / (Mg + Fe^{2+})$

$Cr\text{-}Fe = Cr / (Cr + Fe\ total)$

$Cr\text{-}Al = Cr / (Cr + Al)$

Chapter 3: Geological profiles

3.1 Background information

This chapter will focus on the mapping that was done in the study area. A total of fifteen geological sections were mapped. The mappings were done by method of grid mapping on a scale of 1:100. The key elements indicated on the sections are:

a) Rock types
b) Geological structures
c) Geological textures

The orientation of the structures and textures are indicated in the notation of direction of strike / amount of dip. The positions of all the sampling points are also indicated on the sections.

The following rock types were identified in the study area *(Joubert and Gauert, 2006).*

Talc-carbonate schist: This rock type consists mainly of talc, is very soft and has a light cream color. It formed as a result of late magmatic or deuteric alteration of harzburgite (fig. 3.1.1).

Figure 3.1.1: Talc-carbonate schist.

Figure3.1.2: Fractured talc-carbonate schist.

Fractured talc-carbonate schist: It is similar to talc-carbonate schist, but it is highly fractured and appears to be more greenish in color from a higher concentration of talc and chlorite (fig. 3.1.2).

Massive chromitite: This rock type consists mainly of chromite; it is a hard, fine crystalline rock with a greyish to black color, depending on the amount of interstitial silicates. It is deposited in layers with a thickness that varies between 1m and 6m (fig. 3.1.3).

Figure 3.1.3: Massive chromitite.

Fractured chromitite: This rock type consists of chromite that contains small lenses of talc-carbonate schist that is evenly distributed throughout the layer. It is a fine crystalline and brittle rock. The chromite is dark gray and the talc lenses are yellowish in color. The fractured chromitite is present in a thinner layer with a thickness that varies between 10cm and 2m (fig. 3.1.4).

Figure 3.1.4: Fractured chromitite.

Chromitiferous harzburgite: This rock is characterized by remnants of a poikilitic texture, which are commonly found in harzburgite. The rock consists out of a mixture of chromite crystals and talc. This chromitite is softer and has a lighter color than the massive chromitite. The reason for this is that the chromitiferous harzburgite visibly contains more Talc than the massive chromitite. This is a fine crystalline rock and its color ranges from dark reddish gray to dark green gray to just light gray. The individual chromite crystals can be better observed than in the massive chromitite as they are in contrast with silicate minerals that are lighter in color. The chromitiferous harzburgite is deposited as a single layer with an average thickness of 8m. The talc concentration differs through-out this layer and tends to increase towards the bottom (fig. 3.1.5).

Figure 3.1.5: Chromitiferous harzburgite.

Scattered chromitite: Consist out of a talc matrix with small and scattered lenses of chromitite. The senses are elongated in a horizontal orientation with an average length of 20cm. It is a very soft, fine crystalline rock with a yellowish light gray color.

Sheared chromitite: These are thin layers of chromitite that are highly sheared. It consists of thin foliated layers of chromite and Talc. It is a very brittle rock (see fig. 3.1.6).

Figure 3.1.6: Sheared chromitite.

Figure 3.1.7 presents the lithological and structural legend for the geological sections and will be referred to during the course of the chapter. The massive chromitite, chromitiferous harzburgite, and talc carbonate schist are the most prominent rock types and they occur in most of the geological sections.

The rubble on the legend refers to areas in the open pit were the blasted rock fragments from the mining operation were not yet removed and a portion of the section are covered by these rock fragments.

The surface weathering refers to the areas where the chromitite are weathered and leached by the rain water to produce a type of chromite-rich sand.

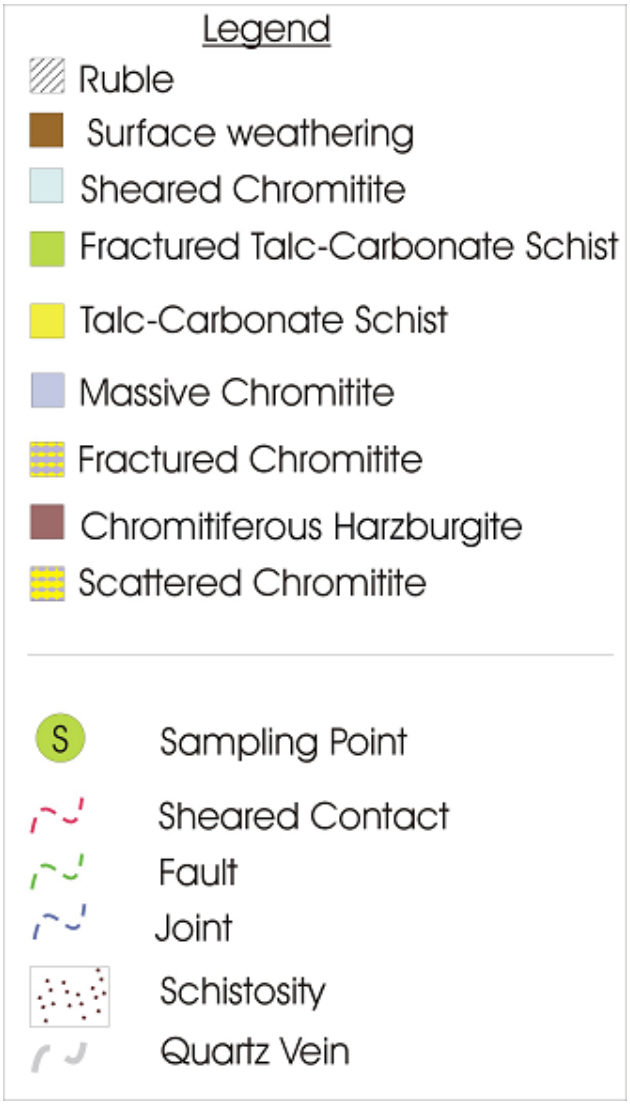

Figure 3.1.7: Standardized legend for the geological sections.

Figure 3.1.8 is the survey plan of open pit three. The green outline is the first survey of the pit during February 2006. This was also the shape of the pit throughout the first mapping exercise. The red outline is the second survey which was done during June 2006. Between the two surveys a big area was blasted in the north-western side of the pit. With every blast new geological sections are exposed.

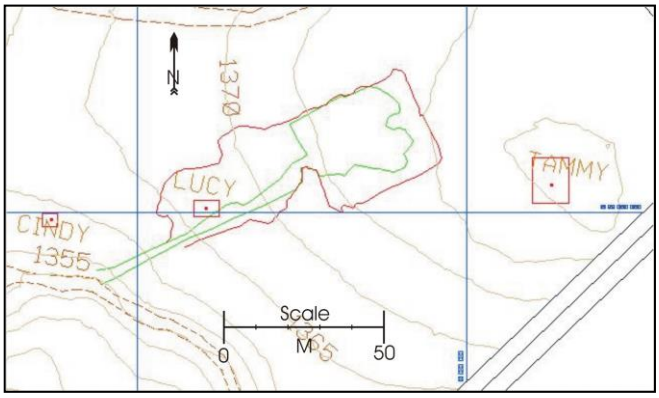

Figure 3.1.8: Survey plan of open pit 3.

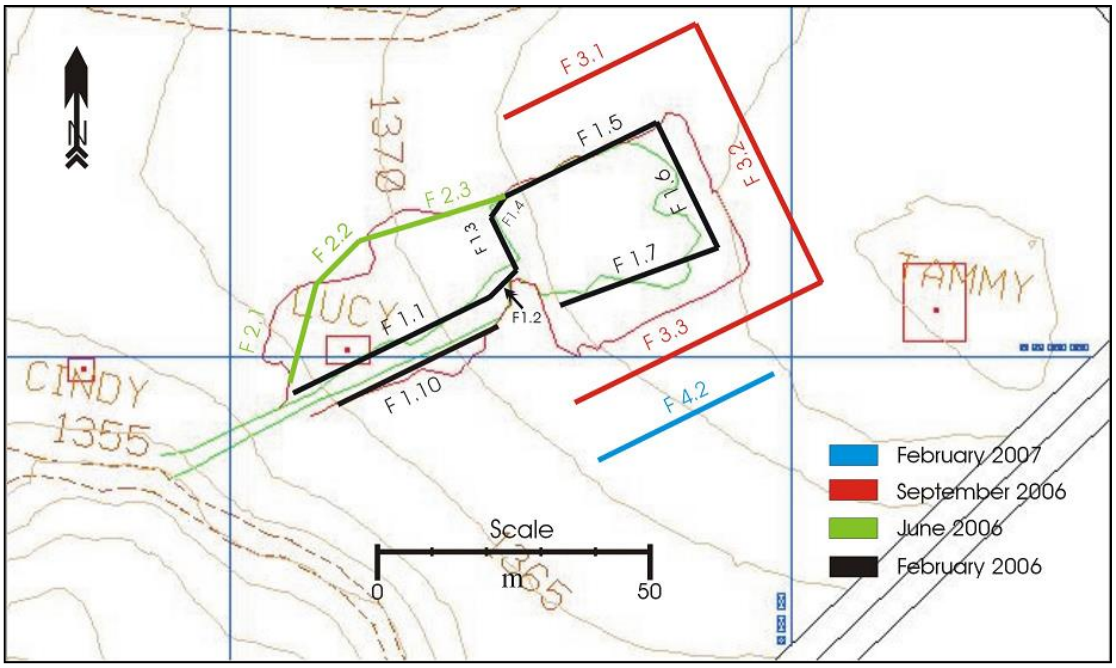

Figure 3.1.9: Simplified plan of geological sections.

Figure 3.1.9 shows the simplified survey plan of the pit. The different colors represent the time intervals during which the mapping took place. The simplified plan (fig. 3.1.9) will regularly be referred to display the position and orientation of each geological section.

3.2 Discussion of geological sections

In this paragraph all the geological sections will be discussed individually. The main criteria of discussion will be the sequences and layering of the rock units and the occurrence of structures and textures. The details of the structures and textures will be discussed in the following chapters.

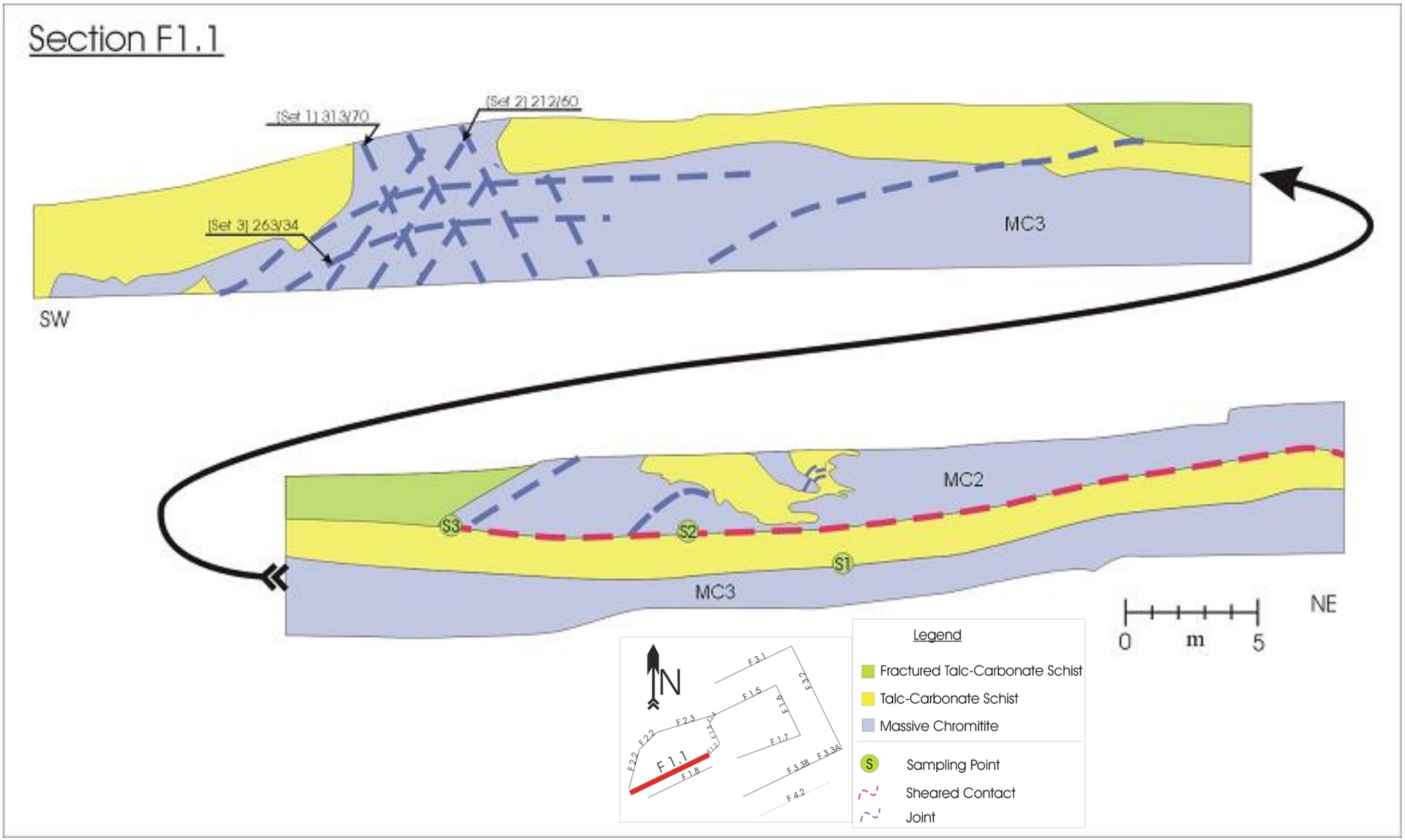

Figure 3.2.1: Geological section F1.1.

3.2.1 Geological section F1.1

Section F1.1 (fig. 3.2.1) was exposed on the northern side of the pathway leading into the pit. This section exposed two layers of massive chromitite. The two layers were separated by a layer of talc-carbonate schist. The top layer of massive chromitite was labeled chromitite layer MC2 and the bottom layer was labeled layer MC3. Layer MC3 is extensively jointed in the south-western side of the section. The jointing is orientated into three distinct directions, which is almost perpendicular to each other resulting in weathering of cubes of chromitite (fig. 3.2.2). The top chromitite layer MC2 only starts in the centre of the section and continues to the north-east. The starting point forms a sharp wedge shape that points towards the south-west. There is irregular jointing and inclusions of talc-carbonate schist associated with the area where chromitite layer MC2 starts. These joints are not continuous and are bent towards the north-east. The bottom contact of layer MC2 is a sheared contact with slickensides. This is the first observation of contact-parallel shearing in the study area. The shearing is only associated with the bottom contact of chromitite lens MC2. In contrast to the bottom contact, the top contact of lens MC3 is a thin gradational contact which indicates insitu crystal settling. It seems as if chromitite layers are lenses rather than layers of chromitite, because they are not continuous.

Figure 3.2.2: Jointing of chromitite lens MC3 to the south-west of section F1.1.

There is some fractured talc-carbonate schist associated with the starting position of chromitite lens MC2. This zone is approximately ten meters wide and it seems as if this zone was subjected to high levels of stress.

3.2.2 Geological section F1.2

Section F1.2 (fig. 3.2.3) is adjacent to section F1.1. This section presents the continuation of lenses MC2 and MC3. The difference between the top contact of chromitite lens MC3 and the bottom contact of chromitite lens MC2 is very prominent in this section. The talc carbonate-schist layer between the two chromitite lenses seems to be continuous.

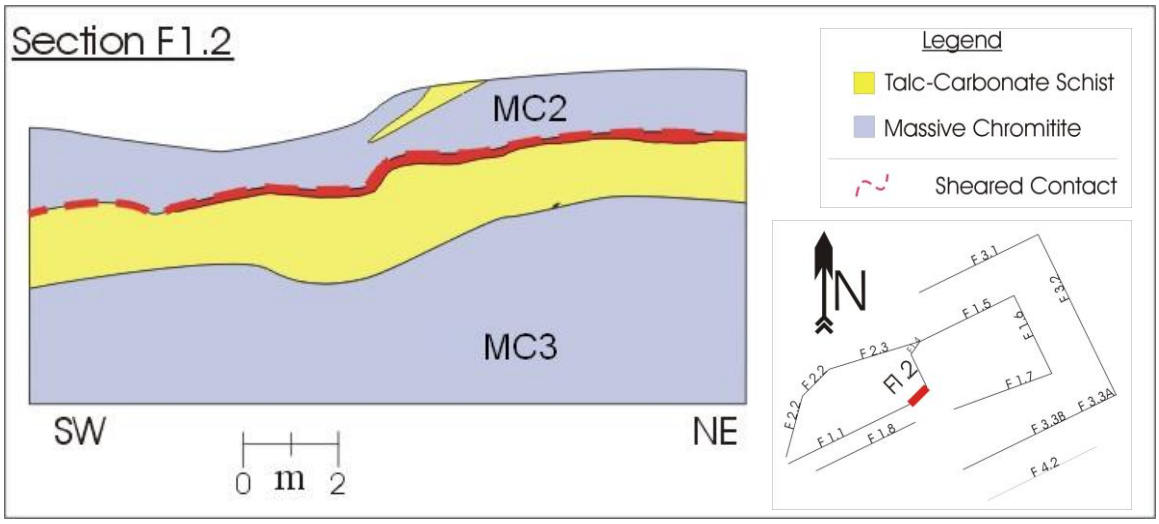

Figure 3.2.3: Geological section F1.2.

3.2.3 Geological section F1.3

Section F1.3 is adjacent to section F1.2. Once again it presents the continuation of chromitite lenses MC2 and MC3 (fig. 3.2.4). Lens MC2 ends again at the northern margin of the section and forms a blunt wedge pointing northwards (fig. 3.2.5). The layer of talc-carbonate schist between the two chromitite lenses drastically thins out in the area that chromitite lens MC2 stops. In the northern side of the section the contact parallel shearing strictly follows the bottom contact of chromitite lens MC2 and the adjacent chromitite lens. The deformation direction is out of the plane into the spectator's direction which is in accordance with the model of NW-SE layer-parallel thrusting.

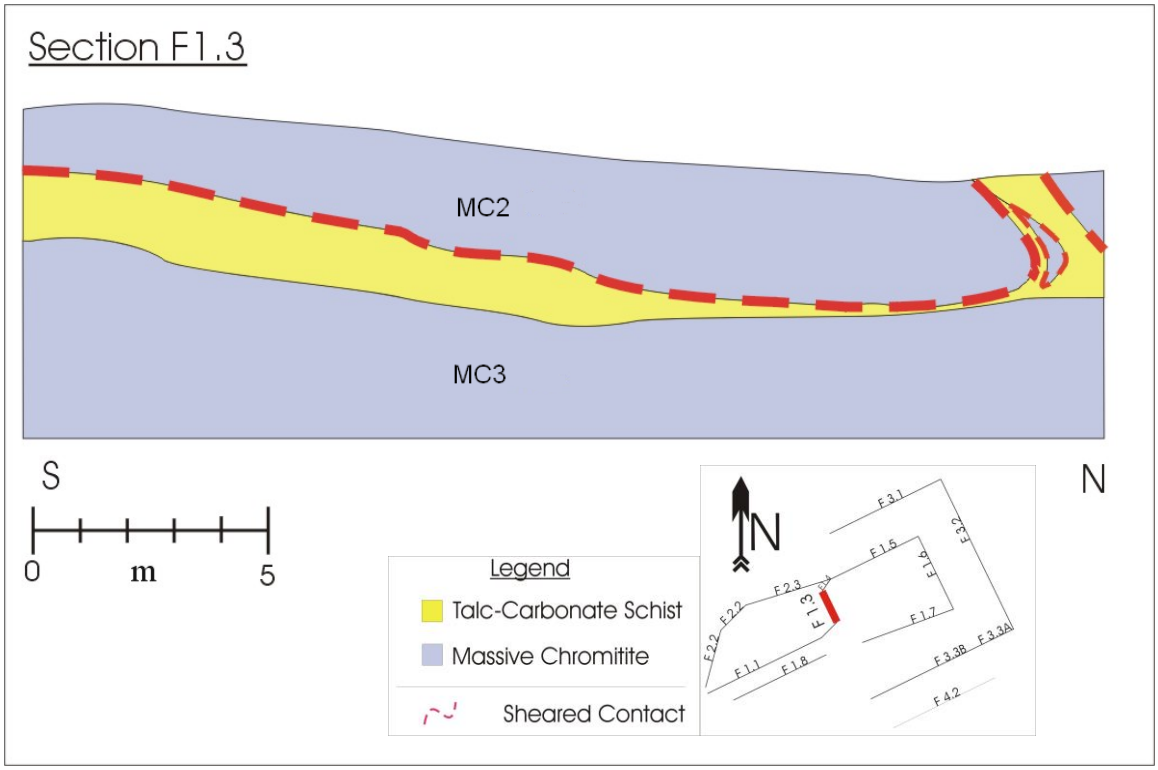

Figure 3.2.4: Geological section F1.3. The deformation direction is out of the plane into the spectator's direction.

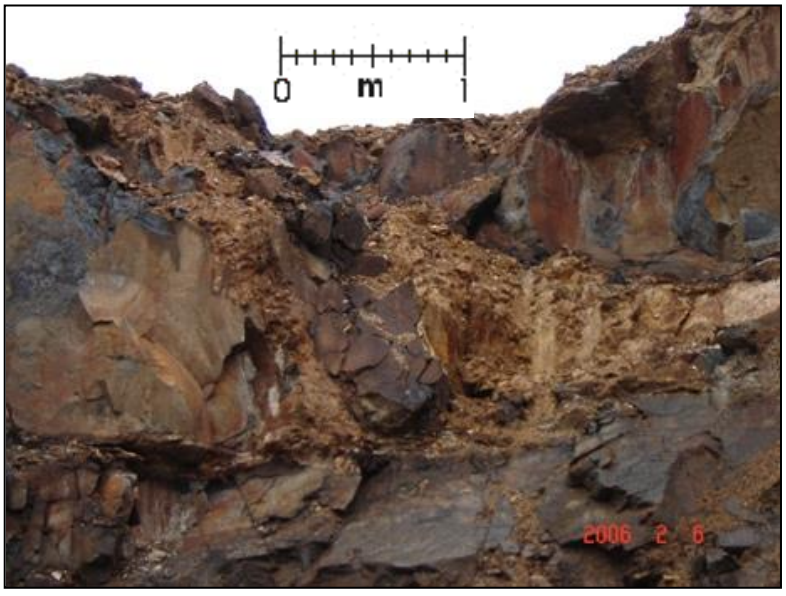

Figure 3.2.5: Photograph of blunt wedge shaped end of chromitite lens MC2.

3.2.4 Geological section F1.4

Section F1.4 (fig. 3.2.6) is adjacent to section F1.3. The prominent massive chromitite lens that occupies the majority of the section is the continuation of chromitite lens MC3. There are two other massive chromitite lenses above MC3. Lens MC2 in the north-east corner of the section is shaped in a wedge that points to the south-west; there is only a small portion of this lens exposed. The other lens in the top middle portion of the section is a new massive chromitite lens and is labeled lens MC1. It seems as if lens MC3 is the older lens of the three lenses and that lens MC2 was deposited on top of lens MC3. Lens MC1 is the youngest and was deposited as a blanket that covers parts of both lenses MC2 and MC3 (fig. 3.2.7).

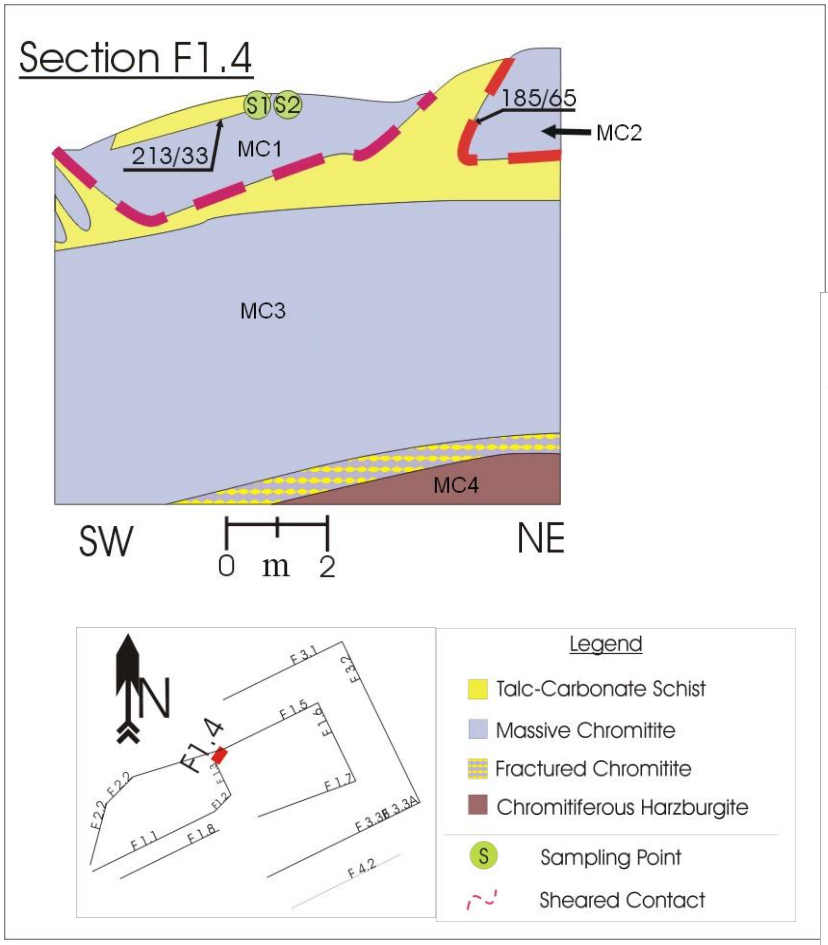

Figure 3.2.6: Geological section F1.4.

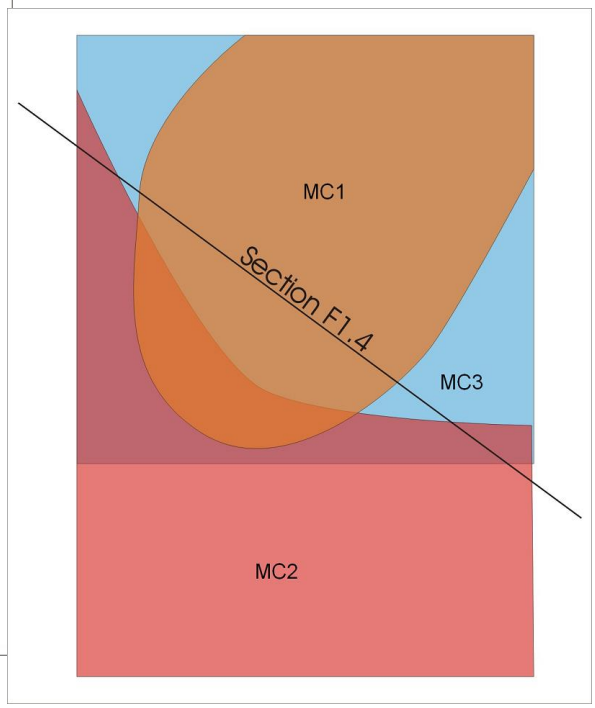

Figure 3.2.7: Sketch of proposed plan view for area around geological section F1.4.

It is interesting to note the consistent pattern of the talc-carbonate schist that divides the chromitite lenses and the sheared bottom contact for both chromitite lenses MC2 and MC1. Below lens MC3 there is a lens of chromitiferous harzburgite. This lens is labeled chromitite lens MC4 and it is separated from lens MC3 by a thin layer of fractured chromitite that represent the contact parallel shearing at the bottom of chromitite lens MC4 (fig. 3.2.8). In this section the contact parallel shearing strictly follows the bottom contat of all three chromitite lenses that are exposed.

Figure 3.2.8: Photograph of section F1.4.

Section F1.5 (fig. 3.2.9) is continuous from section F1.4. Chromitite lens MC2 ends in the south-west side of the section. There is a thin layer of fractured chromitite attached to the end of lens MC2 (fig. 3.2.10). Lenses MC3 and MC4 are very prominent in this section. The layer of fractured chromitite, between lenses MC3 and MC4, thins out to the north-east and disappears into a sheared contact that separated the two chromitite lenses.

3.2.5 Geological section F1.5

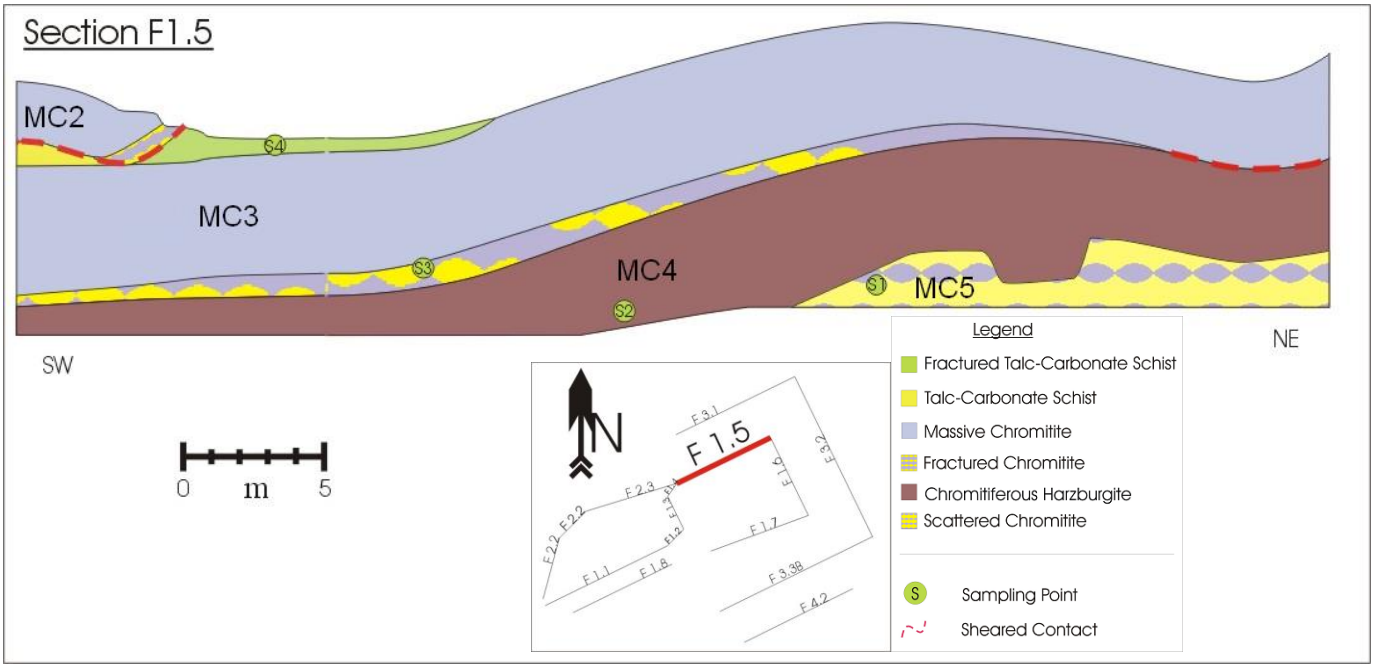

Figure 3.2.9: Geological section F1.5.

Below lens MC4 there is a lens of scattered chromitite exposed and this lens is labeled chromitite lens MC5. There is a soft monocline to the north-east of the section that assists in exposing lens MC5. The layer of Talc-carbonate schist between the chromitite lenses MC3 and MC3 seems to be missing, although the prominent contact parallel shearing zone still follows the bottom contact of chromitite lens MC4. Chromitite lenses MC4 and MC5 are separated by a gradational contact and there is no indication of shearing on this contact.

Figure 3.2.10: Photograph of the south-west portion of section F1.5.

3.2.6 Geological section F3.1

Section F3.1 (fig. 3.2.11) is the next section that was exposed to the north-west, after the area around section F1.5 was removed by the mining operation. Most of this section consists of Chromitiferous Harzburgite (lens MC4). There is a thin layer of fractured chromitite inside the chromitiferous harzburgite layer. There are only remnants that remain of chromitite lens MC3 and it seems as if this chromitite lens does not continue further north. As an exception to the norm the top contact of chromitite lens MC4 is a sheared contact. This implies a discontinued crystallization sequins between chromitite lenses MC4 and MC3 coming from the bottom.

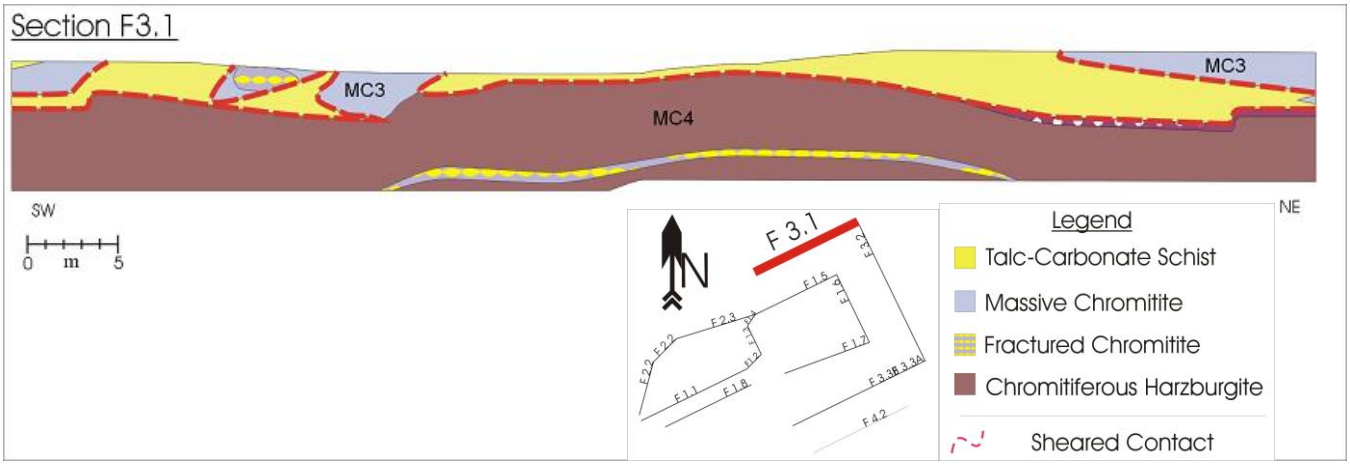

Figure 3.2.11: Geological section F3.1.

3.2.7 Geological section F1.6

Section F1.6 (fig. 3.2.12) continues perpendicularly from section F1.5. In this section chromitite lens MC4 is very prominent. Massive chromitite lens MC3 is much thinner than in section F1.5. Although there was no talc-carbonate schist present between chromitite lenses MC4 and MC3 for the entire extent of section F1.5, geological section F1.6 displays the classic sequence of two chromitite lenses divided by a layer of talc-carbonate schist. The top contact of both the chromitite lenses is a gradational contact. There are two clusters of joints in the section. The cluster on the north-west side of the section extends from the deeper rocks, passing through chromitite lenses MC4 and MC3 and stop at the top contact of lens MC3 with the upper talc-carbonate schist. The second

set of joints on the south-east side of the section only cuts through chromitite lens MC4 and stops at the top contact of this lens with the lower talc-carbonate schist.

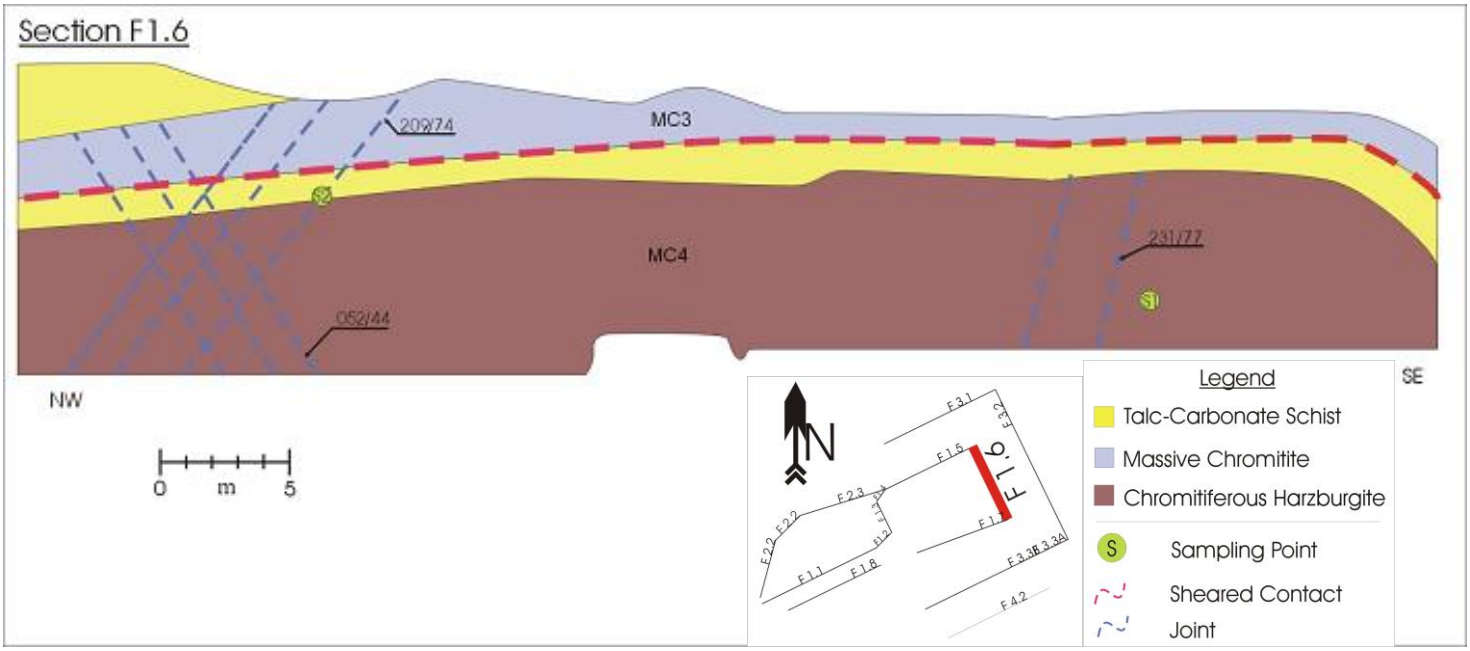

Figure 3.2.12: Geological section F1.6.

It is very important to note that the jointing is not displaced by the contact parallel shear at the bottom of chromitite lens MC3 although the jointing only continues to the top of the chromitite lens. Therefore the jointing is younger than the movement along the bottom contact of the chromitite lenses, but younger than the overlying harzburgite layer

3.2.8 Geological section F3.2

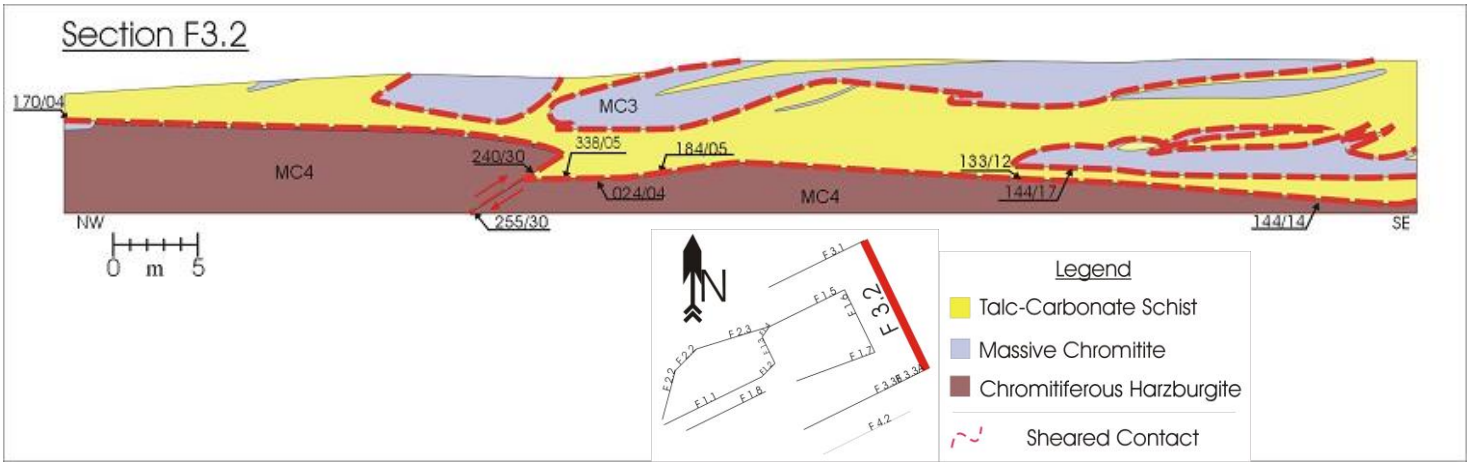

Figure 3.2.13: Geological section F3.2.

Section F3.2 (fig. 3.2.13) is the next face that was exposed to the north-east, after the area around section F1.6 was removed during the mining operation and continues perpendicularly from section F3.1. It is similar to section F3.1 and chromitite lens MC4 forms the bottom of the section. A reverse fault displaces lens MC4, but the displacement does not continue into chromitite lens MC3. Similar to section F3.1 the remains of the thinner chromitite lens MC3 are scattered (fig. 3.2.13).

3.2.9 Geological section F1.7

Section F1.7 (fig. 3.2.14) is the south-eastern continuation from section F1.6. This whole section forms a soft dome shape that is the result of down warping of the sides due to gravity settling. Chromitite lens MC3 is separated from lens MC4 by a layer of talc-carbonate schist. The bottom contact of lens MC3 is sheared. On the north-east side of this section lens MC3 gets thinner. This section exposes the scattered chromitite of chromitite lens MC5 as it has a dome shape. There are also some quartz veins in this section, which are up to 30cm thick. The quartz veins at the top of chromitite lens MC4 extend into the talc-carbonate schist layer overlaying lens MC4, but ends at the bottom contact of the chromitite lens MC3.

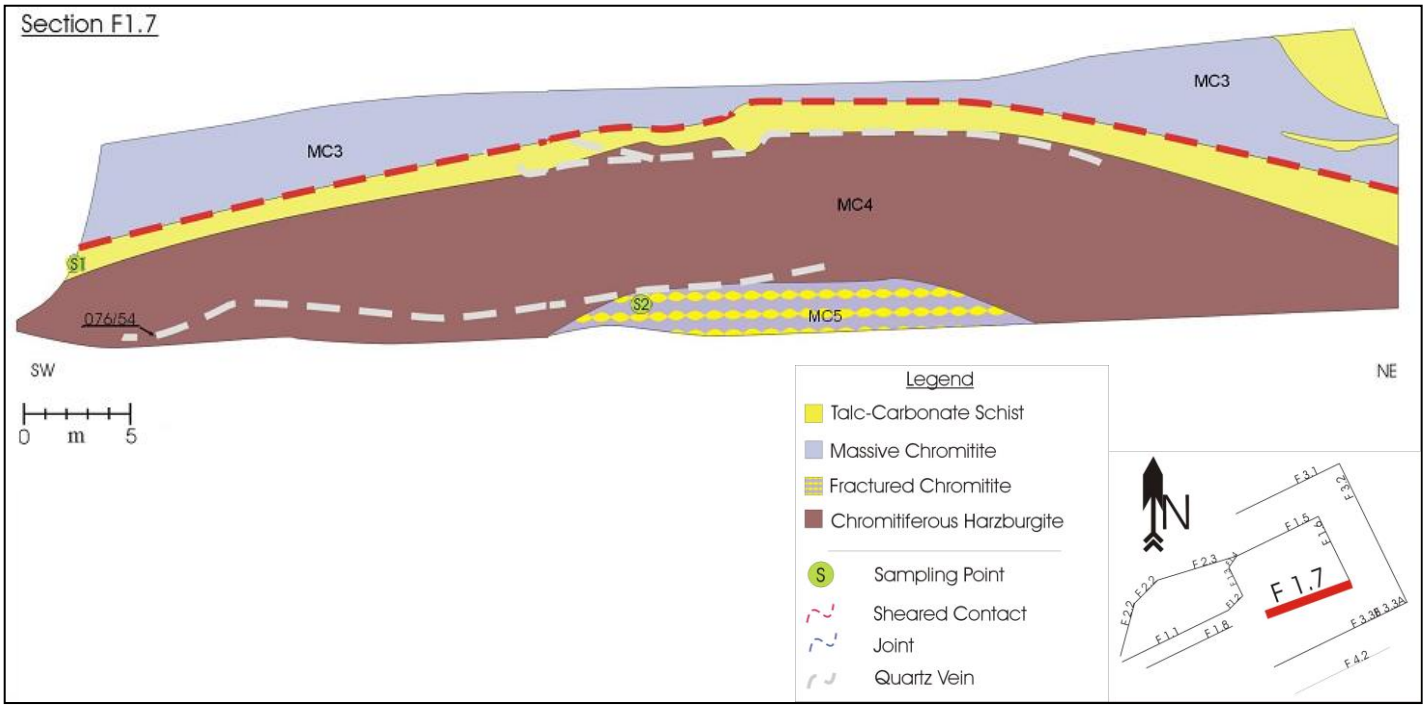

Figure 3.2.14: Geological section F1.7.

3.2.10 Geological section F3.3

Section F3.3 (fig. 3.2.15) is the next face that was exposed to the south, after the area surrounding section F1.7 was removed by the mining operation and continues perpendicularly from section F3.2. At the bottom of section F3.3 there is the continuation of chromitite lens MC4.

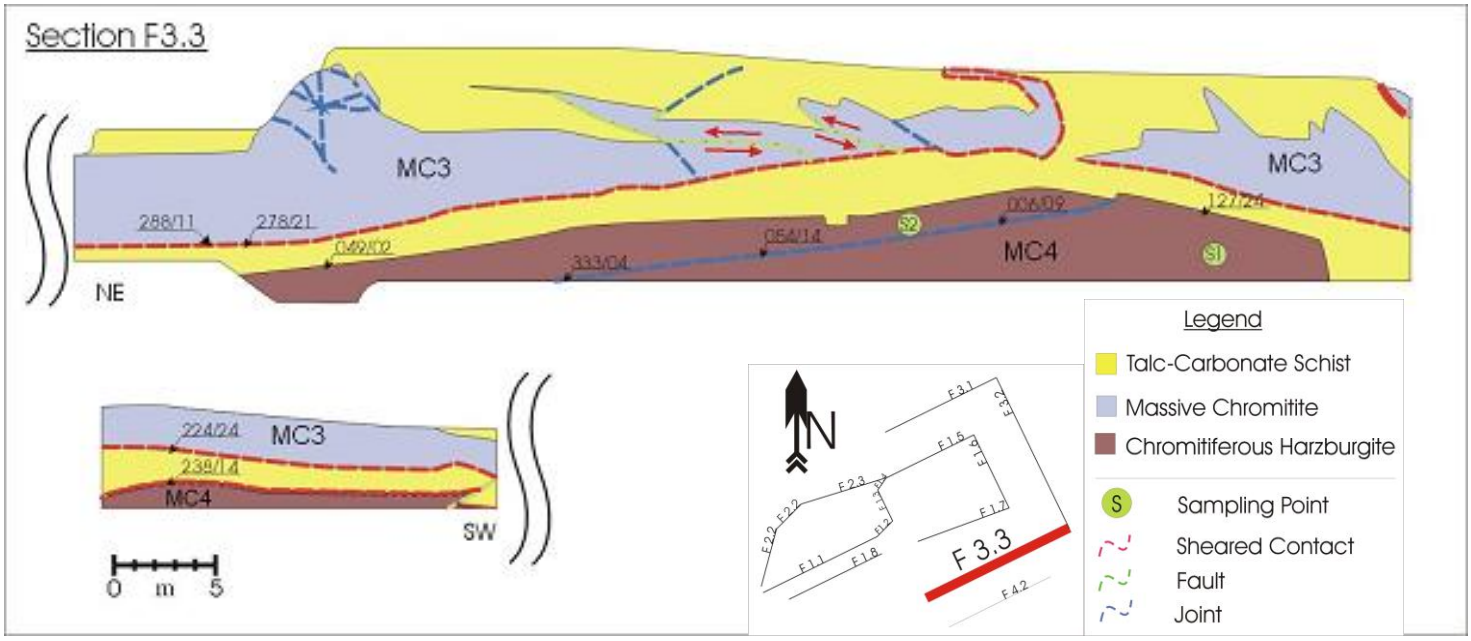

Figure 3.2.15: Geological section F3.3.

Figure 3.1.16: Photograph of reverse fault in section F3.3.

MC3 is deposited on top of lens MC4. This lens has a dome structure similar to section F1.7. Lens MC3 is thinner in the crest of the dome and becomes thicker in the flanks as the strata flattens out. Lens MC3 have two reverse faults on the north-east flank of the dome (fig. 3.2.16). At the base of the north-eastern flank lens MC3 is bulged up. This could be an indication of ductile deformation. All the deformation of lens MC3 is restricted to this lens and does not affect lens MC4 at all. This isolated deformation could mean that the stress was only applied to the specific lens and therefore the process active implies syn-magmatic deformation. The occurrence of ductile deformation could indicate that the rock was still in a plastic or cooling phase at the time that deformation occurred. The gradational contact between chromitite lens MC3 and the overlying talc carbonate schist layer is not disturbed by the deformation.

3.2.11 Geological section F4.2

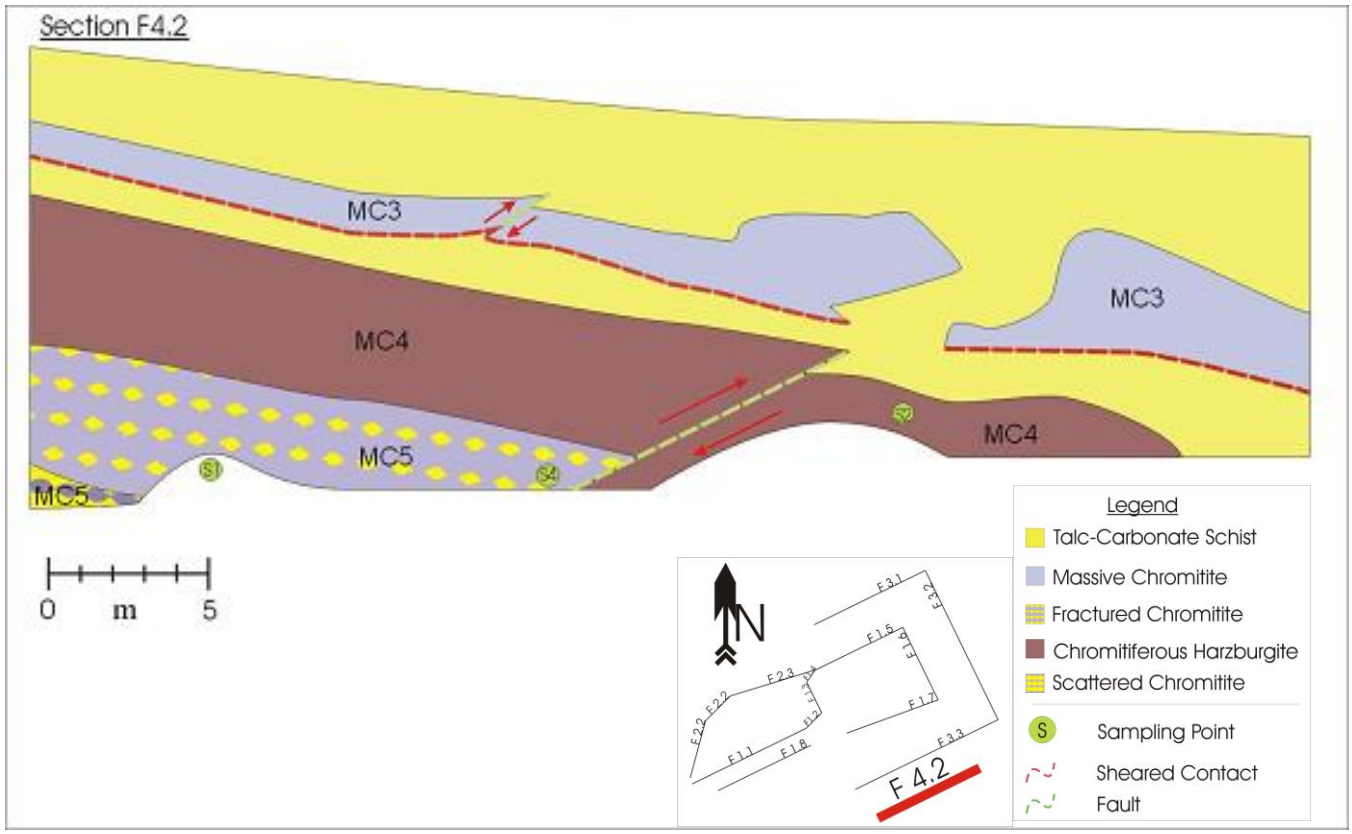

Figure 3.2.17: Geological section F4.2.

Section F4.2 (fig. 3.2.17) is the next section that was exposed to the south, after the area of section F3.3 was removed by the mining operation. Chromitite lens MC3 is becoming thin and it is suspected that the section is close to the edge of this lens. Chromitite lens MC4 is also thinner than in section F1.7. The reverse fault is similar to the fault in section F3.2 and it displaces chromitite lenses MC4 and MC5. Although lens MC3 is broken apart in line with the fault, it does not seem to be displaced by the fault. In the centre of the section there is another reverse fault. This fault it restricted to chromitite lens MC3. Below lens MC4 is a rather thick layer of fractured chromitite and a lens of scattered chromitite is just exposed at the bottom. Both these layers form part of chromitite lens MC5 and there is a clear decrease in the portion of chromite from the top of lens MC4 to the bottom of chromitite lens MC5.

3.2.12 Geological section F1.10

The face of section F1.10 (fig. 3.2.18) is parallel aligned with F1.1. At the south-western side of the section the chromitite is altered through surface weathering and it still contains some remnant stringers of chromitite. Both the two massive chromitite lenses MC2 and MC3 are prominent in this section. Chromitite lens MC2 ends bluntly towards the south-west, similar to section F1.1. There is a prominent joint in the bottom massive chromitite lens MC3 that stops against the shear zone and does not continue into lens MC2. The difference between the top and bottom contacts of the chromitite lenses is clearly visible in figure 3.2.19. At the starting point of lens MC2 the two chromitite lenses are directly on top of each other, but they are separated by a prominent shear zone that continues into the sheared bottom contact of chromitite lens MC2 (fig. 3.2.19). This displays a clear separation between the chromitite lenses MC2 and MC3.

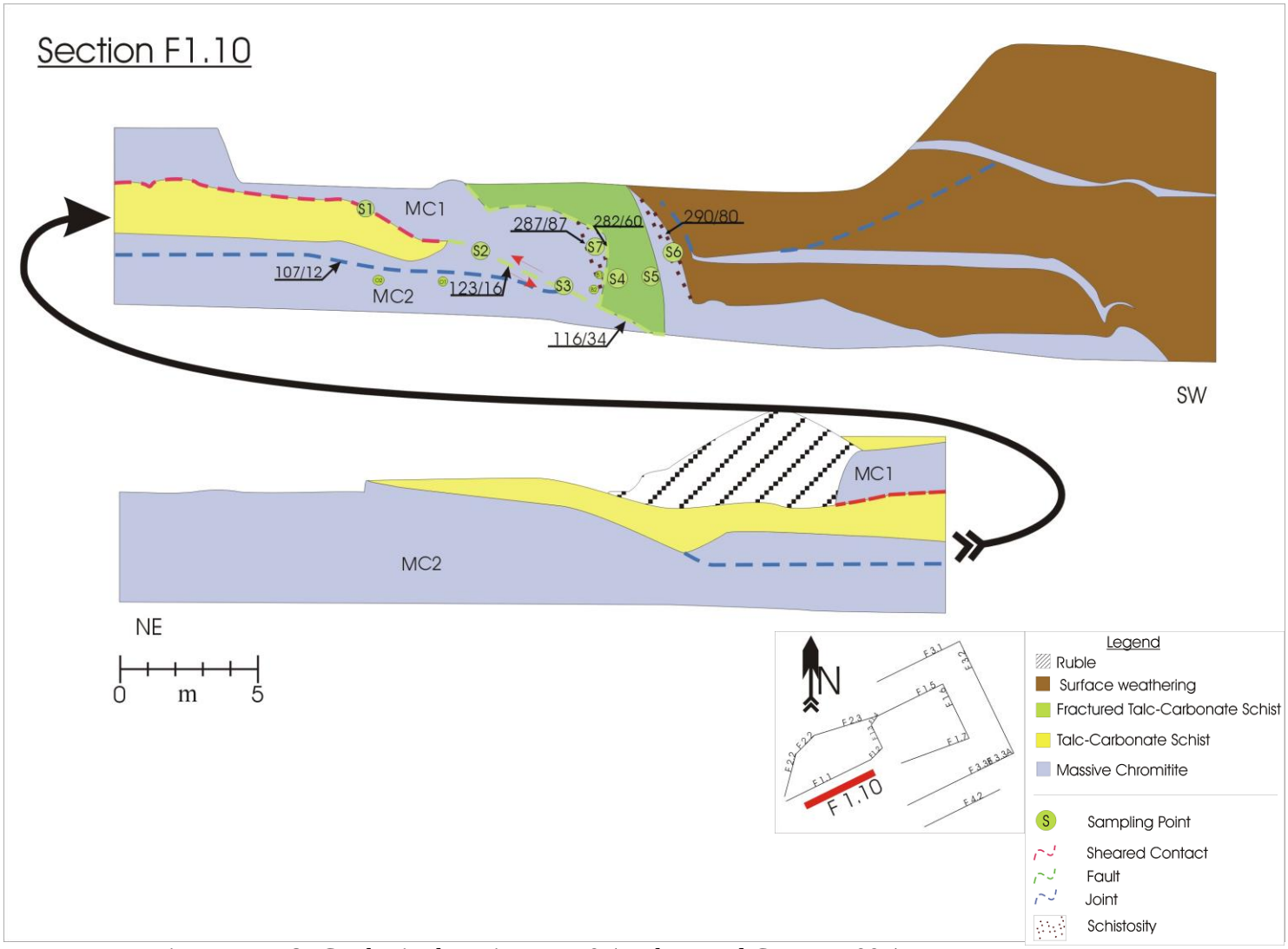

Figure 3.2.18: Geological section F1.10 (Joubert and Gauert, 2006).

Figure 3.2.19: Shear zone between chromitite lenses MC2 and MC3 in geological section F1.10.

3.2.13 Geological section F2.1

In section F2.1 (fig. 3.2.20) a big lens of talc-carbonate schist is enclosed by chromitite. The bottom chromitite lens is a continuation of lens MC3 and the top lens should be the continuation of lens MC1, since lens MC2 only starts about twenty meters to the east. Schistosity is associated with the sheared bottom contact of chromitite lens MC1. There is a good correlation between the orientations of the schistosity and the bottom contact. In the two areas where the two chromitite lenses are in contact with each other they are separated by a shear zone. The contact parallel shearing at the bottom contact of chromitite lens MC1 is not continuous and does not occur in the absence of chromitite lens MC1 on the north-east side of the section.

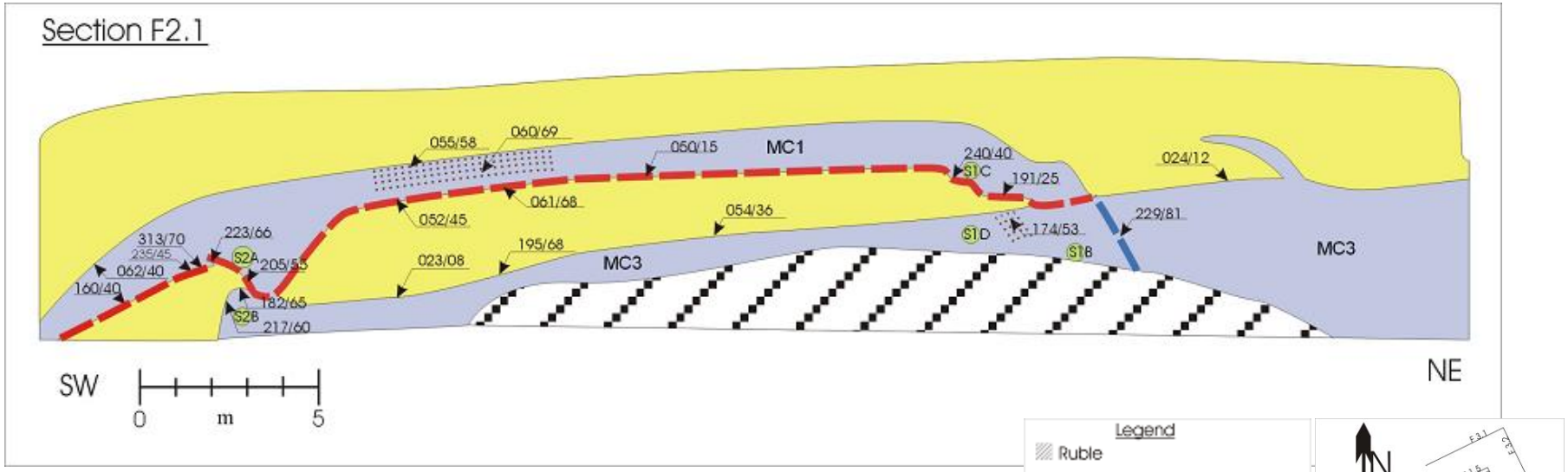

Figure 3.2.20: Geological section F2.1.

3.2.14 Geological section F2.2

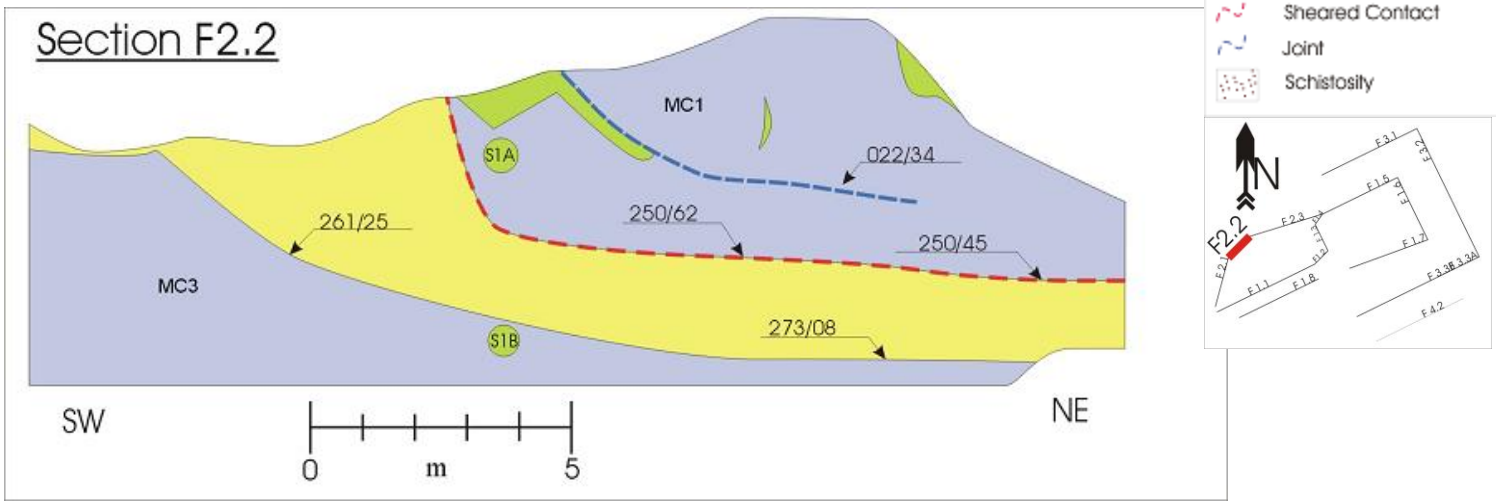

Figure 3.2.21: Geological section F2.2.

Section F 2.2 is situated to the north-east of section F2.1. Chromitite lens MC3 is continues in the section and lens MC1 re-appears with a steep down dip towards the north-east (fig. 3.2.22). The contact parallel shearing at the base of chromitite lens MC1 follows the bottom contact even though there is a sharp bent in the contact.

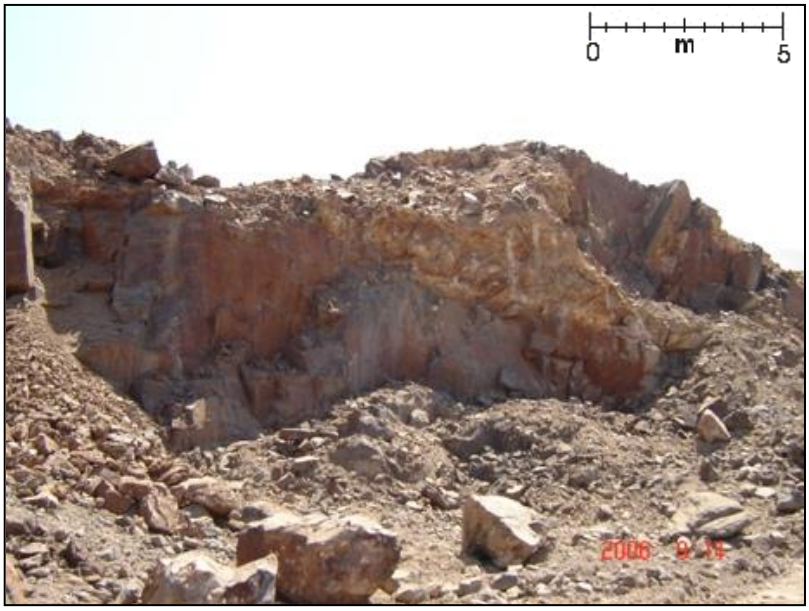

Figure 3.2.22: Photograph of section F2.2.

3.2.15 Geological section F2.3

Section F2.3 (fig. 3.2.23) is the continuation of Section F2.2 towards the north-east. This section consists mainly of chromitite lens MC1. There are two shear zones in the north-east area. Where they intersect it is clear that the upper shear is the younger feature as it cuts the lower shear. There are scattered areas with sheared chromitite. The orientation of the shearing in the sheared chromitite correlates with the orientation of the bottom shear zone. The bottom shear zone seems to be the contact between chromitite lenses MC1 and MC3, since chromitite lens MC3 continues to the north-east in section F1.5. In the bottom north-east corner of the section chromitite lens MC4 is exposed. The top shear could well be part of the large layer parallel shears system, as described by Hornsey (1999), as it continues and cuts the shearing at the bottom of chromitite lens MC1. It is however difficult to proof as the shear is only exposed in a small area.

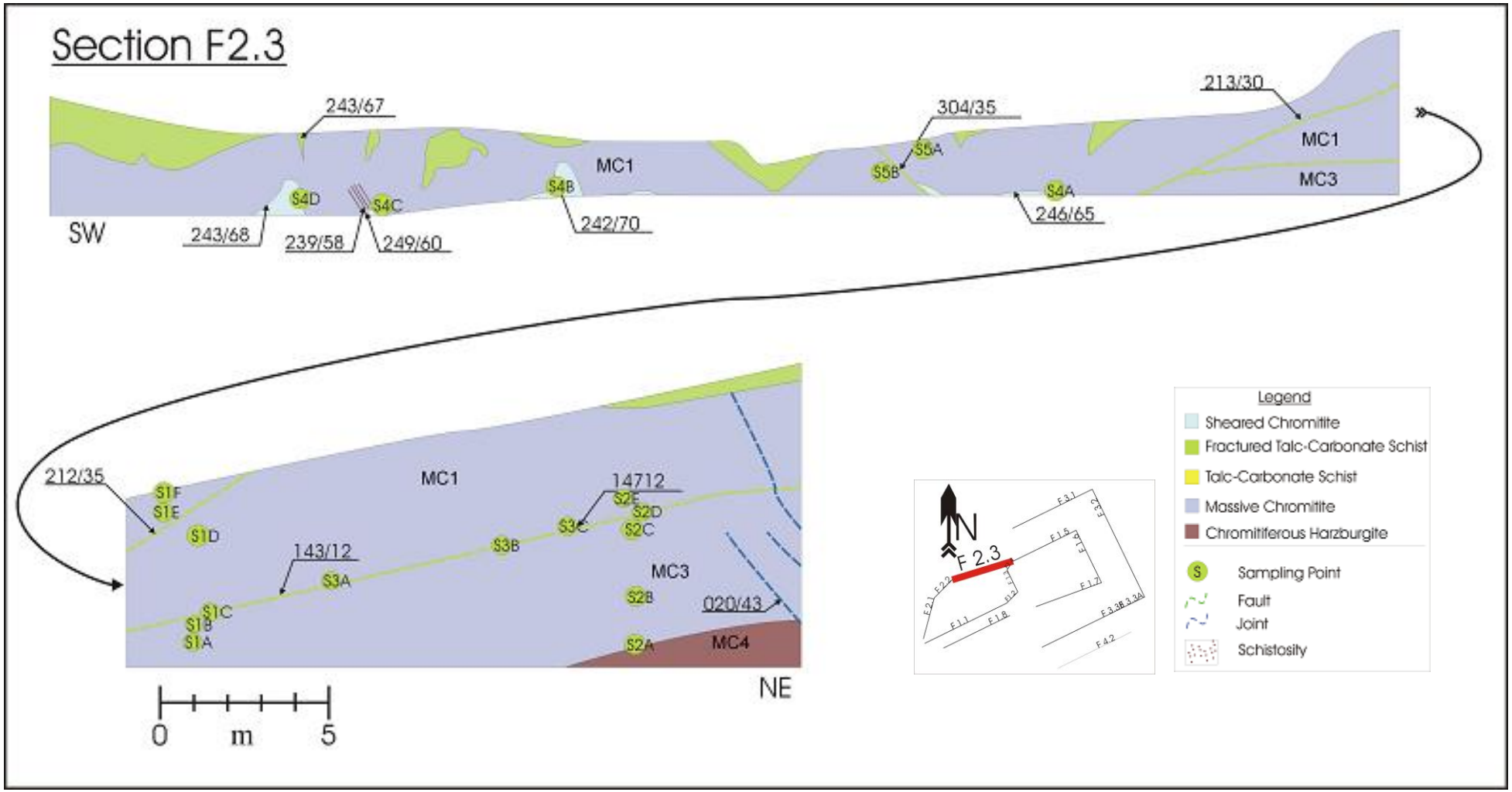

Figure 3.2.23: Geological section F2.3.

3.3 Summary

Five different chromitiferous lenses are identified in the study area (fig. 3.3.1). These lenses are stacked on top of each other. The top three lenses are Massive Chromitite lenses and all three of them are separated by layers of talc-carbonate schist. Lens MC3 extends through the entire study area, but tends to thin out and become scattered to the north and the east. Lenses MC2 and MC1 are much smaller. All three lenses have sheared bottom contacts and even in the areas where the talc-carbonate schist layer is absent the chromitite lenses are separated by a shear zone. Both ductile and brittle deformation affect the chromitite lenses and the deformation of the chromitite lenses are mostly restricted to a specific lens and do not extend into the surrounding units.

Lenses MC4 and MC5 are separated by a prominent gradational contact. There is a layer of talc-carbonate schist that separates chromitite lenses MC4 and MC3. Chromitite lens MC5 consists of fractured chromitite that gradually changes into scattered chromitite. This reveals an upwards increase of chromite abundance from the bottom of lens MC5 to the top of lens MC4.

The most important observation of the chapter is the consistent repetition of alternating chromitite and talc-carbonate schist layers with the chromitite fused to the overlaying talc-carbonate schist layer through a thin gradational contact. The chromitite lenses in this area and at this elevation are separated from the underlying talc-carbonate schist layer by a sharp sheared contact.

The contact parallel shearing on the bottom contacts of the chromitite lenses does not appear to be part of the major Bushveld age, contact parallel shear event as discussed by Hornsey (1999). These shears are not continuous and they do not displace some early jointing that was documented in the study area. One younger shear that displaces the shearing associated with the chromitite lenses has been documented in the study area. This shear could be part of the regional Bushveld age shearing. A mineral Chemical study of the chromitite is needed to confirm whether the shearing of the chromitite bottom contacts is related to the Bushveld-age layer-parallel shearing event or to syn-

intrusive magmatic processes. If the chromite chemistry of the different lenses shows a narrow compositional correlation with one another, it is most likely that the chromitite was deposited as a single layer that was duplicated and stacked through contact-parallel shearing.

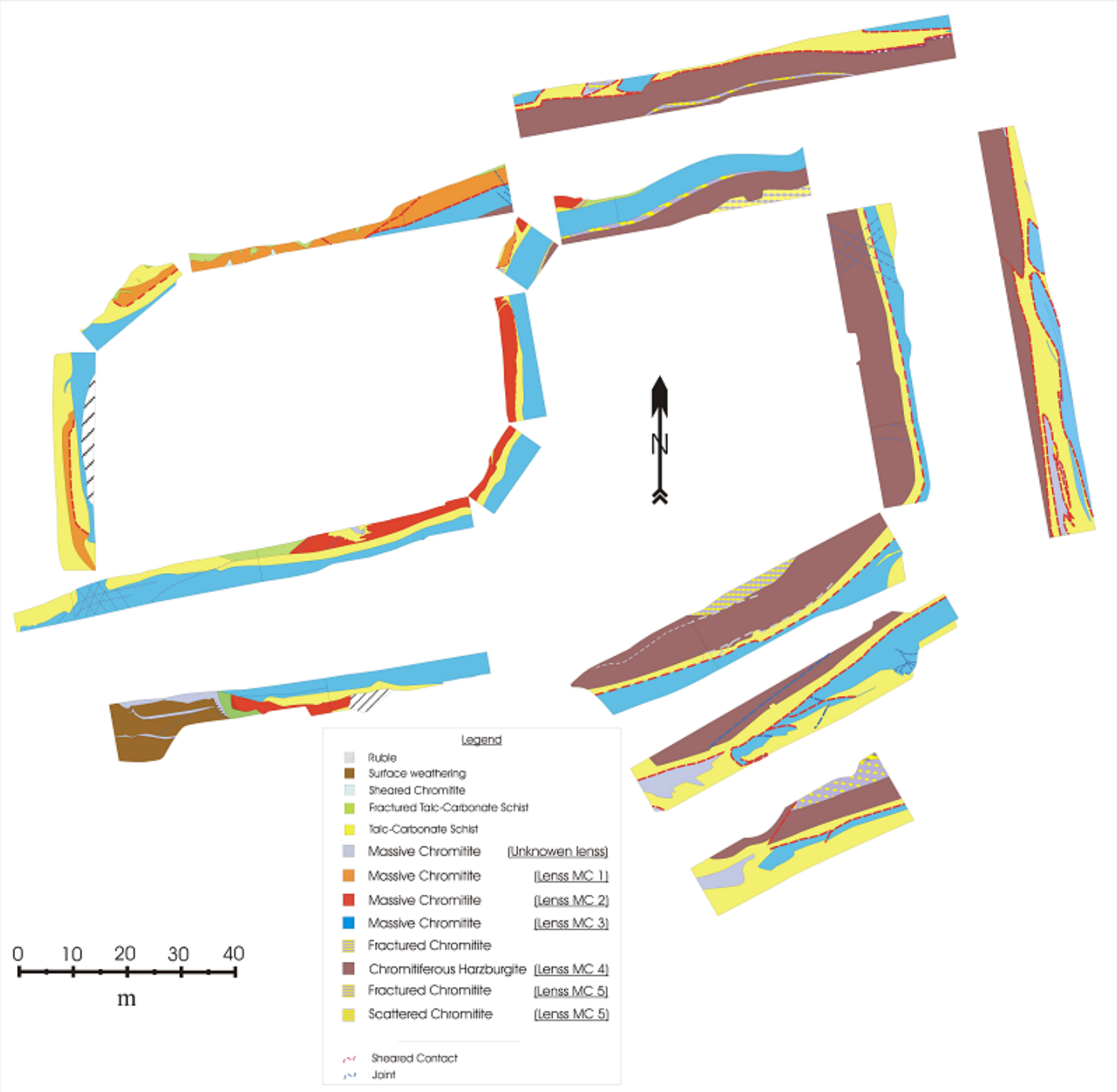

Figure 3.3.1: Complete summary of all the geological sections mapped in open pit 3 with color coding to identify the different chromitite lenses.

Chapter 4: Geological structures and texture

4.1 Background information

This chapter deals with the different structures and textures that were encountered in the study area. All the structures are displayed on the geological sections that are discussed in chapter 3. The orientation of the structures was measured with a compass and is reported on the geological sections in the strike/dip notation.

This orientation of the structures and the textures are presented on stereonet diagrams. The stereonet plots are used to correlate the structures with each other. The general orientation of the Uitkomst Complex is also plotted on stereonet diagrams as a red arrow. As illustrated by figure 4.1, the estimated general strike orientation of the Uitkomst Complex in the region of the study area is N 47° W. This calculates to an orientation of 133° /313°. The relationship between the orientations of the complex and the structures will provide the opportunity to investigate the possibility that the force of the north-west – south-east moving magma, in the conduit, assisted in the fracturing of already consolidated chromitite lenses *(Gauert, 1998; De Waal et al., 2001)*.

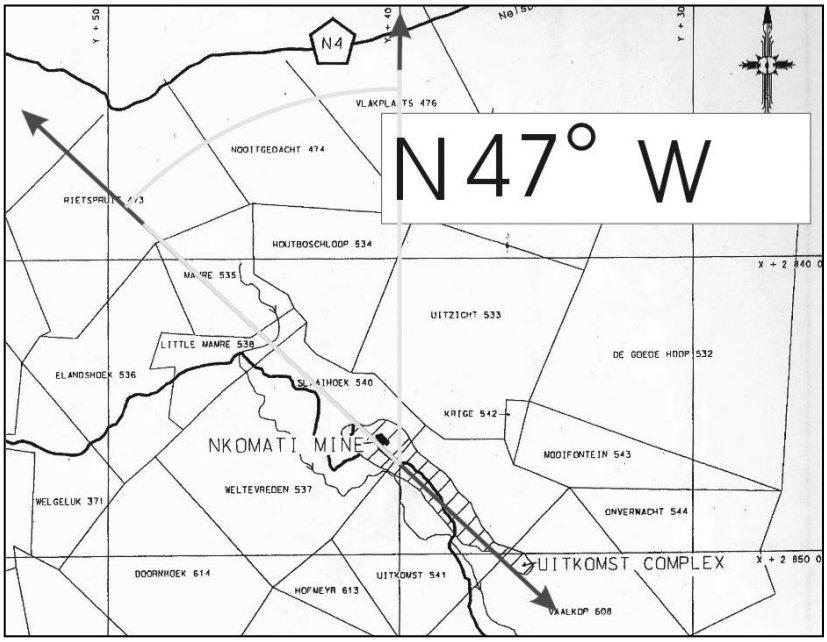

Figure 4.1: Estimated general orientation of the Uitkomst Complex.

A total of 68 structural orientations were measured. The orientation of some of the structures was measured more than once in different areas of the pit.
The following structures will be discussed:

4.2 Contacts

4.3 Faults

4.4 Joints

4.5 Fracture zones

4.6 Quartz veins

The only rock texture that will be discussed is the schistosity in the chromitite.

The orientation of the structures will also be discussed in the context of the structural analysis of the emplacement of the lower units of the complex by Hornsey (1999) as discussed in the introduction (see table 1.1 page 8). According to Hornsey (1999) structures from the Mesozoic and Bushveld age are expected to be prominent in the study area. The Bushveld age contact parallel shearing has a sense of movement towards 150° TN (Hornsey, 1999). This chapter attempts to correlate measured orientations of contacts, structures, faults, fracture zones and late-stage veins with findings of Hornsey (1999) of the lower three rock units including the massive sulphide lenses.

4.2 Contacts

A total of 37 orientations from chromitite contacts were measured. 17 Bottom contacts and 20 top contacts (fig. 4.2). From figure 4.2 it can be concluded that there is no correlation between the orientation of the top- and bottom contacts of the chromitite lenses. The top contacts dip at a lower angle than the bottom contacts, with 50% of the top contacts with a dip that are below 15°. The difference in orientation is not the only difference between the two groups of chromitite contacts. In contrast to the thin gradational top contacts, the bottom contacts are sharp, sheared contacts with striations (fig. 4.3).
This is however only true for the upper three chromitite lenses as there is a prominent gradational contact between chromitite lenses MC4 and MC5. The top contact of lens MC4 is still a thin gradational contact, similar to the three upper chromitite lenses.

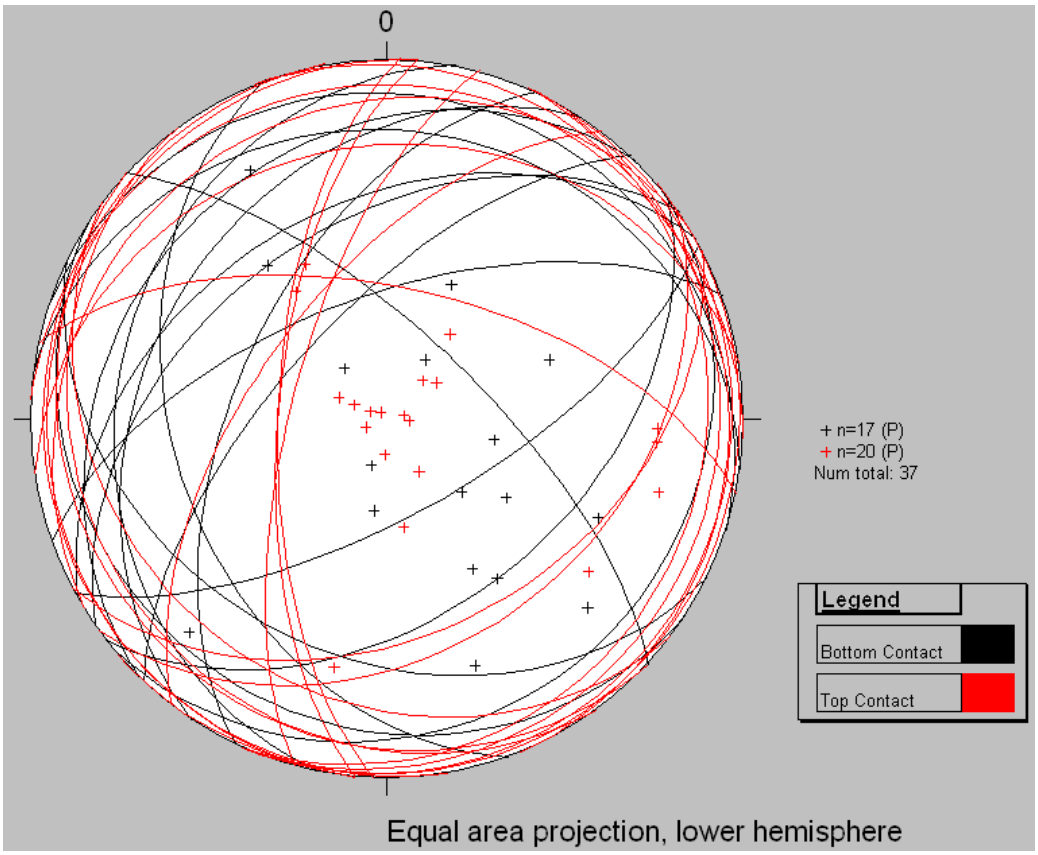

Figure 4.2: Stereonet plot of all the orientations measured from the chromitite contacts.

This division between the upper three chromitite lenses: 'MC1, MC2 and MC3' and the lower two lenses: 'MC4 and MC5' is enhanced by the differences in the geological properties between these two groups of chromitite lenses, as discussed in chapter 3. This might indicate that the two groups of chromitite lenses evolved by different depositional mechanisms.

Figure 4.3: Photograph displaying the top contact of chromitite lens MC4 and the bottom contact of chromitite lens MC3.

The top contacts of the upper three massive chromitite lenses are thin gradational contacts that fuse the two rock units together and therefore there is not a smooth breaking plain developed on these contacts. The irregular breaking plain makes it difficult to measure its orientation.

The fusion of the two rock units indicates continuous crystallization during the transition from chromitite to harzburgite deposition. Therefore it seems as if the top contact of the chromitite lenses developed in accordance with crystal fractionation as the depletion of chromium from the magma resulting in the continuous crystallization of olivine and orthopyroxene. These top contacts are very thin and therefore the depletion of the chromium occurred rapidly.

The orientation of the top contact varies between the different chromitite lenses. The orientation of the individual contacts also varies from one location to the next (fig. 4.4).

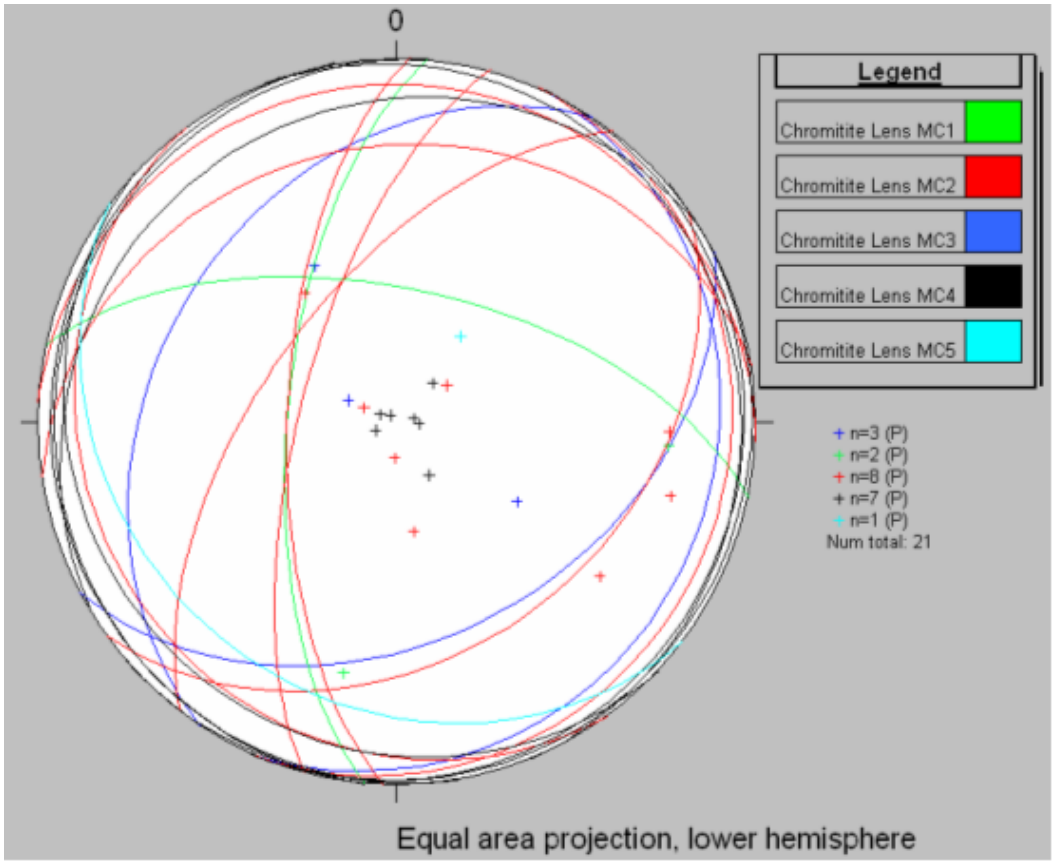

Figure 4.4: Stereonet plot presenting the orientations of the top contacts from the different chromitite lenses.

Figure 4.5 is a rose diagram that displays the preferred orientation of all the top chromitite contacts. The directions of 270°-280° and 110°-120° are the two preferred groups for the direction of dip. These directions are similar to the average orientation of the complex, but it is not in line with it. Therefore it is difficult to estimate how much influence the magma movement had on the development of the top contacts of the chromitite lenses.

Figure 4.5: Density plot presenting the correlation between the directions of dip of the top contacts from the different chromitite lenses.

The bottom contacts of the three upper massive chromitite lenses are fractured contacts that form a smooth breaking plain between the two rock units. The striations on the bottom contacts indicate that some movement took place along these contacts after crystallization of the chromitite. Unfortunately the orientation of the striations was not documented as this would provide a clearer indication to the direction of the movement.

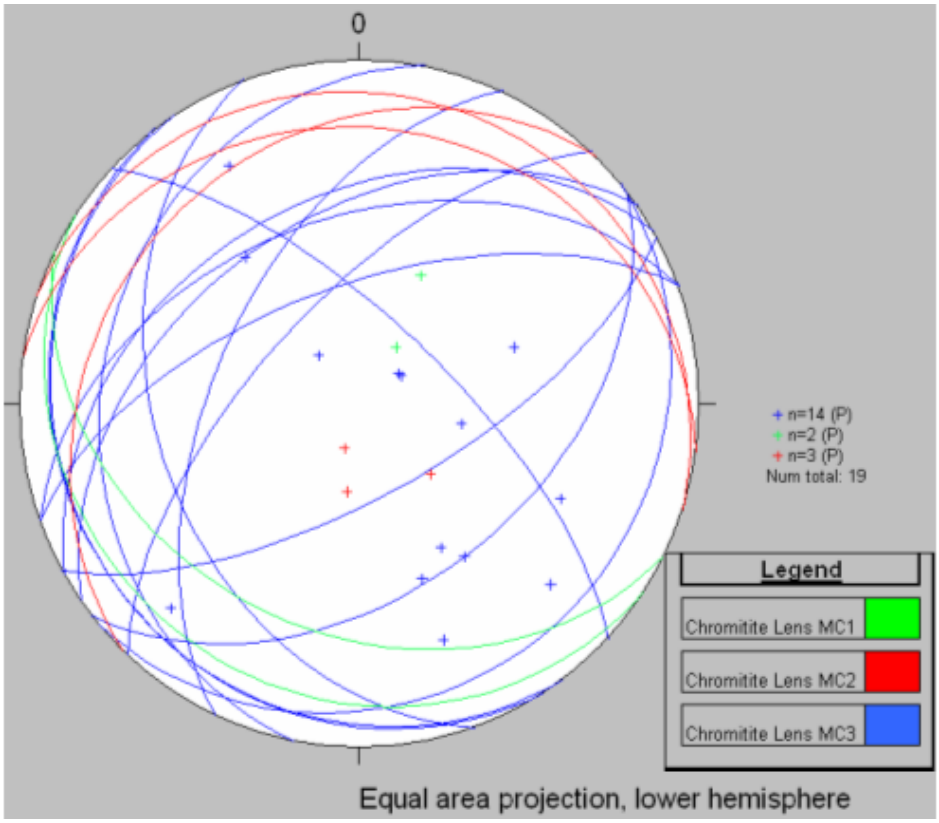

Figure 4.6: Stereonet plot of the bottom contacts of the chromitite lenses.

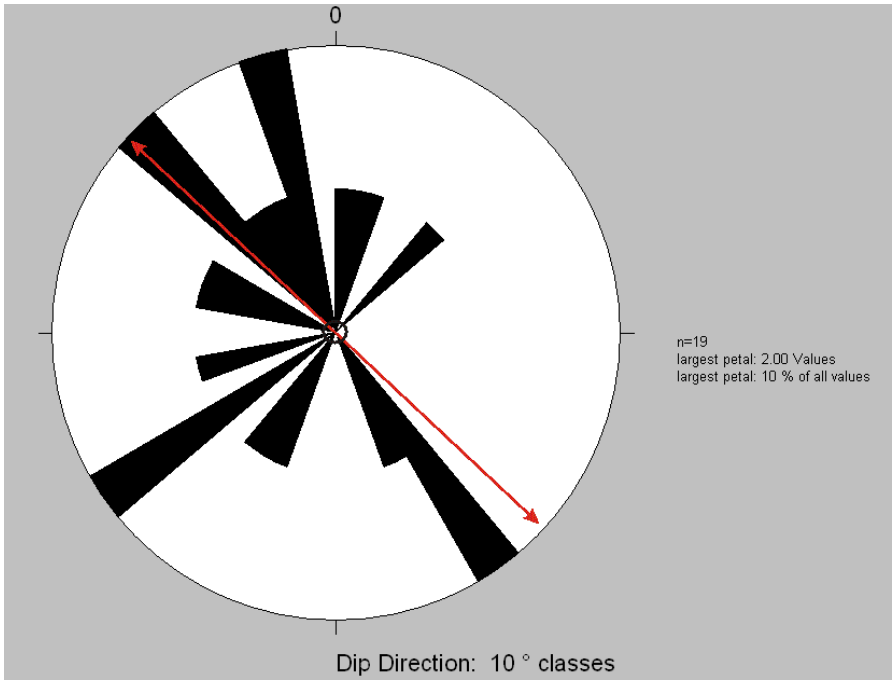

Figure 4.7: Density plot of the chromitite top contacts.

Similar to the top contacts, the orientation of the bottom contacts does not correlate with each other. The majority of the bottom contacts have a steeper dip than the top contacts (fig. 4.6). From the density plot (fig. 4.7) it is evident that the orientations of the bottom contacts have a better correlation with the orientation of the complex. Therefore the force of the magma movement had a greater effect on the development of the bottom contacts and it is possible that the magma influx could be the driving force behind the movement that generated the striations on the bottom contacts. The orientation of the majority of the bottom contacts also correlate with the 150°TN sense of shear of the Bushveld age layer parallel shear event (Hornsey, 1999).

The discussion above only includes the three upper chromitite lenses as the contacts of chromitite lenses MC4 and MC5 are totally different. In contrast to the upper three chromitite lenses there is not a layer of talc-carbonate schist between chromitite lenses MC4 and MC5. These two lower chromitite lenses are separated by a prominent gradational contact that fuses the two lenses together. This is the result of continuous crystallization during the transition from the scattered chromitite of lens MC5 to the chromitiferous harzburgite of lens MC4. This means that these two lenses are deposited during the same crystallization event and they are only distinguished because of their chromitite content. The top contact of lens MC4 is a thin gradational contact similar to the top contacts of the upper three chromitite lenses.

Because lens MC5 is the first chromitite deposit of the Massive Chromitite Layer that is exposed in the study area it seems as if this layer started off with the deposition of small chromitite lenses within the harzburgite. As time progressed the amount of chromite deposited increased until the chromitite was no longer deposited as small lenses and was deposited as a chromitite layer with a high concentration of olivine and pyroxene to form the chromitiferous harzburgite of lens MC4. The concentration of the chromite further increases to the top of lens MC4 before chromite precipitation ceased and only olivine together with orthopyroxene crystallization continued, fusing lens MC4 to the overlaying harzburgite layer by a thin gradational contact. The harzburgite later alters to Talc-carbonate schist through deuteric alteration.

4.3 Faults

There is only a small amount of prominent faults in the study area and the orientations of a total of only three faults were measured. Table 4.1 contains the orientations of the faults. Each of the three faults is color coded.

The direction of dip of faults (B) and (C) is to the North-West. Fault (A) dips towards the North-east and its direction of dip is perpendicular to fault (B) (fig. 4.8). The data on the orientations of the faults are limited and it is difficult to generate significant trends from it. Fault (A) correlate with the Mesozoic age north-east / south-west faulting and indicates the first evidence of this late stage deformation (see structural summary by Hornsey (1999) (table 1.1 page 8).

Nr	Fault	Strike	Direction of dip	Dip	Geological Section
1	A	304°	34°	35°	F2.3
2	B	213°	303°	30°	F2.3
3		212°	302°	35°	F2.3
4	C	240°	330°	30°	F3.2
5		255°	345°	30°	F3.2

Table 4.1: Summary of the orientations of the faults in the study area.

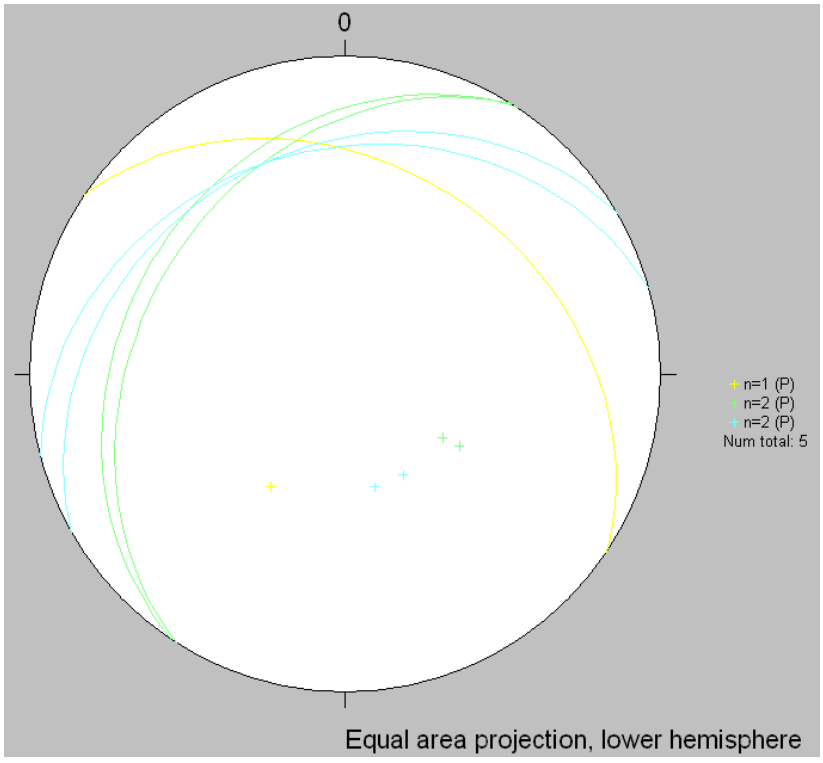

Figure 4.8: Stereonet plot displaying the fault orientations.

A significant observation is that the majority of the faults do not extend through the entire Massive Chromitite Layer and that most of the faults are restricted to individual chromitite lenses (fig. 4.9). In order for faults to be restricted like this, the chromitite lens MC3 must have been able to move independently from the rest of the surrounding layers. It seems as if each lens has fractured and moved along its bottom contact to form the thrust faults and by doing so avoided influencing the older layers below it. In order for the younger layers on top of the lens not to be affected by the faulting they had to be in a highly ductile phase or simply not yet deposited (fig. 4.9).

This means that the faulting had to take place shortly after the deposition of the chromitite lens. The chromitite is also not fused to the harzburgite layer below it, allowing the chromitite to move freely along its bottom contact. This indicates that continuous crystallization did not occur during the development of the chromitite bottom contact. It further implies that within the short time period, before the overlaying harzburgite layer was deposited chromitite lens MC3 was solid enough to be clastically deformed.

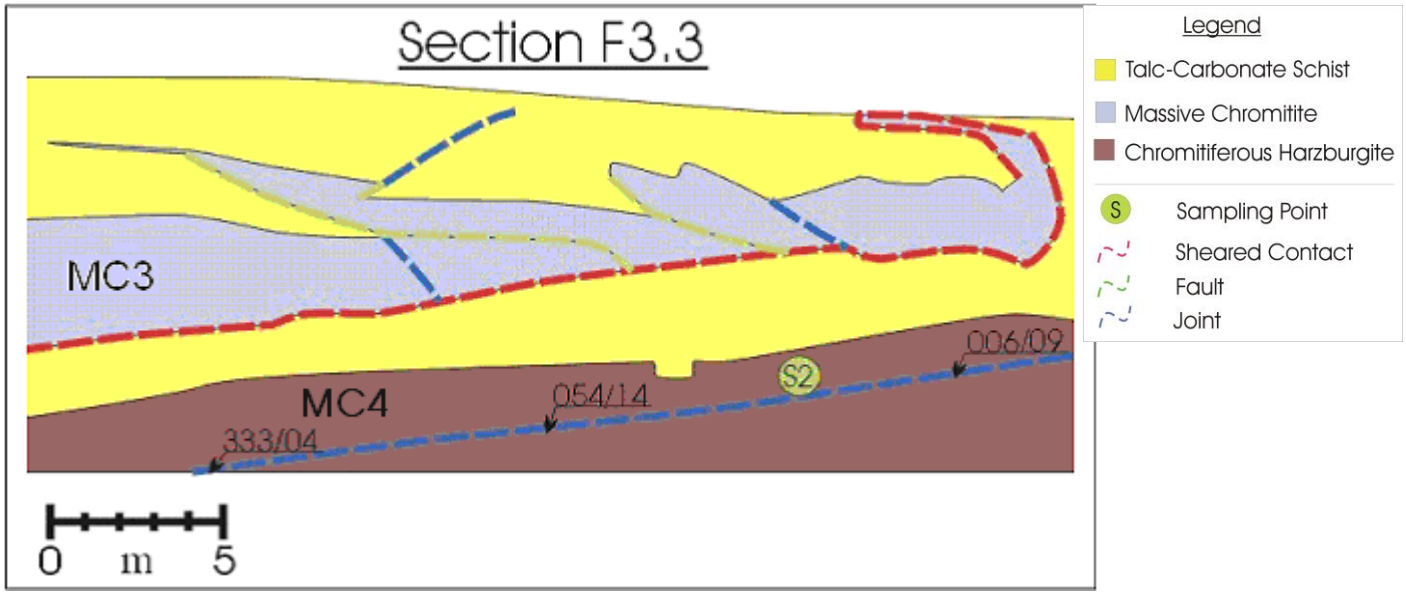

Figure 4.9: Thrust-faults that are restricted to chromitite lens MC2.

4.4 Joints

The quantity of joints in the study area exceeds that of the faults. The joints are clustered together in certain areas of the open pit. A total of 13 orientations were measured from 11 individual joints. The orientations of the joints are summarized in table 4.2. In order to referencing the joints they are alphabetically labeled and the joints that belong to the same cluster are color coded.

Figure 4.10 is a stereonet diagram displaying the orientations of the joints. The color coding of the diagram corresponds with table 4.2. There are some correlations between the orientations of some joints. The first group of joints that correlates with one another consists of joints F, G and I, there is also a correlation between joints A, D, E and J. Each group includes joints from different clusters. Furthermore, the joints that are included in a correlating group do not all occur in the same chromitite lens. The joints clearly show a NE-SW and a less expressed NW-SE strike direction. These are clearly cooling joints and not blasting fractures.

Nr	Joint name	Strike	Direction of dip	Dip	Geological Section
1	A	22°	112°	34°	F2.2
2	B	313°	43°	70°	F1.1
3	C	263°	353°	34°	F1.1
4	D	212°	302°	60°	F1.1
5	E	209°	299°	74°	F1.6
6	F	52°	142°	44°	F1.6
7	G	231°	321°	77°	F1.6
8	H	107°	197°	12°	F1.8
9	I	229°	319°	81°	F2.1
10	J	20°	110°	43°	F2.3
11	K	333°	63°	4°	F3.3
12		54°	144°	14°	F3.3
13		6°	96°	9°	F3.3

Table 4.2: Summary of the orientations of the joints in the study area.

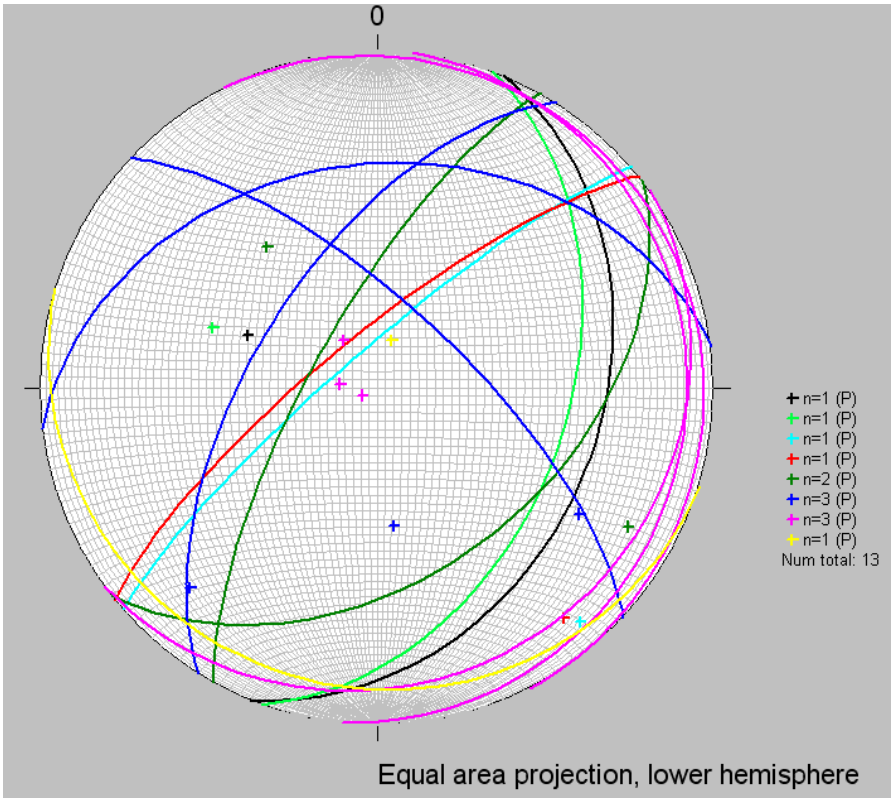

Figure 4.10: Stereonet plot of the joint orientations.

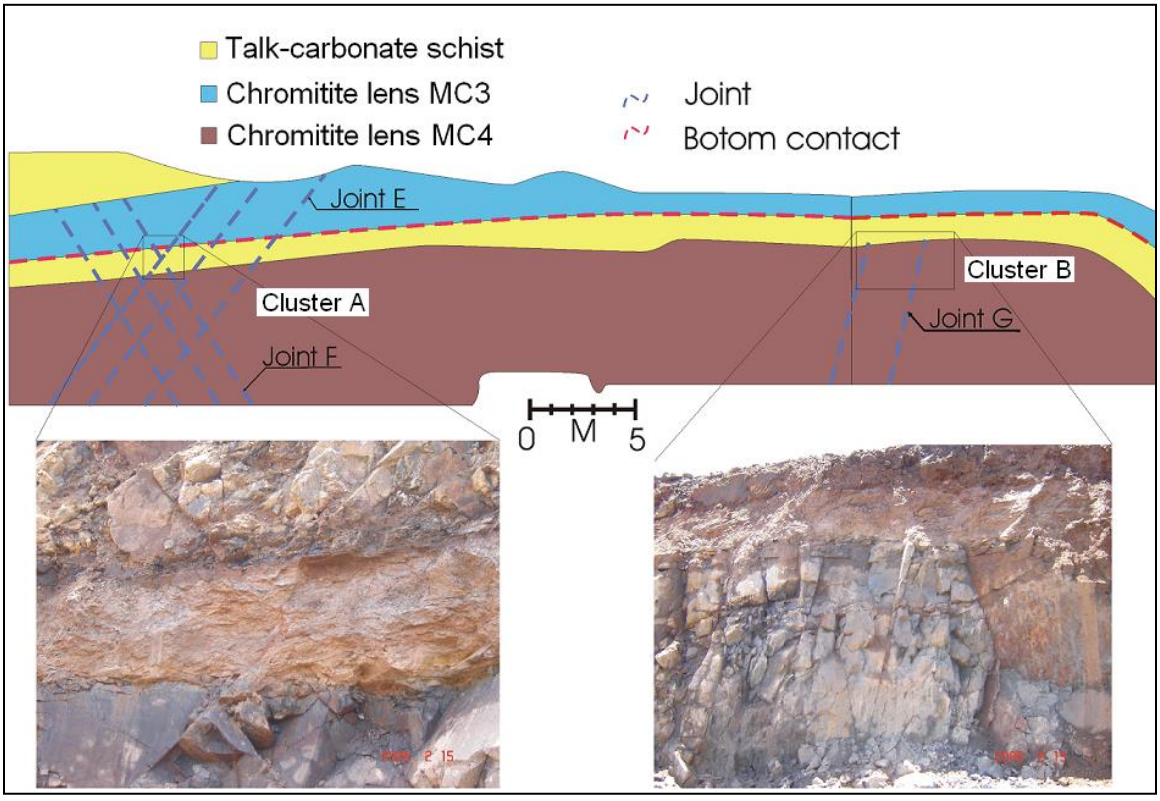

Figure 4.11: A photograph of the joints that stop on the top contact of the chromitite lenses in geological section F1.6.

Geological section F1.6 (fig. 4.11) contains two clusters of joints. The first cluster (cluster A) is on the left-hand side of the section and is represented by joints E and F. The second cluster (Cluster B) is on the right-hand side of the section and is represented by joint G (fig. 4.11). Cluster A extends through both the chromitite lenses MC3 and MC4 as well as the Talc-carbonate schist layer that separates the two chromitite lenses. The joints however do not extend further upwards and stop on the top contact of chromitite lens MC3. The joints are not being displaced by the movement along the bottom contact of chromitite lens MC3. This indicates that the movement along this contact was completed before the jointing took place.

Cluster B extends through the chromitite lens MC4 and stops on the top contact of this lens (fig. 4.11). It does not extend into the two geological units above chromitite lens MC4. It seems as if the joints are not disturbed by the movement along the bottom contact of the chromitite lenses, but are terminated by the top contacts of the chromitite lenses. This is the case for the majority of joints that occur in clusters, the less prominent isolated and individual joints are mostly restricted to a single chromitite lens.

The fact that clusters of cooling joints are terminated at the top contacts of the different chromitite lenses and extend all the way downwards indicates that the overlaying harzburgite layer was still in a highly ductile state at the time when the joints were formed and could absorb the stress in a ductile manner, causing the jointing to only occur in the older rock units. Thus the jointing happened shortly after the chromitite layers were emplaced.

4.5 Fracture zone

Geological section F2.3 contains some remains of a fracture zone which is characterized by lumps of highly fractured chromitite present in the section. The orientation of these fractures is displayed on the stereonet diagram in figure 4.12 and it has an average direction of dip of 335° and a sense of movement in the up-dip direction of 155°. The fractures have a steep dip and there is a good correlation between the individual measurements. The orientation of the fracture zone correlates with the 150°TN sense of shear for the Bushveld age contact parallel shear event and might well represent the first evidence of this deformation event in the study area (Hornsey, 1999).

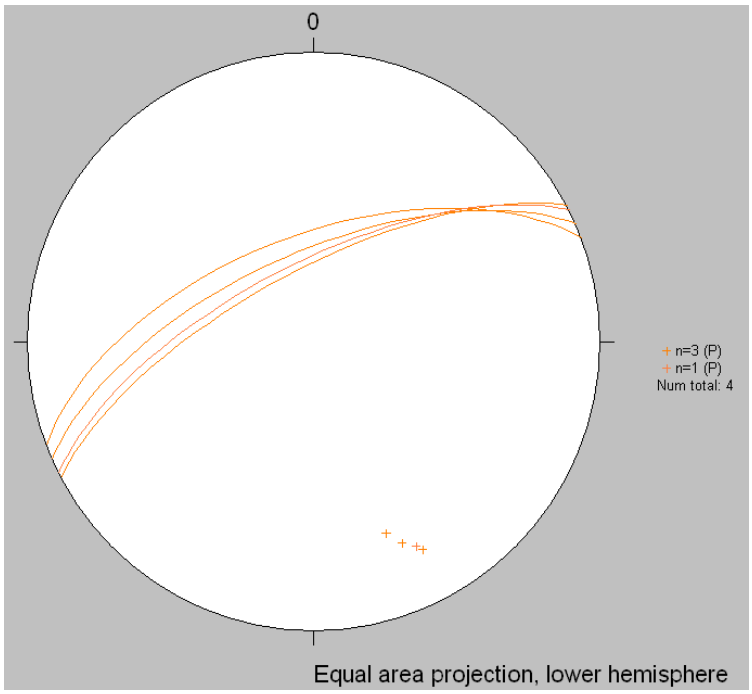

Figure 4.12: Stereonet plot of the fracture zone orientation.

4.6 Quartz veins

There are only two quartz veins in the study area and both occur in geological section F1.7. The orientation of only one of the quartz veins was measured as the other one was out of reach. These are well developed quartz veins that are up to 20cm thick. Because there is no movement on the veins the orientation of this quartz vein is correlated against the orientations of the joints and they are plotted together on a stereonet diagram (fig. 4.13). The strike direction of the measured vein does not correlate with the orientation of the majority of the joints. The quartz veins are more folded and deformed than the joints. Therefore it does not seem likely that the quartz veins were generated by the same event that resulted in the jointing of the chromitite lenses. In the basal units of the complex

quartz veins was found associated with large shears (Hornsey, 1999). The quartz veins in the study area are not associated with shearing and rather follow an irregular crack (see geological section F1.7).

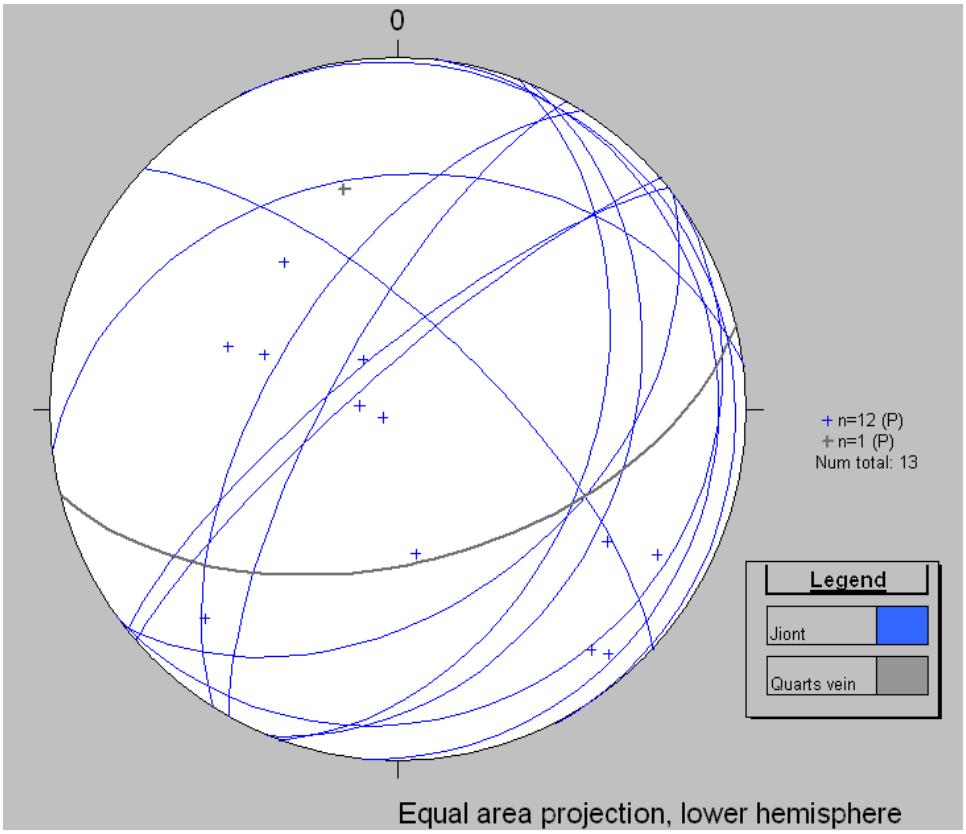

Figure 4.13: Stereonet plot displaying the orientations of the quartz vein and the joints.

4.7 Schistosity

This refers to a thin, alternating layering that occurs in isolated areas of certain chromitite lenses. The layering consists of a series of thin, alternating grey and black plains within the chromitite. On a microscopic scale the dark lines are related to areas where the chromite crystals are highly fractured and resulted in lines with a high concentration of small crystal chips. The chips are densely packed with very little matrix material between them. The light lines are where there are big chromite crystals that are more evenly distributed. The arrangement of the crystals allows for more matrix minerals between the crystals that result in a lighter grey color (fig. 4.14). The schistosity always occurs close to prominent structures. The fracturing of the crystals indicates that there were high levels of stress in these areas.

Nr	Structure	Strike	Direction of dip	Dip	Geological Section
1	**Schistosity**	**239°**	**329**	**58**	**F2.3**
2	Fracture zone	249°	339	60	F2.3
3	**Schistosity**	**55°**	**145**	**58**	**F2.1**
4	Bottom Contact	52°	142	45	F2.1
5	**Schistosity**	**60°**	**150**	**69**	**F2.1**
6	Bottom Contact	61°	151	68	F2.1
7	**Schistosity**	**174°**	**264**	**53**	**F2.1**
8	**Schistosity**	**287°**	**17**	**87**	**F1.8**
9	Top Contact	282°	12	60	F1.8

Table 4.3: A summary of the orientations of schistosity and the related structures.

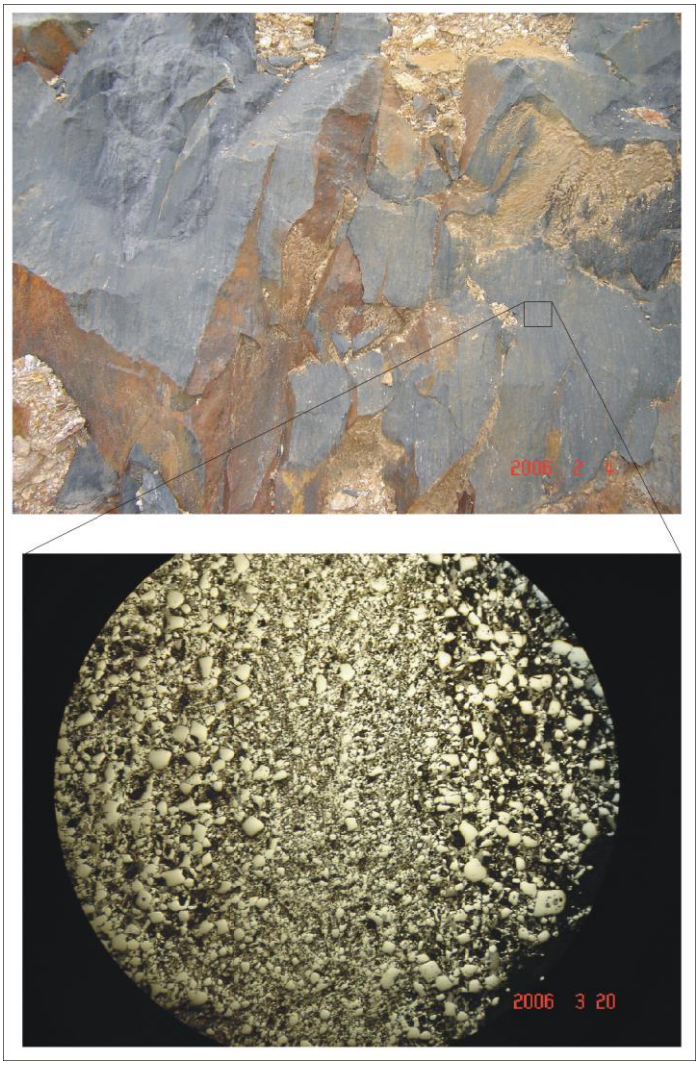

Figure 4.14: An example of chromitite schistosity in both meso scale and micro scale.

Table 4.3 contains all the orientations that were measured from the schistosity and orientations of their related structures. All the schistosity orientations are in bold print. The schistosity and their related structures are color coded. The same color coding is used in the stereonet diagram presented in figure 4.15.

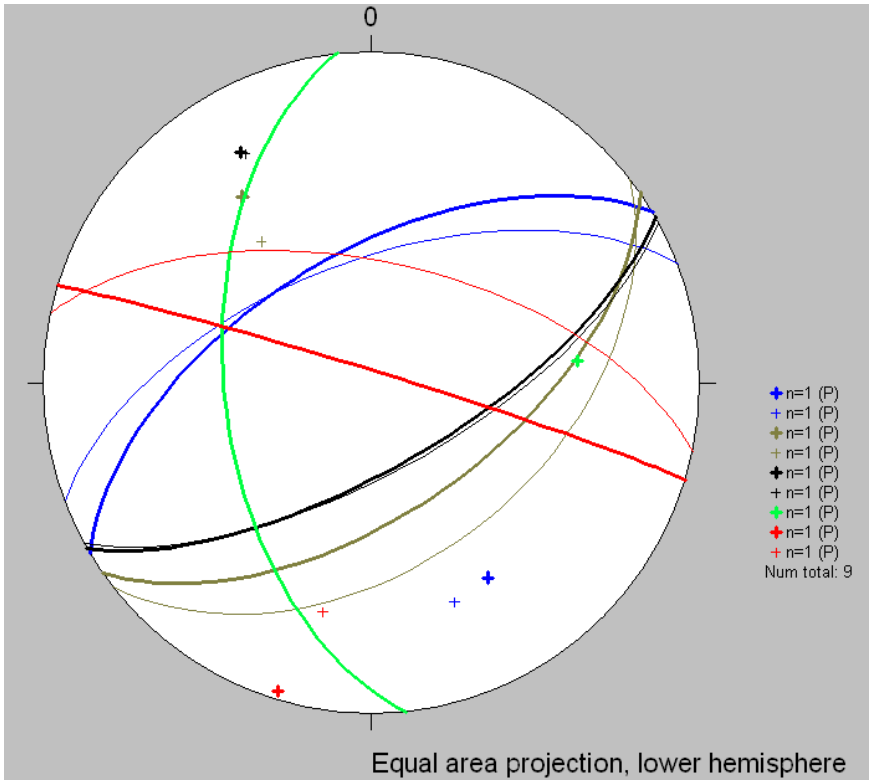

Figure 4.15: Stereonet plot of the schistosity orientations with their related structures.

There is a very strong correlation between the orientation of the schistosity and the orientation of their structures (fig. 4.15). This close correlation indicates that the schistosity is the result of the build-up of stress during the formation of the related structure. Since there is schistosity related to the bottom contacts of chromitite lens MC1, it means that the chromitite layer must have been at least in a semi-solid condition during the time that deposition occurred. Semi-solid refers to the chromite as being crystallized, but the matrix minerals, between the chromite crystals, are still in highly ductile condition.

4.8 Summary and discussion of geological structures

The study area contains structures with orientations that are similar to both the Mesozoic and Bushveld age deformational events as described by Hornsey (1999). The majority of the structures in the study area are not as prominent or on the same large scale as the ones that are discussed by Hornsey (1999) in the basal areas of the complex. The structures in the study area are mostly restricted to certain geological units and do not continue through the entire lithology exposed in the study area.

There is a major difference between the contacts of the upper three chromitite lenses and the bottom two lenses. This difference supports that the first two chromitite lenses of the Massive Chromitite Layer were deposited in a different way compared to the upper three lenses.

There is a significant difference between the top- and bottom contacts of the chromitite lenses. The top contacts are gradational contacts that attach the chromitite lenses to the overlaying carbonate Talc-schist layers. This indicates continuous crystallization during the transition from chromite to the harzburgite deposition. The bottom contacts are sharp contacts with striations. The development of the striations indicates that significant movement took place on the bottom contacts of the chromitite lenses. The orientation of the bottom contacts correlate better with the general orientation of the Complex than the top contacts. Therefore it seems likely that the movement of the magma had a greater influence on the development of the bottom contacts. This orientation is also similar to the sense of shear for the Bushveld age contact parallel shear event as discussed by Hornsey (1999). However as discussed in chapter 3 the shearing associated with the bottom contacts of the chromitite lenses is not continuous and therefore a chromite mineral chemistry study is needed to confirm the nature and origin of the chromitite stacking event.

There are only a few faults present in the study area. Most of the faults are reverse faults (see geological sections F3.2, F3.3 and F4.2). The orientations of the faults correlate with the general orientation of the complex. A lot of the faults are confined to a single

chromitite lens and do not extend through to the surrounding geological units. In order for the faults to be restricted to a single chromitite lens the entire lens had to be well crystallized shortly after deposition, before the overlying harzburgite layer was solid. The time period allowed for the chromitite to solidify became even shorter if the continuation in crystallization at the top contact of the chromitite lens is considered. Therefore according to the faulting of the chromitite lenses it seems likely that the lenses were rather deposited as rafts of semi-solid chromitite and would provide the opportunity for faults to develop shortly after deposition. This would also explain why amalgamation did not occur along the bottom contacts of the chromitite lenses. The 304/35 orientation of the fault in geological section F2.3 correlates with the Mesozoic age north-east / south-west faulting event as discussed by Hornsey (1999).

The joints are concentrated in clusters. The joints are cutting through the bottom contact of the chromitite lenses, but stop on the top contacts of the lenses. This suggests that the harzburgite above the chromitite lens was still in a plastic state which allowed it to absorb the deformational stress causing the jointing, whereas the chromitite was already solid and was jointed with the deeper unit. Therefore the jointing of the chromitite lenses supports the suggestion that chromitite lenses were deposited as rafts of semi-solid chromitite. The jointing also indicates that the movement along the bottom contacts of the chromitite lenses occurred shortly after deposition as the joints are not displaced by the movement along the bottom contacts.

There is schistosity related to the bottom contact of some chromitite lenses as well as the fracture zone in geological section F2.3. The orientation of the schistosity correlates with the orientations of the related structure. The most prominent schistosity is related with the bottom contact of chromitite lens MC3. Since the schistosity is the result of chromitite crystal fracturing it indicates that the chromite crystallization was completed at the time that the movement along this bottom contact took place. Since the jointing suggests that the movement along the bottom contacts of the chromitite lenses took place shortly after deposition, it further supports that the chromitite lenses were deposited as semi-solid rafts. Perhaps as the rafts were transported through the conduit it sank out of the magma

onto the crystallized harzburgite and the friction caused the raft to settle. This friction might be the cause of fracturing of the chromite crystals, resulting in a schistosity to form parallel to the sheared bottom contact. (see fig 4.16).

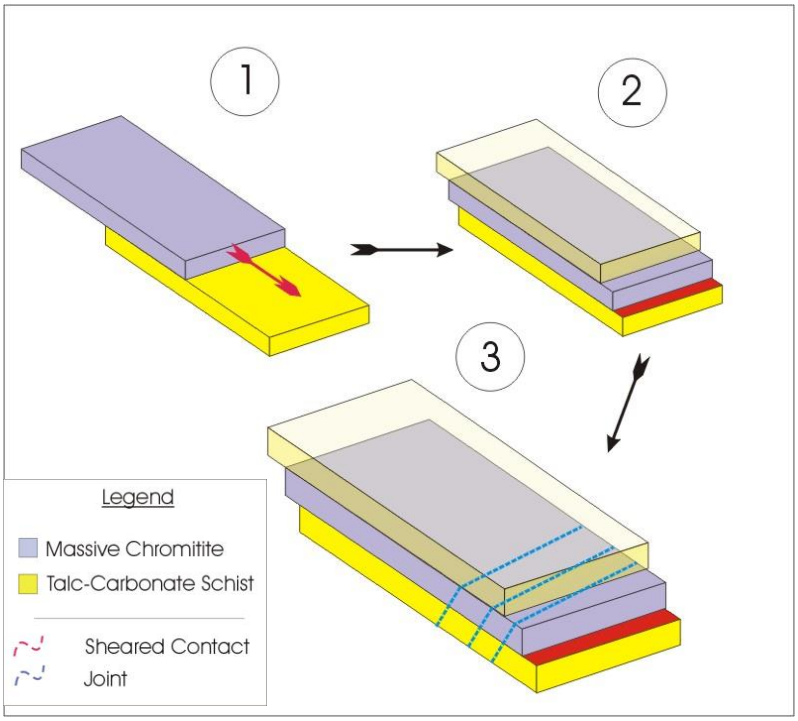

Figure 4.16: Schematic illustration of chromitite raft emplacement and jointing.

1. In placement of chromitite raft – friction between crystallized harzburgite and raft causes raft to settle down in the conduit and results in a fractured contact.
2. Harzburgite crystallization continues on top of chromitite.
3. Chromitite and bottom harzburgite are jointed, but upper harzburgite is still ductile and absorbs the stress of the jointing as plastic deformation.

Chapter 5: Petrography

5.1 Background

The purpose of this chapter is to investigate the shape, size and deformation of the chromite crystals in the various rock units identified during open-pit mapping and core logging. The different crystal properties between the chromitite layers will be correlated.

Microscopic images were captured from thin sections that were prepared from chromitite samples. The grab samples from the open-pit as well as the samples from the drill core of borehole UK33 were photographed. The images were captured with a digital camera that is mounted on top of a petrographic microscope. Images were captured at both 40 times and 100 times magnification.

The thin sections are mainly composed of chromite in a matrix of highly altered ultra-mafic rocks. The main silicate mineral is talc. While small amounts of sulfide and secondary hydrated iron oxide minerals are also present in the samples. Under reflected light the chromite is prominent greyish to brownish and the silicate minerals form the dark matrix (fig. 5.1). Inclusions of silicate as well as sulfide minerals occasionally occur inside some of the chromite crystals. The following chromite crystal shapes were identified from the photomicrographs (fig. 5.1):

Euhedral to subhedral crystals (cc): These are chromite crystals with partly subhedral - euhedral shapes that are not fractured at all. The edges and corners can be rounded to a certain degree.

Fractured crystals (fc): These are chromite crystals or crystal fragments that still have their original outline, but are cracked. The cracks sometimes are filled with silicate minerals.

Crystal fragments (cf): These are simply fragments of chromite crystals. Sometimes a portion of the original crystal can still be recognized. Some fragments are rounded to a certain degree.

Rounded crystals (rc): These are primary crystals or fragments that are well rounded into round to oval spheres.

Chromite chips (ch): These chromite crystals are crushed into small, angular fragments.

Point-counts of the thin sections were performed in order to calculate the percentage of each crystal shape within the sample. The averages of the individual crystal shapes, of all the samples from a specific chromitite lens, are then used to calculate an average percentage of the crystal shapes for the entire lens. Points were counted on a grit of 2µm by 2mm. A total of 2000 points were counted per sample. Apart from the different chromite crystals, the counts also include the altered silicate minerals and hydrated iron oxides. The sum of these two minerals calculates to an amount that represents the total amount of matrix material. The counts were re-calculated into percentages for each crystal shape. These percentages are only calculated from the total amount of chromite in the section, excluding the matrix minerals. Therefore the total portion of chromite is divided into percentages for each of the five crystal shapes.

5.2 Findings

The discussion of the findings is divided into two parts. The first part focuses on the investigation of the grab samples. These samples represent the different chromitite lenses that are exposed in the open-pit. The second part focuses on the samples of the lower PCR unit from the core of borehole UK33. The purpose of the discussion on the core samples is to correlate the findings of the Massive Chromitite Layer with the PCR layers that are deposited deeper down. It is however important to keep in mind that the research is primarily about the deposition of the Massive Chromitite Layer.

5.2.1 Grab samples

The samples were collected in the open-pit of the Nkomati Mine. The sampling positions are indicated on the geological sections discussed in chapter 3 and represent the different chromitite lenses of the Massive Chromitite Layer. The discussion starts with chromitite lens (MC1) at the top through to chromitite lens (MC5) at the bottom. Chromitite lens MC2 was not sampled efficiently because it was encountered during the early stages of the project and therefore it cannot be discussed in this chapter.

Chromitite lens MC1

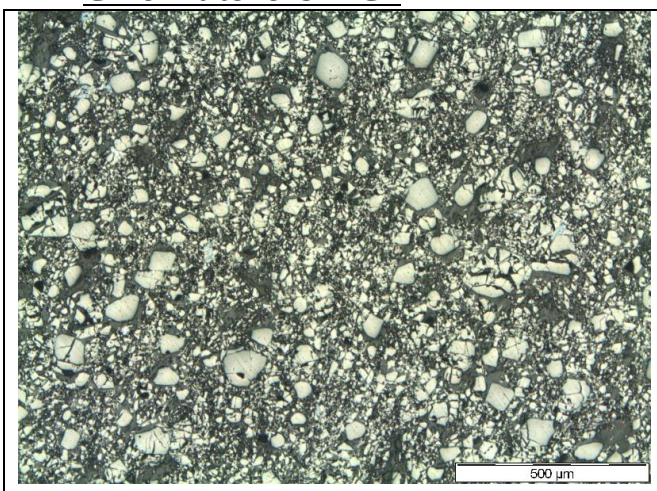

A: Photomicrograph of sample F2.1S1C under reflective light and 40x magnification. The majority of the chromite crystals are fractured into small chips.

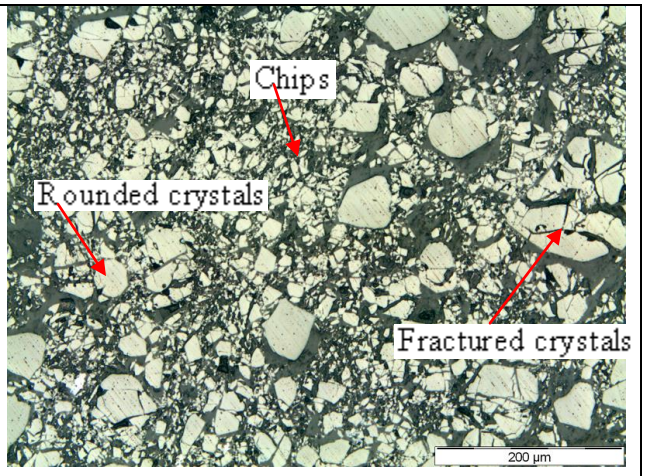

B: Photomicrograph of sample F2.1S1C under reflective light and 100x magnification. Example of a fractured crystal, rounded crystal and crystal chips.

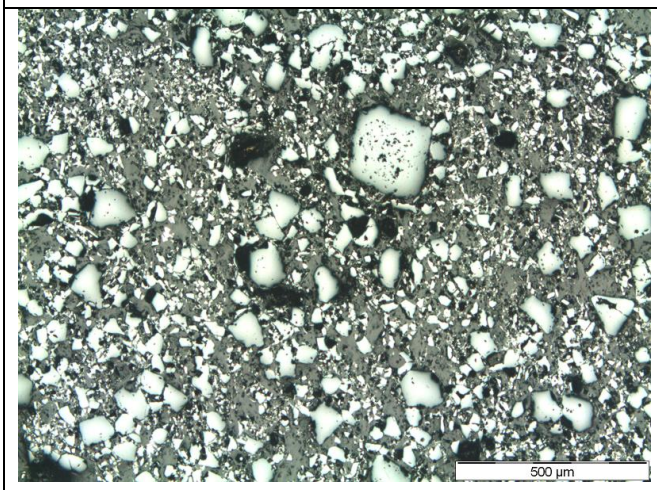

C: Photomicrograph of sample F2.1S2A under reflective light and 40x magnification, revealing a large subhedral - euhedral crystal between the chromite chips.

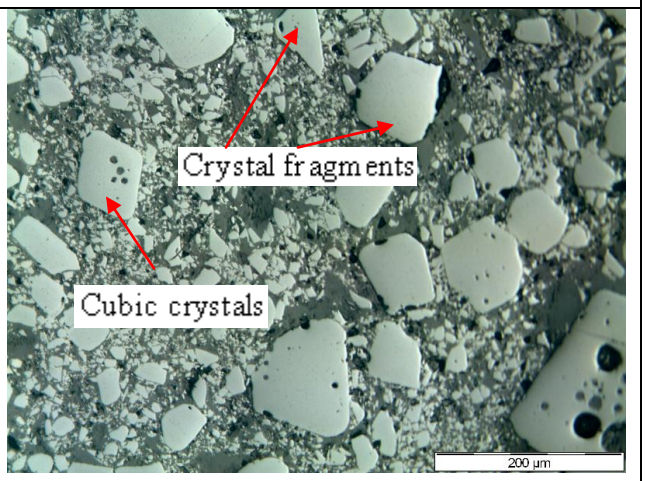

D: Photomicrograph of sample F2.1S2A under reflective light and 100x magnification. Example of crystal fragments and a subhedral - euhedral crystal.

Figure 5.1: Photomicrographs of the samples from chromitite lens MC1.

Two thin sections from chromitite lens MC1 were investigated. The sections were prepared from samples F2.1S1C and F2.1S2A. Both the samples were sampled from geological section F2.1 (fig. 5.2).

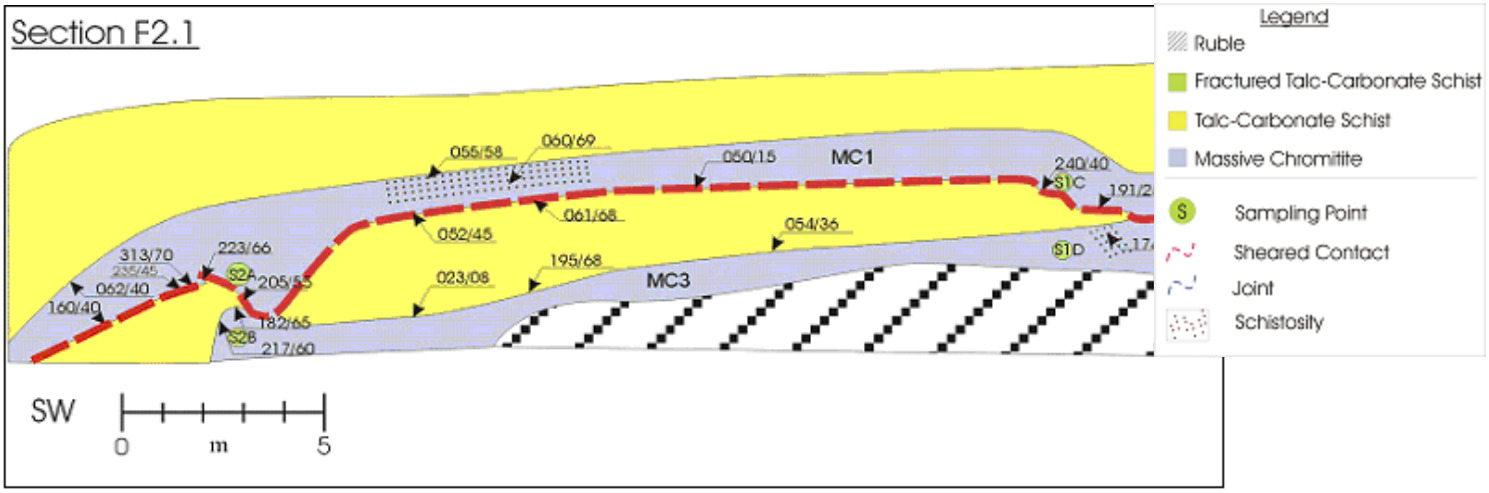

Figure 5.2: Geological section F2.1 displaying the sampling positions of the samples discussed for chromitite lenses MC1 and MC3.

The majority of the chromite crystals in this lens are extremely fractured into small chips (figure 5.1A). Only a few scattered subhedral - euhedral crystals and crystal fragments are preserved in this sample. In Figure 5.1B sample F2.1S1C clearly illustrates the size and shape of the chips. Only a few well-rounded crystals and a number of crystal fragments are present.

In figure 5.1C the photomicrograph of sample F2.1S2A contains chromite crystals and fragments are noticeably bigger than those in the first sample. Apart from the size differences the majority of the chromite crystals are still fractured into small chips. There is a good consistency between figures 5.1A and C. Figure 5.1D provides a clear indication of the magnitude of crystal fracturing that occurred within chromitite lens MC1, in that the size of the chips are extremely small in comparison to the size of the subhedral - euhedral crystals.

		Counts						
Sample	Lens	CC	FC	CF	RC	Ch	Cr total	Cr%
F2.1S1C	MC1	12	78	148	24	1441	1703	85.15
F2.1S2A	MC1	37	61	401	44	1289	1832	91.46
	Total %	1.39	3.93	15.53	1.92	77.23	3535	88.31

		Counts				
Sample	Lens	SiO	FeO (H_2O)	Total Matrix	% Matrix	Total
F2.1S1C	MC1	154	143	297	14.85	2000
F2.1S2A	MC1	171	0	171	8.54	2003
	Total %	8.12	3.57		11.69	4003

Table 5.1: Point count results of samples from chromitite lens MC1.

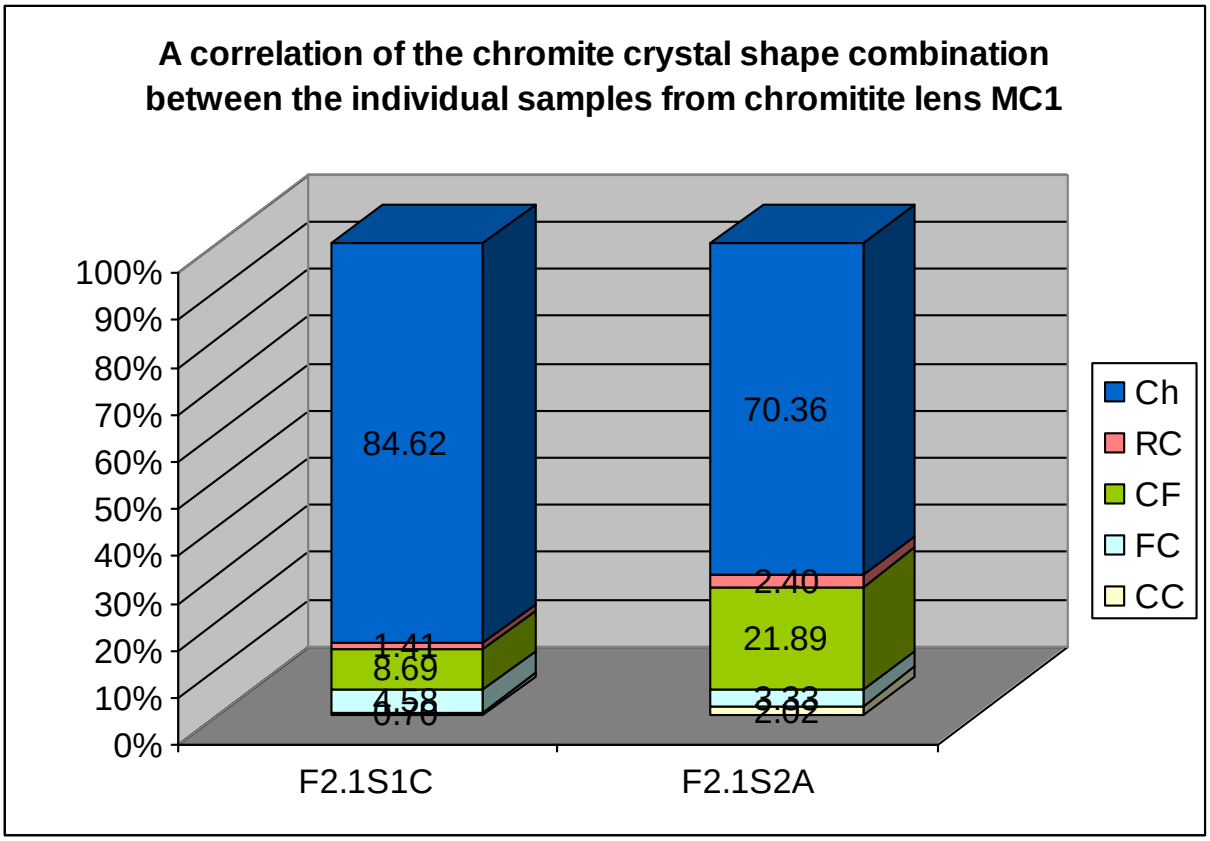

Figure 5.3: A stacked column graph presenting the point count results for the individual samples of chromitite lens MC1.

Table 5.1 presents the point count results of samples F2.1S1A and F2.1S1C. The average of the two samples indicates that 88% of the lens consists of chromite crystals. The remaining 12% are composed of a mixture of minerals that mainly consists of talc and a small amount of hydrated iron oxide minerals. There is a good consistency between the

results of the two samples. In both the samples the majority of the chromite crystals fall into the crystal chip category with a very small percentage of crystals (fig. 5.3). This confirms the observations from the photomicrographs.

Eighty eight percent (88%) of the chromite crystals in lens MC1 are divided into percentages for each crystal shape. 77% of the chromite occurs as chips and 16% as fragments (fig. 5.4). Therefore about 93% of the chromite consists of broken crystals, only 1% of the crystals are not fractured.

In order to fracture 77% of the chromite crystals in chromitite lens MC1 into small crystal chips theses crystals had to be subjected to high stress levels. The discussion on schistosity in chapter 4 indicates that the schistosity in chromitite lens MC1 was the result of crystal fracturing related to movement along the bottom contact.

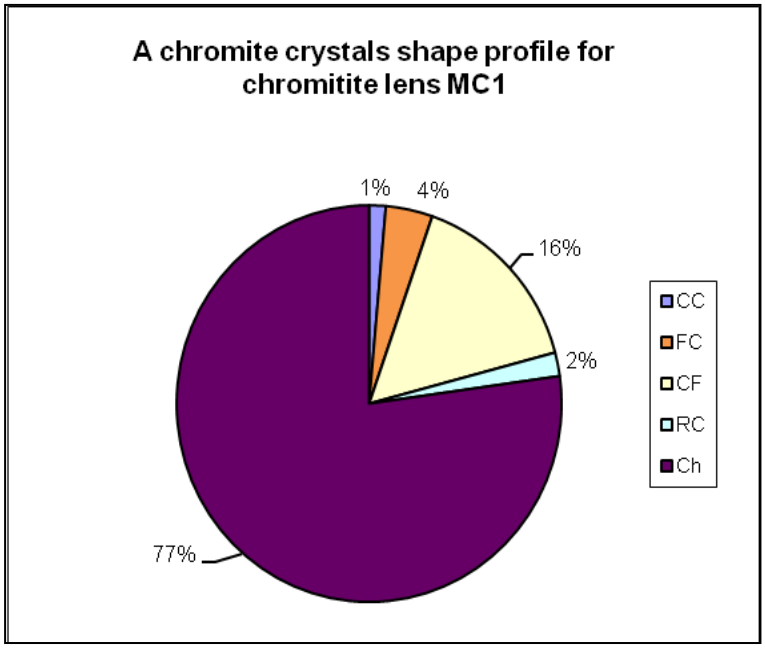

Figure 5.4: A pie chart presenting the point count results of chromitite lens MC1.

Chromitite lens MC3

The two samples that were investigated for chromitite lens MC3 were also sampled from geological section F2.1 and taken in line with those of chromitite lens MC1. In the area where the samples were taken lens MC2 is absent, therefore chromitite lens MC1 is overlying chromitite lens MC3 (fig. 5.2).

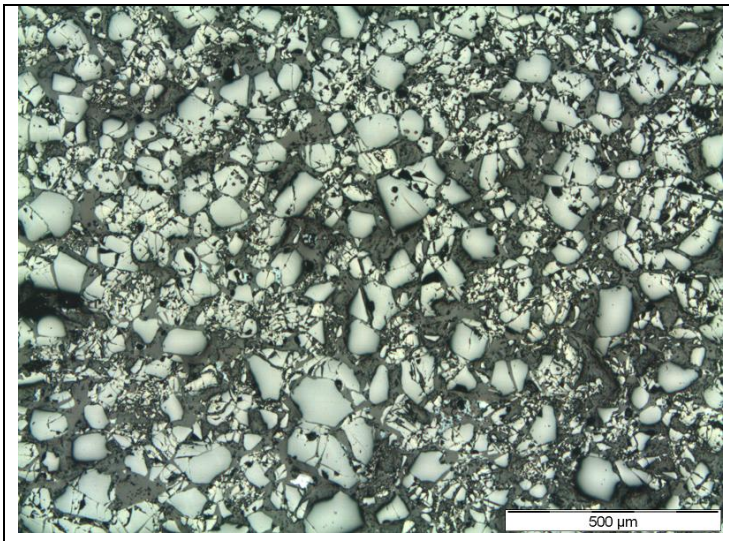

A: Photomicrograph of sample F2.1S1D under reflective light and 40x magnification. The majority of the chromite crystals seem to be fractured.

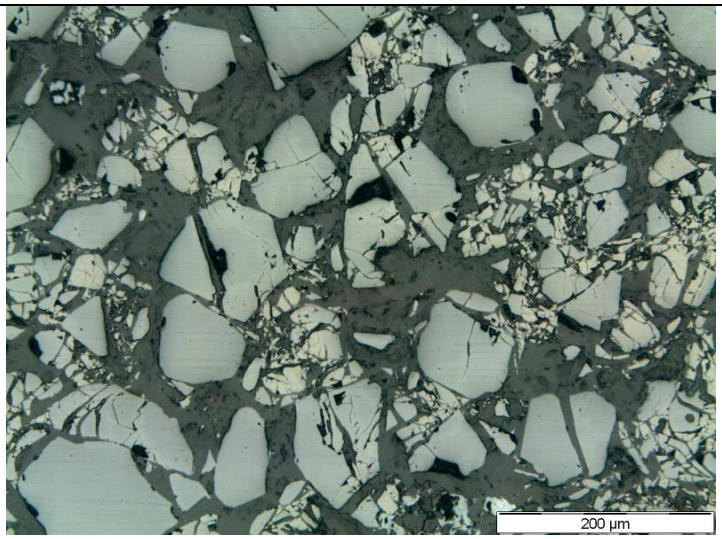

B: Photomicrograph of sample F2.1S1D under reflective light and 100x magnification. The majority of the crystals are cracked.

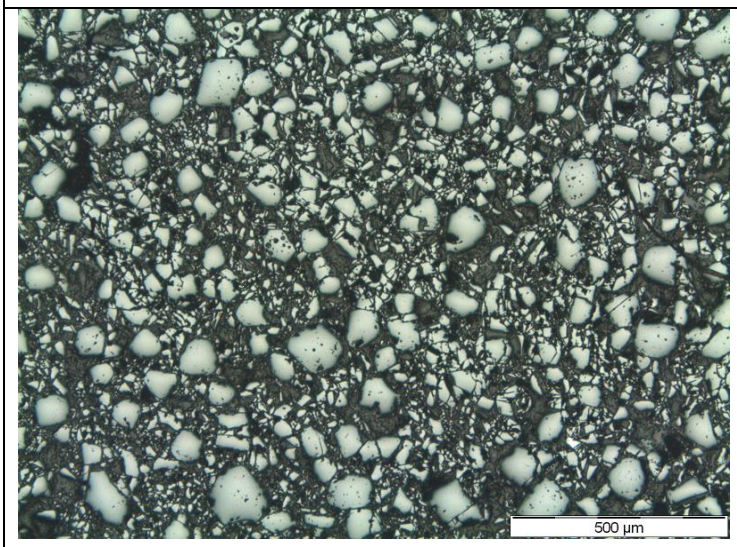

C: Photomicrograph of sample F2.1S2B under reflective light and 40x magnification. There seem to be equal amounts of crystal fragments and chips.

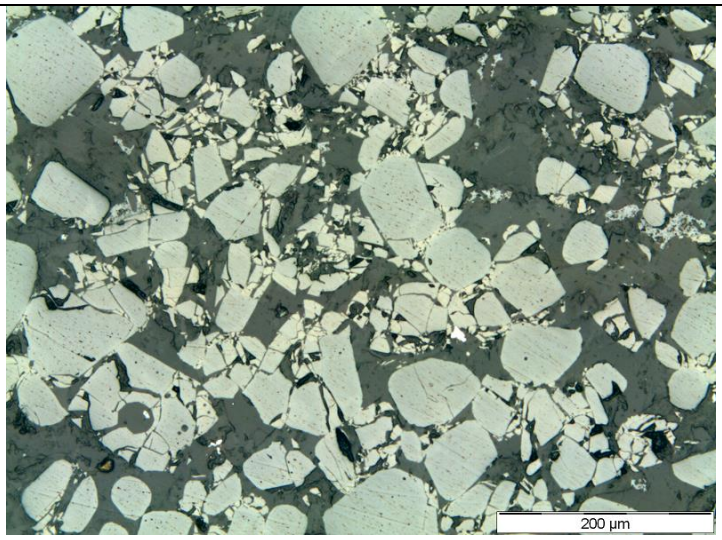

D: Photomicrograph of sample F2.1S2B under reflective light and 100x magnification. There is a substantial amount of rounding on the crystals.

Figure 5.5: Photomicrographs of the samples from chromitite lens MC3.

The chromite crystals in chromitite lens MC3 are less fractured and the size of the chips are bigger than in chromitite lens MC1 (fig. 5.5B and D). In figure 5.5A there is an abundance of fractured crystals and although there are still a lot of chips, the fracturing is less than in the samples from chromitite lens MC1. The chromite crystals of sample

F2.1S2B, in figure 5.5C, are more evenly distributed than in the sample of figure 5.5A. The fracturing of the chromite crystals presented by figures 5.5B and D is similar. The chromite crystals in both the samples are significantly less fractured than the samples from chromitite lens MC1, with a visible difference in crystal preservation between chromitite lenses MC1 and MC3. The differences between these two chromitite lenses are even more prominent if the small distance between the sampling points is considered.

		Counts						
Sample	Lens	CC	FC	CF	RC	Ch	Cr total	Cr%
F2.1S1D	MC3	190	919	272	188	259	1828	91.40
F2.1S2B	MC3	123	595	515	68	592	1893	94.70
	Total %	8.41	40.69	21.15	6.88	22.87	3721	93.05

		Counts				
Sample	Lens	SiO	FeO (H_2O)	Total Matrix	% Matrix	Total
F2.1S1D	MC3	164	8	172	8.60	2000
F2.1S2B	MC3	104	2	106	5.30	1999
	Total %	6.70	0.25	6.95		3999

Table 5.2: Point count results of samples from chromitite lens MC3.

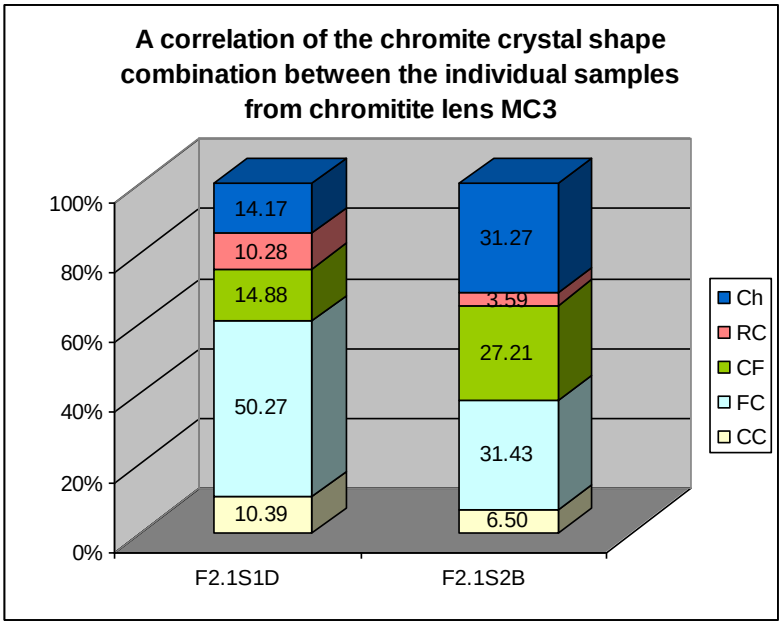

Figure 5.6: A stacked column graph presenting the point count results for the samples of chromitite lens MC3.

The point counts (table 5.2) for lens MC3 were performed on the two photographed samples. The average from the two samples indicates that 93% of lens MC3 consists of chromite crystals. The remaining 7% make up the matrix that is mainly composed of talc and hydrated iron oxides. Although the consistency between the two samples is not as good as for the samples from lens MC1, the majority of the chromite crystals in both samples are concentrated in the fractured crystals category (fig. 5.6). There is however a strong correlation between the chromite-to-matrix ratio.

The percentage of crystal chips in chromitite lens MC3 is much less than in lens MC1 and there is a large increase in the percentages of subhedral - euhedral crystal and fractured crystals. The majority of the chromite crystals (41%) in chromitite lens MC3 were fractured (fig. 5.7). Because there are overall fewer crystal chips and more subhedral - euhedral crystals present in lens MC3, it indicates that less crystal fracturing occurred in chromitite lens MC3. This is clearly visible in the photomicrographs and supported by the point counts.

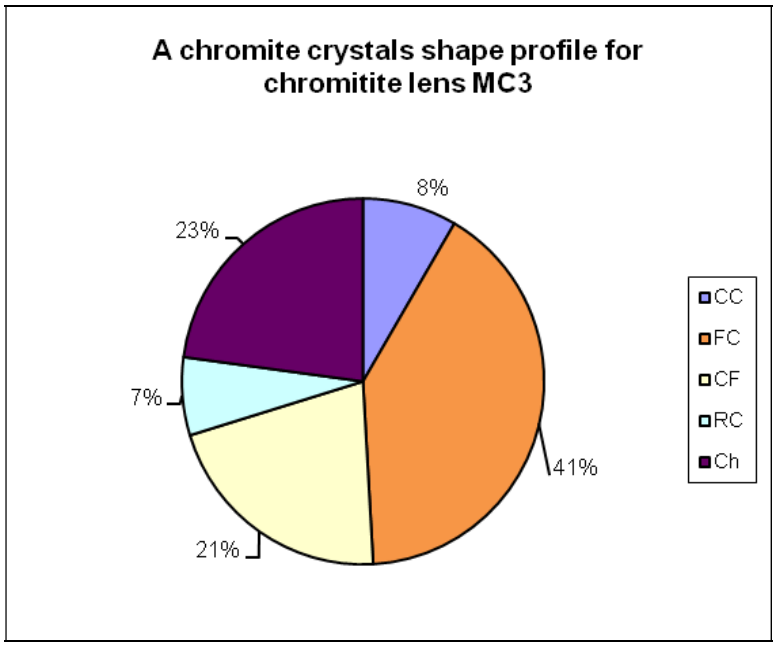

Figure 5.7: A pie chart presenting the point count results of chromitite lens MC3.

Chromitite lens MC4

The two samples from layer MC4 were collected far away from each other. The one was from section F1.5 and the other from F4.2 at the opposite side of the open pit.

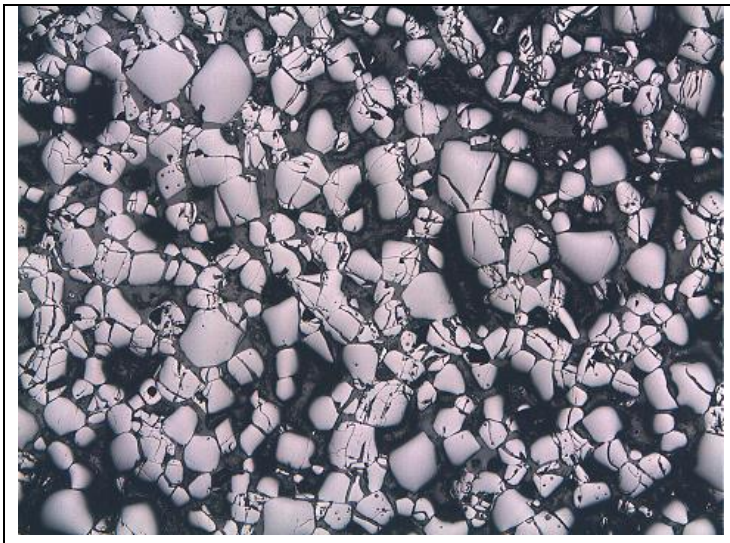

A: Photomicrograph of sample F1.5S2 under reflective light and 40x magnification. The amount of chips has drastically declined.

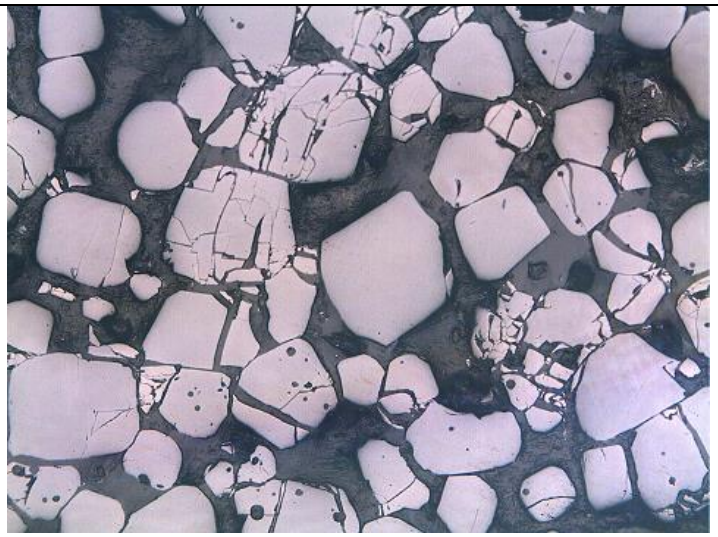

B: Photomicrograph of sample F1.5S2 under reflective light and 100x magnification. The chromite crystals are less fractured.

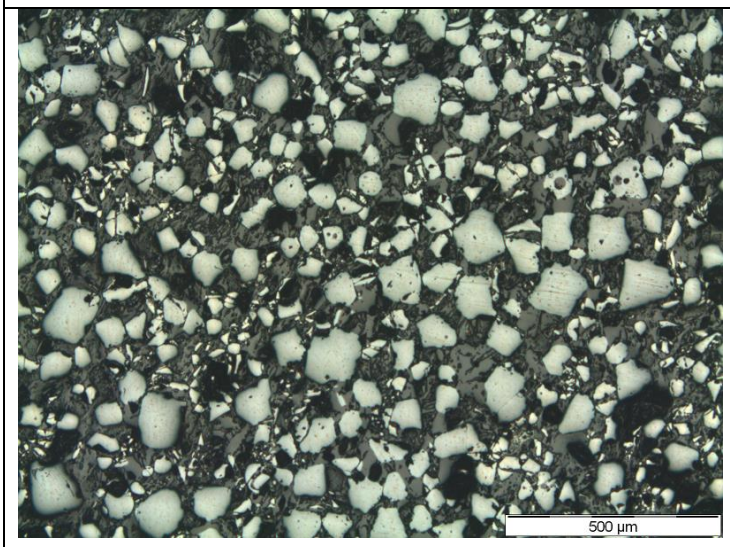

C: Photomicrograph of sample F4.2S2 under reflective light and 40x magnification. The majority of the chromite is crystal fragments.

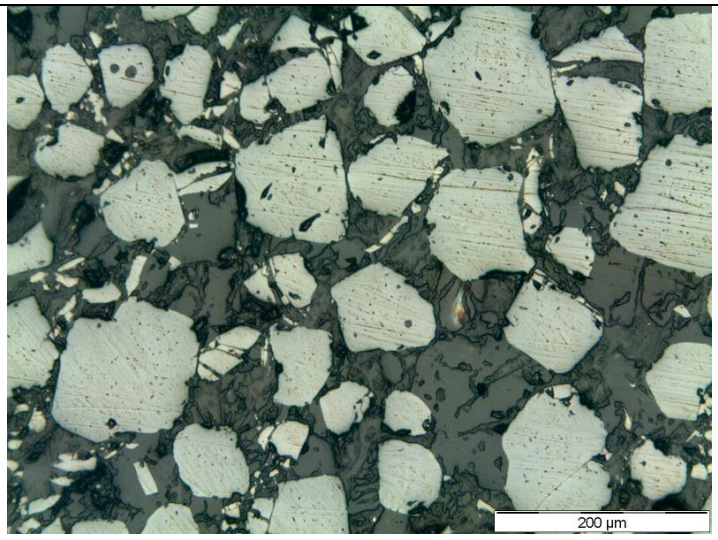

D: Photomicrograph of sample F4.2S2 under reflective light and 100x magnification. The overall size of the crystals increased.

Figure 5.8: Photomicrographs of the samples from chromitite lens MC4.

From the photomicrographs in figure 5.8 it is obvious that sample F1.5S2 has more fractured crystals than sample F4.2S2 with barely any fracturing. Apart from the fracturing there is a good correlation between the shape and size of the chromite fragments in the two samples. Once again the quantity of chips in lens MC4 is less than in chromitite lenses MC1 and MC3 (fig. 5.8A and C). The size of the crystal fragments is more constant in lens MC4 (fig. 5.8B). Although there is a greater consistency in the size of the crystal fragments there are very few un-deformed, subhedral - euhedral crystals in the sample (fig. 5.8D).

		Counts						
Sample	Lens	CC	FC	CF	RC	Ch	Cr total	Cr%
F1.5S2	MC4	43	355	795	38	212	1443	72.15
F4.2S2	MC4	99	47	923	65	329	1463	73.15
	Total %	4.89	13.83	59.12	3.54	18.62	2906	72.65

		Counts				
Sample	Lens	SiO	FeO (H_2O)	Total Matrix	% Matrix	Total
F1.5S2	MC4	536	21	557	27.85	2000
F4.2S2	MC4	535	2	537	26.85	2000
	Total %	26.78	0.58	27.35		4000

Table 5.3: Point count results of samples from chromitite lens MC4.

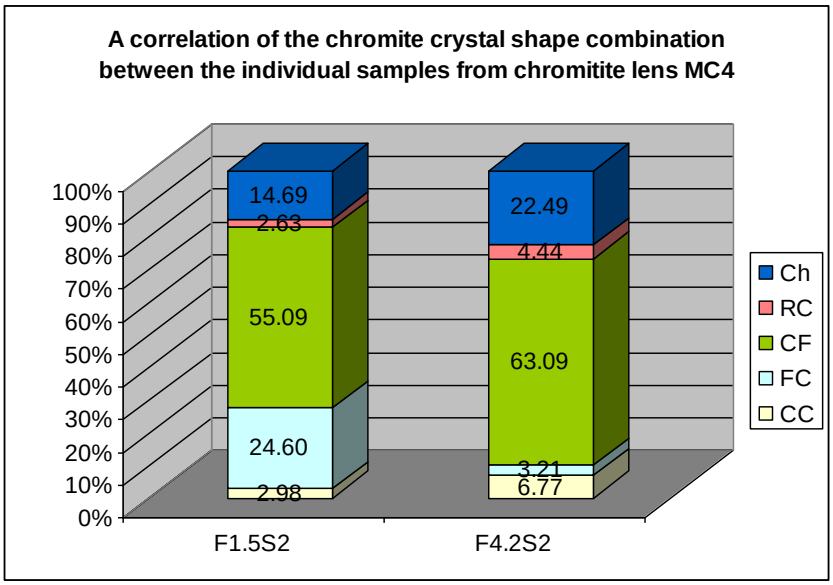

Figure 5.9: A stacked column graph presenting the point count results for samples of chromitite lens MC4.

Table 5.3 indicates a good consistency in the chromite to matrix ratio of the two samples. Point counts also confirm the big difference in the amount of fractured crystals that was observed from the photomicrographs in figure 5.8. Except for the fractured crystals there is a good consistency in the combination of crystal shapes between samples F1.5S2 and F4.2S2, with the majority in both samples in the crystal fragment category (fig. 5.9).

On average the majority of the chromite crystals in chromitite lens MC4 are broken into crystal fragments, with an average of 58% of the chromite crystals in this category. The percentage of chips has decreased from 23% in lens MC3 to 19% in lens MC4 (fig. 5.10).

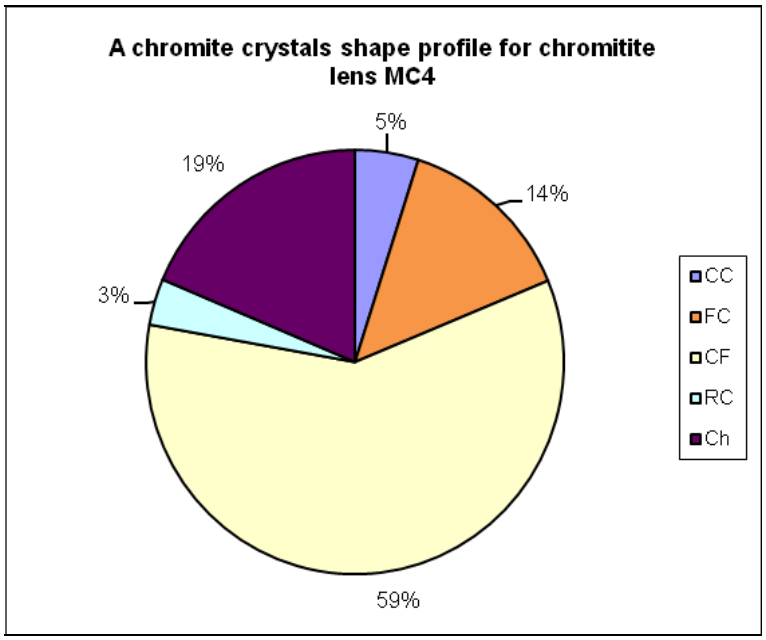

Figure 5.10: A pie chart presenting the point count results of chromitite lens MC4.

Chromitite lens MC5

Because of the limited exposure of the lowermost chromitite lens MC5 in the open pit, only one sample was available for the petrographic investigation. This sample came from geological section F4.2. Fracturing present in this layer is limited and the amount of small chips is minimal. In comparison to the other chromitite lenses fewer big crystals are broken into fragments and fractured crystals. The crystal fracturing in sample F4.2S4 is confined to isolated areas (fig. 5.11A and B).

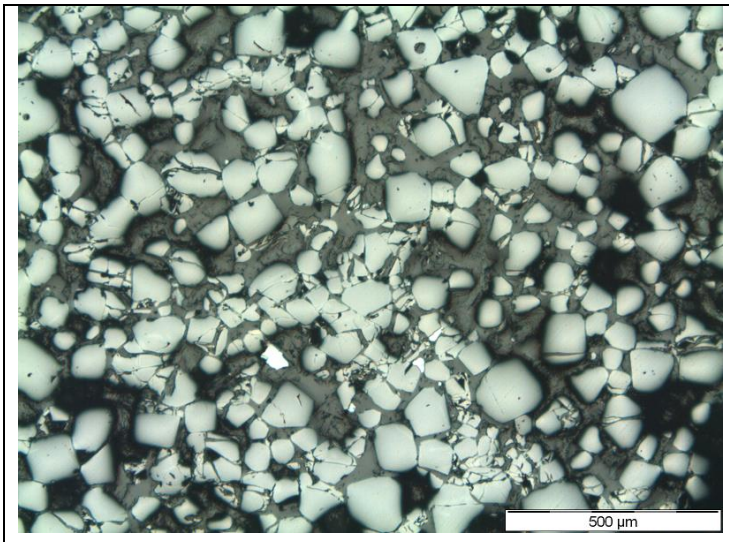

A: Photomicrograph of sample F4.2S4 under reflective light and 40x magnification. The crystal fracturing is restricted to isolated zones.

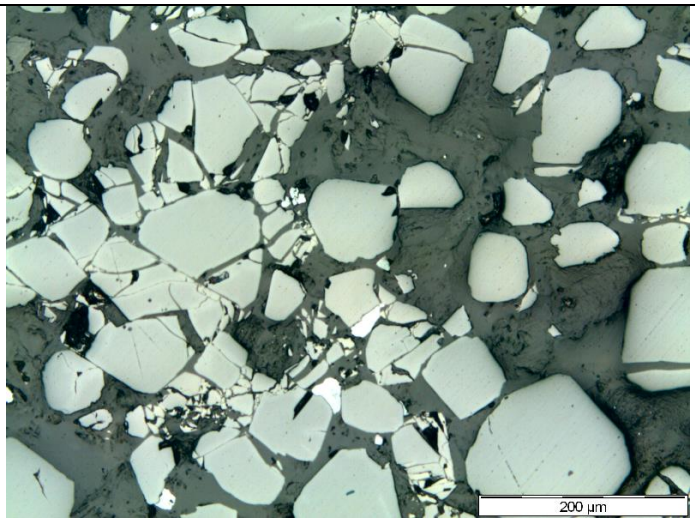

B: Photomicrograph of sample F4.2S4 under reflective light and 100x magnification. Displaying some details within a fractured zone.

Figure 5.11: Photomicrographs of the samples from chromitite lens MC5.

Sample F4.2S4 (figure 5.11A) display a substantial amount of subhedral to euhedral crystals and the isolation of the fracturing is clearly visible. The photomicrograph of figure 5.11B focuses on a fracture area and it is clear that the severity of the fracturing has declined from the previously discussed chromitite lenses, as only a small amount of small chips are present. The deformation mainly resulted into fractured crystals.

The result from the point counts of the samples from chromitite lens MC5 is presented in Table 5.4. The point counts indicate that 77% of chromitite lens MC5 consists of chromite. The remaining 22% represent the matrix material of talc and hydrated iron oxides.

		Counts						
Sample	Lens	CC	FC	CF	RC	Ch	Cr total	Cr%
F4.5S4	MC5	296	221	745	134	153	1549	77.45
	Total %	19.11	14.27	48.10	8.65	9.88	1549	77.45

		Counts				
Sample	Lens	SiO	FeO (H_2O)	Total Matrix	% Matrix	Total
F4.5S4	MC5	440	11	451	22.55	2000
	Total %	22.00	0.55	22.55		2000

Table 5.4: Point count results of samples from chromitite lens MC5.

The crystal shapes composition of the chromite in lens MC5 is similar to that of lens MC4. The majority of the crystals are classified as crystal fragments. There are however more rounded and subhedral - euhedral crystals in lens MC5. The crystal chips are down to 10% and the crystal fragments are 48%. This indicates that in general the chromite crystals are less fractured (fig. 5.12).

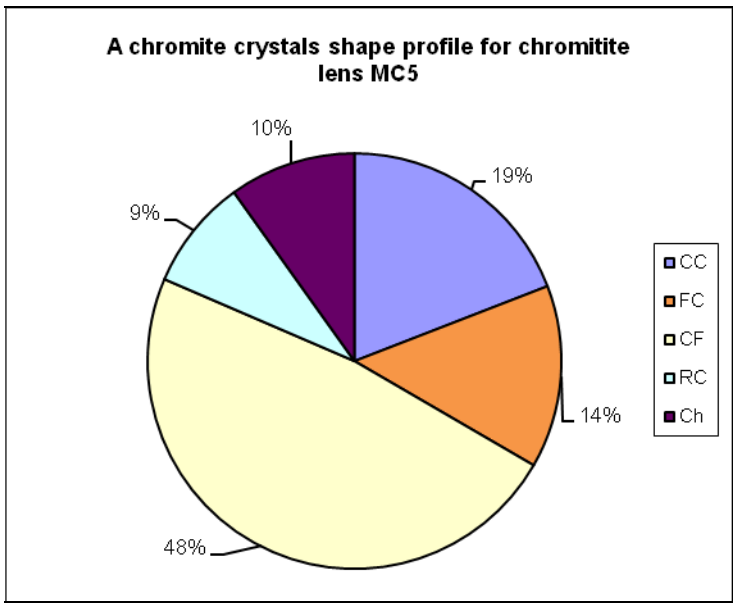

Figure 5.12: A pie chart presenting the point count results of chromitite lens MC5.

5.2.2 Core samples

The core from borehole UK33 was sampled and thin polished sections were petrological investigated. The hole is situated north of the open pit and recovered core of 25mm diameter.

All the chromitite intersections were sampled resulting to a total of 30 samples. The original log of the borehole was optioned from the Nkomati Mine borehole database. The PCR unit is underlying the Massive Chromitite Layer. The borehole intersected two layers of Chromitiferous Harzburgite. The upper PCR layer is about 13m thick and is labeled PCR1. The lower PCR layer is about 6m thick and is labeled PCR2. The two layers of PCR are separated by 4m of pyroxenite (table 5.5).

BHID	FROM	TO	LENGTH	ROCKTYPE	UNIT
UK33	0.00	3.70	3.70	Over Burden	OVB
UK33	3.70	8.81	5.11	Massive Chromitite	MCHR
UK33	8.81	10.18	1.37	Pyroxenite	PCR
UK33	10.18	11.17	0.99	Chromitiferous Harzburgite	PCR
UK33	11.17	11.75	0.58	Pyroxenite	PCR
UK33	11.75	12.10	0.35	CORELOSS	PCR
UK33	12.10	12.55	0.45	Pyroxenite	PCR
UK33	12.55	14.00	1.45	Chromitiferous Harzburgite	PCR
UK33	14.00	14.85	0.85	Pyroxenite	PCR
UK33	14.85	27.96	13.11	Chromitiferous Harzburgite 1 layer	PCR
UK33	27.96	31.71	3.75	Pyroxenite	PCR
UK33	31.71	32.13	0.42	Chromitiferous Harzburgite	PCR
UK33	32.13	32.39	0.26	Pyroxenite	PCR
UK33	32.39	38.74	6.35	Chromitiferous Harzburgite 2 layer	PCR

Table 5.5: Abstract from the original log of borehole UK33.

Table 5.6 presents a summary of the core samples that will be discussed in this chapter. This summary provides the opportunity to correlate the samples from the different layers that are indicated in table 5.5. Point counts were performed on three samples from both the Massive Chromitite Layer (MCHR) and the PCR1 layer. Only one sample from the

layer PCR2 was investigated (table 5.6). The photomicrographs of these samples will also be discussed

BH UK 33		
Sample	**Depth**	**Unit**
B1	1.2	Massive Chromitite
B4	6.2	Massive Chromitite
B9	8.7	Massive Chromitite
B17	18	Chromitiferous Harzburgite 1 layer
B20	23.9	Chromitiferous Harzburgite 1 layer
B23	25	Chromitiferous Harzburgite 1 layer
B29	37.5	Chromitiferous Harzburgite 2 layer

Table 5.6: Summary of the core samples that were used for point counting.

The Massive Chromitite Layer (MCHR)

The Massive Chromitite Layer is the uppermost of the three chromitiferous layers intersected in borehole UK33. It is also the same chromitite layer as the one that was sampled in the open pit. Since the majority of the chromitite lenses in the open pit are considered to be part of the Massive Chromitite Layer, there should be some resemblance between the MCHR layer samples from the borehole and some samples from the pit.

The three samples of the MCHR layer were specifically selected to represent the entire thickness of the layer. Sample B1 was collected at the top; sample B4 was near the middle portion and sample B9 at the bottom. The chromite crystals in sample B1 mostly consist of fractured crystals (fig. 5.13A). The fracturing seems to be quite intense in that some of the fractured crystals are severely deformed into a collection of crystal chips (fig. 5.13B). Sample B4 is similar to sample B1 but the size of the chromite crystals in the first are more constant (fig. 5.13C). According to figure5.13D it seems likely that sample B4 contain more fractured crystals than B1. Sample B9 at the bottom of the layer seems to have experienced the least fracturing. There seems to be less crystal chips (fig. 5.13E), although a large amount of fractured crystals and crystal fragments are still present (fig. 5.13 F).

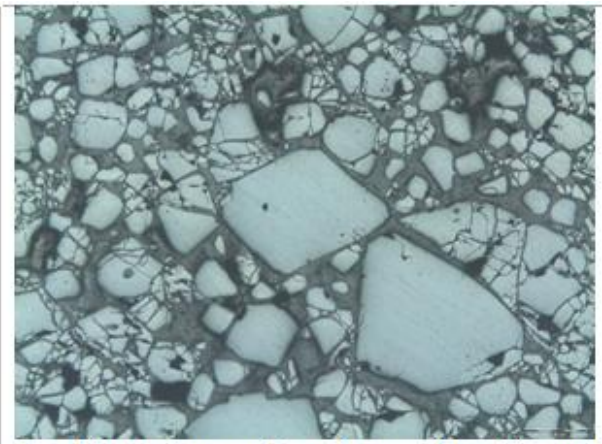

A: Photomicrograph of sample B1 under reflective light and 40x magnification, displaying a subhedral - euhedral crystal and a large number of fracture crystals.

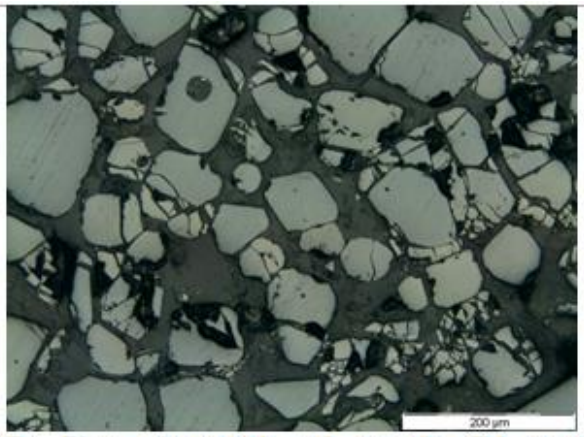

B: Photomicrograph of sample B1 under reflective light and 100x magnification. The majority of the chromite is crystal fragments.

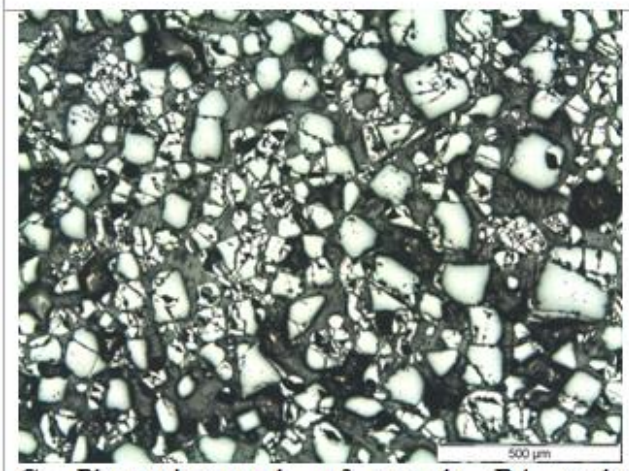

C: Photomicrograph of sample B4 under reflective light and 40x magnification, displaying a better size correlation between the crystals.

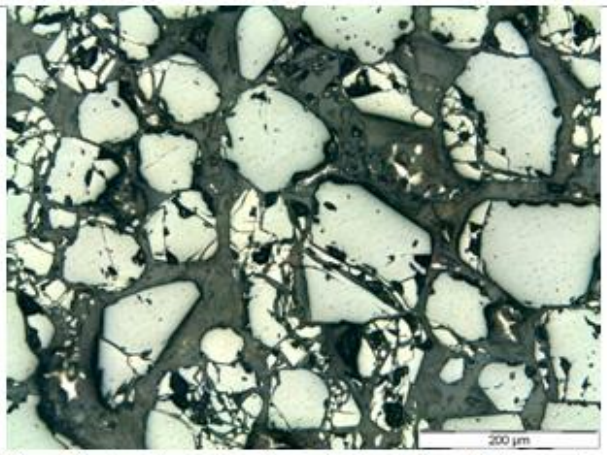

D: Photomicrograph of sample B4 under reflective light and 100x magnification. The majority of the crystals are fractured crystals.

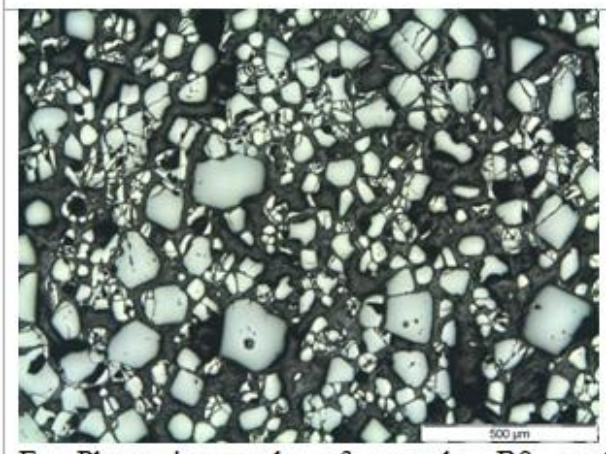

E: Photomicrograph of sample B9 under reflective light and 40x magnification. There is a decrease in the amount of chips.

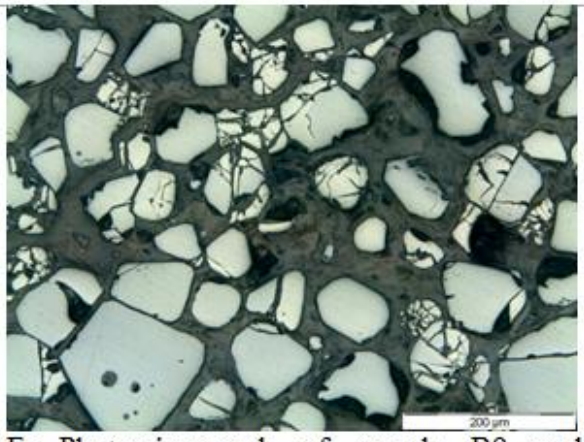

F: Photomicrograph of sample B9 under reflective light and 100x magnification. There is a strong rounding effect on the crystals.

Figure 5.13: Photomicrographs of the samples from the Massive Chromitite Layer.

From the three samples it is clear that there is a good consistency in the fracturing of the chromite crystals through the entire thickness of the MCHR layer. A decrease in the quantity of chips is however an indication that the degree of the fracturing is less towards the bottom of the layer. All these assumptions however will have to be verified by the point counts.

The point counts performed on the three samples of the Massive Chromitite Layer (MCHR) indicate that this layer contains an average of 87% chromite crystals of which 49% are fractured crystals (table 5.7).

		Counts						
Sample	Lens	CC	FC	CF	RC	Ch	Cr total	Cr%
B1	MCH	90	703	667	47	216	1723	86.15
B4	MCH	121	1033	416	70	182	1822	91.10
B9	MCH	107	853	483	128	114	1685	84.25
	Total %	6.08	49.50	29.94	4.68	9.79	5230	87.17
		Counts						
Sample	Lens	SiO	FeO (H_2O)	Total Matrix	% Matrix	Total		
B1	MCH	265	12	277	13.85	2000		
B4	MCH	177	1	178	8.90	2000		
B9	MCH	315	0	315	15.75	2000		
	Total %	12.62	0.22	12.83		6000		

Table 5.7: Point count results of samples from the Massive Chromitite Layer.

The percentages of the different crystal shapes in the three samples from the Massive Chromitite Layer are similar. The majority of the chromite grains are fractured crystals followed by crystal fragments. The sum of these two crystal shapes calculates to an average of 79% for the three samples. The percentage of crystal chips decreases from the top towards the bottom of the layer. These results confirm the observations from the photomicrographs in figure 5.13. As the percentage of chips decrease, the percentage of the rounded crystals increases (fig. 5.14). A strong correlation also exists between the percentage of the subhedral - euhedral crystals from the MCHR layer and the samples from the open pit. The average percentage of subhedral - euhedral crystals for the MCHR layer, calculated from the three core samples, is 6% and the percentage subhedral - euhedral crystals for the grab samples ranges from 1% to 19%, with an average of 7% for

all the grab samples. On average, 49% of the chromite crystals in the MCHR layer are deformed into fractured crystals and another 30% are broken into crystal fragments. Only 6% of the crystals are not fractured at all (fig.5.15). This combination of chromite crystal shapes correlates best with chromitite lens MC3.

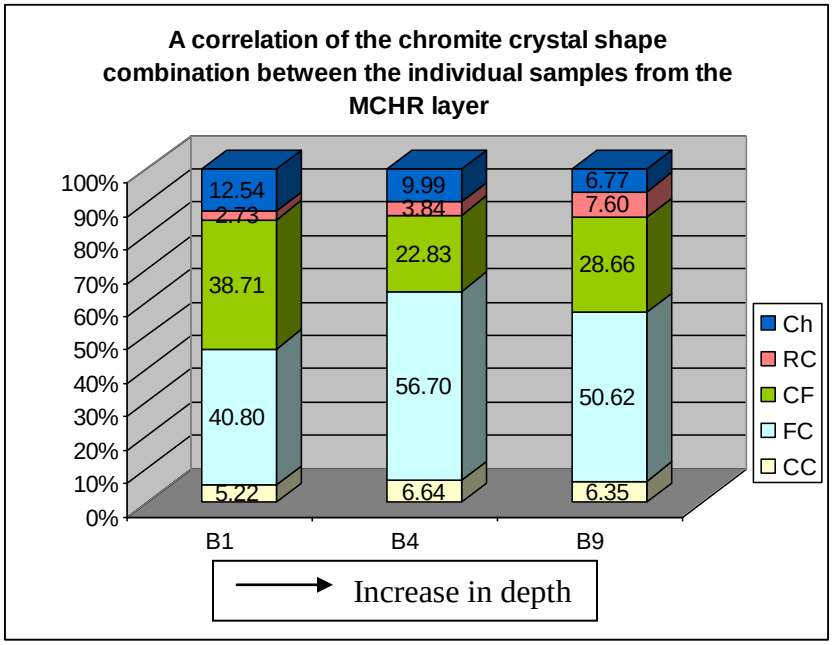

Figure 5.14: A stacked column graph presenting the point count results for the samples of the Massive Chromitite Layer.

The constant decrease in the percentage of chips from the top of the MCHR layer towards the bottom indicates a slight downwards decrease in the fracturing of the chromite crystals. This correlates well with the finding from the grab samples, where the percentage of chips also constantly decreased from lens MC1 to lens MC5.

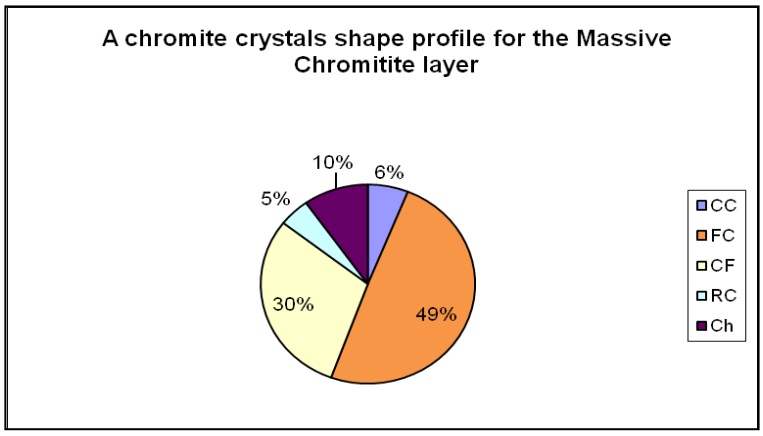

Figure 5.15: A pie chart presenting the averaged point count results of the Massive Chromitite Layer.

Chromitiferous Harzburgite Layer 1 (PCR1)

Chromitiferous Harzburgite Layer PCR1 is overlain by the Massive Chromitite Layer. The two layers are separated by six meters of pyroxenite with thin inter layering of PCR. In borehole UK33 the PCR1 layer was intersected between 14.85m and 27.96m below surface and has an apparent thickness of 13.11m (table 5.5).

Thin sections of three samples from the PCR1 layer were used for point counting. Samples B17, B20 and B23 were collected at the respective depths of 18m, 24m and 25m (table 5.6) to provide a spread of data through the entire thickness of the layer. Photomicrographs were taken from samples B17 and B23. This should provide an indication of any changes that might occur from the top to the bottom of the layer. Figure 5.16A and B are photomicrographs of sample B17 and figure 5.16C and D of sample B23. The images of the two samples in figure 5.16 look similar. The majorities of the chromite crystals are big and barely fractured with almost no crystal chips present. The subhedral - euhedral crystals in sample B17 are all very similar in size (fig. 5.16A). Apart from the majority of subhedral - euhedral crystals in sample B17 there is also a substantial amount of crystal fragments and the rounding effect on the grains is limited (fig. 5.16B). The size of the subhedral - euhedral crystals in sample B23 is much more diverse than in sample B17 (fig. 5.16C). The majority of the chromite crystals and fragments are also more rounded and fused together than in sample B17 (fig. 5.16D). Apart from these minor differences the concentrations of the different chromite crystal shapes in these samples seem to be similar.

All the samples of the Massive Chromitite Layer are distinctly more fractured than the two samples from the PCR1 layer. It almost gives the impression that most of the chromite crystals of the PCR1 formed in-situ. However there are some rounded crystals present which might indicate that the crystals were transported in a highly viscose magma, similar to the rounding effect of pebbles in a stream.

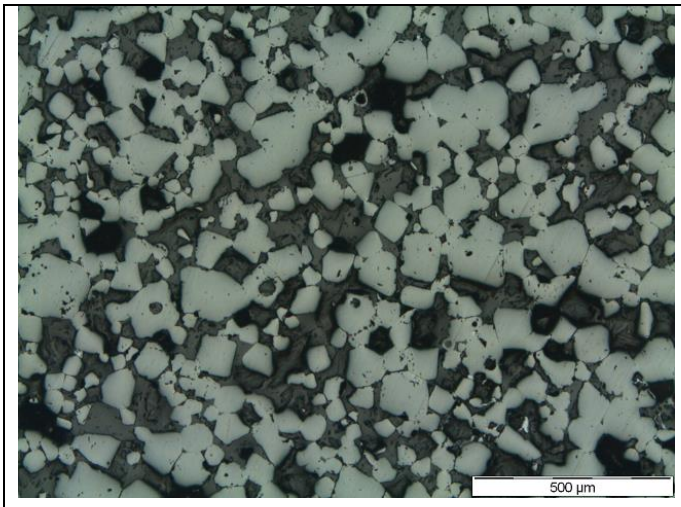 A: Photomicrograph from sample B17 under reflective light and 40x magnification. There is a large amount of subhedral to euhedral crystals.	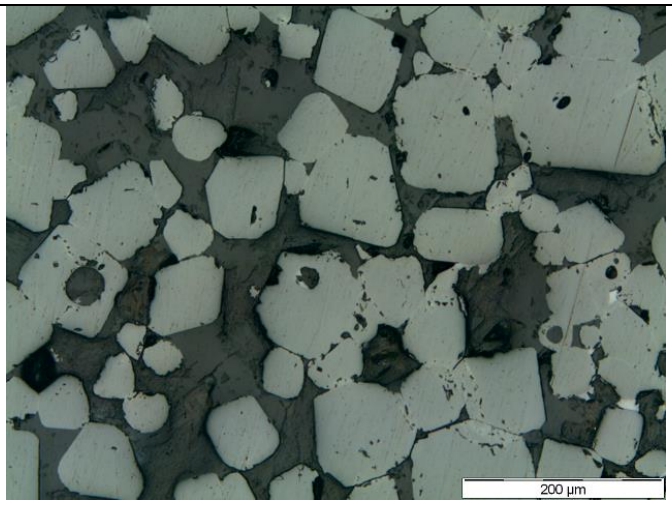 B: Photomicrograph of sample B17 under reflective light and 100x magnification. Only a small amount of crystal fracturing is present in the sample.
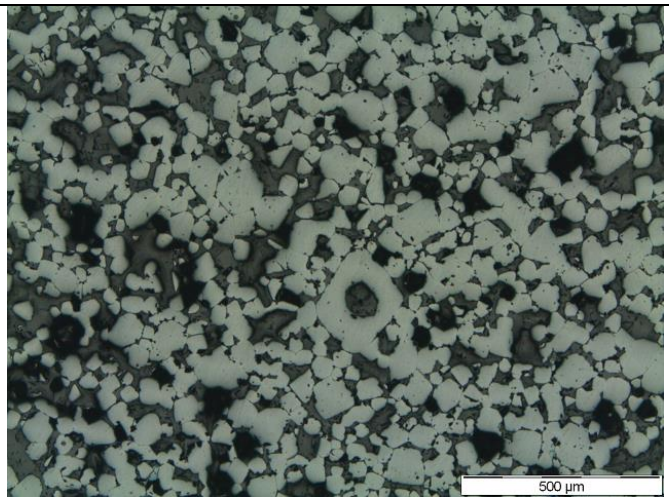 C: Photomicrograph of sample B23 under reflective light and 40x magnification. The chromite crystals are spaced closely together.	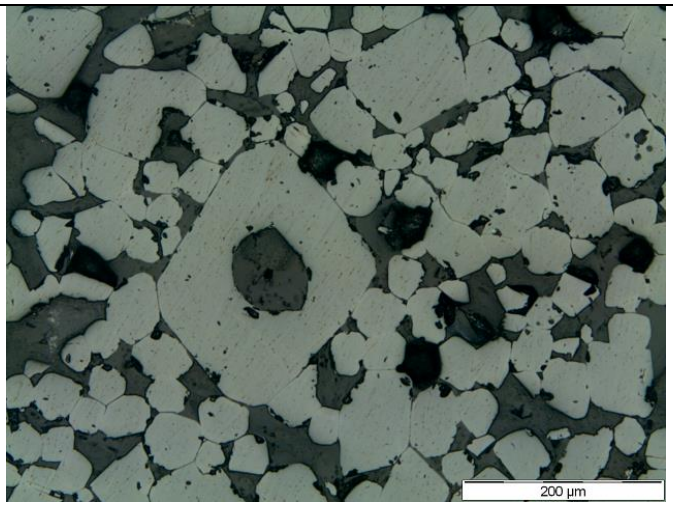 D: Photomicrograph of sample B23 under reflective light and 100x magnification. There is a big size variance between the crystals.

Figure 5.16: Photomicrographs of the samples from the PCR1 layer.

Point counts were performed on samples B17 and B23 displayed in figure 5.16. as well as B20 which was collected from the central part of the PCR1 layer. On average 79% of the PCR1 layer consists of chromite crystals and 21% matrix material (table 5.8). This percentage of chromite crystals in the PCR1 layer is less than the 87% of the Massive Chromitite Layer.

		Counts						
Sample	Lens	CC	FC	CF	RC	Ch	Cr total	Cr%
B17	PCR1	711	41	726	58	33	1569	78.45
B20	PCR1	756	76	538	166	100	1636	81.80
B23	PCR1	818	82	443	133	77	1553	77.65
	Total %	48.02	4.18	35.88	7.50	4.41	4758	79.30
		Counts						
Sample	Lens	SiO	FeO (H_2O)	Total Matrix	% Matrix	Total		
B17	PCR1	431	0	431	21.55	2000		
B20	PCR1	357	7	364	18.20	2000		
B23	PCR1	443	4	447	22.35	2000		
	Total %	20.52	0.18	20.70		6000		

Table 5.8: Point count results of samples from the PCR1 layer.

The results of the three samples are very much the same. The majority of the chromite crystals are subhedral - euhedral without any deformation. A constant increase in the amount of crystal fragments from the bottom to the top causes the quantity of crystal fragments to equalize the subhedral - euhedral fraction. There is also a constant increase of the subhedral - euhedral and the fractured crystals from sample B17 to B23, as well as a constant decrease in the percentage of crystal fragments from sample B17 toB23 (fig. 5.17).

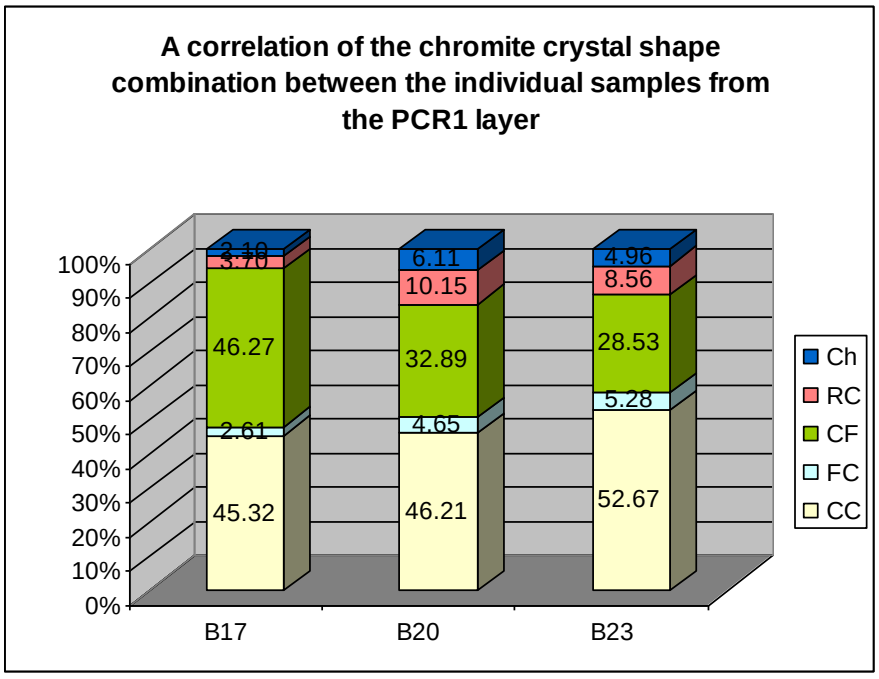

Figure 5.17: A stacked column graph presenting the point count results for the samples of the PCR1 layer.

On average the majority of the chromite crystals in the PCR1 layer are subhedral - euhedral crystals, followed by crystal fragments. Together these two categories occupy 84% of all the chromite in the layer (fig. 5.18). The consistent difference in optical appearance between the photomicrographs of the samples from the MCHR layer and the PCR1 layer are supported by the fundamental differences in the point count results. From the petrography it is clear that the chromite crystals in the MCHR layer are much more fractured than in the PCR1 layer.

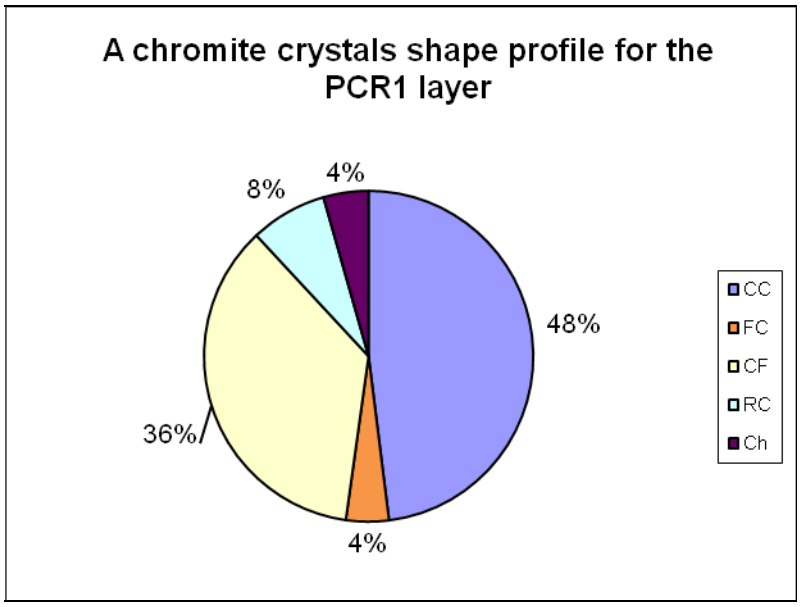

Figure 5.18: A pie chart presenting the averaged point count results of the PCR1 layer.

The constant increase in the percentage of subhedral - euhedral crystal from sample B17 at the top of layer PCR1 to sample B23 at the bottom, clearly indicates that the fracturing of the chromite crystals decrease from the top to the bottom of the layer. The same decreasing pattern in the fracturing of the chromite crystal was detected in the MCHR layer. This pattern is even further supported by the fact that on average the chromite crystals of the MCHR layer is much more fractured than those of the PCR1 layer.

Chromitiferous harzburgite layer 2 (PCR2)

The PCR2 layer is the oldest of the chromitiferous layers that was intersected by borehole UK33. According to the core it is apparently 3.5m thick and is separated from layer PCR1 by 4m of pyroxenite. According to the core log the pyroxenite is not enriched in chromite (table 5.5). Sample B29 was used for the petrographic investigation.

Figure 5.19A and B are photomicrographs of the thin section from sample B29. The chromite crystals in this sample are much smaller in size than in the previous chromitiferous layers (fig. 5.19A). There is a substantial amount of rounding present as most of the chromite crystals have rounded corners. The rounding is much more prominent than in the two previous layers. It is evident that more matrix minerals are present as the chromite crystals are further apart (fig. 5.19B).

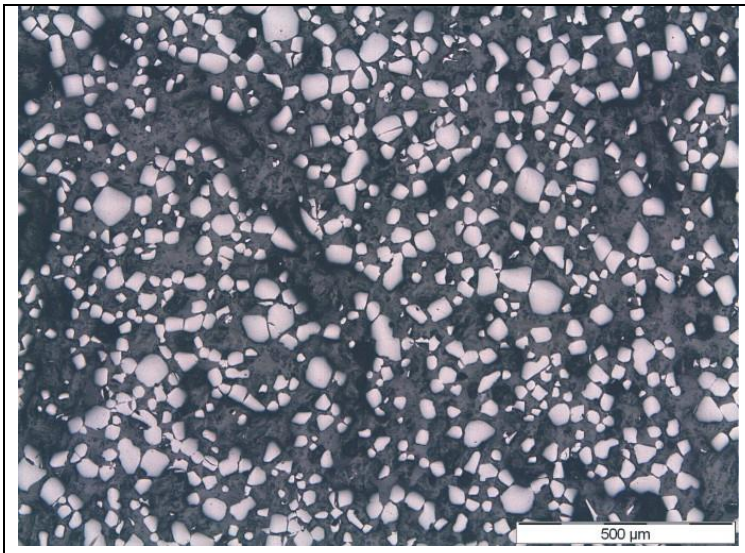

A: Photomicrograph of sample B29 under reflective light and 40x magnification. The chromite crystals are small.

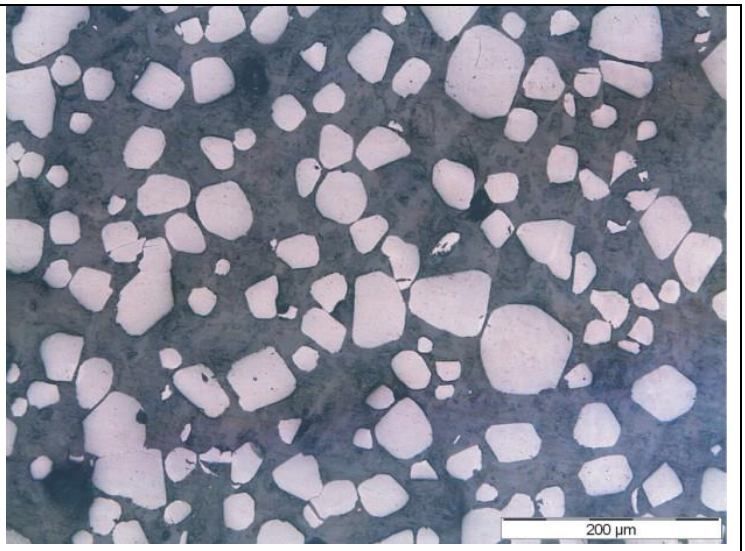

B: Photomicrograph of sample B29 under reflective light and 100x magnification. The majority of the crystals have been deformed by a rounding event.

Figure 5.19: Photomicrographs of the samples from the PCR2 layer.

		Counts						
Sample	Lens	CC	FC	CF	RC	Ch	Cr total	Cr%
B29	PCR2	525	21	730	120	60	1456	72.80
	Total %	36.06	1.44	50.14	8.24	4.12	1456	72.80

		Counts				
Sample	Lens	SiO	FeO (H_2O)	Total Matrix	% Matrix	Total
B29	PCR2	540	4	544	27.20	2000
	Total %	27.00	0.20	27.20		2000

Table 5.9: Point count results of sample B29 from the PCR2 layer.

The point counts of sample B29 indicates that the PCR1 layer contains 73% chromite and 27% matrix material (table 5.9). There is a constant decrease in the percentage of chromite crystals from the MCHR layer to the PCR1 layer.

The majority of the chromite crystals in PCR2 layer are crystal fragments. Thirty six percent of the crystals are subhedral - euhedral crystals (fig. 5.20). This is less than in the PCR1 layer that had 48%. This indicates that more chromite crystals in the PCR2 layer were fractured even though it is older than PCR1. This clearly indicates that the relative age of a chromitite layer is not the only controlling factor of the fracturing of the chromite crystals.

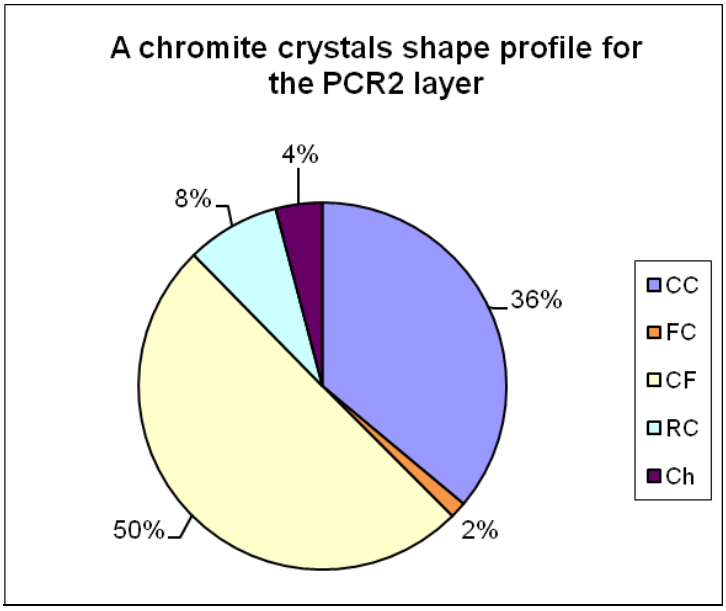

Figure 5.20: A pie chart presenting the averaged point count results of the PCR2 layer.

5.3 Summary

The foremost important fact that can be established from the chapter is that the chromite crystals of all the chromitiferous layers are fractured to a certain degree. The degree of the fracturing varies from one chromitiferous layer to the next. The fracturing deformed the crystals into five distinct shapes. Each of the five crystal shapes represents a distinct level of deformation. The subhedral - euhedral crystals (CC) indicate no crystal deformation. The fractured crystals (FC) indicate low crystal deformation in that the grains are only cracked, but still intact. The crystal fragments (CF) indicate medium to high crystal deformation, in that the chromite grains are broken into a number of smaller pieces that are separated from each other. The crystal chips (Ch) indicate extremely high deformation in that a chromite crystal is crushed into a large quantity of small angular pieces. The rounded crystals (RC) seem to be the result of a different, but related event and rather represent crystals that have been abraded in a flowing magma.

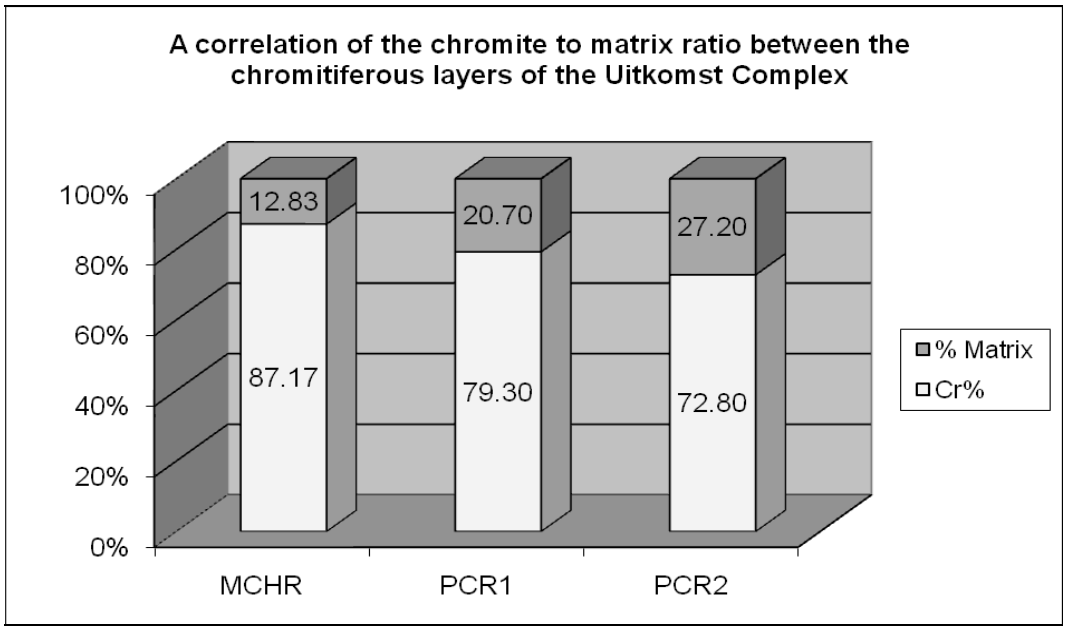

Figure 5.21: A stacked column graph presenting a summary of the average chromite to matrix ratio for the chromitiferous layers intersected by borehole UK33.

The ratio of chromite to matrix displays a decreasing trend from the youngest (MCHR) to the oldest PCR2 layer (fig. 5.21). One of the controlling factors on this ratio is the relative speed of chromite crystallization in relation to that of the harzburgite matrix

(orthopyroxene and olivine). The tempo of crystallization intern is controlled by the temperature at which the crystallization takes place. Garnet-free harzburgite crystallizes from both 'cratonic' and 'oceanic' peridotite at temperatures above 1450°C - 1600°C and pressures below 4.5–5 GPa *(Canil, 1991).* The melting temperature of chromite on the other hand is between 1538°C - 1907°C (fig. 5.22). Therefore once a chromium-rich influx of magma starts mixing with the parental magma, from which olivine and pyroxene are crystallizing, the temperature of the new magma will drop rapidly to below the melting point of chromite which then will crystallize faster than the matrix minerals. This is in accordance with Irvine (1977) who stated that for a high concentration chromitite layer to form an intervention like magma replenishment is necessary.

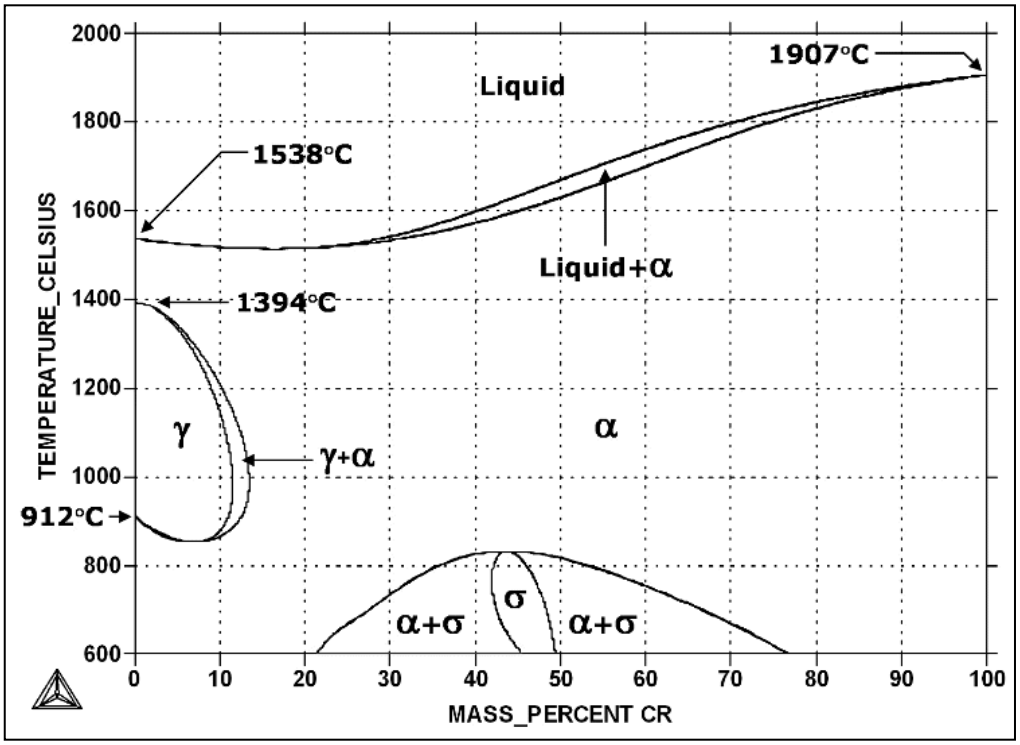

Figure 5.22 Fe-Cr phase diagram shows which phases are to be expected at equilibrium for different combinations of chromium content and temperature. The Fe-Cr phase diagram was calculated with Thermo-Calc, coupled with PBIN thermodynamic database. The melting point of iron and chromium at the pressure of 101325 Pa is 1538 °C and 1907 °C, respectively (*Computational Thermodynamics, 2011,).*

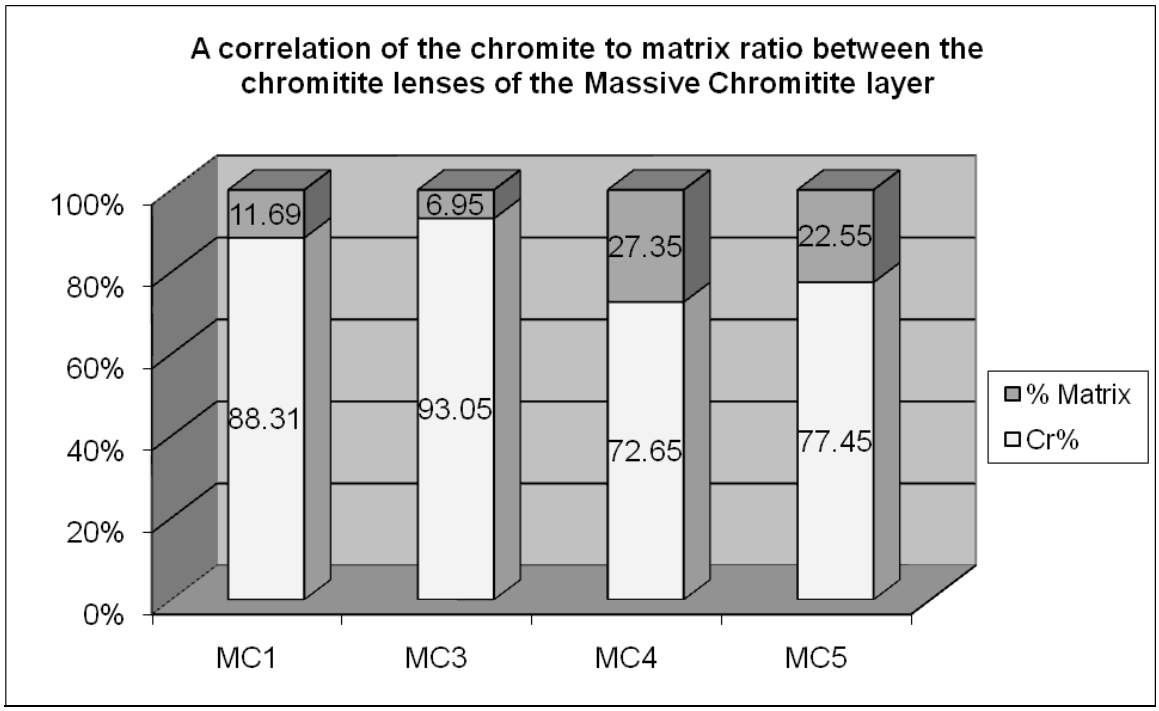

Figure 5.23: A stacked column graph presenting a summary of the average chromite to matrix ratio of the individual chromitite lenses of the Massive Chromitite Layer.

Figure 5.23 presents the average percentage of chromite crystals within the massive chromitite lenses that are exposed in the pit. The first observation from figure 5.23 is that the four chromitite lenses are divided into two definite groups. The first group consists of chromitite lenses MC1 and MC3, with their respective chromite percentages of 88% and 93%. The second group consists of chromitite lenses MC4 and MC5 with their respective chromite percentages of 63% and 78%. The percentages of chromite crystals in chromitite lenses MC4 and MC5 is much lower than in lenses MC1 and MC3. This illustrates that the deposition of lenses MC4 and MC5 differs from the other lenses in the study area.

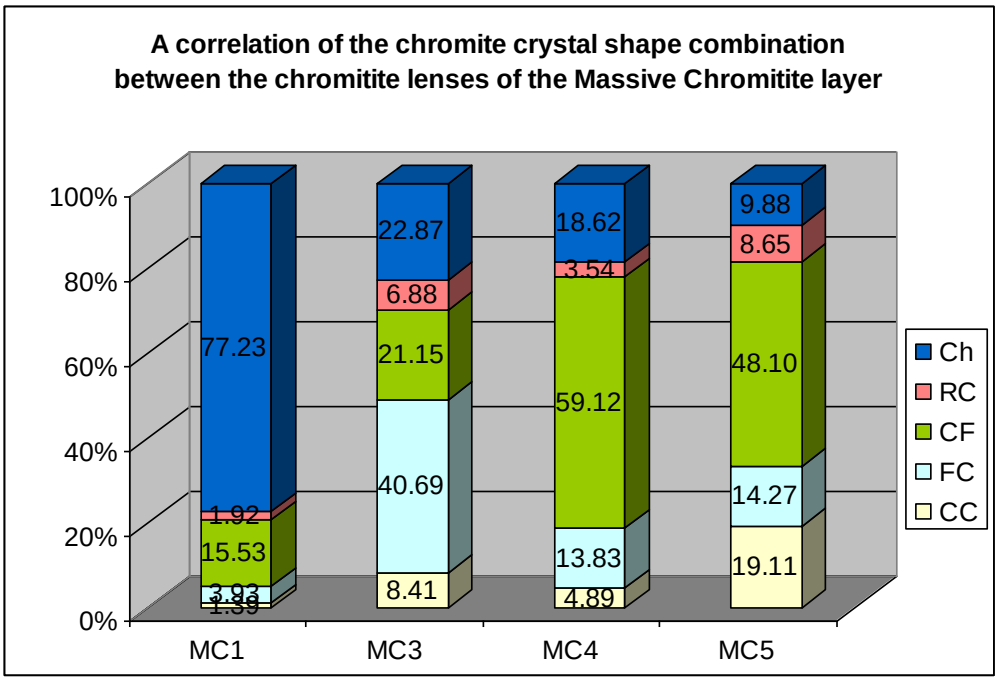

Figure 5.24: A stacked column graph presenting a summary of the average point count results for the massive chromitite lenses in the pit.

Figure 5.24 presents the shape combination of the chromite crystals within each of the chromitite lenses of the Massive Chromitite Layer. The majority of the grains in the MC1 lens are fractured into chips whereas those in lens MC3 occur in the form of fractured crystals occur. Chromitite lenses MC4 and MC5 are the only two lenses that show a correlation on the graph. The majority of the chromite crystals in both the lenses are crystal fragments (CF). This once again distinguishes chromitite lenses MC4 and MC5 from the other lenses. The graph in figure 5.24 reveals a constant decrease in the percentage of chips from chromitite lens MC1 to lens MC5. This means that less chromite crystals were crushed into small chips which would imply that the degree of the crystal fracturing increased over time from the deposition of chromitite lens MC5 to MC1.

The samples from the borehole UK33 was used to correlate the chromite crystal fracturing of the Massive Chromitite Layer with the older and stratigraphically lower chromitiferous layers. The core samples revealed that the decreasing trend in the crystal chips continues further down from the Massive Chromitite Layer to the PCR2 layer (fig.

5.25). This is a clear indication that the degree of the chromite crystal fracturing increased over time from the deposition of the PCR1 layer to that of chromitite lens MC1.

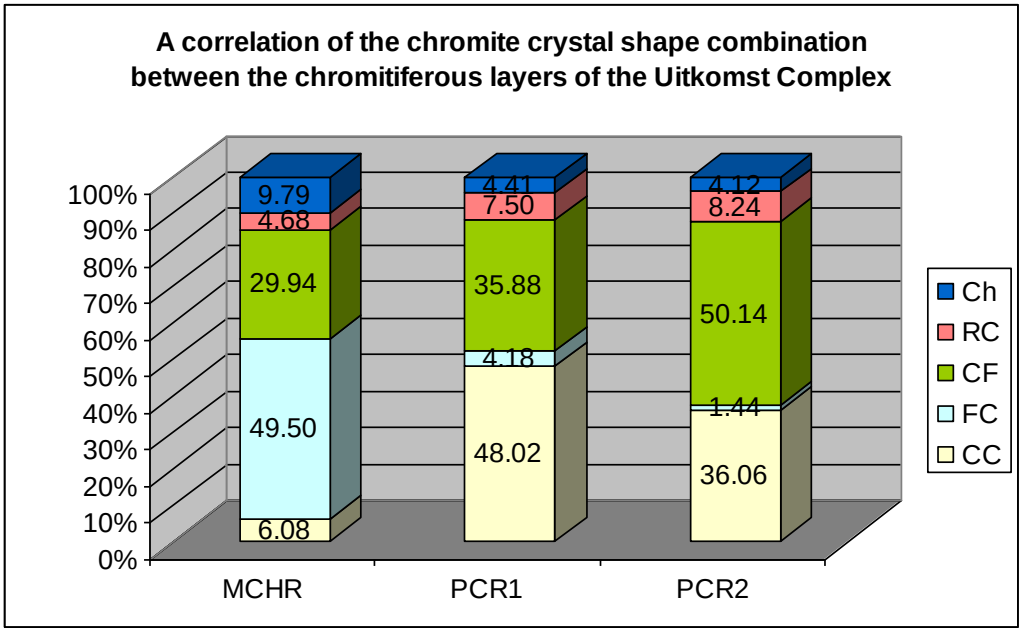

Figure 5.25: A stacked column graph presenting a summary of the average point count results for the chromitiferous layers intersected by borehole UK33.

The rounded crystals as well as the crystal fragments also display the constantly decreasing trend from the PCR2 layer upwards. A strong rounding effect was also observed on the chromite crystals of the PCR2 layer. This further supports the notion that the relative time of deposition of the chromitiferous layers affected the fracturing of the chromite crystals. In figure 5.26 the percentage of each chromite crystal shape is plotted against the elevation of the chromitiferous layer below surface. The elevation of a layer represents the relative time during which the deposition of the layer took place. Figure 5.26 illustrates that the amount of chips decreases with depth while that of the crystal fragments increases. This clearly indicates that although the chromite crystals in all the chromitiferous layers are fractured, the size of the fragments increases from the younger layers downwards. This once again shows that the degree of the crystal fracturing decreased over time from the deposition of the PCR2 layer onwards.

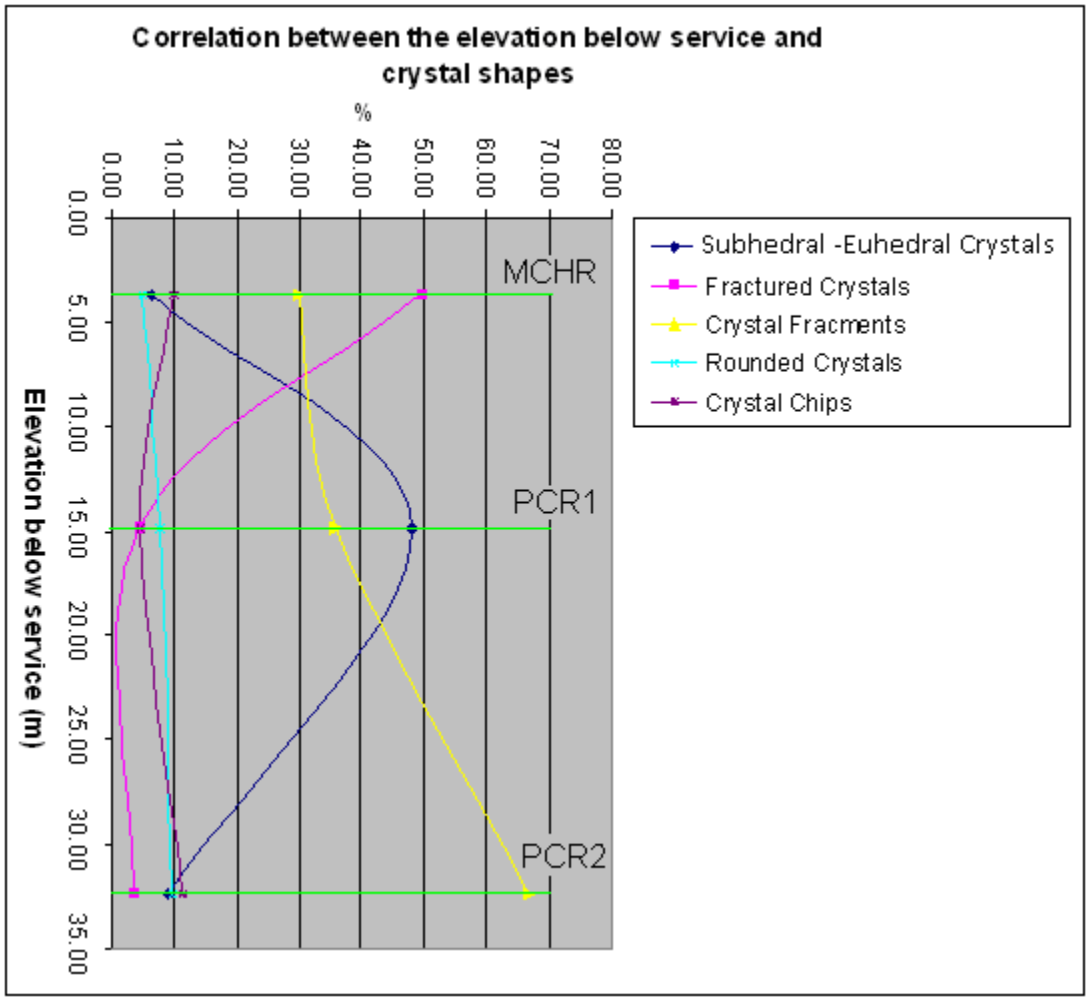

Figure 5.26: A line diagram of the correlation between the relative elevations below surface of the chromitiferous layers against the percentages of the various crystal shapes.

It is however important to remember that the Uitkomst Complex is situated in a conduit system and the magma that flows through the channel comes from a primary chamber in which the cooling and crystallizing was slow. Therefore the temperature of the magma flowing through the conduit should also change over time. Since there are time gaps between the deposition of the different chromitiferous layers according to Bowen's reaction series it is possible that each chromitite layer was deposited from magma with specific characteristics such as chemistry and viscosity as these two characteristics are related to the temperature of magma (fig 5.27). These differences in magma characteristics should contribute to the variances in the degree of crystal fracturing between the chromitiferous layers.

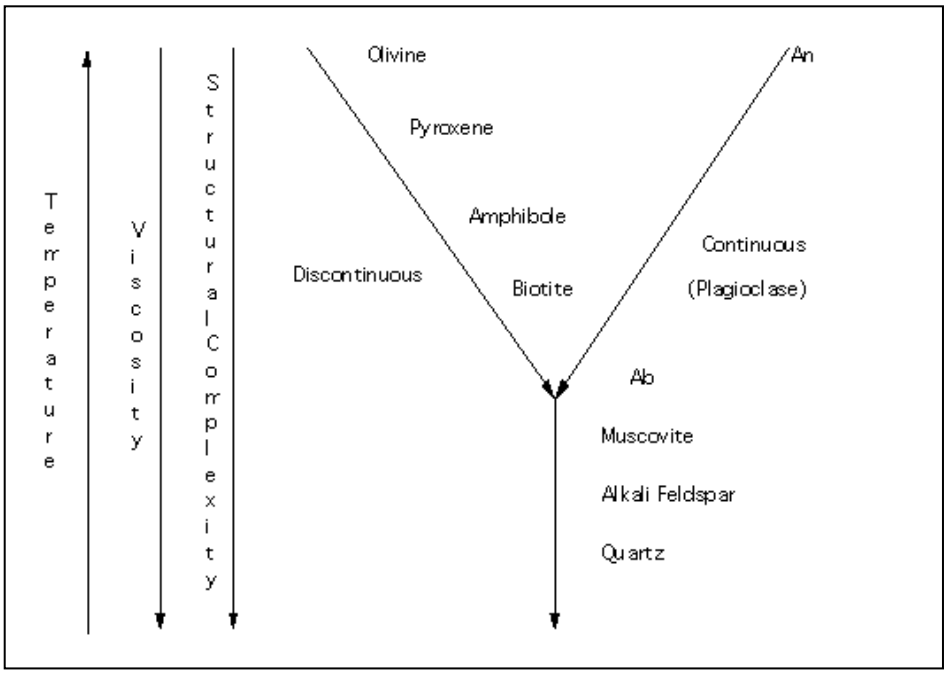

Figure 5.27: Bowen's reaction series displaying the relation between temperature and viscosity in a cooling magma (University of Houston, 2011).

In order to determine the percentage of crystal fracturing that occurred within a chromitite layer it is important to consider all the crystal shapes. Because the amount of each crystal shape within the chromitiferous layers is known, it is possible to calculate the average percentage of crystal fracturing that occurred within each of the layers. This is done by assigning a certain weight to each crystal shape and calculating a weighted average for the entire chromitite lens. The weight that is assigned to a crystal shape must represent its influence on the crystal fracturing of the entire layer. Because the rounded crystals are the result of abrasion it is not included in the calculation.

The weighting of the crystal shapes will be according to a scale from zero to ten, where zero = no fracturing and ten = total fracturing.

The weighting is categorized as follow:

Subhedral - euhedral crystals (cc)	0/10
Fractured crystals (fc)	2/10
Crystal fragments (cf)	5/10
Crystal chips (ch)	10/10

Sample	Lens	cc	Weight	fc	Weight	cf	Weight	ch	Weight	Weight	Counts	% Fracturing
		Counts	0	Counts	2	Counts	5	Counts	10	Total	Total	
F2.1S1C	MC1	12	0	78	156	148	740	1441	14410	15306	1679	91.2
F2.1S2A	MC1	37	0	61	122	401	2005	1289	12890	15017	1788	84.0
	Total	49	0	139	278	549	2745	2730	27300	30323	3467	87.5
F2.1S1D	MC3	190	0	919	1838	272	1360	259	2590	5788	1640	35.3
F2.1S2B	MC3	123	0	595	1190	515	2575	592	5920	9685	1825	53.1
	Total	313	0	1514	3028	787	3935	851	8510	15473	3465	44.7
F5S2	MC4	43	0	355	710	795	3975	212	2120	6805	1405	48.4
F4.2S2	MC4	99	0	47	94	923	4615	329	3290	7999	1398	57.2
	Total	142	0	402	804	1718	8590	541	5410	14804	2803	52.8
F4.5S4	MC5	296	0	221	442	745	3725	153	1530	5697	1415	40.3
	Layer											
B1	MCHR	90	0	703	1406	667	3335	216	2160	6901	1676	41.2
B4	MCHR	121	0	1033	2066	416	2080	182	1820	5966	1752	34.1
B9	MCHR	107	0	853	1706	483	2415	114	1140	5261	1557	33.8
	Total	318	0	2589	5178	1566	7830	512	5120	18128	4985	36.4
B17	PCR1	711	0	41	82	726	3630	33	330	4042	1511	26.8
B20	PCR1	756	0	76	152	538	2690	100	1000	3842	1470	26.1
B23	PCR1	818	0	82	164	443	2215	77	770	3149	1420	22.2
	Total %	2285	0	199	398	1707	8535	210	2100	11033	4401	25.1
B29	PCR2	525	0	21	42	730	3650	60	600	4292	1336	32.1

Table 5.10: Summary of the fracturing percentage calculation.

Table 5.10 presents a summary of the calculations that are used to determine the percentage of crystal fracturing for each of the samples that are discussed in the chapter. The percentages of all the samples from a specific layer are averaged to calculate the average for the entire layer and are indicated by the red cells in the % fracturing column (table 5.10).

Although there is an overall increase in the percentage of fracturing from the oldest chromitiferous layer upwards there is some deviation from this pattern (fig. 5.28). This again indicates that the relative time period of deposition is not the only controlling factor on the fracturing of the chromite crystals. Therefore secondary factors that could influence crystal fracturing, such as layer thickness, should be considered

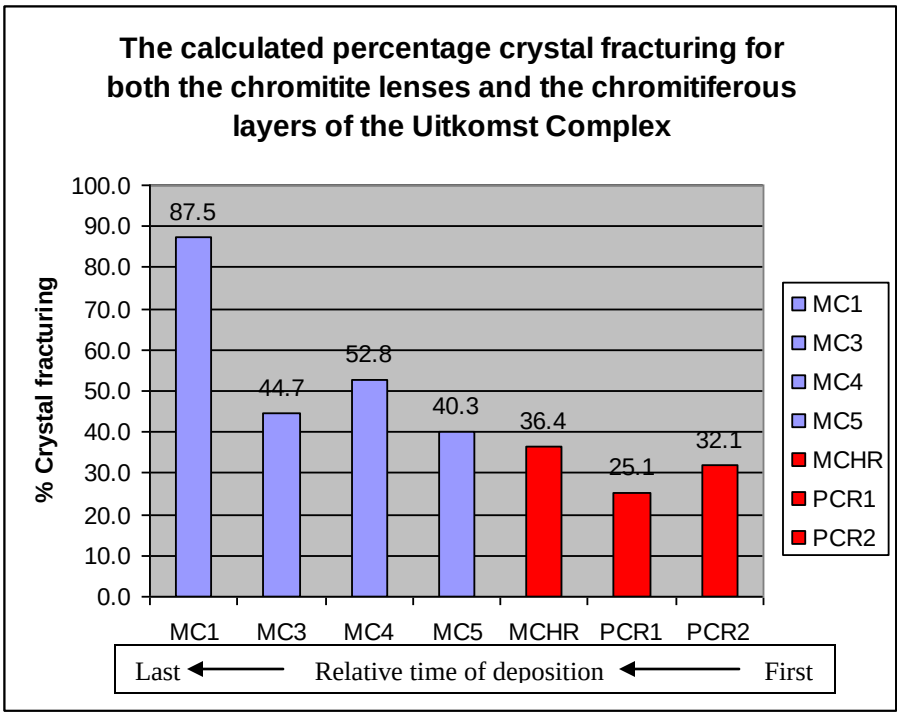

Figure 5.28: A column diagram displaying the average percentage of crystal fracturing for all the chromitite lenses and chromitiferous layers.

In order to investigate the effect of layer thickness on crystal fracturing only the results from the drill core samples will be used, since the thicknesses of the chromitiferous layers are recorded in the core log of borehole UK33. According to the log the PCR1 layer has the largest thickness of the three chromitiferous layers and it is about double the thickness of the other two layers (table 5.11).

BHID	FROM	TO	LENGTH	UNIT
UK33	3.70	8.81	5.11	MCHR
UK33	14.85	27.96	13.11	PCR 1
UK33	32.39	38.74	6.35	PCR 2

Table 5.11: Summary of the chromitiferous intersections from borehole UK33.

Figure 5.29 displays the correlation between the apparent thicknesses of the chromitiferous layers and the percentage of crystal fracturing. There is a strong negative correlation on the graph (fig. 5.29) and the fracturing percentage increases as the thickness of the layers decreases. In a case where each chromitiferous layer is the result of an influx of new chromium-rich magma into the primary magma chamber, the thickness of the layer would be representative of the relative volume of the influx.

Once again the volume of the influx will affect the temperature of the magma that is transporting the chromite crystals, as a small volume, high temperature addition of chromium-enriched magma into a cooler parental magma will be cooled down faster by the parental magma than a larger influx. The temperature once again influences the viscosity of magma *(Whitten and Davis, 1992),* which internally determines the amount of stress that is applied to the chromite crystals in suspension in the magma. Before this theory can be accepted the idea of multiple influxes has to be investigated by means of mineral chemistry.

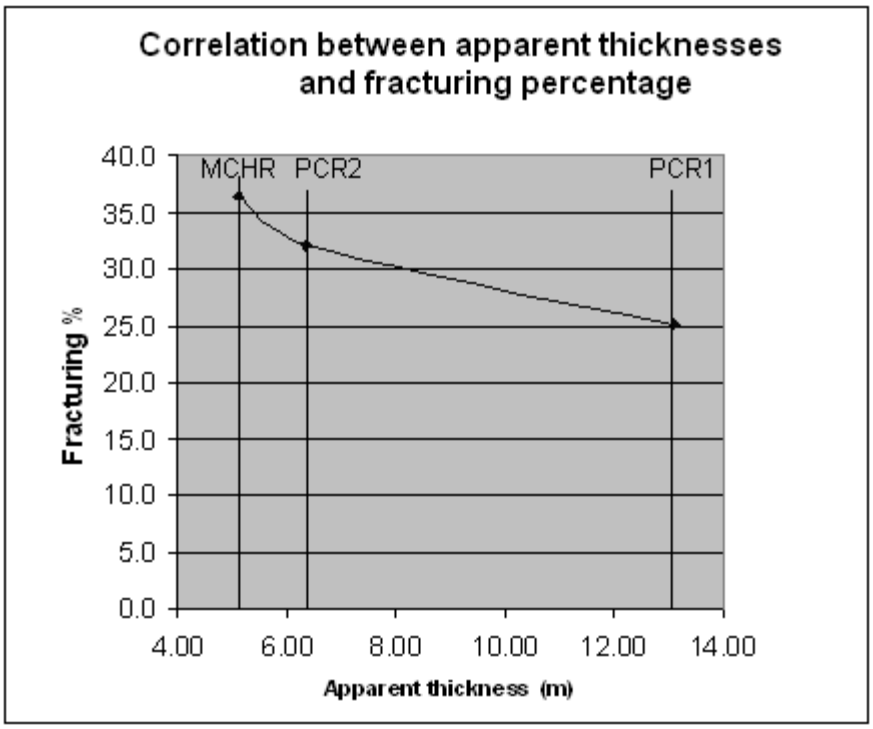

Figure 5.29: A line diagram of the correlation between the vertical thickness and the percentage of crystal fracturing of the chromitiferous layers.

Chapter 6: Chromite mineral chemistry

6.1 Background

A mineral chemical investigation is necessary in order to achieve better understanding of the development and deposition of the multiple chromitite lenses of the Uitkomst Complex. The aim is to determine whether the chromite from the different depositions has its own unique composition. This may provide the opportunity to create a chemical fingerprint for each chromitite layer.

The chromite crystal chemistry depends on the following factors:

1. The position in the magma body where the chromite crystallization occurred
2. The composition of the initial melt in the lower feeder channel
3. The composition of the differential melts higher up in the channel
4. Re-equilibration of crystals with melt during cooling and crystallization.

The chromite is extremely resistant to weathering as well as alteration and is the best preserved phase in the Massive Chromitite Layer. Because of this resistance the original chemical conditions of the magma during deposition are best preserved in the chemical properties of the chromite crystals. According to figure 6.1 there is no significant chemical variation between the core and the rim of the chromite crystals since both populations of analysis overlap. This indicates that not even the rims of the chromite crystals are altered. It also implies that the chromite crystals crystallized from a magma that was at equilibrium with its cumulate crystals since there is no zoning present in the chromite crystals. *Hatton and von Gruenewaldt (1984)* suggested that sub-solidus re-equilibration occurs between chromite and silicate minerals during deposition. The degree of this re-equilibration strongly depends on the modal amounts of chromite in the rock and chromitite layers reflect the composition of solidus chromite more closely than disseminated chromite. This research is based on the LG-6 chromitite layer of the Bushveld Complex that has an average thickness of 80cm *(Hatton and von Gruenewaldt, 1984).* Considering the thickness of the layers of massive chromitite of the Uitkomst Complex this re-equilibration effect should be minimized.

A total of 387 electron-microprobe analyses have been carried out on 38 samples. Twenty two of the samples are grab samples from the open pit. The position of each sample is marked on the geological sections. The remaining 16 samples are from borehole UK33.

The data from the core samples will be used to identify the geochemical differences between the major chromitite layers. This profile will then be used as the standard dataset and will be compared to the data of the grab samples.

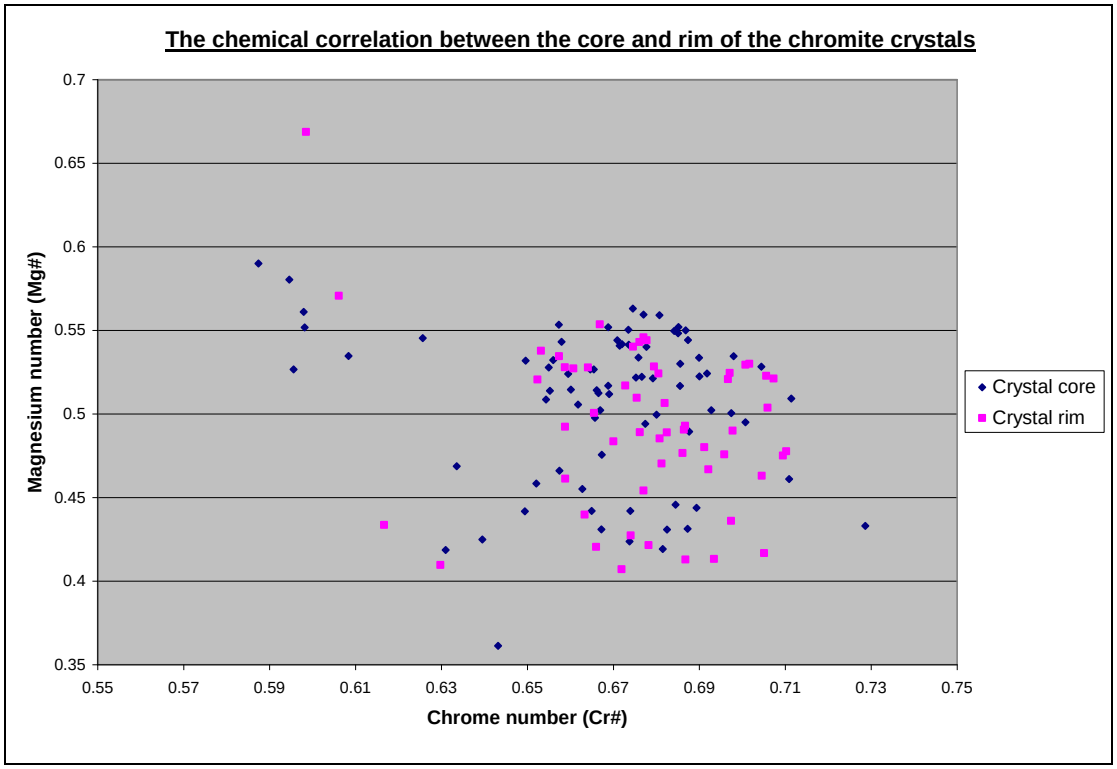

Figure 6.1: A scattered plot illustrating the chemical comparison of both the cores and rims of the chromite crystals.

The crystal deformation of the chromite crystals that were analyzed was also documented. Therefore all five of the different crystal shapes, as discussed in chapter 5, are represented in the geochemical data. This will provide the opportunity to check for a possible correlation between the deformation and chemical composition of the chromite crystals, thereby assessing the effects of post-magmatic hydrothermal alteration. All the mineral chemical analyses are plotted on scatter diagrams to identify any correlations and

patterns in the data. Total iron was analyzed as FeO; using these values the Barns Spinel stoichiometry calculation, version Dec 21 2004, with correction from C-J De Hoog, was used to determine FeO and Fe_2O_3 proportions. Most bi-variant discrimination diagrams use chrome number (Cr#), magnesium number (Mg#), chrome-iron ratio (Cr-Fe) and the chrome-aluminium ratio (Cr-Al). These ratios are calculated as follows:

Cr# = $Cr / (Cr + Fe^{3+} + Al)$

Mg# = $Mg / (Mg + Fe^{2+})$

Cr-Fe ratio = $Cr / (Cr + Fe^{3+} + Fe^{2+})$

Cr-Al ratio = $Cr / (Cr + Al)$

6.2 Drill core samples

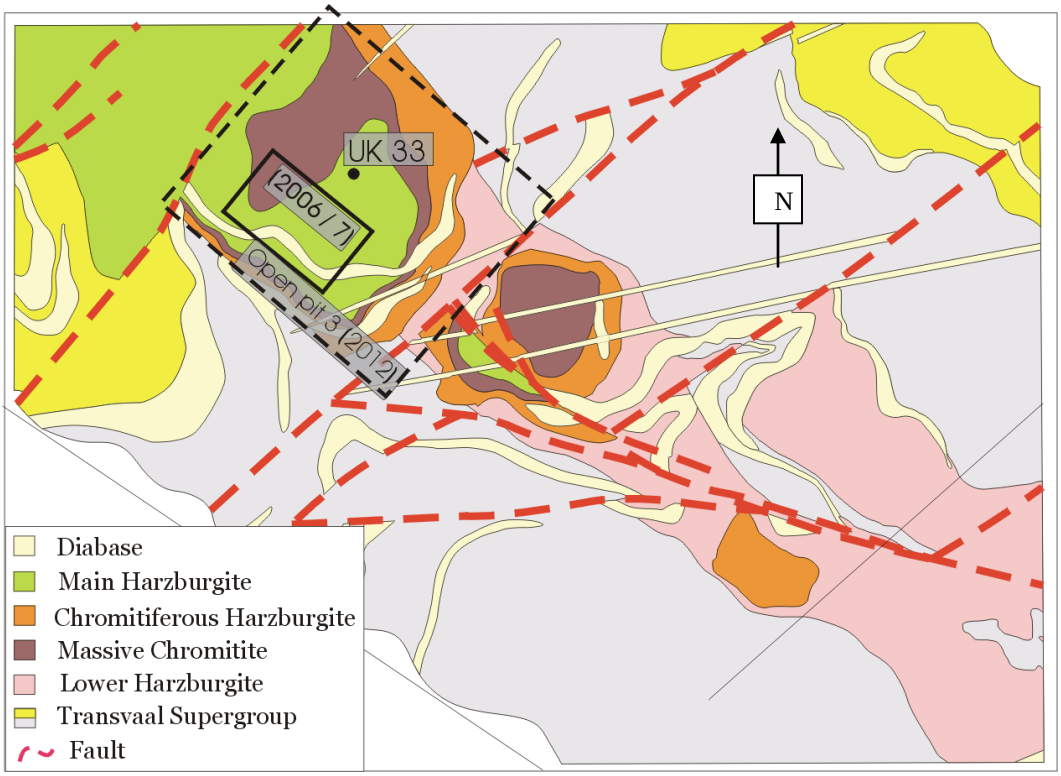

Figure 6.2: Geological map of the Uitkomst Complex also showing the position of bore-hole UK 33 in relation to open pit3.

All the chromitiferous layers from borehole UK33 were sampled and analyzed. The borehole is situated north-east from the open-pit, (fig. 6.2). The original core log of borehole UK33 was accessed from the Nkomati Mine borehole database. Table 6.1 provides a summary of all the core samples from the borehole. All the samples that are

indicated with a yellow color were used in the mineral geochemistry analyses. Four of these analyses have amounts of SiO_2 that exceed 2.5% and therefore they are considered to be outliers to the dataset and are indicated as such on all the diagrams.

UK 33		
Sample	Depth (m)	Geological unit
B1	1.2	MCHR
B2	5	MCHR
B3	5.5	MCHR
B4	6.2	MCHR
B5	6.7	MCHR
B6	7	MCHR
B7	7.4	MCHR
B8	7.8	MCHR
B9	8.7	MCHR
B10	9	MCHR
B11	9.4	MCHR
B12	10.1	Talc
B13	13	PCR
B14	13.26	PCR
B15	14.8	PCR
B16	16	PCR
B17	18	PCR
B18	23	PCR
B19	23.58	PCR
B20	23.9	PCR
B21	24	PCR
B22	24.2	PCR
B23	25	PCR
B24	26	PCR
B25	27.41	PCR
B26	31.9	PCR
B27	34.8	PCR
B28	35.5	PCR
B29	37.5	PCR
B30	41	PCR

Table 6:1: Summary of all the samples taken from borehole UK 33.

Table 6.2 is a statistical summary of the mineral chemical data from the core samples. The chemical elements are summarized separately for each of the different geological units. The summary contains the average, median, and standard deviation of each of the three major chromitiferous layers. The median is the value in the center of the dataset. The standard deviation indicates the distance by which the points in the data set differ from the median. The deviation is a direct function of the spread or range of the data points.

The bigger the deviation, the more scattered the points are. The cells are color coded the ones highlighted in blue indicate that the value is higher than the average of the combined data set. The green values are lower.

Elements	Stats Function	MCHR	PCR 1	PCR 2	Total Data set
Cr_2O_3	Average	51.2149	50.0769	47.4335	50.1408
	Median	51.0650	50.3900	47.7350	50.5000
	Std deviation	0.9450	1.8129	1.9719	2.0012
FeO	Average	18.6925	19.7210	20.2444	19.3795
	Median	18.1381	20.2709	20.9304	19.8220
	Std deviation	1.5877	2.1537	2.2258	2.0463
Fe_2O_3	Average	3.7723	5.4186	6.8402	4.9608
	Median	4.4603	5.2667	6.5174	5.1679
	Std deviation	1.8147	1.6749	1.6426	2.0497
AL_2O_3	Average	13.9956	12.9952	13.9877	13.5556
	Median	14.0300	12.8500	13.9100	13.6900
	Std deviation	0.6158	0.9813	0.5833	0.9368
MgO	Average	9.8681	9.0453	8.7638	9.3394
	Median	10.3250	8.8200	8.4150	9.1400
	Std deviation	1.3262	1.1830	1.2088	1.3262
TiO_2	Average	0.5627	0.6747	0.6615	0.6268
	Median	0.5600	0.6400	0.6700	0.6100
	Std deviation	0.0719	0.1426	0.1230	0.1276
MnO	Average	0.3229	0.4733	0.4815	0.4130
	Median	0.3200	0.4700	0.4750	0.4300
	Std deviation	0.0348	0.0634	0.0497	0.0912
SiO2	Average	0.0609	0.5172	0.6696	0.3536
	Median	0.0400	0.0600	0.0600	0.0500
	Std deviation	0.0842	1.8780	1.9481	1.4838
CaO	Average	0.0043	0.0449	0.0092	0.0229
	Median	0.0000	0.0000	0.0000	0.0000
	Std deviation	0.0069	0.3039	0.0154	0.2029
ZnO	Average	0.0706	0.0971	0.1050	0.0874
	Median	0.0700	0.0900	0.0950	0.0800
	Std deviation	0.0353	0.0432	0.0620	0.0461
NiO	Average	0.0331	0.0768	0.1069	0.0635
	Median	0.0300	0.0800	0.1000	0.0600
	Std deviation	0.0227	0.0319	0.0334	0.0397
Average	Std deviation	0.5950	0.9335	0.8967	0.9410

Table 6.2 Statistical summary of the chromite mineral chemical data from the core samples.

According to table 6.2 which is a statistical summary of the electron microprobe analyses from the core samples, there is an increase in Si, Mn, Zn, Ni, and Fe content of the chromite from the Massive Chromitite Layer (MCHR) down to the second Chromitiferous Harzburgite layer (PCR2). There is also a downwards decrease in the Mg and Cr content through the geological units. The PCR1 layer has less aluminium than the other two units, but this pattern is reversed in the calcium content. The average standard deviation of the data from the MCHR layer is 53% less than that of the PCR1 layer, and 52% less than that of the PCR2 layer.

Figure 6.3 is a scatter plot of magnesium number against depth of the sample below surface. It is clear from the diagram that the Mg# does not follow a smooth chronological evolution as crystallization progresses and the graph displays a saw-tooth pattern.

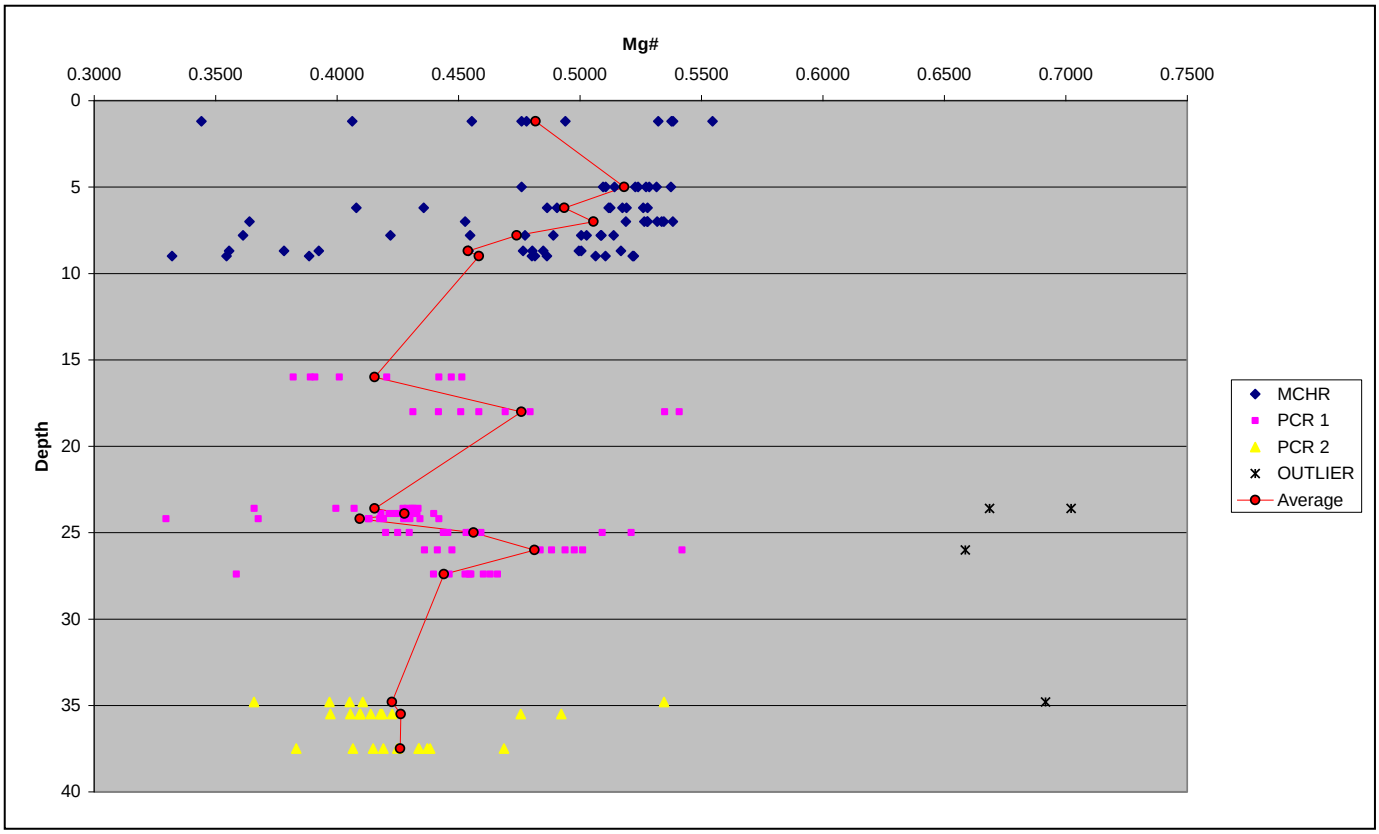

Figure 6.3: Scatter plot of magnesium number against depth of samples in borehole UK33.

The PCR2 layer is the first chromitiferous deposition in the study area and its average Mg# remains constant at around 0.426 during the course of deposition. There is a slight decrease to the top of the layer. This event is followed by an increase in Mg# during the transition from layer PCR2 to PCR1. There is a sharp increase in Mg# at the base of the PCR1 layer. This is followed by a constant and stable decrease in the average Mg # over the next 4 samples with a small disturbance at the top of this cycle. This pattern of an increase followed by a decrease in Mg# repeats itself in the upper half of the PCR1 layer. The average Mg# from the samples from PCR1 varies between 0.383 and 0.4094. The transition from the PCR1 to MCHR layer is marked by a similar increase in Mg# as the previous transition. The majority of the MCHR layer displays a strong increase in Mg# as crystallization continues. At the top of the MCHR layer the Mg# suddenly decreases again. The average Mg# from the samples from MCHR varies between 0.45 and 0.52.

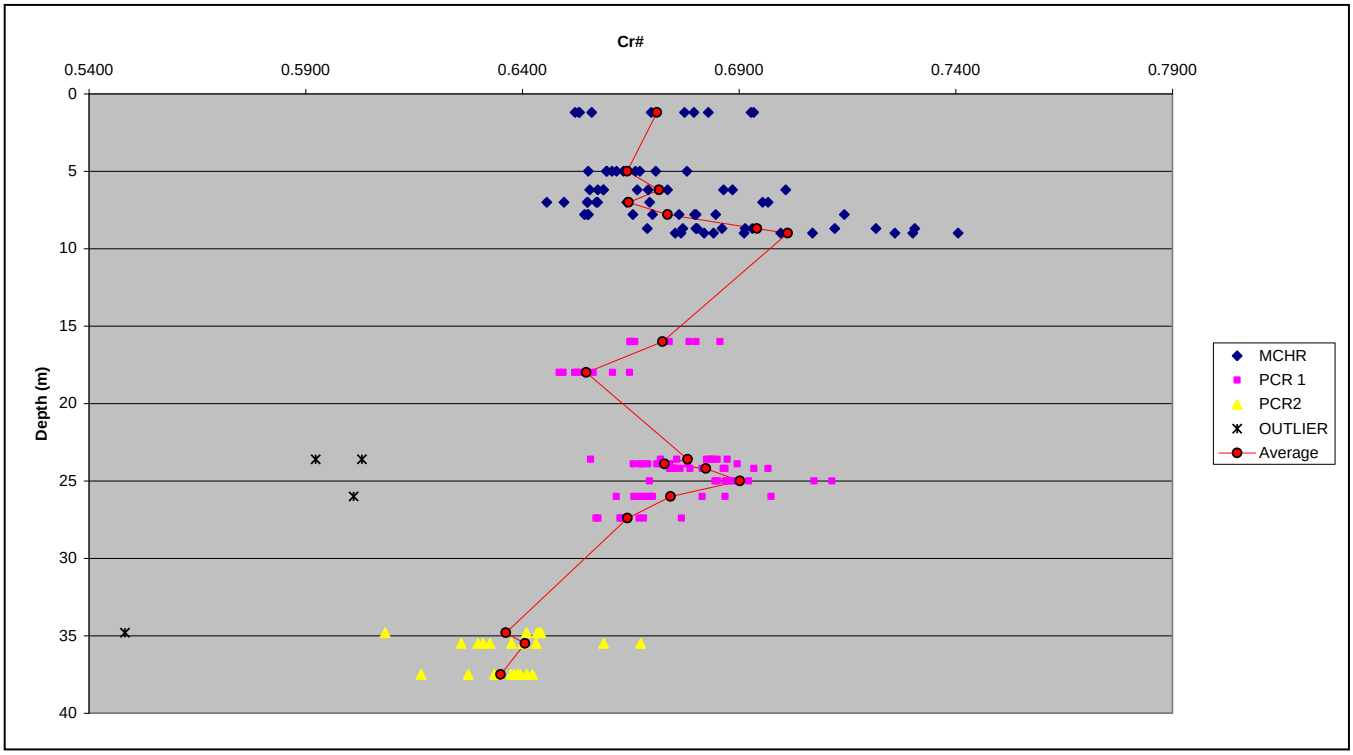

Figure 6.4: Scatter plot of chrome number against depth of samples from borehole UK33.

Figure 6.4 is a scatter plot of chrome number against depth of the sample below surface. This diagram displays a saw-tooth pattern. An increase in the average Cr# from the top of

the older layer to the base of the more recent layer during transitions from both PCR2 to PCR1 and from PCR1 to MCHR is obvious. The gradient of the Cr# increase for these two transitions are similar. Thus the Mg# and Cr# evolve in a similar pattern during the deposition of the three major chromitiferous layers. Both increase during the transition from one layer to the next and reveal a lot of variances during the deposition of especially the two younger layers PCR1 and MCHR.

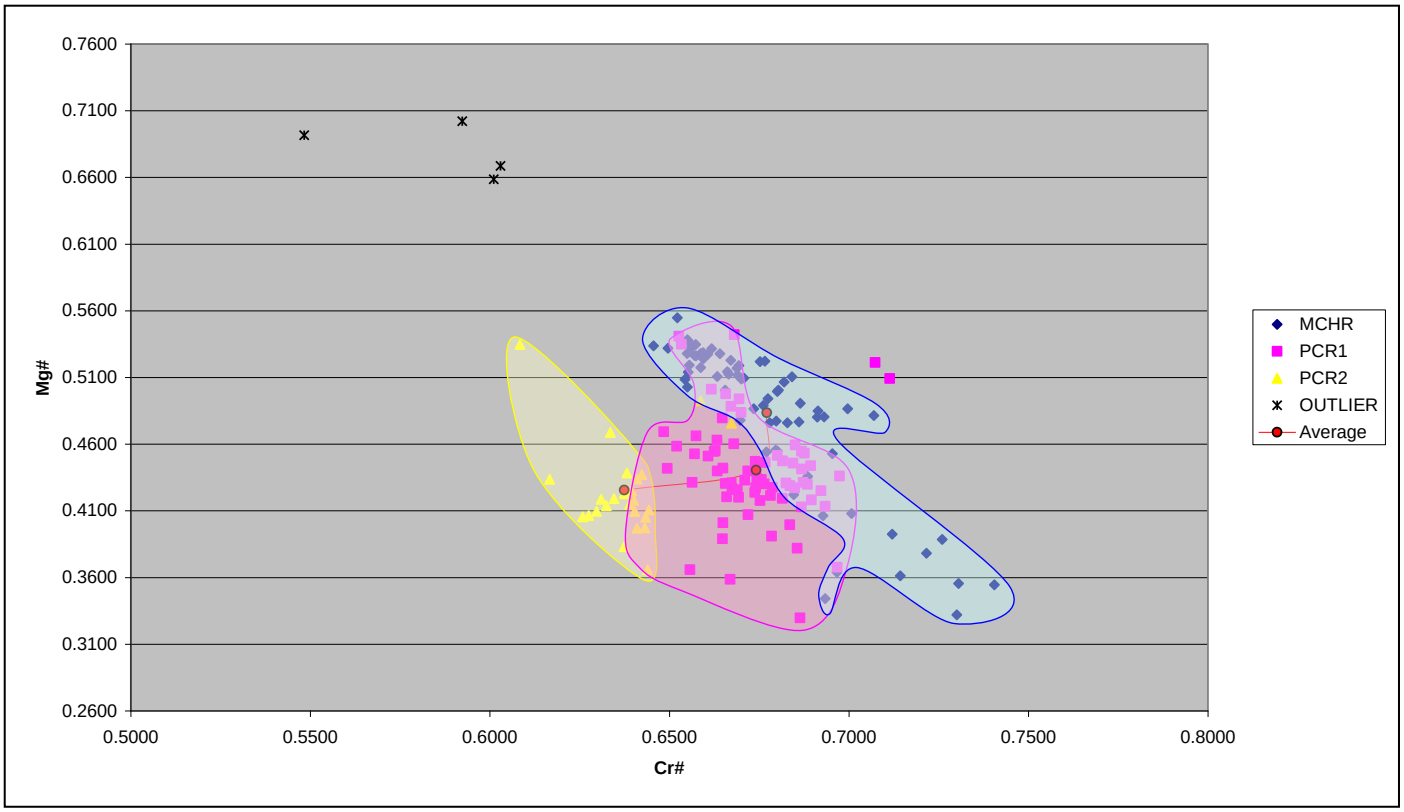

Figure 6.5: Scatter plot of magnesium number against chrome number.

Figure 6.5 is a bi-variant diagram of magnesium number against chrome number. Although there are some data points that overlap, the three individual chromitiferous layers plot in distinct areas on the diagram. Although the average Mg# and Cr# value of each chromitiferous layer increases as deposition progresses it does not evolve in a smooth line or curve. From PCR2 to PCR1 there is an increase of 5.4% in Cr# and a 3.4% increase Mg#, whereas from PCR1 to MCHR only a 0.44% increase in Cr# and an 8.9% increase in Mg# is illustrated.

Figure 6.6 is a bi-variant diagram of chrome/aluminium-ratio against chrome/iron-ratio. The majority of the data from the three individual chromitiferous layers plot separately on the graph, with small overlaps. There is not a good correlation between the data of the complete dataset; the average values of the individual units show some correlation with each other. A positive correlation exists between the average values of the PCR1 and PCR2 layers in the diagram. The average values of the PCR2 and MCHR layers however show a negative correlation. In effect the MCHR has the highest chrome/iron ratio and the PCR2 has the highest chrome/aluminium ratio.

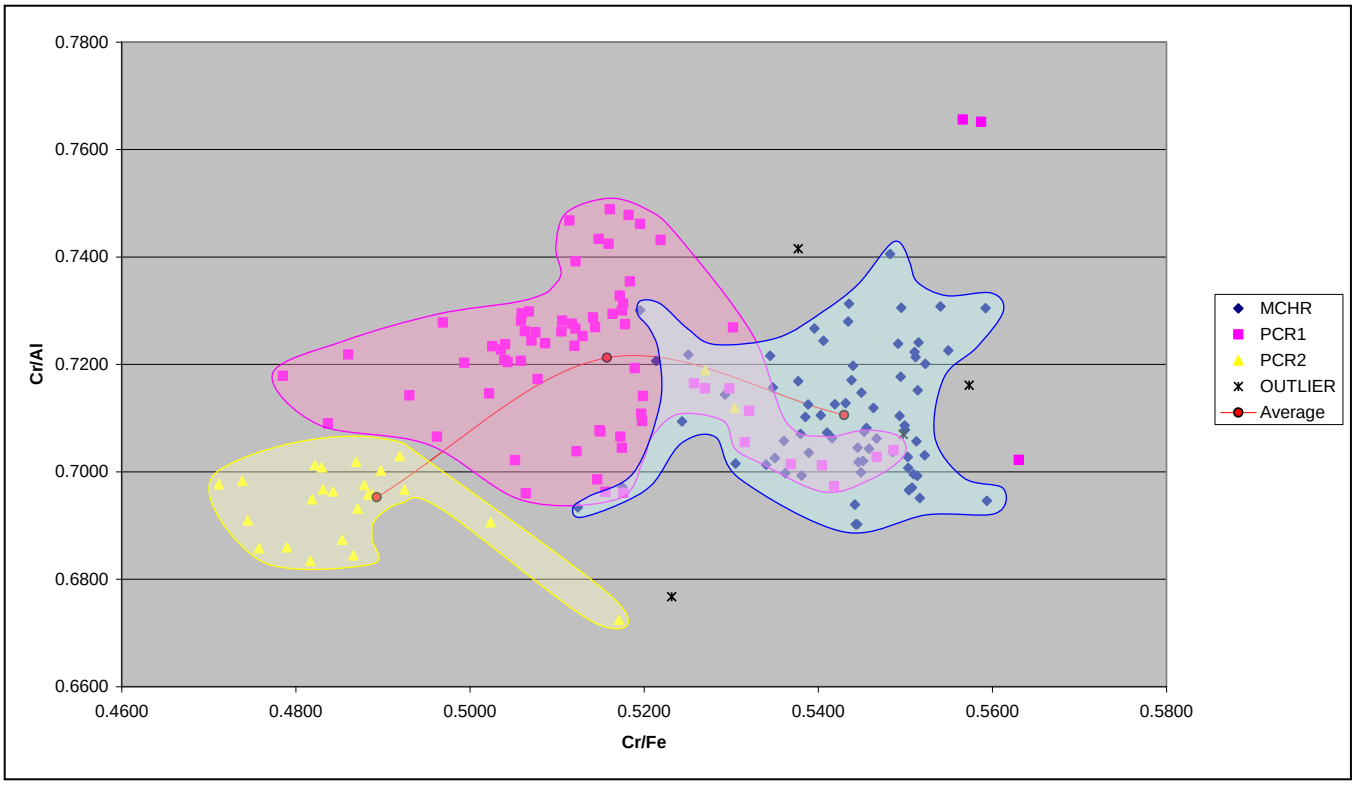

Figure 6.6: Scatter plot of chrome / aluminium ratio against chrome / iron ratio.

Both figures 6.5 and 6.6 display a similar pattern. The data from each geological unit is clustered together, but separated from each other. In both diagrams the differentiation trend of the chromite chemistry does not follow a straight line from one geological unit to the next.

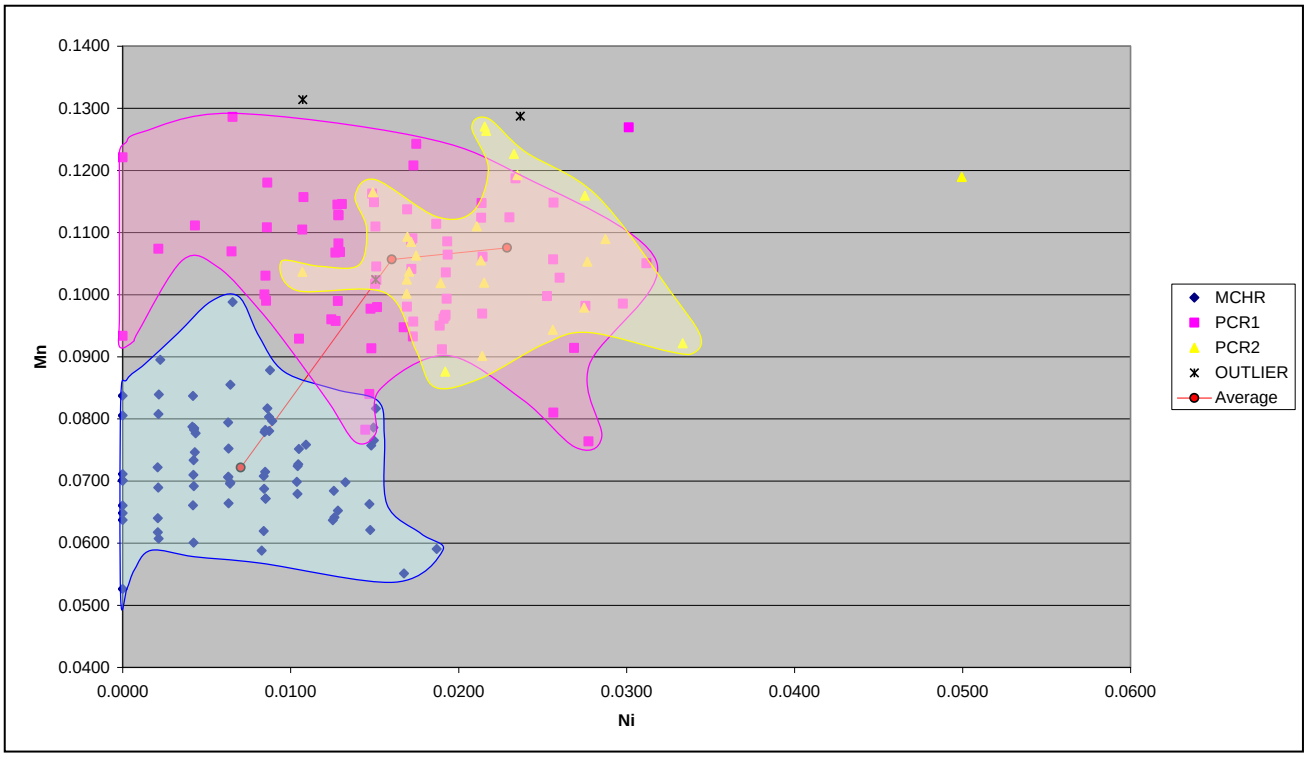

Figure 6.7: Bi-variant diagram of manganese content against nickel content.

Figure 6.7 is a bi-variant diagram of manganese content against nickel content. The MCHR plot separately from the two PCR units and have less Mn and Ni. The two PCR units however are not separate, but the PCR2 has more Ni.

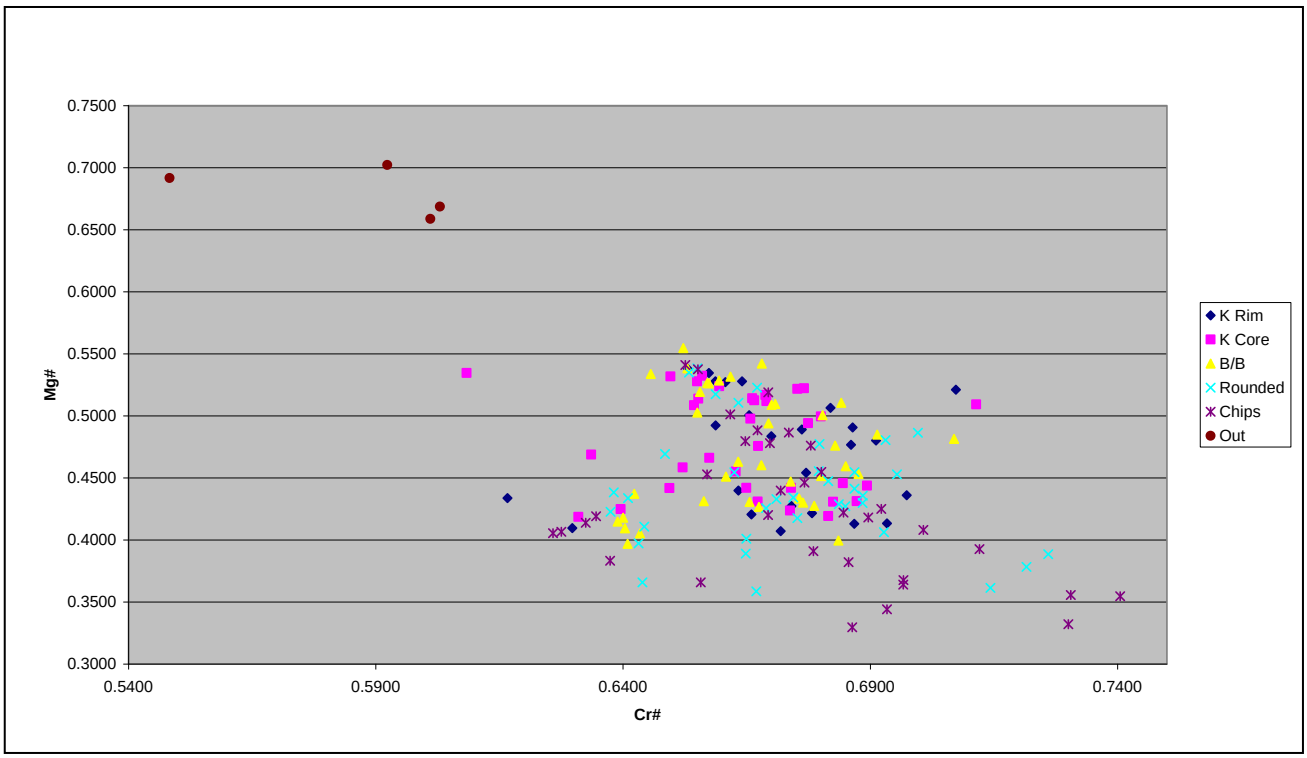

Figure 6.8: Scatter plot to illustrate correlation between the shape and chemistry of the chromite crystals.

Figure 6.8 is a scatter diagram of chrome number against magnesium number, but is color coded according to the shape of the chromite crystals. In the diagram there is no distinct pattern or correlation suggesting a relationship between the chemistry and fracturing of the crystals indicating that no late stage hydrothermal modification had occurred.

6.2.1 Interpretation of chemical date form drill core samples

From the diagrams and the geochemical data of the three major chromitiferous layers it is clear that the chromite crystals from each chrome bearing unit have their own unique chemical composition. The chromite crystal chemistry does not evolve in a straight line as crystallization progresses. This is an indication that the different chromitiferous layers did not develop as a result of continuous crystallization and fractionation from a single source. The saw-tooth pattern of alternating increasing and decreasing Cr# as well as Mg# indicates that new magma influxes were added to the parental magma and it seems as if each chromitiferous layer represents a period of multiple replenishments. Time periods of multiple replenishments were also described in the Bushveld complex *(Andrew, Mitchell, Hugh, Eales and Kruger, 1998)*

According to Bowen's reaction series, Mg is the first chemical element to be removed from the liquid phase during crystallization, therefore the Mg# of the silicate rocks should decrease as magma evolves. According to figure 6.3 the Mg# increases during the transition from one layer to the next resulting in the latest deposit being the least evolved *(Kiviets, 1991).*

6.3 Grab samples

The grab samples were gathered during the mapping exercise from the rock faces that were created during the mining operation in open pit 3 from 2006 to early 2007. At that early stage, only the upper chromitite layers were exposed.

The analyses from the drill core data indicated a significant difference in the chromite mineral geochemistry between the three major chromitiferous layers. The data from the grab samples compare mainly with the different chromitite lenses of the Massive Chromitite Layer (MCHR).

Table 6.3 gives a short description of the different chromitite lenses that were encountered and sampled in open pit 3. The first three lenses are similar, but are separated by layers of altered harzburgite. The last three lenses are very unique and can be identified visually. The thin fractured chromitite layer between MC3 and MC4 is more likely to be a fracture zone between the two lenses, and it only occurs in isolated areas where the two lenses are directly in contact with each other.

Chromitite lens	Description	Samples	Analyses
MC1	Very hard chromitite, that mainly consists out of fine crystalline chromite	8	80
MC2	Very hard chromitite, that mainly consists out of fine crystalline chromite	2	20
MC3	Very hard chromitite, that mainly consists out of fine crystalline chromite	5	50
FC	This is a thin layer of fractured chromitite between lenses MC1 and MC4. This layer consists out of chromitite with lenses of talc carbonate schist	1	9
MC4	This chromitite lens has a decrease of chromite concentration from the top to the bottom of the lens. As the amount of chromite decreases, the rock also becomes softer.	2	19
MC5	This lens consists out of chromite with lenses of talc carbonate schist	1	10
	Total	19	188

Table 6.3: Summary of the chromitite lenses that were sampled in open pit 3 and analyzed by means of electron-microprobe.

Table 6.4 is a statistical summary of the geochemical data gathered from the grab samples. This provides an overview of the mineral chemical differences between each chromitite lens. The cells that are highlighted in blue indicate that the value of that chromitite lens is higher than the average value of the combined data set. The green values are lower.

ELEMENT	STATS FUNCTION	MC1	MC2	MC3	MC4	MC5	All Data
Cr_2O_3	Average	52.1263	46.7200	50.8040	52.8547	50.9260	51.1631
	Median	52.2750	46.5900	51.3950	52.8200	50.8500	51.8700
	Std deviation	1.0710	0.9078	2.0237	0.4878	0.4663	2.1770
FeO	Average	17.7358	16.4483	17.8060	18.9529	18.8709	17.8042
	Median	17.1281	16.4617	17.3725	18.7152	18.2816	17.2803
	Std deviation	1.7026	0.6329	1.3728	1.1123	1.9029	1.6030
Fe_2O_3	Average	4.6954	6.4099	4.8456	2.8775	4.5789	4.7295
	Median	4.6643	6.3713	4.7637	2.7095	4.8325	4.7505
	Std deviation	1.1310	0.4721	1.0258	0.9421	0.9373	1.3055
AL_2O_3	Average	12.8485	16.5845	13.7056	12.8895	13.4940	13.5458
	Median	12.9250	16.6750	13.7900	13.0200	13.5500	13.2700
	Std deviation	0.5267	0.7507	0.4391	0.6107	0.3882	1.2614
MgO	Average	10.5285	11.7435	10.4350	9.5211	9.7760	10.4892
	Median	10.9650	11.7600	10.8250	9.6700	10.3250	10.8300
	Std deviation	1.2099	0.5129	1.0490	0.8303	1.4175	1.2079
TiO_2	Average	0.6348	0.6500	0.5714	0.5495	0.6250	0.6092
	Median	0.6300	0.7000	0.5750	0.5500	0.6600	0.6100
	Std deviation	0.0916	0.1134	0.0828	0.0559	0.0951	0.0951
MnO	Average	0.3323	0.3105	0.3256	0.3437	0.3440	0.3298
	Median	0.3200	0.3100	0.3200	0.3500	0.3400	0.3200
	Std deviation	0.0521	0.0188	0.0507	0.0530	0.0310	0.0487
SiO_2	Average	0.1845	0.0945	0.3406	0.0937	0.0530	0.2011
	Median	0.0500	0.0250	0.0400	0.0500	0.0450	0.0400
	Std deviation	0.5876	0.2915	1.1721	0.2301	0.0330	0.7451
CaO	Average	0.0049	0.0030	0.0490	0.0037	0.0010	0.0166
	Median	0.0000	0.0000	0.0000	0.0000	0.0000	0.0000
	Std deviation	0.0087	0.0073	0.3191	0.0076	0.0032	0.1688
ZnO	Average	0.0496	0.0645	0.0582	0.0611	0.0940	0.0574
	Median	0.0500	0.0650	0.0650	0.0700	0.0800	0.0500
	Std deviation	0.0286	0.0398	0.0328	0.0254	0.0983	0.0386
NiO	Average	0.0528	0.0770	0.0522	0.0247	0.0420	0.0517
	Median	0.0500	0.0800	0.0500	0.0200	0.0400	0.0500
	Std deviation	0.0301	0.0198	0.0307	0.0244	0.0253	0.0309
Average	Std deviation	0.5855	0.3424	0.6908	0.3981	0.4907	0.7893

Table 6.4: Statistical summary of the chromite mineral chemical data from the grab samples.

In figures 6.9 and 6.10 all the data from the grab samples are plotted together with those from the drill core. The drill core data is divided into the three groups, representing chromitiferous layers MCHR, PCR1 and PCR2. The majority of the grab sample data plot in area "A" on figure 6.9 and overlaps with and extend beyond the data from the MCHR layer with a higher Mg# and Cr#. A small amount of data points plot in area "B", that is to the left of the other grab sample data. This group of data has a lower Cr#, but has a similar Mg#.

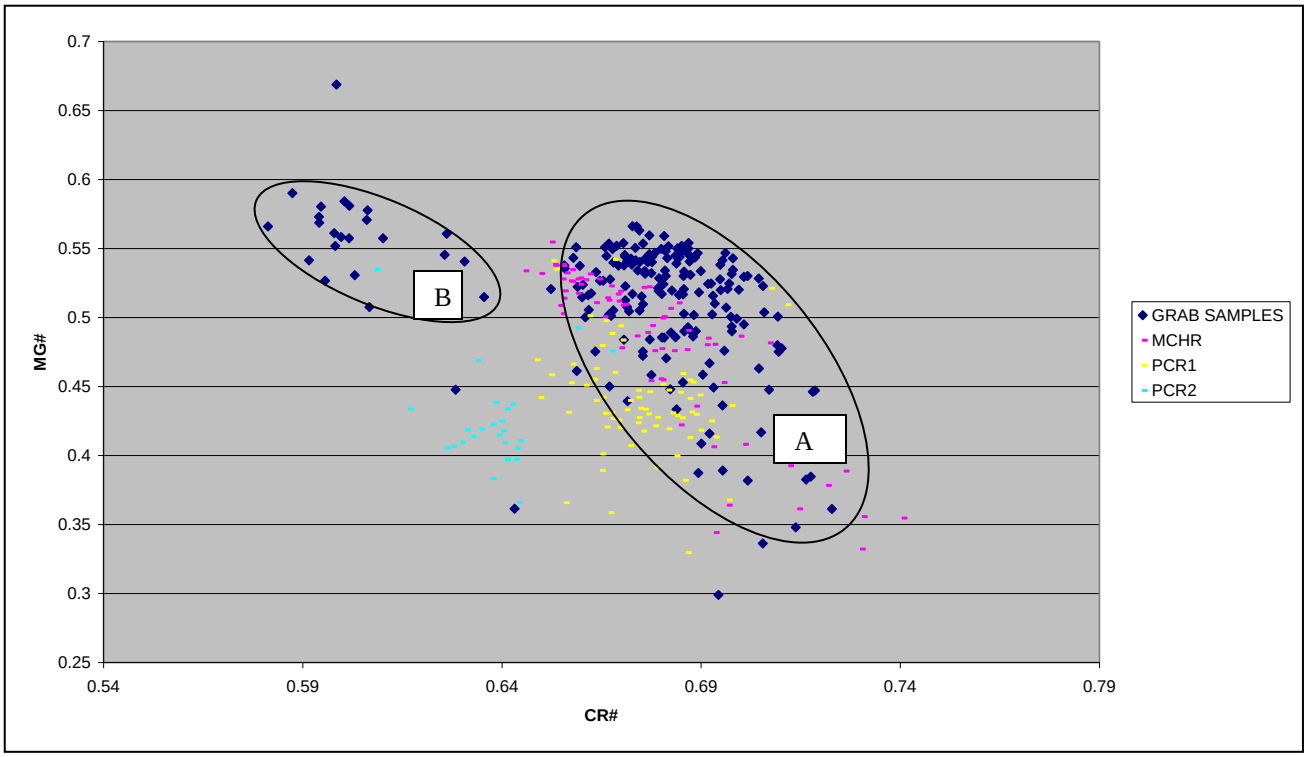

Figure 6.9: Scattered plot of chrome number against magnesium number for all the geochemical data.

In figure 6.10 the data from the grab samples, once again plot in two areas. The majority of the data plot in area "A" and overlaps and extends beyond the MCHR data from the drill core. The data in area "B" has a lower chrome / aluminium and chrome / iron ratio than the data in area "A". The data in area "B" do not overlap with any of the data from the core samples. This might indicate that some of the chromitite lenses in the open-pit are not present at borehole UK 33. The positive trend of the data further indicates that

these are later chromitite deposits than layer MCHR and therefore they are probably removed in the area of the borehole by erosion.

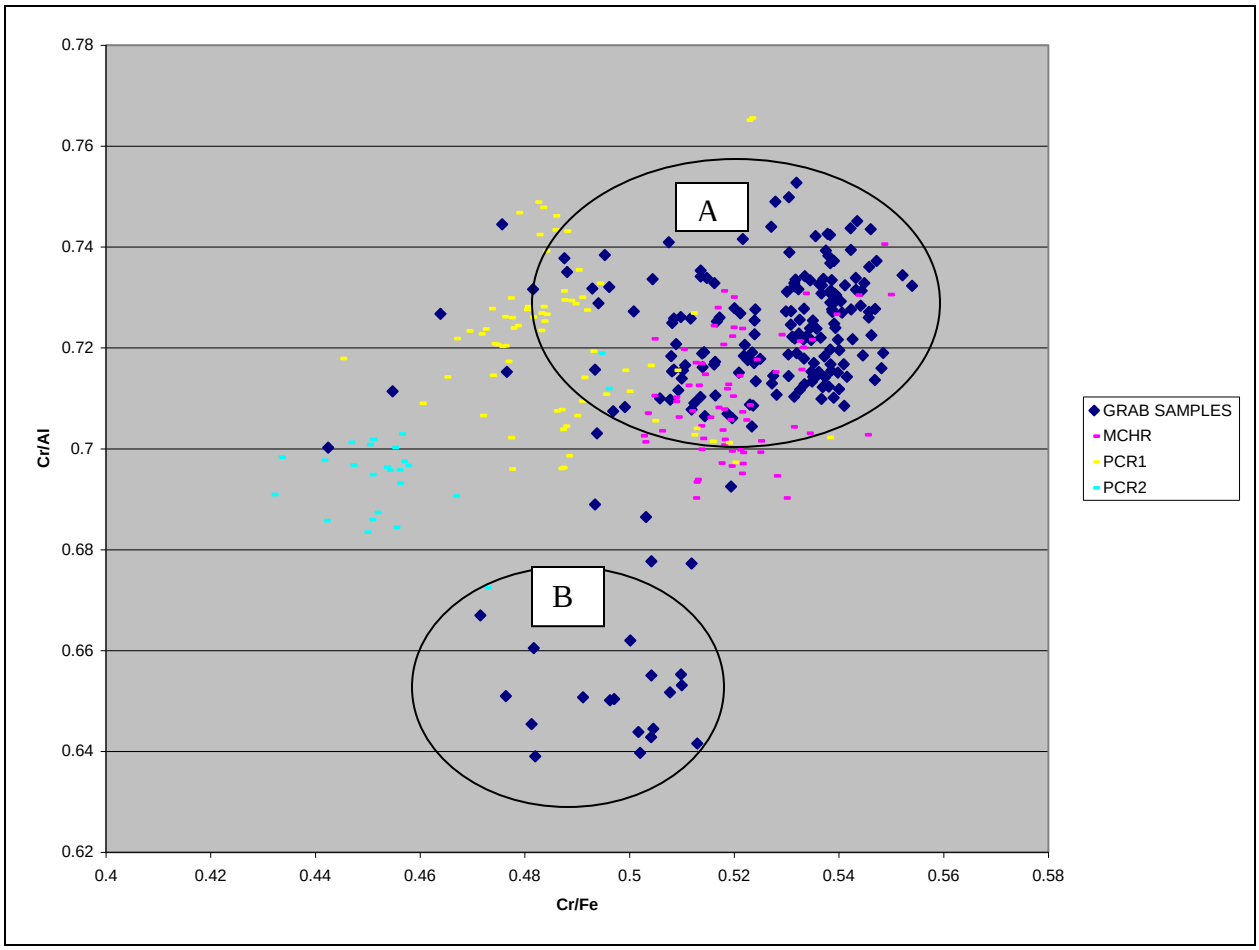

Figure 6.10: Scattered plot of chrome / iron ratio against chrome / aluminium ratio for all the geochemical data.

From the overlap of the grab samples with the MCHR from the borehole figure 6.9 and 6.10, it is clear that the chromitite lenses that are exposed in the open pit form part of the MCHR layer. From the constant increasing trend in Cr/Fe ratio from the oldest layer (PCR2) to the more recent layer (MCHR) it is likely that the grab samples with a higher Cr/Fe ratio than that of the MCHR layer comes from chromitite lenses that are younger than the chromitite intersected in the MCHR layer by BH UK 33. Only a few of the grab samples overlap with the PCR1 and PCR2 data. An investigation of the chemical dynamics between the individual chromitite lenses in pit 3 should enable us to better

understand the deposition and evolution of the entire Massive Chromitite Layer of the Uitkomst Complex.

In figures 6.11, 6.12 and 6.13 the data of the grab samples are plotted. The data is color-coded according to the chromitite lens it represents and corresponds with the lenses discussed in table 6.3.

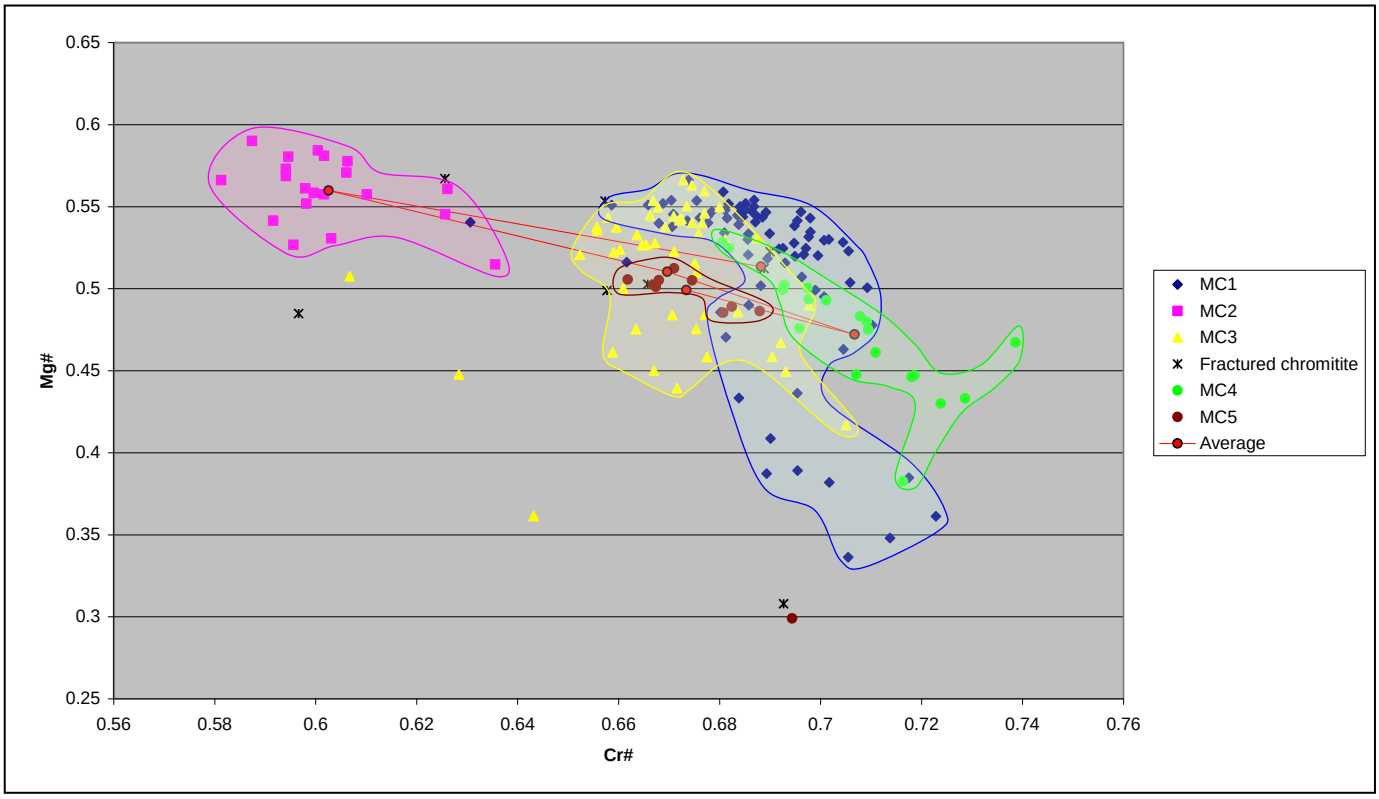

Figure 6.11: Scattered plot of chrome number against magnesium number, the different chromitite lenses are plotted as individual series.

Figure 6.11 is a scattered plot of chrome number against magnesium number. The plot clearly indicates that the data from each individual chromitite lens is clustered together even though there are some discrepancies. In order to discuss the data from figure 6.11 it is fundamental to systematically look at each chromitite lens and to correlate the data with the stratigraphy of the Massive Chromitite Layer. Chromitite lens MC1 is the top chromitite lens in the study area and the data from this lens partially overlaps with the

data from chromitite lenses MC3 and MC4. Stratigraphically chromitite lens MC2 is deposited below lens MC1 and only in the areas where lens MC2 is not developed MC1 is overlying lens MC3. The Cr# values from lens MC2 do not overlap with the other chromitite lenses. Therefore there is no correlation between the stratigraphy and the mineral geochemical properties of the three upper chromitite lenses in the study area. The data from chromitite lens MC5 totally overlaps with that of MC3 but are stratigraphically separated by chromitite lens MC4. Although the data from lens MC4 partially overlaps with MC1 and MC3 it does not overlap with that of lens MC5. The data from the thin fractured chromitite lens between MC3 and MC4 does not plot in a cluster and is scattered over the entire graph. In general the diagram displays a saw tooth pattern (fig. 6.11)

The grab sample data in figure 6.12 is plotted according to their Cr/Al and Cr/Fe ratios. This graph is similar to diagram 6.11 and the data from the different chromitite lenses are clustered together in isolated areas of the diagram. The data from lenses MC1, MC2 and MC3 is well separated according to its Cr/Al ratios. Lenses MC4 and MC5 also plot separately from each other, but respectively overlap with the data from MC1 and MC3. It is however important to recall that lenses MC4 and MC5 were classified in chapters 3 and 5 as being part of the same depositional event that is characterized by a constant increase in chromite content from the bottom of MC5 to the top of MC4. Chromitite lenses MC1, MC2 and MC3 on the other hand had similar physical characteristics (table 6.3).

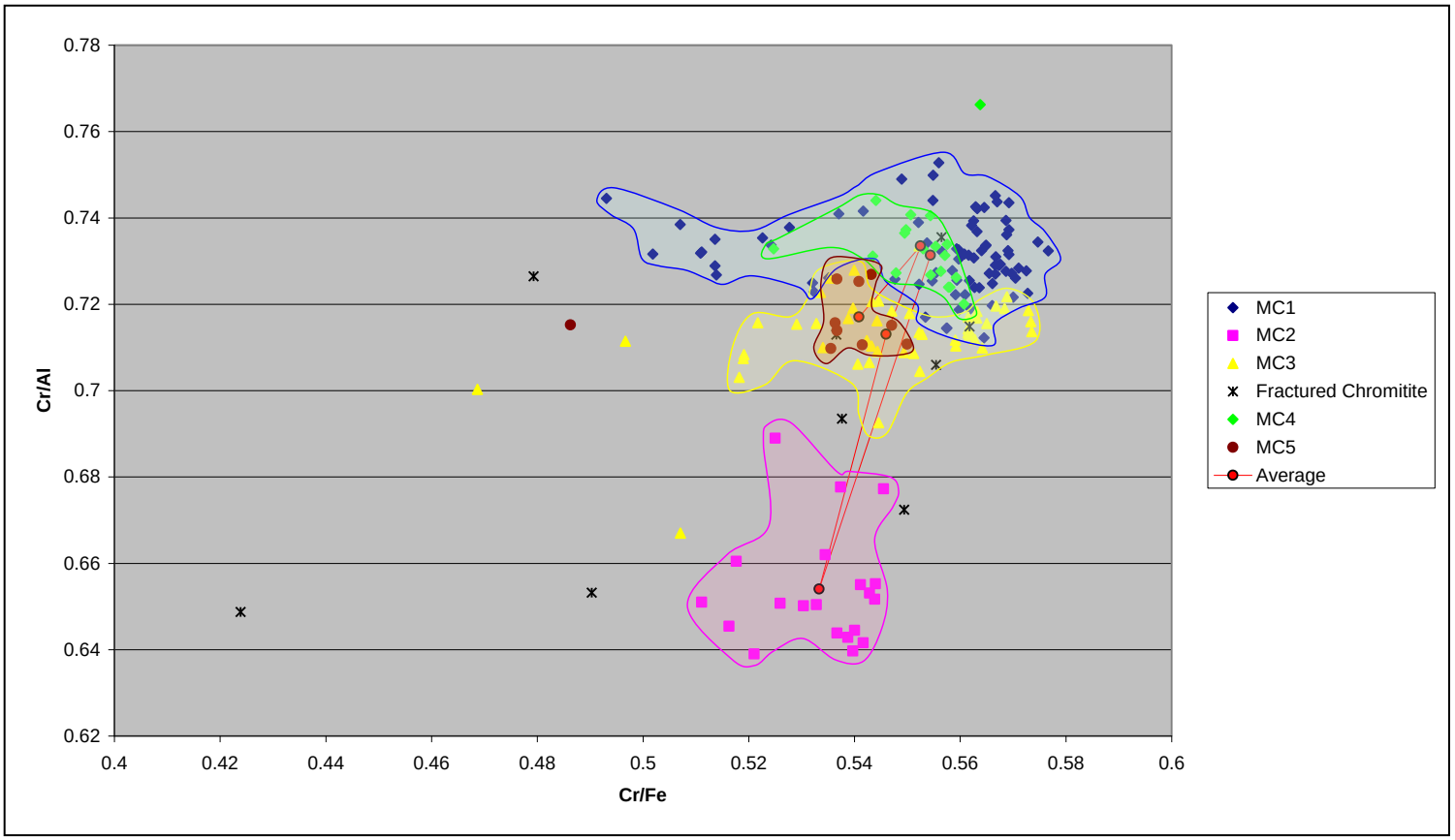

Figure 6.12: Scattered plot of chrome / aluminium ratio against chrome / iron ratio, the different chromitite lenses are plotted as individual series.

6.4 Summary and interpretation

It is clear that although the chemical data of the chrome spinel from the various chromitiferous layers as well as the individual chromitite lenses within the MCHR layer are partly cluster together that they plot separately from one another. The mineral chemical data from borehole UK 33 revealed an increasing trend in both chrome and magnesium numbers as deposition continues from the bottom to top (fig. 6.3), which does not coincide with normal fractionation trend *(Kiviets, 1991).* The upwards increase in both Mg# and Cr# implies that, as deposition continued, the magma producing the chromite became more primitive in composition. During the deposition of the three individual chromitiferous layers several increasing and decreasing trends for chrome and magnesium numbers result in a saw tooth pattern (fig. 6.3 and fig. 6.4).

The saw tooth pattern could indicate that each chromitiferous layer developed as a result of multiple influxes of new magma into the parental magma. These replenishments enrich the resident magma once again with elements such as Cr, Mg and Fe that were depleted from the resident magma through crystallization. The influxes are therefore placed into a partially evolved and cooler resident magma in the evolving chamber. Density differences between the replenished and resident magmas should prevent major magma mixing to occur in the chamber *(Hatton and von Gruenewaldt, 1984)*. The resident magma will absorb heat from the influx causing the replenished magma to cool down more rapidly than during the normal magma chamber maturing processes. This faster cooling of the influx will result in the crystallizing of chromite from a lesser evolved magma as there is less time available for Mg and Fe to be removed from melt this results in higher concentrations of Mg and Fe which became incorporated in the chromite crystal structure. For the Uitkomst Complex both the volume and temperature of the replenished magma in relation to the parental magma should be considered as controlling factors on the cooling rate of the influx *(Whitten and Davis, 1992).*

From the geological sections in chapter 3 it is clear that chromitite lenses MC5 and MC4 are part of the same depositional event since they are separated by a large gradational contact as the content of chromite crystals in this unit increase to the top of lens MC4. The chemical evolution from lens MC5 to MC4 on average reveals a slight decrease in magnesium number and an increase in chrome number (fig. 6.11). This is a normal crystallization trend that leads to depletion of magnesium and iron of the melt as crystallization continues. Chromitite lenses MC3, MC2 and MC1 are separated from one another by layers of talc carbonate schist which indicates that their depositions were separated by phases of silicate crystallization. The chrome number and magnesium number of these lenses do not evolve in a straight line and lens MC2 has a lower Cr# and a higher Mg# than both lenses MC1 and MC3 (fig. 6.11).

Figure 6.13 displays the evolution of chrome and magnesium numbers as chrome deposition continues and summarizes the entire chapter.

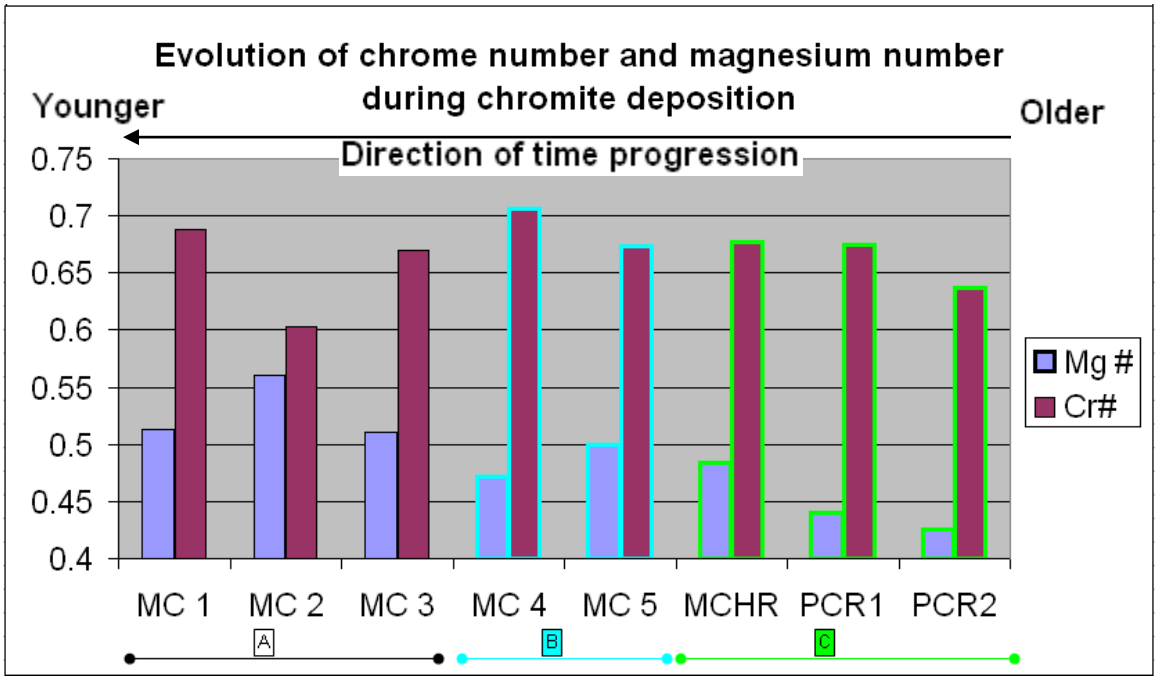

Figure 6.13: Evolution of chrome number and magnesium number during chromite deposition.

Part C: Contains the three major chromitiferous layers and displays a constant increase in magnesium number from the PCR2 layer to the MCHR layer. This is a clear indication that the replenished magma from which the chromite crystallizes became progressively more primitive as the temperature in the parental magma chamber decreased over time (fig. 6.13).

Part B: Displays a decrease in magnesium number and an increase in chrome number during the deposition of chromitite lenses MC4 and MC5. This is a normal crystallization trend that indicates that the chromitite lenses were deposited as a result of continuous crystallization after a high volume magma replenishment (fig. 6.13).

Part A: Displays an irregular pattern as time progresses from the deposition of chromitite lens MC3 to the deposition of lens MC1, this indicates that lenses crystallized from various magma replenishments. Previous discussions indicated that this variation in chemical composition between these chromitite lenses is mainly dictated by the volume and temperature of the influx relative to parental magma (fig. 6.13).

Chapter 7: Discussion

The aim of this chapter is to discuss the findings of the study and to synthesize them to achieve better understanding of the deposition of the Massive Chromitite Layers of the Uitkomst Complex.

7.1. Geological profiles (chapter 3):

In the study area the Massive Chromitite Layer consists of five individual chromitite units that are stacked on top of each other. The upper three chromitite lenses are not continuous throughout the study area. As indicated by figure 7.1 chromitite lens MC3 is the largest of these three lenses. It thins out to the north and the east of the study area and is not expected to continue much further outside the open pit. The western boundary of lens MC2 was defined during the mapping campaign whereas the eastern margin is likely to be influenced by erosion and the original boundary is expected to be situated further east. The same applies for lens MC1. Figure 7.2 shows the estimated original boundaries of these three chromitite lenses.

The upper three lenses have similar geological characteristics such as chromite abundance, color and the hardness. These three lenses are each separated by layers of talc-carbonate schist which are the result of deuteric alteration of the original interbedded harzburgite layers. The sequence of chromitite overlain by talc-carbonate schist is very prominent and the complete sequence is duplicated three times. Because of these similarities between the upper three lenses, the first impression was that the repetition was the result of a post-magmatic contact parallel shearing event that resulted in the structural duplication and stacking of a single chromitite, harzburgite sequence (fig. 7.3). A correlation between this duplication and the Bushveld age contact parallel shearing that was described by Hornsey (1999) in the lower parts of the complex was furthermore implied and investigated. On the other hand each of the three chromitite lenses could represent individual intervals of chromite deposition. For this reason a mineral chemical study was necessary to correlate the different chromitite lenses.

Figure 7.1: Plan of upper three chromitite lenses as documented from open pit 3.

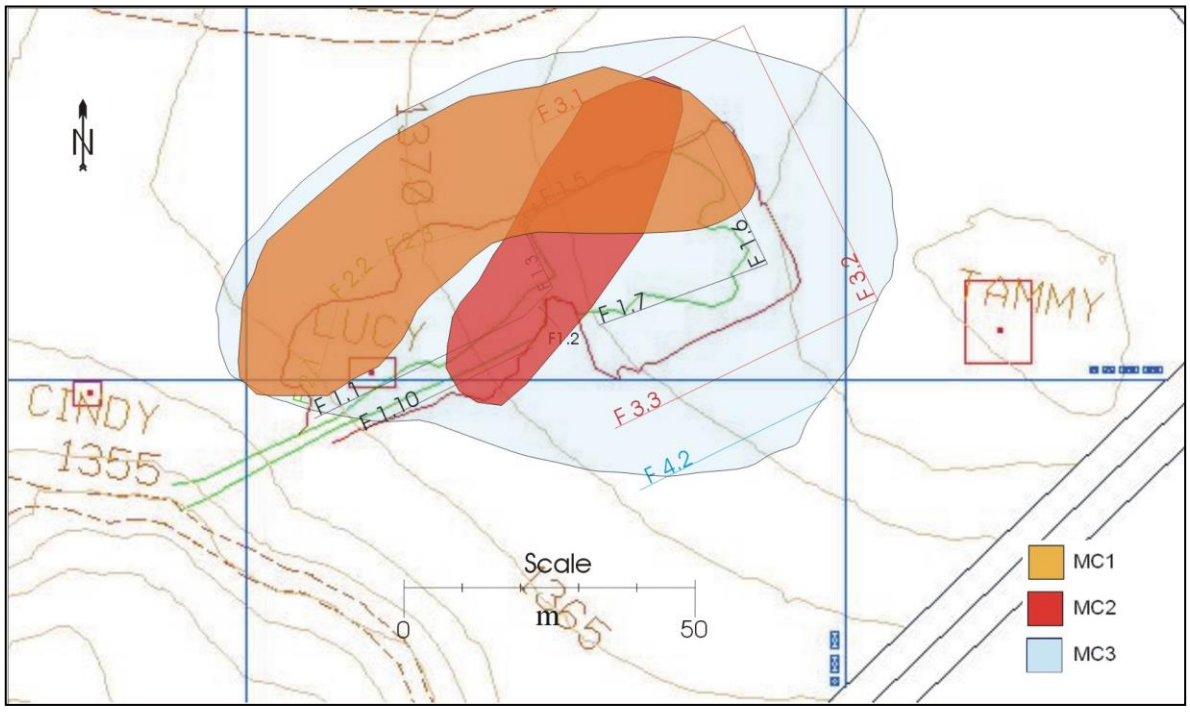

Figure 7.2: Plan showing the expected original extent of the upper three chromitite lenses before erosion.

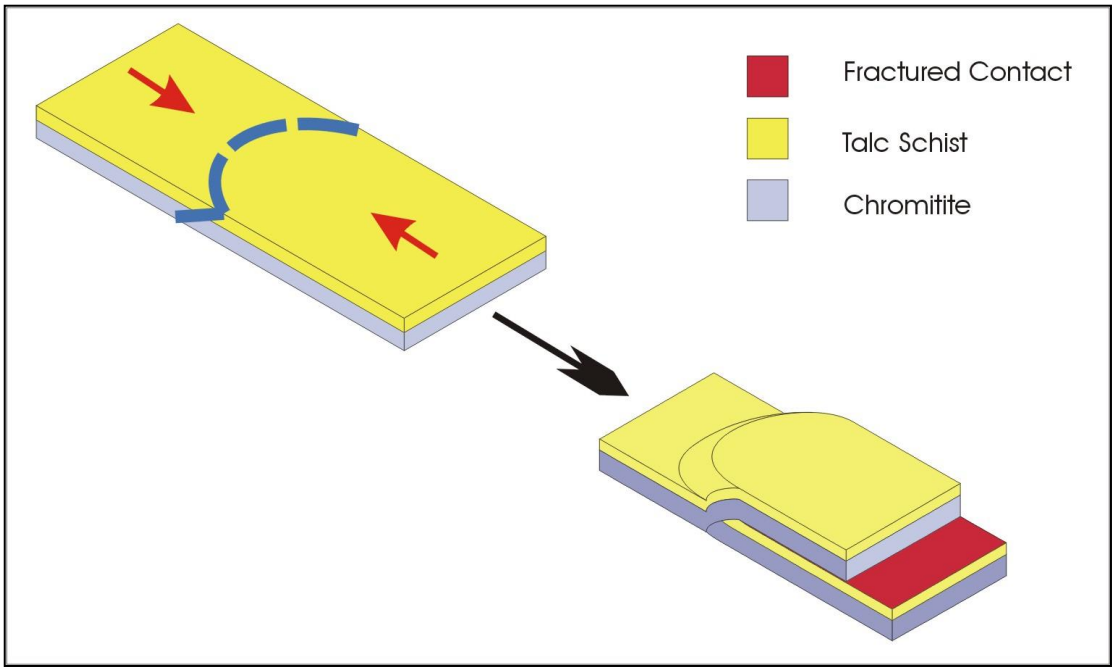

Figure 7.3: Diagram displaying the structural duplication model.

The bottom two chromitite lenses have a lower chromite to matrix ratio than the three upper chromitite lenses. This ratio shows a constant upwards increase from the bottom of lens MC5 to the top of lens MC4. This constant increase in chromite content suggests that these two lenses were deposited during the same magmatic event by means of continued crystal fractionation. As the chromite content decreases the color of the chromitite becomes lighter and the rock becomes softer. This explains why chromitite from the lower two lenses is softer and lighter in color whereas the upper three lenses are hard and dark gray to black. This difference between the chromite of the upper three and the lower two chromitite lenses indicate that at least two separate events of chromitite deposition had contributed to the development of the Massive Chromitite Layer.

7.2. Geological structures and textures (chapter 4):

7.2.1 Contacts

A big difference exists between the top- and bottom contacts of the upper three massive chromitite lenses. The top contacts are thin gradational and the bottom contacts are sharp and fractured with striations. The bottom two chromitite lenses (MC4 and MC5) are only separated by a prominent gradational contact, whereas the upper three lenses are separated by layers of talc carbonate schist and fractured bottom contacts. This emphasizes the differences between the lower two and upper three chromitite lenses and supports that they were deposited by different magmas. The top contact of lens MC4 is however similar to the thin gradational top contact of the upper three chromitite lenses.

The thin gradational top contacts of chromitite lenses MC1, MC2, MC3 and MC4 mark the depletion of chromium from the resident magma. The continuation of olivine and orthopyroxene crystallization that co-precipitated with the last chromite resulted in the formation of these gradational contacts. The striations on the fractured bottom contacts of all three lenses indicate movement along these contacts and support the structural duplication theory (fig. 7.3), suggesting that after the depletion of chromium and some harzburgite deposition, a contact parallel shearing event (Hornsey, 1999) took place along the bottom contact, resulting in the triple stacking of the chromitite – harzburgite package. The orientations of the majority of the bottom contacts have a good correlation with the orientation of the complex. This orientation also correlates with the 150°TN sense of shear of the Bushveld age contact parallel shear event (Hornsey, 1999). Therefore the origin of the shearing along the bottom contacts of the chromitite lenses could be either the result of separate depositions of rafts of semi-solid chromitite or form part of the Bushveld age contact parallel shearing event. This must be confirmed by means of a mineral chemistry study.

7.2.2 Faults

Only a few faults are present in the study area. The orientations of most faults correlate with the general orientation of the complex. This implies that the faults are the result of a force that was applied parallel to the direction of the magma movement. There are three faults in the study area with displacements that remain constant through both the bottom two chromitite lenses (MC4 and MC5), but stop in the talc-carbonate schist layer on top of lens MC4. The displacement however does not extend further upwards into the upper chromitite lenses. This once again indicates at least two separate events of chromite deposition during the development of the Massive Chromitite Layer.

The faults in the upper three chromitite lenses are restricted to a specific chromitite lens and the displacement does not extend to the surrounding talc-carbonate schist layers. This restriction of the faults poses a real threat to the structural duplication model, as the faults should extend into the overlaying talc schist layer that was supposedly duplicated with the chromitite layer. In contrast to the normal crystallization process it seems as if the chromitite lenses were sudden depositions that were detached from the older units. Thereby the stress applied to a chromitite lens could form faults before the crystallization of the harzburgite continued. This also means that the chromitite would have to be in a well solidified state during deposition to experience brittle deformation in the short period that the overlying harzburgite was still ductile or not yet deposited.

The 304/35 orientation of the fault in geological section F2.3, correlates with the Mesozoic age north-east / south-west faulting event. The fracture zone in geological section F2.3 also correlates with the 150°TN sense of shear for the Bushveld age contact parallel shear event (Hornsey, 1999). This indicates that this late stage regional deformation might be present in the study area. The majority of the structures in the study area are however restricted to certain geological units and do not continue through the entire study area.

7.2.3 Joints

There are numerous joints in the study area and they are concentrated in isolated areas. Different to the faults, the joints were cut off at the top contacts of the chromitite lenses and extend downwards through the older layers. This indicates that either the harzburgite layer above the chromitite lens was still ductile and absorbed the stress causing the joints, or the harzburgite layer was not yet deposited. All the joints do not stop on the top contact of the same chromitite lens. The joints however are not deformed by the fracturing along the bottom contacts of the chromitite lenses. Therefore the fracturing along the bottom contacts of the chromitite lenses had to be completed before jointing took place. This also implies that chromitite emplacement took place in pulses with some cooling time in-between

The jointing in the study area indicates that each of the three upper chromitite lenses had to be solidified to a degree to experience brittle deformation during the precipitation of the overlaying harzburgite. It further implies that the movement and fracturing along the bottom contacts of these chromitite lenses is the result of syn-magmatic deformation. This supports the chromitite raft emplacement theory as the deformation along the bottom contact took place as the raft was deposited as a solid to semi-solid body, providing time for joints to form while the overlying harzburgite was still ductile.

7.2.4 Schistosity

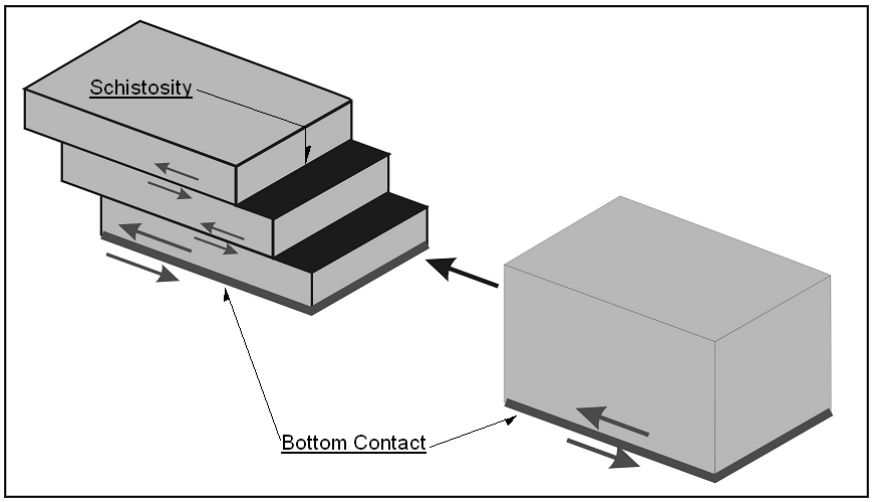

Figure 7.4: An illustration of the development of schistosity in the chromitite lenses.

The schistosity is related to specific structures and the orientation thereof correlates with the orientation of the related structure. The schistosity is defined by thin layers of crushed chromite crystals. These thin layers have higher concentrations of chromite and formed as the softer matrix minerals were squeezed out from between the crushed chromite chips. This high concentration of chromite results in thin darker layers (fig. 4.14). There is schistosity that developed in the chromitite close to the bottom contact of chromitite lenses MC1 and MC3. The good correlation between the orientation of this texture and the orientation of the associated contact implies that the schistosity formed in conjunction with the fracturing along the bottom contacts (fig. 7.4). The schistosity is most expressed near the shear planes.

7.3. Petrography (chapter 5):

The most important trend that is revealed through the point count study is the upwards increasing trend in the chromite to matrix ratio, as this creates a better understanding in the origin of the chromitite raft. The matrix minerals mostly consist of talc, representing the original olivine and orthopyroxene matrix. This overall increasing trend is present in all the chromitiferous layers from the PCR2 layer to the top of the Massive Chromitite Layer. There are at least two possible methods according to which the chromitite rafts could form and being deposited in the conduit system. The first scenario is that the chromite starts to crystallize and settle out from the resident magma as the temperature in the magma chamber decreases. As the chromite accumulates, portions floated in suspension down the conduit powered by the magma pulses. This scenario will generate rafts that are all very similar to each other in their chemistry, crystal size and ratio of chromite to matrix. This scenario fails to explain an increase in the percentage of chromite to matrix from one chromitite lens to the next.

The second scenario is similar to the first, with the exception that each raft is initiated by replenishment of magma into the primary magma chamber. The replenishing magma, enriched in chromium, was injected into the magma chamber depleted of chromium by

means of crystallization. Since the temperature of the resident magma in the chamber already decreased below the solidus of chromite it will absorb heat and cause the magma from the influx to cool down more rapidly than during normal chamber conditions. The faster cooling of the replenishment will increase crystallization of chromite from the replenishment, whereas the matrix material will crystallize slower than the chromite as crystallization from the resident magma continues at the solidus. Therefore there is an overall increase in the chromite to matrix ratio as time progresses (fig. 5.21 and 5.23). The replenishments are supported by the mass balance calculations of the Massive Chromitite Layer which indicates that a magma column with an approximate 4000m thickness was needed to deposit the massive chromitites unless replenishment took place *(Gauert, 2001)*.

The petrographic investigation established that there are two prominent physical properties of the chromitiferous layers that correlate with the degree of chromite crystal deformation. The first is the relative age of the chromitiferous layer (fig. 5.28) and the second is the relative thickness of the layer (fig. 5.29). Both of these properties are influential to the cooling tempo of the magma replenishments. The relative age of an influx will determine the temperature of the resident magma that the replenishment gets injected into. The cooler the surrounding resident magma the faster the replenished magma will cool down. On the other hand, the width of a chromitiferous layer represents the volume of the replenishment. Larger volume replenishments will be more resistant to the cooling effect by the resident magma.

The petrographic investigation strongly suggests that the stacked chromitiferous deposits of the Uitkomst Complex are the result of multiple replenishments of chromium rich magma into the resident magma that resulted in the formation of chromitite rafts that came to rest as lenses in the conduit. This is supported by the percentage of abraded crystals, the chromite to matrix ratio and the crystal fracturing that indicates that each chromitiferous deposition had a unique cooling tempo. The integrity of the statement however will have to be tested by the mineral chemistry of the chromite crystals.

7.4. Chromite mineral chemistry (chapter 6):

The chromitite lenses exposed in the pit are all part of the bigger Massive Chromitite unit and their mineral chemistry correlates with that of the MCHR unit that was intersected in borehole UK33. The mineral chemistry of the chromite crystals revealed that the chemical composition of the five chromitite lenses in the pit is significantly different from each other. This indicates that each chromitite lens has precipitated from individual magma influxes into the resident magma chamber and no major re-equilibration of chromite crystals took place.

There is an increasing trend in both average chrome number and magnesium number as deposition continues from the PCR2 layer to the MCHR layer. This trend does not form a straight line (fig. 6.5) and implies that the magma from which the chromite crystallized became more primitive as time continued. During the deposition of each of the three individual chromitiferous layers there was a number of increasing and decreasing trends for both chrome number and magnesium number that resulted in a saw tooth pattern (fig. 6.3 and 6.4). The above observations are all contradicting to the chemical evolution of a normal fractionation sequence.

The saw tooth pattern is a clear indication that the chromitiferous layers developed as a result of individual influxes of new magma into the resident chamber. The influxes are placed into a partially evolved and cooler resident magma that will absorb heat from the replenishment causing it to cool down more rapidly than during the normal magma chamber maturing processes. This faster cooling of the influx magma will enhance the crystallizing of chromite from a lesser evolved magma. So there is less time available for Mg and Fe to be removed from the melt before chromite starts to crystallize, they are incorporated into the chromite crystals framework.

The chemical evolution from lens MC4 to MC5 reveals a normal maturing trend, whereas chromitite lenses MC3, MC2 and MC1 reveal an irregular pattern (fig. 6.13). This might indicate that chromitite lenses MC4 and MC5 were deposited as a result of continued

crystallization from high volume replenished magma that was flushed through the conduit. Chromitite lenses MC3, MC2 and MC1 in shearing that duplicated a single turn were represented by semi-solid chromitite rafts.

The distinct variance in chromite mineral chemistry between the chromitite lenses clearly proves that the stacking of the chromitite lenses is not the result of contact parallel deposit of chromitite. Therefore although the orientation of the Bushveld age contact parallel shearing discussed by Hornsey (1999) does correlate with the fracture zone in the study area it seems like the stacking of the chromitite lenses as well as the shearing along the bottom contact are the result of localized syn-magmatic deformation event of a cyclic cumulate sequence.

7.5. Geological model

The physical appearance and properties of the five chromitite lenses exposed in the study area show that lenses MC4 and MC5 have larger quantities of matrix minerals and therefore were deposited as a result of continued crystallization from the same magma source *(Robb, 2005).* Chromitite lenses MC1, MC2 and MC3 seem to be structurally duplicated.

During the structural investigation the continuity between chromitite lenses MC4 to MC5 could be established, supporting that they were deposited as a single and continued depositional event. The structural deformation of chromitite lenses MC1, MC2 and MC3 suggest that they were deposited as chromitite rafts which ruled out the possibility of structural duplication.

The petrographic investigation revealed that each chromitite lens experienced a unique degree of crystal fracturing and had a unique chromite to matrix ratio. This does not only support that the chromitite of the Massive Chromitite Layer was deposited as rafts but also suggests that the rafts represent individual magma replenishments into the primary

magma chamber. These trends were confirmed against the older PCR1 and PCR2 chromitiferous deposits of the Uitkomst Complex.

All the findings from the previous investigations had to be proven by a mineral chemical investigation. This mineral chemical investigation did reveal a normal fractionating trend between chromitite lenses MC4 and MC5 supporting that theses two lenses were deposited by means of continued crystallization from high volume replenishment. The irregular geochemical pattern of the upper three chromitite lenses supports that they were deposited from different magma influxes into the resident magma chamber. A comparison between the degree of chromite crystal fracturing and the chromite crystal chemistry is shown in figure 7.5. This indicates that the variance in both the crystal fracturing and the crystal chemistry had the same controlling factor. These controlling factors include the cooling rate of the magma replenishments and the temperature of the magma that the replenishment gets introduced to. The cooling rate controls the mineral chemistry by influencing the differentiation trend. One of the direct controls on the crystal fracturing is the temperature of the replenished magma at the time that the chromitite rafts get transported through the conduit. Rafts of semi-solid chromitite at a lower temperature will have a higher internal viscosity that in turn allows for less free movement of individual crystals. Therefore during the transportation of the chromitite rafts the chromitite crystals within the entire raft will be exposed to higher shear stress as the temperature of the raft decreases. The temperature of the magma that the replenishments gets introduced to sets the minimum temperature that the replenishment can reach, whereas the cooling rate determines how close the temperature of the chromitite raft will be to the minimum temperature at the time that transportation commences. The cooling rate in turn is governed by the temperature and volume of the replenishment relative to that of the resident magma. The chemical trends in figure 7.5 were multiplied by a hundred to fit the scale on the diagram. The mineral chemistry will not be influenced by the temperature of the raft during transportation like the crystal fracturing. This is also indicated by figure 7.5 as chromitite lens MC1 is the last chromitite deposition in the study area and therefore has the lowest minimum temperature. The effect of this low minimum temperature is much higher on the crystal

fracturing than on the mineral chemistry. The only effect that the lower temperature in the resident magma chamber has on the mineral chemistry is that it increases the cooling rate of the replenished magma that in turn influences the differentiation trend.

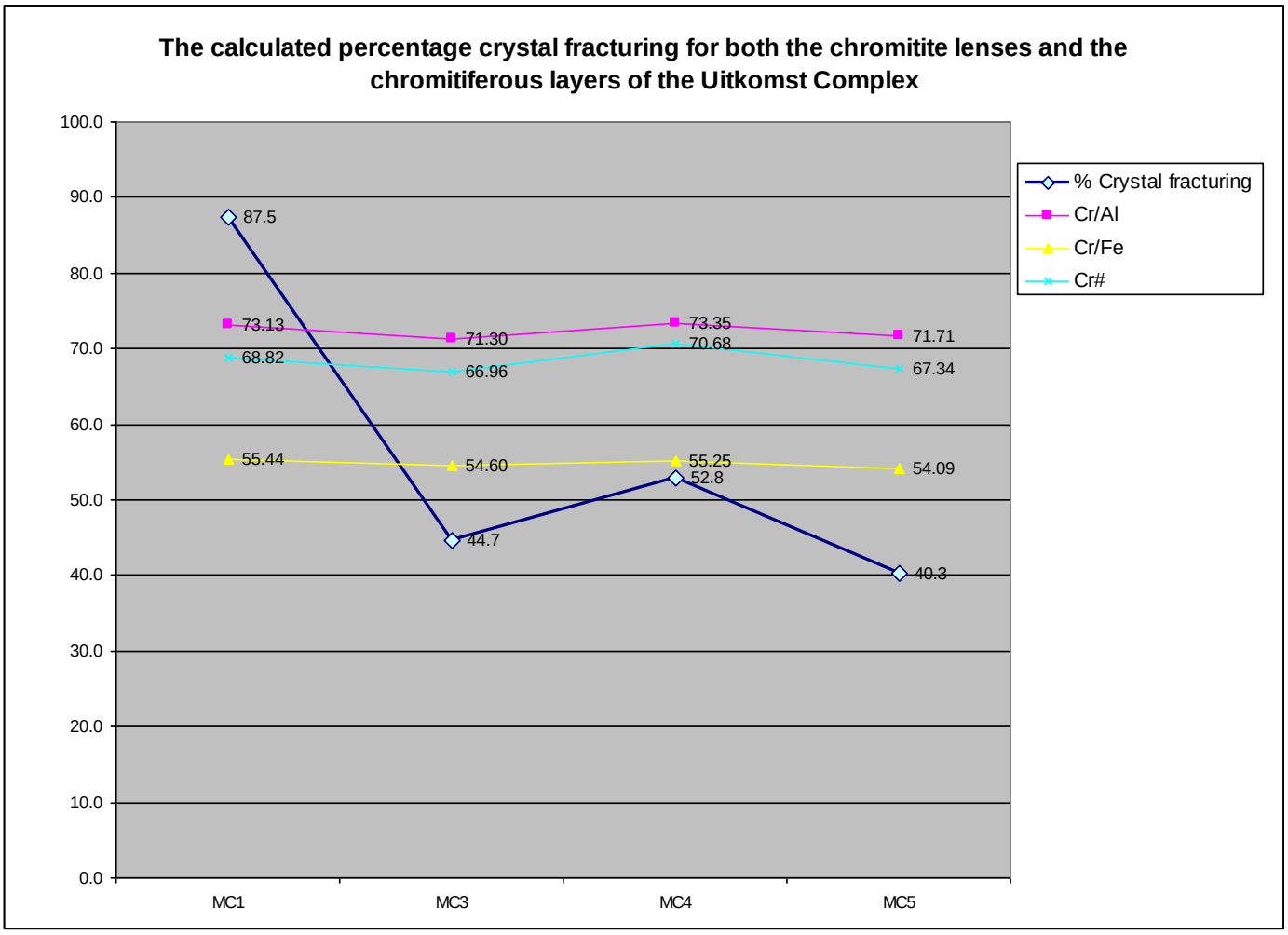

Figure 7.5: Correlation between fracturing and chemistry of chromite crystals.

Chapter 8: Conclusions.

The aim of this chapter is to conclude the evolution and deposition of the Massive Chromitite Layer of the Uitkomst Complex into an emplacement mode. The model will start off with the oldest chromitite that is exposed in the study area and will continue in a chronological manner upwards.

The deposition of the Massive Chromitite Layer begins with an influx of primitive, chromium-rich magma into a magma chamber that contains a partially evolved resident magma depleted of chromium through earlier crystallization (Fig.8.1). The resident magma is cooler than the influx and has physical conditions that allow chromium to be stable in a solid crystalline phase as the mineral had already crystallized earlier during the deposition of the Chromitiferous Harzburgite layers. At the time of the magma replenishment olivine and orthopyroxene are crystallizing from the resident magma to form harzburgite in both the magma chamber and the conduit leading to the study area. The density differences between the replenished and the resident magmas will prevent major magma mixing to take place (fig. 8.1).

This initial magma replenishment during the evolution of the Massive Chromitite Layer released a high volume of magma into the primary magma chamber. Some of this chromium-rich magma was flushed into the conduit resulting in the flotation and transportation of both primitive and partially evolved magma for some time (fig. 8.1). Small scale magma mixing occurred on the contact between the two magmas resulting in the crystallization of chromite. These crystals typically clustered together to form small lumps of chromitite which sank to the bottom of the chamber as well as the conduit where lumps of chromitite are enclosed by olivine and orthopyroxene crystals. They too formed harzburgite with lenses of disseminated chromite similar to lens MC5 of the Massive Chromitite Layer.

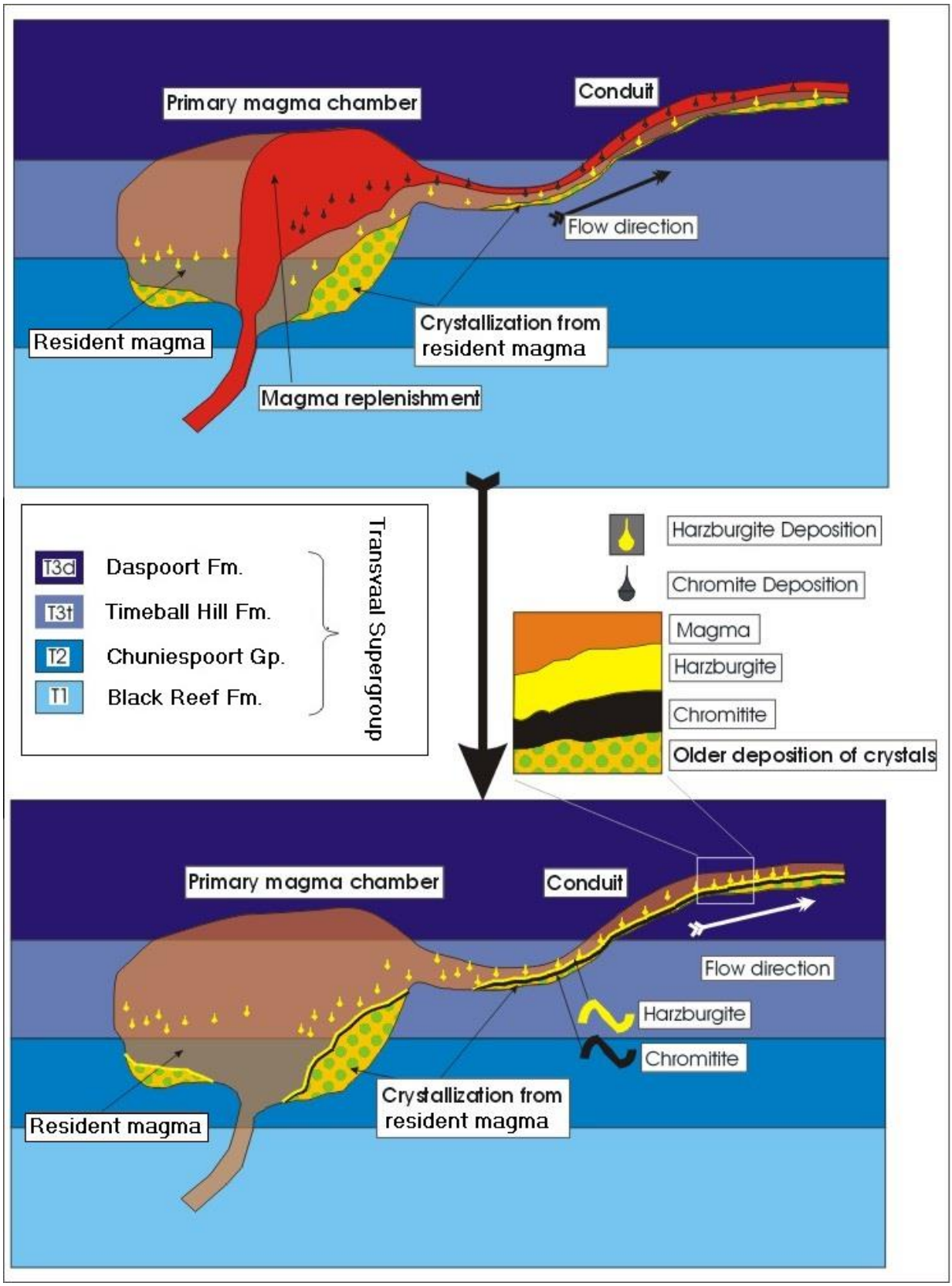

Figure 8.1: Schematic illustration of the deposition of chromitite lenses MC4 and MC5.

As the replenished magna cooled down it started to evolve and chromitite will start to crystallize directly from it and not only from the mixing zone. The individual chromite crystal sank to the bottom and will formed chromitite with more evenly spread crystals. As the replenishment continuously lost heat to the resident magma the crystallization rate of the chromite increased resulting in a constant increase in the ratio of chromite to matrix minerals in the rock that forms. This corresponds with the MC4 lens of the Massive Chromitite Layer that has a gradual upward increase in its chromite to matrix ratio *(Robb, 2005).* The chromite mineral chemistry further reveals a normal evolution trend from chromitite lens MC5 to MC4. After the chromium is removed from the replenishment and the new magna is mixed with the resident magma the deposition of harzburgite will continue and form a layer of harzburgite on top of chromitite lens MC4, separated by a thin gradational contact (fig. 8.1).

The deposition of chromitite lens MC3 resulted from a second replenishment (fig. 8.2). The chromite mineral chemistry of lens MC3 indicates that it crystallized from a more primitive magma than chromitite lens MC4. This replenishment was considerably smaller in volume and was not extracted into the conduit. Density differences once again prevented magma mixing. The resident magma constantly absorbed heat from the replenishment as it is more evolved and much cooler than the magma from the influx. This caused the replenishing magma to cool down more rapidly and resulted in a rapid crystallization of chromite from a primitive magma. The rapid chromite crystallization in turn caused the chromite crystals to congregate into large lumps or sheets of chromitite. These sheets were heavier than their surrounding and sank from the replenished magma into the resident magma. As the sheet of chromitite moved into the resident magma it entered a cooler environment and the solidification process became more rapid. Some of these chromitite sheets were pushed into the conduit along with the resident magma and were transported as rafts of semi-solid chromitite (fig. 8.2).

The combination of the kinetic energy from the transportation process and the semi-solid nature of the raft resulted in brittle deformation of the chromite crystals. The weight of the chromitite raft caused it to sink to the bottom of the conduit until it came in contact

with the older harzburgite at the base of the conduit. Friction between the raft and the harzburgite caused the chromitite raft to settle down which results in the fracturing along the bottom contact of the chromitite. All of this happened in a system that was co-precipitating harzburgite. Therefore after the chromitite raft settled down, the deposition of harzburgite continued and formed the gradational top contact of the chromitite.

Chromitite lens MC2 was crystallized from a magma that was even more primitive than for lens MC3. Therefore it is considered that chromitite lens MC2 crystallized from a third replenishment. The further depositional process of lens MC2 is similar to that of lens MC3.

Chromitite lens MC1 crystallized from a magma that was more evolved than for lens MC2. Therefore it is possible that chromitite lens MC1 crystallized from the same replenishment as lens MC2, but at a later stage to allow the magma influx to become more mature.

In summary, the Massive Chromitite Layer was deposited during a time period of multiple magma replenishments into the resident magma with temperatures that allowed the formation of chromitite with a high chromite to matrix ratio. The flow-energy in the conduit is also very significant in the formation of this multi-layered Massive Chromitite Layer. It had to be sufficient to transport rafts through the conduit and also allowed the rafts to settle down along the way. Therefore the deposition and evolution of the combined Massive Chromitite Layer of the Uitkomst Complex is governed by a combination of very unique and specific factors that are revealed by the prominence of syn-magmatic deformation and supported by mineral chemistry.

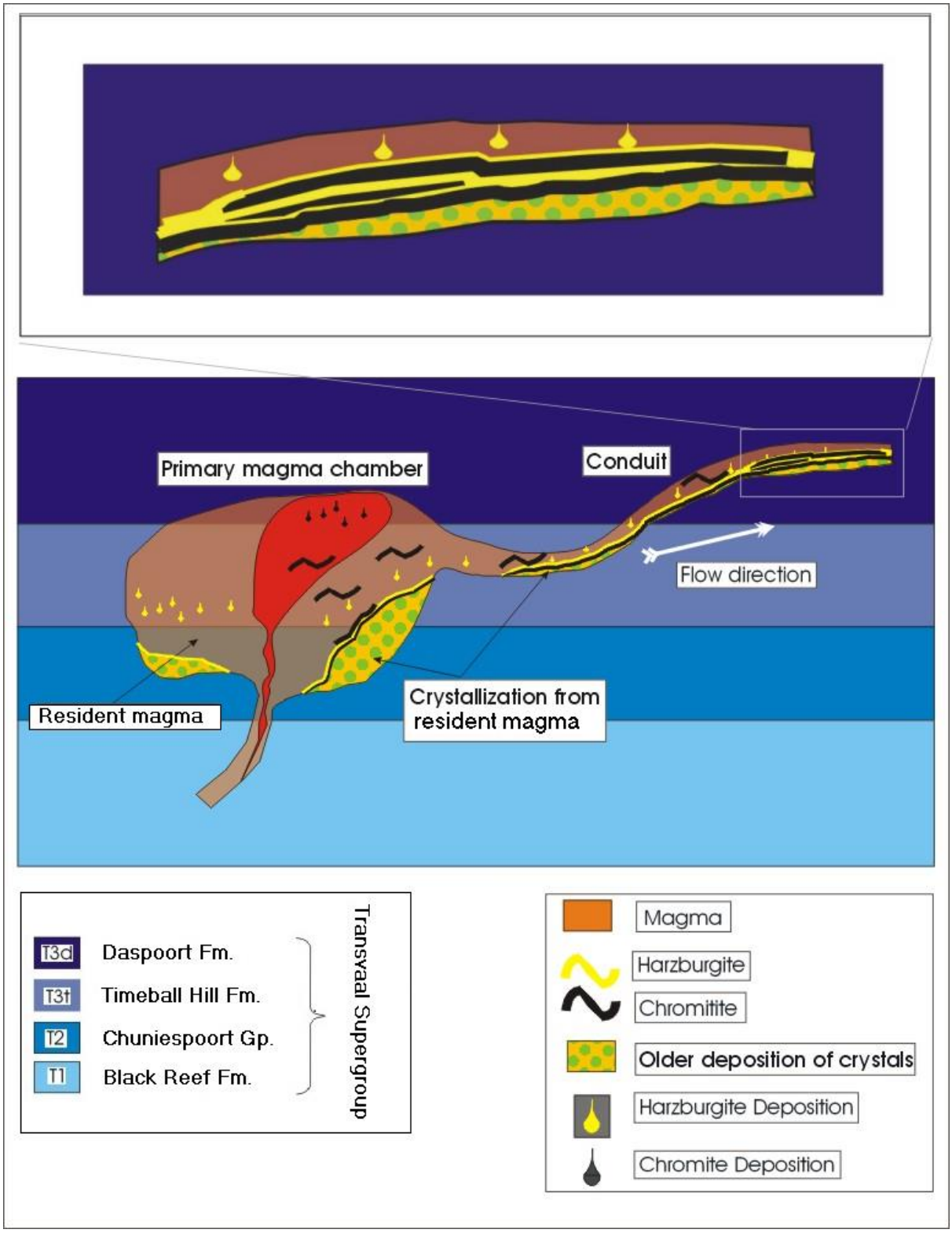

Figure 8.2: Schematic illustration applicable to the deposition of chromitite lenses MC1, MC2 and MC3.

References

Andrew, A., Hugh, M., Eales, V. and Kruger, F. J., (1998). *Magma replenishment and the significance of poikilitic textures in the Lower Main Zone of the Western Bushveld Complex*, South Africa, Mineralogical Magazine, **62/4**, 435-450.

Anhaeusser, C.R., Robb, L.J., Barton, J.M. (jr), (1979). *Mineralogy, Petrology, and origin of the Archaean Bosmanskop syenite, Barberton Mountain Land, South Africa.* Inf. Circ. Econ. Geol. Res. Unit, University of the Witwatersrand, **139**.

Anonymous, (1997). *Nkomati - South Africa's first primary nickel mine*, South African Mineral, Coal, Gold and Base Metals, 27-31.

Boer, R.H., Meyer, F.M., Robb, L.J., Graney, J.R., Venneman, T.W., and Kesler, S.E., (1995). *Mesothermal-Type Mineralisation in the Sabie-Pelgrim`s Rest Gold Field, South Africa.* Economic Geology, **90**, 860-876.

Bumby, A., (1997). *The Rusternberg Fault*. Tectonics Division of the Geological Society of South Africa field trip guide.

Button, A., (1973). *A regional study of the stratigraphy and development of the Transvaal basin in the eastern and northeastern Transvaal.* Unpublished Ph.D. thesis, University of the Witwatersrand.

Canil, D., (1991). *Experimental evidence for the exsolution of cratonic peridotite from high-temperature harzburgite*, Earth and Planetary Science Letters, **106**, 64–72.

Corner, B., (1991). *Crustal architecture of the Precambrian of the Kaapvaal Province from geophysical data.* Terra abstracts supplement 3 to Terra Nova **3**, 5.

De Waal, S.A., Gauert, C.D.K., (1997). *The Basal Gabbro Unit and the identity of the parental magma of the Uitkomst Complex, Badplaas, South Africa*, South African Journal of Geology, **100**, 349-361.

De Waal, S.A. and Gauert, C.D.K., (1998). *The Basal Gabbro Unit of the parental magma of the Uitkomst Complex, Badplaas, South Africa*, South African Journal of Geology, **100**, 32-48.

De Waal, S.A., Maier, W., Armstrong, R. and Gauert, C.D.K., (2001). *Chemical constraints on the differentiation and emplacement of the Uitkomst Complex, Mpumalanga Province, South Africa*, Canadian Mineralogist, **39**, 557-571.

Eriksson, P.G. and Reczko, B.B.F., (1995). *The sedimentary and tectonic settings of the Transvaal Supergroup floor rocks to the Bushveld Complex.* Journal of Africa Earth Science, **21**, (4), 487-504.

Gauert, C.D.K., De Waal, S.A., Wallmach, T., (1995). *Geology of the ultrabasic to basic Uitkomst complex, eastern Transvaal, South Africa*: an overview. – Journal of African Earth Sciences, **21**, 553-570.

Gauert, C.D.K., (1998). *The petrogenesis of the Uitkomst Complex, Mpumalanga Province, South Africa*, Unpublished Ph.D. thesis, University Pretoria.

Gauert, C.D.K., (2001). *The importance of a magmatic conduit mechanism for the formation of the sulfide and oxide mineralization in the Uitkomst Complex*, South Africa, Journal of African Earth Science, **32/2**, 149-161.

Harley, M., and Charlesworth, E.G., (1991). *Compressive deformation of a pre-Bushveld diabasic sill, Sudwala, eastern Transvaal*. South African Journal of Geology, **94**, (5/6), 348-354.

Harley, M., and Charlesworth, E.G., (1995)a. *The role of fluid pressure in the formation of bedding-parallel, thust-hostedgold deposits, Sabie-Pilgrim`s Rest, eastern Transvaal.* GSSA Centennial Geocongress abstracts, 77-80.

Harley, M., and Charlesworth, E.G., (1995)b. *Structural Development and controls to epigenetic mesothermal gold mineralization in the Sabie-Pelgrim`s Rest goldfield, eastern Transvaal, South Africa.* GSSA Centennial Geocongress abstracts, 73-76.

Hartzer, F.J.,(1995). *Transvaal Supergroup inliers: geology, tectonic development and relationship with the Bushveld complex, South Africa.* Journal of Africa Earth Science, **21**, (4), 521-547.

Hatton, C.J. and von Gruenewaldt, G., (1984). *Chromite from the Swartkop Chrome Mine an estimate of the effects of subsolidus reequilibration*, Economic Geology, **80**, 911-924.

Hornsey, R.A., (1999). The *genesis and evolution of the Nkomati Mine Ni-sulphide deposit, Mpumalanga Province, South Africa*, Unpublished M.Sc. thesis, Department Geology and Applied Geology, University of Natal, Durban.

Irvine, T. N., (1977). Origin *of chromitite layers in the Muskox Intrusion and other strativorm intrusions: a new interpretation*. Geology, **5**, 273-277

Joubert, P.L. and Gauert, C.D.K., (2006). *Syn- to post-intrusive deformation in the chromitiferous harzburgite, Uitkomst Complex*, South Africa, 21st. Colloquium of African Geology, Geological Mining Association of Mozambique (AGMM), Mozambique, Maputo, 78 – 80.

Joubert, P.L. and Gauert, C.D.K., (2007). *Deformasie van chroomhoudende harzburgietlaag in die Uitkomst-Komplex*, Die Suid-Afrikaanse Tydskrif vir Natuurwetenskap en Tegnologie, **26/2**, 157-158.

Kenyon, A.K., Attridge, R.L., Coetzee, G.L., (1986). The *Uitkomst nickel-copper deposit, Eastern Transvaal*. in: Anhaeusser, C.R., Maske, S., (Eds.): Mineral Deposits of Southern Africa Vol. I & II: 1009-1017, Johannesburg (Geological Society of South Africa).

Kiviets, G.B., (1991). *The petrography and geochemistry of chromitite seams from the Uitkomst Layered Ultramafic Complex, Eastern Transvaal*, Unpublished Hons. thesis, Department Geochemistry, University of Cape Town,

Laubscher, D.H., (1986). *The New Amianthus Chrysotile Asbestos Deposit, Kaapsehoop, Barberton Greenstone Belt.* In: Anheaeusser, C.R., and Maske, S., (Eds)., *Mineral Deposits of South Africa.,* **1**, Geological Society of South Africa., 421-426.

Li, C., Ripley, E.M., Maier, W.D., and Gomwe, T.E.S., (2002). *Olivine and sulfur isotopic compositions of the Uitkomst Ni-Cu sulfide ore-bearing complex, South Africa: Evidence for sulfur contamination and multiple magma emplacements*, Chemical Geology, **188**, 149–159.

Maier, W.D., Gombwe, T., Barnes, S.J., Li, C., and Theart, H.F.J., (2004*). Platinum Group Elements in the Uitkomst Complex, South Africa*. Economic Geology, **99**, 499–516.

Menell, R.P, Brewer, T.H., Delve, J.R., and Anhaeusser, C.R., (1986). *The Kalkkloof Chrysotile Asbestos Deposit and surrounding area, Barberton Mountain Land.* In: Anheaeusser, C.R., and Maske, S., (Eds)., *Mineral Deposits of South Africa.,* **1**, Geological Society of South Africa., 427-436.

Robb, L.J., (2005). *Introduction to ore forming processes*, Blackwell Publishing, Victoria, Australia, 49-53.

Rozendaal, A., Toros, M.S., and Anderson, J.R., (1986). *The Rooiberg tin deposit, west-centrel Transvaal*. In Anhaeusser, C.R., and Maske, S., (Eds)., *Mineral Deposits of South Africa*., Geological Society of South Africa, **2**, 1307-1327.

Sharper, M.R. and Snyman, J.A., (1978). *A model for the emplacement of the eastern compartment of the Bushveld Complex.* Institution for Geological Research Bushveld Complex, Research Report 11.

Theart, H.F.J., and de Nooy, C.D., (2001). The *platinum-group minerals in two parts of the massive sulphide body of the Uitkomst Complex, Mpumalanga, South Africa*: South African Journal of Geology, 104, 287–300.

Uken, R., and Watkeys, M.K. (1997). *An interpretation of mafic dyke swarms and their relationship with major magmaticevents on the Kaapvaal Craton.* South African Journal of Geology, **100**, (4), 341-348.

Visser, J.N.J., (1957). *The Transvaal Basin – A new sedimentary model?* Annual Geological Survey for South Africa, **8**, 75-85

Whitten, K.W. and Davis, R.E., (1992). *General chemistry with qualitative analysis*, Fourth edition, Orlando, Florida, Saunders College Publishing.

Web references

Computational Thermodynamics. (2011). Iron-Chromium (Fe-Cr) Phase Diagram, Online, Available: http://www.calphad.com/iron-chromium.html

European Commission. Joint Research Center. (1995). afr_za2003_3toge.jpg, Online, Afailable:http://eusoils.jrc.ec.europa.eu/esdb_archive/EuDASM/Africa/images/maps/download/afr_za2003_3toge.jpg,

LionOre. (2005). Operations, Online, Available: http://www.lionore.com/operations/nkomatnickel.asp.

University of Houston. (2011). phase17.gif, Online, Available: http://www.uh.edu/~jbutler/petrography/phase17.gif

Acknowledgments

The author would like to thank the personnel of the Nkomati Mine for their support especially during the field work stage of the project. A special thanks to Mr. Mark Davidson the geology leader at the Nkomati Mine for supporting me in every way and allowing me accesses to the mining operation, borehole data and providing me with rock samples from both the operation as well as core samples. I would like to further more express my gratitude towards the Nkomati Mine for sponsoring a portion of the expenses towards the project.

I want to thank Harmony Gold mine for their financial contribution in order to support the project. A special thanks to Mr. Johann Ackermann the Ore Reserve Manager at Harmony Gold Mine during the course of the project for supporting me with ample time to complete the research.

The Council for Geo-Science is thanked for initial financial support.

It is further more a pleasure to express my greatest gratitude to my study leader Prof. C.D.K. Gauert for the full support that was provided by him during the entire course of the project. Also to the technical team at the University of the Free State for the provisional technical support.

Mr. H.C. Cilliers is thanked for assisting in language editing

Lastly, but not least I would like to thank my family for supporting my all the way.

Appendixes

Appendix 1- Chromite mineral geochemical data

Oxide															
DataSet/Point	SiO2	TiO2	V2O3	Al2O3	Cr2O3	FeO	MnO	MgO	CoO	NiO	ZnO	CaO	Total	Comment	Point#
1 / 1 .	0.37	0.66	0	14.72	51.88	20.41	0.35	9.13	0	0.07	0.1	0	97.69	B6 R1	1
2 / 1 .	0.06	0.63	0	14.95	49.66	21.99	0.31	11.1	0	0.05	0.07	0.02	98.85	B6 B/B1	2
3 / 1 .	0.03	0.67	0	14.78	49.94	22.09	0.24	11.12	0	0	0.04	0	98.91	B6 K1 CORE B	3
4 / 1 .	0.04	0.61	0	14.62	50.67	21.67	0.32	11.15	0	0	0.04	0	99.12	B6 K1 RIM B	4
5 / 1 .	0.07	0.68	0	14.4	50.06	22.08	0.3	10.94	0	0.02	0.1	0	98.66	B6 K2 CORE M	5
6 / 1 .	0.02	0.6	0	14.28	51.04	21.78	0.29	10.97	0	0	0.08	0	99.06	B6 K2 RIM M	6
7 / 1 .	0.08	0.62	0	14.47	50.5	21.88	0.36	11.2	0	0.02	0.1	0	99.24	B6 R2	7
8 / 1 .	0.05	0.67	0	14.25	50.04	22.04	0.32	10.87	0	0.04	0.05	0	98.35	B6 B/B2	8
9 / 1 .	0.08	0.67	0	14.05	50.94	21.7	0.29	10.72	0	0.06	0.01	0	98.52	B6 CHIP 1	9
10 / 1 .	0.04	0.62	0	14.91	51.16	22.57	0.34	7.23	0	0.04	0.04	0	96.95	B6 CHIP 2	10
11 / 1 .	0.05	0.52	0	16.76	46.48	22.23	0.33	11.69	0	0.09	0.13	0.01	98.31	FIS2 K1 CORE S	11
12 / 1 .	0.06	0.44	0	17.32	46.67	21.91	0.29	11.96	0	0.11	0.04	0	98.81	FIS2 RI	12
13 / 1 .	0.02	0.71	0	16.47	46.62	21.67	0.3	12.21	0	0.07	0.07	0.01	98.16	FIS2 R2	13
14 / 1 .	0.01	0.67	0	17.48	46.26	21.69	0.31	12.6	0	0.05	0.01	0	99.09	FIS2 K2 CORE M	14
15 / 1 .	0.04	0.68	0	16.64	46.7	21.21	0.31	11.91	0	0.07	0.08	0	97.63	FIS2 K2 RIM M	15
16 / 1 .	0.01	0.71	0	16.82	46.91	21.5	0.34	12.37	0	0.08	0.05	0	98.79	FIS2 K2 B/B1	16
17 / 1 .	0.02	0.74	0	16.55	46.89	21.31	0.3	12.16	0	0.05	0.02	0	98.04	FIS2 K2 B/B2	17
18 / 1 .	0.03	0.53	0	17.23	46.22	21.49	0.31	11.98	0	0.08	0.08	0	97.95	FIS2 CHIP 1	18
19 / 1 .	1.33	0.53	0	15.93	46.19	23.49	0.32	10.91	0	0.08	0.13	0	98.91	FIS2 CHIP 2	19
20 / 1 .	0.01	0.72	0	17.23	46.56	21.61	0.29	12.32	0	0.11	0.09	0	98.94	FIS2 K3 CORE M	20
21 / 1 .	0.04	0.5	0	12.39	51.34	24.86	0.46	8.61	0	0.08	0.1	0.01	98.39	B19 K1 CORE M	21
22 / 1 .	13.85	0.46	0	9.13	39.05	21.59	0.54	11.49	0	0.15	0.14	2.65	99.05	B19 K1 RIM M	22
23 / 1 .	1.17	0.43	0	12.85	49.36	25.27	0.57	7.93	0	0.05	0.17	0.2	98.01	B19 K2 RIM M	23
24 / 1 .	0.07	0.56	0	12.72	51.11	24.9	0.49	8.64	0	0.05	0.13	0	98.67	B19 K2 CORE M	24
25 / 1 .	0.08	0.53	0	12.63	50.91	24.61	0.48	8.48	0	0.08	0.16	0	97.95	B19 R1	25
26 / 1 .	6.41	0.4	0	11.81	44.41	22.8	0.52	13.95	0	0.09	0.16	0	100.55	B19 CHIP 1	26
27 / 1 .	0.02	0.57	0	12.79	50.89	24.52	0.51	8.54	0	0.05	0.17	0	98.04	B19 R2	27
28 / 1 .	2.19	0.45	0	12.45	47.22	27.27	0.82	6.92	0	0.07	0.27	0	97.67	B19 CHIP 2	28
29 / 1 .	0.03	0.57	0	12.82	50.45	25.06	0.48	8.68	0	0.09	0.06	0	98.25	B19 B/B 1	29
30 / 1 .	0.2	0.59	0	12.64	50.47	25.44	0.53	7.9	0	0.08	0.12	0	97.99	B19 B/B 2	30
31 / 1 .	0.04	0.49	0	12.71	51.43	21.05	0.35	9.61	0	0	0.07	0.01	95.75	B10 R1	31
32 / 1 .	0.08	0.47	0	13.48	53.42	21.58	0.33	7.67	0	0.05	0.07	0	97.15	B10 R2	32
33 / 1 .	0.05	0.48	0	13.09	52.88	20.84	0.33	9.67	0	0.02	0.08	0.01	97.45	B10 B/B1	33
34 / 1 .	0.15	0.49	0	13.32	51.72	21.51	0.32	10.36	0	0.04	0.1	0	98.01	B10 B/B2	34
35 / 1 .	0.06	0.52	0	13.14	51.4	22.11	0.35	10.67	0	0.04	0.04	0.01	98.34	B10 K1 CORE B	35
36 / 1 .	0.04	0.49	0	12.81	51.97	22.58	0.38	9.68	0	0.03	0.09	0.01	98.08	B10 K1 RIM B	36
37 / 1 .	0.03	0.53	0	13.17	51.06	21.99	0.35	10.61	0	0.02	0.09	0	97.84	B10 K2 CORE B	37
38 / 1 .	0.03	0.51	0	13.2	51.57	22.08	0.29	10.33	0	0	0.02	0.03	98.05	B10 K2 RIM B	38
39 / 1 .	0.18	0.51	0	12.96	52.25	22.84	0.38	6.37	0	0.01	0.17	0	95.67	B10 K2 CHIP 1	39
40 / 1 .	0.06	0.49	0	12.77	54.33	21.16	0.34	6.52	0	0.04	0.1	0	95.81	B10 K2 CHIP 2	40

Oxide															
DataSet/Point	SiO2	TiO2	V2O3	Al2O3	Cr2O3	FeO	MnO	MgO	CoO	NiO	ZnO	CaO	Total	Comment	Point#
1 / 1 .	0.05	0.57	0	12.66	50.23	24.98	0.49	8.82	0	0.07	0.14	0.02	98.05	B22 K1 CORE B	1
2 / 1 .	0	0.58	0	12.5	51.1	24.42	0.5	8.17	0	0.06	0.09	0.01	97.41	B22 K1 RIM B	2
3 / 1 .	0.03	0.63	0	12.64	50.47	25.11	0.47	8.35	0	0.03	0.15	0.03	97.91	B22 K2 CORE M	3
4 / 1 .	0.03	0.49	0	12.78	51.18	24.89	0.52	8.22	0	0.04	0.07	0.04	98.25	B22 K2 RIM M	4
5 / 1 .	0.31	0.5	0	12.67	50.93	25.06	0.54	7.16	0	0.08	0.13	0.05	97.44	B22 CHIP 1	5
6 / 1 .	0.21	0.61	0	12.99	50.25	26.82	0.56	6.46	0	0.03	0.2	0	98.13	B22 CHIP 2	6
7 / 1 .	0.03	0.7	0	12.74	50.35	25.23	0.45	8.64	0	0.07	0.13	0	98.34	B22 B/B1	7
8 / 1 .	0	0.67	0	12.89	50.26	25.03	0.48	8.72	0	0.08	0.08	0.02	98.24	B22 R1	8
9 / 1 .	0.04	0.64	0	12.8	50.72	25.17	0.5	8.59	0	0.06	0.11	0	98.64	B22 B/B2	9
10 / 1 .	0.01	0.6	0	12.92	50.63	25.67	0.51	8.39	0	0.12	0.09	0	98.94	B22 R2	10
11 / 1 .	0.02	0.65	0	11.64	51.17	25.85	0.49	8.61	0	0.02	0.09	0	98.52	B23 R1	11
12 / 1 .	0	0.71	0	11.48	51.03	25.4	0.47	8.88	0	0.06	0.08	0.03	98.15	B23 K1 CORE S	12
13 / 1 .	0.03	0.67	0	11.9	51.32	24.99	0.47	9.27	0	0.12	0.06	0	98.81	B23 B/B1	13
14 / 1 .	0.06	0.68	0	11.84	50.88	25.31	0.47	8.94	0	0.09	0.05	0	98.31	B23 K2 CORE S	14
15 / 1 .	0.02	0.68	0	11.62	50.91	25	0.41	9.07	0	0.08	0.06	0	97.85	B23 B/B2	15
16 / 1 .	0	0.75	0	11.5	50.83	25.19	0.46	9.11	0	0.07	0.09	0.01	98.01	B23 R2	16
17 / 1 .	0.02	0.61	0	11.87	51.25	25.24	0.43	8.47	0	0.07	0.08	0.01	98.06	B23 CHIP 1	17
18 / 1 .	0.83	0.62	0	12.98	49.95	25.76	0.51	8.42	0	0.08	0.08	0	99.23	B23 CHIP 2	18
19 / 1 .	0.09	0.48	0	11	53.55	22.68	0.34	10.27	0	0.13	0.03	0	98.58	B23 K3 CORE M	19
20 / 1 .	0.04	0.48	0	10.95	53.18	22.54	0.36	10.48	0	0.12	0.09	0.04	98.28	B23 K3 RIM M	20
21 / 1 .	0.05	0.67	0	13.68	50.05	22.82	0.28	10.86	0	0.04	0.09	0.01	98.55	B4 B/B 1	21
22 / 1 .	0.01	0.64	0	13.93	50.12	22.98	0.36	10.73	0	0.03	0.07	0	98.88	B4 B/B2	22
23 / 1 .	0.02	0.69	0	13.21	51.09	23.46	0.37	8.76	0	0.01	0.11	0.02	97.74	B4 R1	23
24 / 1 .	0.21	0.65	0	13.75	50.81	22.63	0.25	10.6	0	0.08	0.01	0	98.99	B4 K1 CORE B	24
25 / 1 .	0.02	0.64	0	12.89	51.42	22.44	0.34	9.94	0	0.07	0.04	0.01	97.81	B4 K1 RIM B	25
26 / 1 .	0.05	0.62	0	13.96	52.05	22.55	0.36	8.2	0	0.04	0	0.01	97.82	B4 CHIP 1	26
27 / 1 .	0.02	0.54	0	13.74	50.77	22.49	0.35	9.88	0	0.02	0.04	0	97.85	B4 CHIP 2	27
28 / 1 .	0.06	0.59	0	14.08	50.47	22.63	0.38	10.68	0	0.02	0.1	0	99.02	B4 R2	28
29 / 1 .	0.07	0.54	0	13.69	51.13	22.49	0.34	10.51	0	0.05	0.12	0	98.94	B4 K2 CORE B	29
30 / 1 .	0.03	0.56	0	14.1	50.83	22.55	0.32	10.99	0	0	0.06	0	99.45	B4 K2 RIM B	30
31 / 1 .	0	0.51	0	13.78	53.24	21.92	0.35	7.48	0	0.04	0.07	0	97.38	B9 R1	31
32 / 1 .	0	0.45	0	13.53	52.21	21.49	0.31	9.7	0	0.03	0.1	0	97.82	B9 R2	32
33 / 1 .	0.05	0.43	0	13.61	52.19	21.42	0.31	9.81	0	0.03	0.06	0.01	97.93	B9 B/B1	33
34 / 1 .	0.02	0.44	0	13.89	51.99	21.75	0.32	10.25	0	0.02	0.08	0.01	98.77	B9 B/B2	34
35 / 1 .	0.02	0.43	0	13.69	51.88	22	0.33	10.2	0	0.02	0.1	0	98.68	B9 K1 CORE B	35
36 / 1 .	0.07	0.49	0	14.82	51.49	22.22	0.31	9.28	0	0.01	0.1	0	98.79	B9 K1 RIM B	36
37 / 1 .	0.41	0.46	0	13.97	52.42	21.73	0.34	7.75	0	0.02	0.08	0.01	97.18	B9 CHIP 1	37
38 / 1 .	0.04	0.5	0	13.41	54.2	21	0.3	6.5	0	0.06	0.14	0	96.15	B9 CHIP 2	38
39 / 1 .	0.07	0.54	0	13.34	51.07	22.79	0.34	10.61	0	0.03	0.12	0.02	98.93	B9 K2 CORE B	39
40 / 1 .	0.03	0.51	0	13.2	51.72	22.66	0.36	9.65	0	0.01	0.1	0	98.24	B9 K2 RIM B	40

Oxide															
DataSet/Point	SiO2	TiO2	V2O3	Al2O3	Cr2O3	FeO	MnO	MgO	CoO	NiO	ZnO	CaO	Total	Comment	Point#
1 / 1 .	0.08	0.66	0	12.84	49.89	25.95	0.51	8.58	0	0.07	0.11	0	98.69	B20 B/B1	1
2 / 1 .	0.02	0.63	0	12.8	49.89	26.17	0.44	8.7	0	0.04	0.07	0	98.75	B20 B/B2	2
3 / 1 .	0	0.63	0	12.81	50.02	25.94	0.5	8.56	0	0.06	0.08	0	98.61	B20 R1	3
4 / 1 .	0.02	0.62	0	12.94	49.76	25.59	0.49	8.65	0	0.04	0.06	0	98.17	B20 K1 CORE M	4
5 / 1 .	0.05	0.66	0	12.78	50.47	25.68	0.44	8.63	0	0.06	0.09	0.01	98.87	B20 K1 RIM M	5
6 / 1 .	0.05	0.61	0	12.75	50.4	25.78	0.43	8.53	0	0.1	0.05	0.01	98.7	B20 K2 CORE B	6
7 / 1 .	0.07	0.66	0	12.47	50.22	25.58	0.45	8.43	0	0.07	0.02	0	97.96	B20 K2 RIM B	7
8 / 1 .	0.02	0.63	0	12.84	50.19	25.5	0.48	8.71	0	0.06	0.1	0	98.54	B20 R2	8
9 / 1 .	0.11	0.63	0	12.04	50.86	25.24	0.45	8.29	0	0.12	0.1	0	97.84	B20 CHIP 1	9
10 / 1 .	0.13	0.53	0	13.83	50.67	24.09	0.48	8.89	0	0.01	0.09	0.05	98.77	B20 CHIP 2	10
11 / 1 .	0.05	0.66	0	13.51	50.69	23.16	0.33	10.34	0	0.08	0.01	0	98.83	F4.2S4 K1 CORE B	11
12 / 1 .	0.03	0.61	0	13.07	51.43	22.74	0.36	9.95	0	0.03	0.07	0	98.31	F4.2S4 K1 RIM B	12
13 / 1 .	0.04	0.7	0	13.02	51.65	22.43	0.34	9.89	0	0.07	0.09	0	98.22	F4.2S4 R1	13
14 / 1 .	0.03	0.71	0	13.78	50.22	23.01	0.33	10.42	0	0.06	0.02	0	98.57	F4.2S4 K2 CORE B	14
15 / 1 .	0.05	0.69	0	12.89	50.87	22.95	0.36	9.82	0	0.06	0.09	0	97.78	F4.2S4 K2 RIM B	15
16 / 1 .	0.05	0.73	0	13.59	50.55	22.96	0.36	10.31	0	0.04	0.05	0	98.63	F4.2S4 B/B1	16
17 / 1 .	0.04	0.66	0	13.89	50.83	22.5	0.31	10.42	0	0.02	0.06	0.01	98.76	F4.2S4 B/B2	17
18 / 1 .	0.07	0.47	0	14.06	51.49	21.75	0.3	10.35	0	0.02	0.09	0	98.6	F4.2S4 CHIP 1	18
19 / 1 .	0.03	0.52	0	13.63	50.99	22.17	0.34	10.46	0	0.04	0.1	0	98.29	F4.2S4 R2	19
20 / 1 .	0.14	0.5	0	13.5	50.54	26.24	0.41	5.8	0	0	0.36	0	97.49	F4.2S4 CHIP 2	20
21 / 1 .	0.04	0.95	0	15.93	44.72	25.04	0.36	9.98	0	0	0.07	0.02	97.11	F5S3 R1	21
22 / 1 .	0.28	0.96	0	15.87	43.69	29.39	0.35	4.3	0	0.01	0.11	0.01	94.99	F5S3 CHIP 1	22
23 / 1 .	0.05	0.64	0	13.95	49.92	21.36	0.3	11.41	0	0	0	0	97.64	F5S3 K1 CORE S	23
24 / 1 .	0.04	0.74	0	14.58	49.17	21.81	0.25	10.14	0	0.1	0.1	0	96.95	F5S3 B/B1	24
25 / 1 .	26.97	0.44	0	8.04	28.24	18.06	0.23	17.62	0	0.1	0.05	0.01	99.74	F5S3 CHIP 2	25
26 / 1 .	0	0.74	0	13.73	51.31	20.2	0.28	10.39	0	0.01	0.11	0	96.8	F5S3 R2	26
27 / 1 .	0.03	0.71	0	15.89	48.61	21.4	0.27	11.97	0	0.05	0.06	0.01	98.99	F5S3 B/B2	27
28 / 1 .	0.05	0.66	0	12.72	52.73	22.1	0.31	10.82	0	0.02	0.05	0.02	99.48	F5S3 K2 CORE M	28
29 / 1 .	0.11	0.66	0	12.77	50.55	27.56	0.36	6.08	0	0.05	0.09	0	98.23	F5S3 CHIP 3	29
30 / 1 .	0.04	0.74	0	13.61	50.39	22.94	0.37	10.32	0	0.06	0.09	0	98.56	F5S3 R3	30
31 / 1 .	0.06	0.62	0	15.63	48.89	22.04	0.33	11.79	0	0.09	0.14	0	99.59	F1S3 CHIP 1	31
32 / 1 .	0.02	0.75	0	16.71	46.29	22.21	0.28	11.73	0	0.06	0.06	0	98.12	F1S3 B/B1	32
33 / 1 .	0.02	0.75	0	16.14	47.12	22.26	0.3	11.69	0	0.1	0.09	0	98.46	F1S3 B/B2	33
34 / 1 .	0.01	0.41	0	17.66	47.12	21.15	0.29	11.69	0	0.04	0.06	0	98.43	F1S3 CHIP 2	34
35 / 1 .	0.02	0.79	0	16.77	45.5	23.18	0.35	11.34	0	0.07	0.03	0	98.05	F1S3 R1	35
36 / 1 .	0.03	0.54	0	15.45	48.42	22.51	0.31	11.37	0	0.06	0.02	0.01	98.71	F1S3 K1 CORE M	36
37 / 1 .	0.07	0.72	0	16.6	46.1	22.58	0.29	11.53	0	0.09	0.08	0.03	98.09	F1S3 K2 CORE S	37
38 / 1 .	0.03	0.69	0	16.42	45.65	23.72	0.32	10.96	0	0.06	0	0	97.86	F1S3 K3 CORE S	38
39 / 1 .	0.05	0.73	0	17.27	45.57	23.15	0.31	12.04	0	0.09	0.07	0	99.29	F1S3 R2	39
40 / 1 .	0	0.75	0	14.61	48.24	23.41	0.33	10.62	0	0.09	0.04	0	98.08	F1S3 B/B3	40

Oxide															
DataSet/Point	SiO2	TiO2	V2O3	Al2O3	Cr2O3	FeO	MnO	MgO	CoO	NiO	ZnO	CaO	Total	Comment	Point#
1 / 1 .	0.02	0.7		13.16	52.43	20.53	0.32	11.48		0.05	0.04	0	98.72	F2.3S1E R1	1
2 / 1 .	100.85	0.03		0.05	0.05	0.3	0	0.1		0	0.02	0	101.4	F2.3S1E B/B1	2
3 / 1 .	0.02	0.69		13.49	51.63	20.93	0.28	11.47		0.13	0.04	0	98.69	F2.3S1E B/B2	3
4 / 1 .	0.06	0.63		13.45	52.2	20.5	0.29	11.6		0.11	0	0	98.84	F2.3S1E K1 CORE B	4
5 / 1 .	0.15	0.65		13.24	52.02	23.8	0.44	9.69		0.05	0.04	0.02	100.11	F2.3S1E K1 RIM B	5
6 / 1 .	0.06	0.64		13.24	51.73	21.19	0.32	11.29		0.07	0.01	0	98.54	F2.3S1E R2	6
7 / 1 .	0.01	0.59		12.91	52.67	21.11	0.3	11.38		0.08	0.05	0.01	99.11	F2.3S1E K2 CORE S	7
8 / 1 .	0.04	0.65		13.15	52.2	20.97	0.3	11.21		0.06	0.12	0	98.68	F2.3S1E CHIP 1	8
9 / 1 .	0.06	0.56		12.9	52.69	21.54	0.38	10.54		0.08	0.06	0	98.8	F2.3S1E CHIP 2	9
10 / 1 .	0.08	0.63		12.94	53.34	20.45	0.33	11.24		0.02	0.01	0	99.03	F2.3S1E CHIP 3	10
11 / 1 .	0.04	0.59		13.99	51.89	21.33	0.28	11.37		0.03	0.07	0	99.59	F2.1S2B K1 CORE B	11
12 / 1 .	0.05	0.6		14.25	51.97	21.21	0.35	11.65		0.03	0.03	0	100.13	F2.1S2B K1 RIM B	12
13 / 1 .	0.05	0.56		13.66	51.92	21.14	0.35	11.15		0.06	0.08	0	98.97	F2.1S2B R1	13
14 / 1 .	0.07	0.54		13.55	52.38	20.87	0.27	11.41		0.06	0.06	0	99.22	F2.1S2B B/B1	14
15 / 1 .	0.04	0.56		13.8	52.63	20.48	0.29	10.98		0	0.04	0.01	98.83	F2.1S2B R2	15
16 / 1 .	0.06	0.56		13.89	51.76	21.26	0.33	11.24		0.03	0.08	0	99.22	F2.1S2B K2 CORE B	16
17 / 1 .	0.07	0.56		13.88	52.42	21.52	0.33	11.32		0.04	0.02	0	100.17	F2.1S2B K2 RIM B	17
18 / 1 .	0.07	0.59		13.7	51.66	22.89	0.38	9.95		0.03	0.08	0	99.36	F2.1S2B B/B2	18
19 / 1 .	0.78	0.53		13.84	50.5	23.32	0.35	10.29		0.05	0	0	99.67	F2.1S2B CHIP 1	19
20 / 1 .	0.03	0.59		13.49	51.87	22.45	0.34	9.94		0.06	0.04	0.01	98.82	F2.1S2B CHIP 2	20
21 / 1 .	0.06	0.49		13.59	51.86	22.32	0.31	9.26		0	0.09	0	97.99	F1S1 R1	21
22 / 1 .	0.04	0.54		13.52	51.27	21.93	0.38	10.53		0.04	0.03	0	98.27	F1S1 B/B1	22
23 / 1 .	0.03	0.48		13.89	51.43	21.8	0.31	10.77		0.01	0.04	0.01	98.78	F1S1 B/B2	23
24 / 1 .	0.09	0.4		13.89	51.54	22.12	0.3	10.9		0.05	0.08	0	99.37	F1S1 R2	24
25 / 1 .	0.04	0.4		13.63	51.86	20.5	0.29	11.6		0.01	0.04	0	98.38	F1S1 K1 CORE B	25
26 / 1 .	0.04	0.43		13.62	52.09	20.97	0.32	11.24		0.02	0.11	0	98.85	F1S1 K1 RIM B	26
27 / 1 .	0.07	0.38		14.25	51.03	22.3	0.35	9.83		0.04	0.05	0.01	98.31	F1S1 CHIP 1	27
28 / 1 .	4.72	0.4		12.57	48.36	22.06	0.3	10.54		0.12	0	0	99.08	F1S1 CHIP 2	28
29 / 1 .	0.01	0.56		14.08	51.84	20.87	0.27	11.05		0.02	0.08	0	98.78	F1S1 K2 CORE B	29
30 / 1 .	0.03	0.51		13.51	52.49	22.55	0.33	8.35		0	0.07	0	97.84	F1S1 K2 RIM B	30
31 / 1 .	0.08	0.55		13.36	52.22	21.67	0.3	10.81		0.1	0.07	0	99.16	F5S2 B/B1	31
32 / 1 .	0.02	0.61		13.25	52.54	21.65	0.37	10.22		0.02	0.08	0.01	98.77	F5S2 R1	32
33 / 1 .	0.02	0.48		13.51	51.79	21.15	0.27	10.81		0.01	0.09	0	98.13	F5S2 B/B2	33
34 / 1 .	0.04	0.6		13.37	52.86	20.92	0.29	10.06		0	0.04	0	98.18	F5S2 R2	34
35 / 1 .	0.05	0.56		12.34	53.47	22.13	0.36	8.56		0.03	0.05	0	97.56	F5S2 CHIP 1	35
36 / 1 .	1.04	0.37		10.76	52.57	20.44	0.38	8.86		0.06	0.07	0	94.54	F5S2 CHIP 2	36
37 / 1 .	0.03	0.54		12.68	54	21.4	0.24	8.68		0	0.04	0	97.61	F5S2 KI CORE S	37
38 / 1 .	0.07	0.55		12.68	52.82	21.69	0.29	9.24		0	0.09	0.02	97.47	F5S2 K2 CORE S	38
39 / 1 .	0.05	0.52		12.55	53.39	21.86	0.35	9.81		0.01	0.03	0	98.58	F5S2 B/B3	39

Oxide															
DataSet/Point	SiO2	TiO2	V2O3	Al2O3	Cr2O3	FeO	MnO	MgO	CoO	NiO	ZnO	CaO	Total	Comment	Point#
1 / 1 .	0.05	0.82	0	12.32	52.86	21.67	0.3	11.17	0	0.09	0.04	0.02	99.34	F2.1S1C R1	1
2 / 1 .	0.04	0.73	0	13.05	52.34	21.15	0.29	11.45	0	0.02	0.08	0	99.16	F2.1S1C R2	2
3 / 1 .	0.06	0.87	0	13.25	52.19	21.44	0.33	11.37	0	0.07	0.05	0	99.63	F2.1S1C B/B1	3
4 / 1 .	0.03	0.69	0	12.12	52.51	22.27	0.33	10.66	0	0.01	0.06	0.01	98.68	F2.1S1C R3	4
5 / 1 .	0.08	0.8	0	13.03	51.93	21.48	0.33	10.96	0	0	0.06	0	98.68	F2.1S1C K1 CORE B	5
6 / 1 .	0.06	0.76	0	13.46	52.16	21.77	0.32	11.41	0	0.02	0.04	0.01	100.01	F2.1S1C K1 RIM B	6
7 / 1 .	0.11	0.77	0	12.66	51.98	24.14	0.36	8.88	0	0.03	0.05	0	98.98	F2.1S1C K1 CHIP 1	7
8 / 1 .	0.06	0.75	0	12.7	51.61	26.26	0.44	7.86	0	0.08	0.05	0	99.8	F2.1S1C K1 CHIP 2	8
9 / 1 .	0.61	0.71	0	12.19	50.41	24.99	0.4	8.64	0	0.08	0.11	0.01	98.15	F2.1S1C K1 CHIP 3	9
10 / 1 .	0.05	0.8	0	13.06	51.61	23.46	0.39	10.02	0	0.07	0.07	0	99.53	F2.1S1C K1 CHIP 4	10
11 / 1 .	0.03	0.62	0	13.84	50.58	22.65	0.3	10.83	0	0.06	0.1	0.02	99.02	F2.1S1D R1	11
12 / 1 .	0.05	0.68	0	13.39	50.36	22.51	0.29	10.83	0	0.02	0.08	0	98.21	F2.1S1D K1 CORE B	12
13 / 1 .	0.08	0.66	0	14.26	50.33	24.39	0.31	9.53	0	0.08	0.07	0.02	99.73	F2.1S1D K1 RIM B	13
14 / 1 .	0.01	0.69	0	13.55	50.8	23.05	0.33	9.69	0	0.07	0.07	0	98.25	F2.1S1D R2	14
15 / 1 .	0.02	0.74	0	13.68	49.7	22.36	0.3	11.07	0	0.05	0.12	0.01	98.05	F2.1S1D B/B1	15
16 / 1 .	0.01	0.64	0	13.29	48.88	22.26	0.29	10.82	0	0.06	0.02	0	96.27	F2.1S1D B/B2	16
17 / 1 .	0.17	0.64	0	13.07	49.04	23.8	0.33	9.5	0	0.05	0.08	0.01	96.7	F2.1S1D CHIP 1	17
18 / 1 .	6.62	0.47	0	13.53	40.39	21.4	0.24	9.09	0	0.11	0.05	0	91.9	F2.1S1D CHIP 2	18
19 / 1 .	0.41	0.57	0	13.46	46.87	27.92	0.35	7.08	0	0.09	0.11	0.01	96.87	F2.1S1D K2 CORE B	19
20 / 1 .	0.04	0.67	0	14.04	50.37	22.48	0.3	10.81	0	0.06	0.07	0.02	98.87	F2.1S1D R3	20
21 / 1 .	0.03	0.67	0	13.63	51.47	22.12	0.33	11.28	0	0.02	0.03	0	99.58	F2.2S1A R1	21
22 / 1 .	0.03	0.6	0	13.86	51.68	21.63	0.32	11.2	0	0.06	0	0	99.38	F2.2S1A B/B1	22
23 / 1 .	0.03	0.54	0	13.58	51.72	21.65	0.33	11.3	0	0.07	0.09	0	99.3	F2.2S1A B/B2	23
24 / 1 .	0.01	0.58	0	14.07	51.9	21.16	0.31	11.53	0	0.07	0.12	0	99.75	F2.2S1A K1 CORE B	24
25 / 1 .	0.05	0.59	0	13.37	52.44	21.91	0.32	10.33	0	0	0.07	0	99.09	F2.2S1A R2	25
26 / 1 .	0.03	0.63	0	13.53	51.59	21.46	0.26	11.53	0	0.09	0.06	0	99.17	F2.2S1A B/B3	26
27 / 1 .	0.14	0.6	0	12.54	52.77	25.42	0.49	6.91	0	0.06	0.07	0.01	99.01	F2.2S1A CHIP 1	27
28 / 1 .	1.79	0.53	0	11.94	50.9	23.35	0.4	9.77	0	0.02	0.08	0	98.78	F2.2S1A CHIP 2	28
29 / 1 .	0.09	0.62	0	13.39	51.89	21.43	0.29	11.18	0	0.08	0.05	0	99.02	F2.2S1A K2 CORE B	29
30 / 1 .	0.06	0.72	0	13.75	51.29	21.72	0.3	11.54	0	0.01	0.07	0	99.48	F2.2S1A B/B4	30
31 / 1 .	0.1	0.6	0	12.97	52.7	21.89	0.29	11.24	0	0.03	0.03	0	99.84	F2.3S1C B/B1	31
32 / 1 .	0.04	0.59	0	13.25	52.22	21.67	0.3	11.07	0	0.04	0.03	0	99.22	F2.3S1C B/B2	32
33 / 1 .	0.07	0.53	0	13.16	52.6	20.83	0.28	11.42	0	0.07	0.02	0	98.99	F2.3S1C K1 CORE B	33
34 / 1 .	0.08	0.56	0	13.4	52.36	21.56	0.35	11.32	0	0.07	0.03	0	99.74	F2.3S1C K1 RIM B	34
35 / 1 .	0.05	0.55	0	13.06	52.37	21.23	0.31	11.41	0	0.08	0.05	0	99.1	F2.3S1C B/B3	35
36 / 1 .	0.01	0.64	0	12.39	53.23	21.58	0.32	10.97	0	0.04	0.08	0	99.25	F2.3S1C R1	36
37 / 1 .	0.05	0.62	0	12.87	52.51	21.42	0.29	11.19	0	0.02	0.04	0	99.01	F2.3S1C R2	37
38 / 1 .	0.18	0.55	0	11.93	51.82	27	0.43	6.64	0	0.01	0.06	0.02	98.64	F2.3S1C CHIP 1	38
39 / 1 .	3.51	0.5	0	11.42	47.89	23.79	0.41	10.01	0	0.08	0.06	0	97.67	F2.3S1C CHIP 2	39
40 / 1 .	0.04	0.68	0	13.11	51.63	22.18	0.29	11.26	0	0.03	0.05	0.02	99.28	F2.3S1C K2 CORE B	40
41 / 1 .	0.05	0.63	0	11.84	52.91	22.14	0.31	10.24	0	0.02	0	0	98.14	F2.3S1C K2 RIM B	41

Oxide															
DataSet/Point	SiO2	TiO2	V2O3	Al2O3	Cr2O3	FeO	MnO	MgO	CoO	NiO	ZnO	CaO	Total	Comment	Point#
1 / 1 .	0.05	0.72	0	12.94	51.44	21.49	0.29	10.62	0	0.06	0.02	0.03	97.65	F2.1S2A B/B1	1
2 / 1 .	0.01	0.75	0	12.76	53.05	20.87	0.34	11.05	0	0.08	0.01	0	98.93	F2.1S2A K1 CORE S	2
3 / 1 .	0.04	0.75	0	12.62	53.06	21.54	0.32	10.85	0	0.1	0.04	0.01	99.31	F2.1S2A K1 RIM S	3
4 / 1 .	0.04	0.8	0	12.69	52.25	21.6	0.3	10.18	0	0.08	0.05	0	98	F2.1S2A B/B2	4
5 / 1 .	0.09	0.72	0	13.18	52.36	20.6	0.33	11.21	0	0.1	0.03	0.03	98.63	F2.1S2A R1	5
6 / 1 .	0.05	0.61	0	12.55	52.37	21.23	0.28	10.76	0	0.06	0.05	0	97.96	F2.1S2A R2	6
7 / 1 .	0.06	0.67	0	12.55	52.95	22.15	0.3	10.15	0	0.06	0.02	0	98.91	F2.1S2 K2 CORE S	7
8 / 1 .	0.04	0.77	0	13.53	52.6	21.84	0.31	6.93	0	0.08	0.11	0.03	96.24	F2.1S2 K2 CHIP 1	8
9 / 1 .	0.03	0.79	0	12.7	52.6	23.55	0.4	7.67	0	0.05	0.07	0.02	97.87	F2.1S2 K2 CHIP 2	9
10 / 1 .	0.01	0.72	0	13.05	52.96	21.46	0.27	10.91	0	0.08	0.03	0	99.48	F2.1S2 K2 R3	10
11 / 1 .	0.02	0.58	0	13.39	51.74	20.85	0.27	11.74	0	0.03	0.08	0	98.7	F2.3 S1D B/B1	11
12 / 1 .	0	0.63	0	13.24	52.3	20.58	0.29	11.28	0	0.04	0.05	0.02	98.43	F2.3 S1D R1	12
13 / 1 .	0.05	0.6	0	12.99	52.15	20.97	0.32	11.24	0	0.06	0.05	0.03	98.47	F2.3 S1D B/B2	13
14 / 1 .	0.02	0.57	0	13.04	53.18	20.24	0.29	11.28	0	0.04	0.04	0	98.69	F2.3 S1D R2	14
15 / 1 .	0.24	0.53	0	12.95	52.31	21.11	0.27	10.27	0	0.02	0.07	0.02	97.79	F2.3 S1D CHIP1	15
16 / 1 .	0.08	0.65	0	12.76	51.97	24.95	0.46	7.64	0	0.01	0.03	0.01	98.55	F2.3 S1D CHIP2	16
17 / 1 .	0.04	0.65	0	13.03	51.89	20.7	0.33	11.24	0	0.04	0.07	0	97.99	F2.3 S1D K1 CORE B	17
18 / 1 .	0.04	0.67	0	12.66	52.95	20.71	0.29	10.84	0	0.11	0.04	0	98.31	F2.3 S1D K1 RIM B	18
19 / 1 .	0.08	0.67	0	12.79	52.52	21.4	0.29	11.28	0	0.04	0.03	0.02	99.1	F2.3 S1D K2 CORE B	19
20 / 1 .	0.04	0.58	0	11.8	52.48	22.19	0.31	9.53	0	0.02	0.09	0	97.04	F2.3 S1D K2 RIM B	20
21 / 1 .	0.03	0.66	0	12.96	52.64	20.92	0.31	11.32	0	0.04	0.03	0	98.92	F2.3S1B B/B1	21
22 / 1 .	0.01	0.62	0	13.21	51.86	20.96	0.28	11.3	0	0.03	0.03	0.01	98.31	F2.3S1B B/B2	22
23 / 1 .	0.19	0.61	0	12.29	53.11	20.87	0.33	10.76	0	0.01	0.1	0	98.27	F2.3S1B K1 CORE S	23
24 / 1 .	0.05	0.62	0	12.28	53.52	21.25	0.33	10.72	0	0.05	0.05	0	98.86	F2.3S1B K1 RIM S	24
25 / 1 .	0.05	0.65	0	13.12	52.12	21.09	0.31	11.25	0	0.05	0.04	0	98.69	F2.3S1B R1	25
26 / 1 .	0	0.63	0	12.49	52.83	21.08	0.32	11.13	0	0.04	0.05	0	98.56	F2.3S1B R2	26
27 / 1 .	0.07	0.46	0	12.64	51.41	25	0.45	7.69	0	0.04	0.05	0	97.81	F2.3S1B CHIP 1	27
28 / 1 .	1.33	0.41	0	12.55	49.53	22.63	0.44	11.04	0	0.05	0.07	0.01	98.07	F2.3S1B CHIP 2	28
29 / 1 .	0.03	0.59	0	12.83	51.97	21.08	0.28	11.28	0	0.1	0	0.01	98.16	F2.3S1B K2 CORE B	29
30 / 1 .	0.02	0.6	0	12.21	52.82	21.08	0.32	10.79	0	0.05	0.01	0	97.91	F2.3S1B K2 RIM B	30
31 / 1 .	0.04	0.5	0	14.12	50.77	22.27	0.33	10.65	0	0.03	0.09	0	98.81	F4.2S6 B/B1	31
32 / 1 .	0.06	0.58	0	13.56	51.27	22.7	0.31	10.46	0	0.05	0.05	0	99.04	F4.2S6 B/B2	32
33 / 1 .	0.14	0.62	0	13.09	52.13	22.38	0.33	10.34	0	0.03	0.03	0	99.08	F4.2S6 R1	33
34 / 1 .	0.04	0.59	0	13.4	51.08	22.84	0.32	10.36	0	0.03	0.04	0	98.71	F4.2S6 R2	34
35 / 1 .	0.11	0.61	0	12.95	51.47	24.25	0.4	8.33	0	0.06	0.1	0	98.27	F4.2S6 CHIP 1	35
36 / 1 .	0.06	0.5	0	13.46	51.38	22.94	0.36	9.11	0	0.03	0.1	0	97.93	F4.2S6 CHIP 2	36
37 / 1 .	0.03	0.61	0	13.97	50.44	22.74	0.33	10.63	0	0.04	0.03	0	98.82	F4.2S6 K1 CORE B	37
38 / 1 .	0	0.57	0	13.62	51.59	22.28	0.34	10.66	0	0.16	0.03	0	99.25	F4.2S6 K1 RIM B	38
39 / 1 .	0.06	0.74	0	12.54	51.62	23.11	0.28	10.01	0	0.02	0.07	0	98.46	F4.2S6 K2 CORE B	39
40 / 1 .	0.06	0.7	0	12.58	51.71	23.04	0.35	10.07	0	0.01	0.09	0	98.6	F4.2S6 K2 RIM B	40

Oxide															
DataSet/Point	SiO2	TiO2	V2O3	Al2O3	Cr2O3	FeO	MnO	MgO	CoO	NiO	ZnO	CaO	Total	Comment	Point#
1 / 1 .	0.05	0.63	0	13.98	50.67	21.79	0.26	11.01	0	0.05	0.07	0.02	98.51	F2.2S1B R1	1
2 / 1 .	0.02	0.7	0	13.97	50.68	21.85	0.31	10.89	0	0.02	0.08	0	98.51	F2.2S1 K1 CORE B	2
3 / 1 .	0.01	0.62	0	13.38	50.88	22.04	0.39	10.37	0	0.03	0.03	0.01	97.76	F2.2S1 K1 RIM B	3
4 / 1 .	0.02	0.55	0	13.99	51.14	21.31	0.27	11.27	0	0.06	0.06	0	98.67	F2.2S1 B/B 1	4
5 / 1 .	0	0.57	0	13.93	51.54	21.31	0.3	11.43	0	0.11	0.03	0	99.22	F2.2S1 R2	5
6 / 1 .	0.03	0.54	0	14.05	51.7	21.45	0.35	11.15	0	0.12	0.06	0	99.45	F2.2S1 B/B 2	6
7 / 1 .	0.02	0.6	0	14	50.46	24.15	0.32	9.21	0	0.04	0	0	98.8	F2.2S1 CHIP 1	7
8 / 1 .	0.05	0.63	0	14.27	50.69	21.82	0.24	11.35	0	0.07	0	0	99.12	F2.2S1 K2 CORE B	8
9 / 1 .	0.06	0.58	0	14.96	50.23	21.97	0.32	10.81	0	0.04	0.08	0	99.05	F2.2S1 K2 RIM B	9
10 / 1 .	0.03	0.55	0	13.95	50.49	23.95	0.34	8.91	0	0.03	0.01	0	98.27	F2.2S1 CHIP 2	10
11 / 1 .	0.05	0.45	0	12.4	53.32	21.66	0.29	10.63	0	0.04	0.1	0	98.96	F2.3S5A R1	11
12 / 1 .	0.02	0.63	0	12.8	52.17	21.74	0.34	10.6	0	0.04	0.07	0	98.39	F2.3S5A B/B 1	12
13 / 1 .	0.14	0.6	0	12.87	51.57	24.96	0.39	8.22	0	0.06	0.1	0.01	98.91	F2.3S5A CHIP 1	13
14 / 1 .	0.01	0.63	0	11.81	53.6	22.3	0.4	10.22	0	0.03	0.04	0	99.05	F2.3S5A R2	14
15 / 1 .	3.46	0.48	0	11.63	46.11	25.19	0.37	10.59	0	0.12	0.02	0	97.97	F2.3S5A CHIP 2	15
16 / 1 .	0.08	0.61	0	12.73	52.05	21.69	0.3	10.95	0	0.02	0.07	0	98.5	F2.3S5A B/B 2	16
17 / 1 .	0.03	0.5	0	12.82	52.58	21.29	0.32	10.92	0	0.09	0.04	0	98.59	F2.3S5A K1 CORE B	17
18 / 1 .	0.04	0.45	0	12.5	52.84	21.49	0.38	10.58	0	0.06	0.01	0	98.35	F2.3S5A K1 RIM B	18
19 / 1 .	0.03	0.59	0	12.2	52.18	22.62	0.44	9.25	0	0	0.02	0	97.34	F2.3S5A K2 RIM M	19
20 / 1 .	0	0.59	0	12.94	52.34	21.14	0.34	10.71	0	0.05	0.02	0	98.12	F2.3S5A K2 CORE M	20
21 / 1 .	0.05	0.55	0	12.94	52.91	23.44	0.44	7.6	0	0.02	0.03	0	97.98	F4.2S2 CHIP 1	21
22 / 1 .	0.05	0.57	0	13.02	52.78	22.12	0.43	9	0	0.01	0.03	0	98.02	F4.2S2 CHIP 2	22
23 / 1 .	0.05	0.6	0	12.89	52.98	21.06	0.37	9.67	0	0.02	0.07	0.02	97.73	F4.2S2 B/B1	23
24 / 1 .	0.02	0.54	0	13.05	53.36	21.07	0.31	8.94	0	0.02	0.11	0	97.43	F4.2S2 B/B2	24
25 / 1 .	0.07	0.62	0	12.82	52.57	21.64	0.35	10.2	0	0.03	0.04	0	98.34	F4.2S2 K1 CORE B	25
26 / 1 .	0.04	0.51	0	13.27	52.74	22.12	0.4	9.69	0	0.03	0.02	0	98.83	F4.2S2 K1 RIM B	26
27 / 1 .	0.02	0.58	0	13.08	53.07	21	0.32	9.59	0	0.04	0.07	0	97.79	F4.2S2 K2 RIM B	27
28 / 1 .	0	0.54	0	13.47	52.66	21.26	0.32	10.28	0	0.03	0.07	0	98.64	F4.2S2 K2 CORE B	28
29 / 1 .	0.05	0.58	0	13.19	52.52	21.26	0.36	10.02	0	0	0.08	0	98.07	F4.2S2 R1	29
30 / 1 .	0.03	0.57	0	12.67	52.99	21.42	0.38	8.86	0	0.04	0.08	0.02	97.07	F4.2S2 R2	30
31 / 1 .	0.04	0.66	0	13.77	51.62	20.91	0.3	11.44	0	0.06	0.01	0	98.8	F2.3S1A K1 CORE B	31
32 / 1 .	0.05	0.57	0	12.86	52.77	21.97	0.37	9.96	0	0.1	0.06	0.02	98.72	F2.3S1A K1 RIM B	32
33 / 1 .	0	0.64	0	13.79	51.36	21.06	0.33	11.21	0	0.06	0.05	0	98.51	F2.3S1A B/B1	33
34 / 1 .	0.11	0.66	0	13.85	52.04	20.28	0.32	11.63	0	0.07	0.08	0.01	99.04	F2.3S1A K2 CORE B	34
35 / 1 .	0.11	0.59	0	12.93	51.55	22.49	0.43	9.35	0	0.08	0.07	0	97.59	F2.3S1A K2 RIM B	35
36 / 1 .	0.03	0.61	0	13.5	50.57	23.14	0.41	9.21	0	0.11	0.04	0	97.62	F2.3S1A K2 B/B 2	36
37 / 1 .	0.04	0.62	0	13.79	52.02	20.87	0.31	10.93	0	0.04	0.12	0	98.74	F2.3S1A R1	37
38 / 1 .	0.05	0.61	0	13.94	51.78	20.28	0.28	11.8	0	0.04	0.01	0	98.8	F2.3S1A R2	38
39 / 1 .	2.47	0.44	0	12.47	45.82	25.97	0.5	8.15	0	0.06	0.09	2.26	98.22	F2.3S1A CHIP 1	39
40 / 1 .	0.01	0.55	0	13.19	52.1	22.99	0.46	9.05	0	0.07	0.1	0	98.51	F2.3S1A CHIP 2	40

Oxide															
DataSet/Point	SiO2	TiO2	V2O5	Al2O3	Cr2O3	FeO	MnO	MgO	CoO	NiO	ZnO	CaO	Total	Comment	Point#
1 / 1 .	0.05	0.72	0	13.91	47.62	26.16	0.4	8.86	0	0.1	0.05	0	97.87	B29 R1	1
2 / 1 .	0.06	0.72	0	13.55	47.41	27.18	0.45	8.33	0	0.1	0.03	0.03	97.85	B29 B/B 1	2
3 / 1 .	0.03	0.68	0	13.58	47.65	26.86	0.48	8.54	0	0.08	0.06	0	97.94	B29 K1 CORE S	3
4 / 1 .	0.04	0.85	0	13.74	47.84	26.54	0.39	8.84	0	0.09	0	0	98.32	B29 R 2	4
5 / 1 .	0.04	0.84	0	14.35	47.75	25.3	0.44	9.61	0	0.13	0.03	0	98.48	B29 K2 CORE M	5
6 / 1 .	1.43	0.65	0	13.51	45.02	27.28	0.46	8.53	0	0.05	0.12	0.01	97.06	B29 K2 RIM M	6
7 / 1 .	0.06	0.84	0	13.59	47.93	26.44	0.42	8.87	0	0.12	0.09	0	98.36	B29 B/B 2	7
8 / 1 .	0.11	0.67	0	13.91	47.64	27.26	0.47	8.47	0	0.13	0.08	0	98.73	B29 CHIP 1	8
9 / 1 .	0.09	0.75	0	14.43	46.94	27.45	0.47	8.24	0	0.1	0.01	0	98.5	B29 CHIP 2	9
10 / 1 .	0.58	0.6	0	14.68	47.79	27.08	0.55	7.69	0	0.11	0.1	0	99.18	B29 CHIP 3	10
11 / 1 .	0.02	0.54	0	14.94	50.65	21.1	0.27	11.61	0	0.04	0.07	0	99.23	B1 B/B 1	11
12 / 1 .	0.06	0.58	0	15.2	50.49	21.04	0.3	9.72	0	0.04	0.11	0	97.54	B1 CHIP 1	12
13 / 1 .	0.04	0.7	0	14.39	51.09	21.17	0.27	9.69	0	0.01	0.06	0	97.42	B1 B/B 2	13
14 / 1 .	0.47	0.63	0	15.01	50.6	22.76	0.43	6.7	0	0.03	0.12	0.02	96.77	B1 CHIP 2	14
15 / 1 .	0.04	0.58	0	14.71	50.99	21.69	0.29	9.24	0	0.06	0	0	97.62	B1 R1	15
16 / 1 .	0.02	0.5	0	14.75	51.68	22.06	0.36	8.13	0	0.07	0.07	0	97.65	B1 R2	16
17 / 1 .	0.04	0.47	0	14.6	51.53	21.06	0.27	10.1	0	0.02	0.08	0.01	98.18	B1 K1 CORE S	17
18 / 1 .	0.05	0.58	0	14.67	50.31	21.53	0.3	11.02	0	0	0.1	0	98.54	B1 K2 CORE B	18
19 / 1 .	0.05	0.61	0	14.72	50.37	21.72	0.33	11.21	0	0.01	0.06	0.02	99.1	B1 K2 RIM B	19
20 / 1 .	0.03	0.6	0	14.83	50.4	21.57	0.27	11.22	0	0.09	0.06	0	99.07	B1 B/B 3	20
21 / 1 .	0.02	0.56	0	13.68	51.89	21.46	0.32	10.73	0	0.02	0.1	0	98.77	F4.2S5 K1 CORE B	21
22 / 1 .	0.03	0.51	0	13.84	52.21	21.16	0.34	10.81	0	0.04	0.05	0	98.99	F4.2S5 K1 RIM B	22
23 / 1 .	0.05	0.57	0	13.49	52.12	21.44	0.29	10.62	0	0.03	0.04	0	98.65	F4.2S5 B/B 1	23
24 / 1 .	0.04	0.42	0	13.94	52.16	21.02	0.3	10.97	0	0.05	0.06	0	98.95	F4.2S5 B/B 2	24
25 / 1 .	0.07	0.53	0	13.48	52.19	21.31	0.27	10.6	0	0.02	0.1	0	98.56	F4.2S5 K1 CORE S	25
26 / 1 .	4.46	0.42	0	13.68	44.65	20.84	0.33	13.36	0	0.04	0.04	0.01	97.82	F4.2S5 K1 RIM S	26
27 / 1 .	0.91	0.46	0	13.08	49.73	22.77	0.32	9.34	0	0.03	0.02	0.01	96.69	F4.2S5 CHIP 1	27
28 / 1 .	0.05	0.55	0	13.91	52.08	21.3	0.36	10.66	0	0.04	0.04	0	98.98	F4.2S5 R 1	28
29 / 1 .	0.04	0.5	0	13.98	52.07	21.19	0.31	10.7	0	0.01	0.09	0	98.9	F4.2S5 R 2	29
30 / 1 .	0.1	0.46	0	13.69	51.59	23.37	0.36	9.08	0	0	0.07	0.01	98.72	F4.2S5 CHIP 2	30
31 / 1 .	0.02	0.47	0	14.02	51.75	21	0.34	11	0	0.03	0.06	0	98.68	F2.4S1 R1	31
32 / 1 .	0.04	0.51	0	14.33	51.92	20.82	0.34	11.23	0	0.05	0.07	0	99.3	F2.4S1 K1 CORE B	32
33 / 1 .	0.07	0.51	0	13.9	51.8	20.73	0.33	10.82	0	0.05	0.08	0	98.3	F2.4S1 K1 RIM B	33
34 / 1 .	0.04	0.61	0	13.35	51.6	21.35	0.35	10.61	0	0	0.08	0	98	F2.4S1 R 2	34
35 / 1 .	0.07	0.63	0	13.81	51.72	21.27	0.33	11.01	0	0.01	0.05	0	98.92	F2.4S1 B/B 1	35
36 / 1 .	0	0.58	0	14.08	51.42	20.79	0.36	11.1	0	0	0.07	0	98.4	F2.4S1 B/B 2	36
37 / 1 .	0.06	0.49	0	13.44	52	21.66	0.38	9.91	0	0.1	0.06	0	98.11	F2.4S1 CHIP 1	37
38 / 1 .	0.03	0.57		12.95	52.41	21.39	0.41	10.36	0	0.02	0.04	0.09	98.28	F2.4S1 CHIP 2	38

Oxide															
DataSet/Point	SiO2	TiO2	V2O3	Al2O3	Cr2O3	FeO	MnO	MgO	CoO	NiO	ZnO	CaO	Total	Comment	Point#
1 / 1 .	0.03	0.6	0	14.3	50.35	23.18	0.33	10.56	0	0.05	0.07	0	99.45	B8 K1 CORE B	1
2 / 1 .	0	0.55	0	13.89	50.74	22.82	0.31	10.28	0	0.04	0.08	0.01	98.72	B8 K1 RIM B	2
3 / 1 .	0.05	0.59	0	13.57	51.22	22.66	0.3	9.72	0	0.04	0.05	0	98.19	B8 R1	3
4 / 1 .	0.06	0.56	0	14.25	49.88	22.95	0.28	10.32	0	0.07	0.07	0	98.44	B8 B/B 1	4
5 / 1 .	0.01	0.52	0	13.59	52.26	22.98	0.38	7.1	0	0.04	0.08	0	96.97	B8 R 2	5
6 / 1 .	0.03	0.48	0	13.63	51.49	22.8	0.33	10.48	0	0.05	0.11	0.01	99.41	B8 B/B 2	6
7 / 1 .	0.04	0.51	0	14.06	51.16	23.17	0.37	8.48	0	0	0.06	0	97.86	B8 CHIP 1	7
8 / 1 .	0	0.53	0	14.45	51.66	22.44	0.34	9.28	0	0.07	0.09	0.01	98.87	B8 CHIP 2	8
9 / 1 .	0.03	0.48	0	14.21	50.27	22.82	0.31	10.58	0	0.06	0.07	0	98.85	B8 K2 CORE B	9
10 / 1 .	0.05	0.48	0	13.92	51.49	22.32	0.32	10	0	0	0.1	0.01	98.69	B8 K2 RIM B	10
11 / 1 .	0	0.81	0	13.9	49.39	24.14	0.43	9.5	0	0.09	0.13	0.01	98.42	B25 K1 CORE B	11
12 / 1 .	0.09	0.85	0	14.09	49.91	24.51	0.46	8.99	0	0.08	0.13	0.02	99.13	B25 K1 RIM B	12
13 / 1 .	0.04	0.78	0	13.9	49.89	24.21	0.44	9.28	0	0.13	0.08	0.01	98.76	B25 K2 CORE	13
14 / 1 .	0.08	0.77	0	13.66	49.72	24.02	0.44	9.39	0	0.14	0.11	0	98.34	B25 B/B 1	14
15 / 1 .	0.04	0.87	0	13.73	49.56	24.33	0.46	9.26	0	0.04	0.12	0.02	98.44	B25 R 1	15
16 / 1 .	0.09	0.84	0	13.56	50.49	24.35	0.45	9.44	0	0.12	0.13	0.03	99.5	B25 B/B2	16
17 / 1 .	0.01	0.85	0	13.34	50.96	24.44	0.41	9.14	0	0.07	0.15	0.01	99.39	B25 CHIP 1	17
18 / 1 .	0.82	0.8	0	14.27	49.3	24.09	0.43	9.22	0	0.09	0.1	0	99.12	B25 CHIP 2	18
19 / 1 .	0.06	0.81	0	13.59	49.36	26.98	0.56	7.16	0	0.14	0.17	0	98.82	B25 R 2	19
20 / 1 .	0.06	0.55	0	14.33	50.73	22.02	0.29	10.97	0	0.06	0.01	0	99.02	B2 B/B 1	20
21 / 1 .	0.02	0.58	0	14.61	50.7	21.85	0.32	11.22	0	0.05	0.05	0.01	99.42	B2 CHIP 1	21
22 / 1 .	0.04	0.56	0	14.01	50.59	21.92	0.3	10.96	0	0.07	0.03	0	98.46	B2 B/B 2	22
23 / 1 .	0.02	0.59	0	14.22	51.22	22.02	0.35	9.71	0	0.04	0.02	0	98.2	B2 CHIP 2	23
24 / 1 .	0.06	0.62	0	14.4	50.52	21.94	0.3	10.53	0	0.03	0.03	0	98.44	B2 R 1	24
25 / 1 .	0.02	0.65	0	14.06	50.86	22.17	0.32	10.62	0	0.03	0.11	0	98.85	B2 K1 CORE S	25
26 / 1 .	0.06	0.66	0	14.16	50.32	22.2	0.29	10.86	0	0.01	0.01	0.01	98.58	B2 K2 CORE B	26
27 / 1 .	0.03	0.63	0	14.1	50.52	22.13	0.28	10.93	0	0.01	0.04	0	98.66	B2 K2 RIM B	27
28 / 1 .	0.01	0.61	0	13.96	51.05	22	0.32	10.81	0	0.03	0.07	0	98.86	B2 R 2	28
29 / 1 .	0.01	0.54	0	13.8	50.83	22.02	0.31	10.42	0	0.02	0.01	0	97.97	B2 B/B3 RIM	29
30 / 1 .	0.06	0.81	0	13.24	50.07	25.54	0.44	9.04	0	0.08	0.08	0	99.37	B16 K1 CORE S	30
31 / 1 .	0.04	0.81	0	13.47	50.27	25.98	0.48	8.6	0	0.06	0.16	0	99.89	B16 K2 RIM B	31
32 / 1 .	0.09	0.51	0	13.84	49.67	25.92	0.54	7.77	0	0	0.1	0.02	98.45	B16 R 1	32
33 / 1 .	0.04	0.87	0	13.25	49.36	26.41	0.47	8.1	0	0.1	0.09	0	98.69	B16 R 2	33
34 / 1 .	0.06	0.88	0	12.48	50.63	24.77	0.43	9.16	0	0.09	0.1	0	98.61	B16 B/B 1	34
35 / 1 .	0.04	0.9	0	12.59	50.12	25.2	0.46	9.08	0	0.09	0.03	0	98.51	B16 B/B 2	35
36 / 1 .	0.04	0.84	0	12.67	50.49	26.18	0.41	7.68	0	0	0.08	0	98.39	B16 CHIP 1	36
37 / 1 .	0.02	0.73	0	13.05	50.1	25.77	0.42	7.82	0	0.08	0.07	0	98.06	B16 CHIP 2	37

Oxide															
DataSet/Point	SiO2	TiO2	V2O3	Al2O3	Cr2O3	FeO	MnO	MgO	CoO	NiO	ZnO	CaO	Total	Comment	Point#
1 / 1 .	0.07	0.43	0	13.31	50.75	24.11	0.46	9.64	0	0.08	0.06	0.02	98.91	B28 K core	1
2 / 1 .	0.07	0.41	0	13.81	50.88	24.02	0.42	10.1	0	0.16	0.12	0	99.99	B28 K rim	2
3 / 1 .	0.05	0.67	0	13.96	47.72	26.7	0.56	7.89	0	0.1	0.24	0.01	97.88	B28 R1	3
4 / 1 .	0.03	0.71	0	14.36	48.35	26.78	0.52	8.3	0	0.13	0.2	0	99.39	B28 B/B1	4
5 / 1 .	2.31	0.39	0	12.93	44.61	26.91	0.52	7.62	0	0.23	0.17	0	95.7	B28 CHIP	5
6 / 1 .	1.93	0.59	0	13.8	47.04	26.22	0.46	8.37	0	0.09	0.11	0.06	98.67	B28 R2	6
7 / 1 .	0.06	0.63	0	14.62	47.91	26.96	0.5	8.51	0	0.1	0.21	0	99.49	B28 K2 CORE	7
8 / 1 .	0.06	0.66	0	14.77	47.53	26.98	0.49	8.32	0	0.08	0.1	0.02	99.01	B28 K2 RIM	8
9 / 1 .	0.05	0.57	0	14.84	47.98	26.65	0.45	8.4	0	0.08	0.2	0.02	99.24	B28 CHIP 2	9
10 / 1 .	0.08	0.64	0	14.11	48.11	26.63	0.52	8.43	0	0.07	0.15	0.03	98.77	B28 B/B2	10
11 / 1 .	9.94	0.51	0	12.72	39.7	23.6	0.52	13.35	0	0.09	0.15	0	100.59	B27 CHIP1	11
12 / 1 .	0.07	0.66	0	15.39	47.09	24.27	0.42	11.15	0	0.13	0.06	0	99.23	B27 K1 CORE S	12
13 / 1 .	0.08	0.67	0	14.19	48.17	27.24	0.53	8.02	0	0.11	0.08	0	99.09	B27 B/B1	13
14 / 1 .	0.06	0.78	0	13.75	48.01	27.18	0.51	8.18	0	0.1	0.09	0	98.65	B27 B/B2	14
15 / 1 .	0.02	0.81	0	13.87	47.71	28.01	0.58	7.32	0	0.11	0.14	0	98.57	B27 R1	15
16 / 1 .	0.04	0.75	0	14	48.12	26.57	0.53	8.28	0	0.11	0.08	0.04	98.53	B27 R2	16
17 / 1 .	0.06	0.59	0	14.46	49.41	24.22	0.43	9.34	0	0.06	0.08	0	98.65	B17 K1 CORE B	17
18 / 1 .	0.06	0.59	0	14.54	49.64	24.34	0.51	9.62	0	0.11	0.1	0.01	99.52	B17 R1	18
19 / 1 .	0.06	0.59	0	13.78	49.68	24.46	0.43	9.11	0	0.09	0.08	0	98.29	B17 B/B1	19
20 / 1 .	0.08	0.58	0	14.2	50.05	22.16	0.43	11.01	0	0.08	0.06	0	98.65	B17 R2	20
21 / 1 .	0.03	0.58	0	14.14	50.5	23.11	0.45	9.8	0	0.04	0.04	0.01	98.7	B17 CHIP 1	21
22 / 1 .	0.06	0.61	0	14.45	49.31	25.12	0.44	9.02	0	0.07	0.1	0	99.19	B17 K2 CORE B	22
23 / 1 .	0.08	0.65	0	14.07	49.45	25.22	0.52	8.75	0	0.07	0.03	0	98.85	B17 B/B2	23
24 / 1 .	0.1	0.53	0	14.25	50.53	22.32	0.44	11.22	0	0.06	0.09	0	99.54	B17 CHIP 2	24
25 / 1 .	0.09	0.83	0	13.49	50.82	23.39	0.5	9.06	0	0.1	0.05	0.01	98.35	B24 R1 S	25
26 / 1 .	1.86	0.9	0	13.4	49.23	22.92	0.51	10.15	0	0.09	0.1	0	99.15	B24 CHIP 3	26
27 / 1 .	0.06	0.79	0	13.07	51.85	23.14	0.44	8.8	0	0.09	0.07	0.01	98.31	B24 K1 RIM	27
28 / 1 .	0.01	0.92	0	14.68	50.41	21.77	0.42	10.3	0	0.05	0.1	0	98.66	B24 K2 CORE	28
29 / 1 .	0	0.98	0	14.39	50.39	22.14	0.41	9.96	0	0.09	0.12	0	98.48	B24 K2 RIM B	29
30 / 1 .	0.03	0.97	0	14.48	50.65	21.98	0.38	10.26	0	0.07	0.04	0	98.87	B24 B/B1	30
31 / 1 .	0.06	0.79	0	14.69	51.64	20.72	0.36	11.4	0	0.07	0.05	0	99.76	B24 B/B2	31
32 / 1 .	0.06	0.96	0	13.64	51.14	23.11	0.51	8.99	0	0.06	0.05	0	98.51	B24 R2	32
33 / 1 .	6.02	0.51	0	12.39	44.56	22.5	0.61	12.99	0	0.11	0.1	0.02	99.81	B24 CHIP 1	33
34 / 1 .	2.02	0.86	0	13.19	49.45	23.11	0.48	9.84	0	0.15	0.04	0	99.13	B24 CHIP 2	34

Appendix 2- Point count results

		Counts							Counts				
Sample	Lens	CC	FC	CF	RC	Ch	Cr total	Cr%	SiO	FeO (H2O)	Si+Fe total	% Matrix	Total
F2.1S1C	MC1	12	78	148	24	1441	1703	85.15	154	143	297	14.85	2000
F2.1S2A	MC1	37	61	401	44	1289	1832	91.46	171	0	171	8.54	2003
	Total %	1.39	3.93	15.53	1.92	77.23	3535	88.31	8.12	3.57	11.69		4003
F1.2S1	MC2	52	534	779	19	354	1738	86.90	156	106	262	13.10	2000
	Total %	2.99	30.72	44.82	1.09	20.37	1738	86.90	7.80	5.30	13.10		2000
F2.1S1D	MC3	190	919	272	188	259	1828	91.40	164	8	172	8.60	2000
F2.1S2B	MC3	123	595	515	68	592	1893	94.70	104	2	106	5.30	1999
F2.2S1A	MC3	233	298	670	44	563	1808	90.40	189	3	192	9.60	2000
	Total %	8.41	40.69	21.15	6.88	22.87	3721	93.05	6.70	0.25	6.95		3999
F1.5S2	MC4	43	355	795	38	212	1443	72.15	536	21	557	27.85	2000
F4.2S2	MC4	99	47	923	65	329	1463	73.15	535	2	537	26.85	2000
	Total %	4.89	13.83	59.12	3.54	18.62	2906	72.65	26.78	0.58	27.35		4000
F4.5S4	MC5	296	221	745	134	153	1549	77.45	440	11	451	22.55	2000
	Total %	19.11	14.27	48.10	8.65	9.88	1549	77.45	22.00	0.55	22.55		2000
B1	MCHR	90	703	667	47	216	1723	86.15	265	12	277	13.85	2000
B4	MCHR	121	1033	416	70	182	1822	91.1	177	1	178	8.9	2000
B9	MCHR	107	853	483	128	114	1685	84.25	315	0	315	15.75	2000
	Total %	6.08	49.50	29.94	4.68	9.79	5230	87.17	12.62	0.22	12.83		6000
B17	PCR1	711	41	726	58	33	1569	78.45	431	0	431	21.55	2000
B20	PCR1	756	76	538	166	100	1636	81.80	357	7	364	18.20	2000
B23	PCR1	818	82	443	133	77	1553	77.65	443	4	447	22.35	2000
	Total %	48.02	4.18	35.88	7.50	4.41	4758	79.30	20.52	0.18	20.70		6000
B29	PCR2	525	21	730	120	60	1456	72.80	540	4	544	27.20	2000
	Total %	36.06	1.44	50.14	8.24	4.12	1456	72.80	27.00	0.20	27.20		2000

Appendix 3 - Core log of borehole UK33 from the Nkomati database

BHID	XSTART	YSTART	ZSTART	XEND	YEND	ZEND
UK33	-37,835.90	-48,270.70	1,377.24	-37,835.90	-48,270.70	1,218.07
FROM	**TO**	**LENGTH**	**Z**	**ROCKTYPE**	**UNIT**	**RD**
0.00	3.70	3.70	1,375.39	OVB	OVB	
3.70	5.00	1.30	1,372.89	MCHR	CRMT	3.95
5.00	6.32	1.32	1,371.58	MCHR	CRMT	4.05
6.32	7.65	1.33	1,370.26	MCHR	CRMT	3.97
7.65	8.81	1.16	1,369.01	MCHR	CRMT	3.99
8.81	8.90	0.09	1,368.39	PXT	PCR	3.99
8.90	9.07	0.17	1,368.26	MCHR	CRMT	3.99
9.07	10.00	0.93	1,367.70	MCHR	CRMT	3.75
10.00	10.18	0.18	1,367.15	MCHR	CRMT	3.37
10.18	11.17	0.99	1,366.56	PCR	PCR	3.37
11.17	11.48	0.31	1,365.92	PXT	PCR	3.37
11.48	11.75	0.27	1,365.63	PXT	PCR	3.29
11.75	12.10	0.35	1,365.31	CORELOSS	PCR	3.29
12.10	12.55	0.45	1,364.92	PXT	PCR	3.29
12.55	13.26	0.71	1,364.33	PCR	PCR	3.29
13.26	14.00	0.74	1,363.61	PCR	PCR	3.11
14.00	14.76	0.76	1,362.86	PXT	PCR	3.11
14.76	14.85	0.09	1,362.44	PXT	PCR	3.34
14.85	16.30	1.45	1,361.67	PCR	PCR	3.34
16.30	23.58	7.28	1,357.30	PCR	PCR	3.84
23.58	26.00	2.42	1,352.45	PCR	PCR	3.64
26.00	27.41	1.41	1,350.54	PCR	PCR	3.54
27.41	27.96	0.55	1,349.56	PCR	PCR	3.08
27.96	28.90	0.94	1,348.81	PXT	PCR	3.08
28.90	29.50	0.60	1,348.04	PXT	PCR	2.79
29.50	30.95	1.45	1,347.02	PXT	PCR	2.75
30.95	31.71	0.76	1,345.91	PXT	PCR	3.04
31.71	32.13	0.42	1,345.32	PCR	PCR	3.04
32.13	32.39	0.26	1,344.98	PXT	PCR	3.04
32.39	32.44	0.05	1,344.82	PCR	PCR	3.04
32.44	33.75	1.31	1,344.15	PCR	PCR	3.45
33.75	37.26	3.51	1,341.73	PCR	PCR	3.39
37.26	38.74	1.48	1,339.24	PCR	PCR	3.13
38.74	38.75	0.01	1,338.49	PXT	PCR	3.13
38.75	40.19	1.44	1,337.77	PXT	PCR	2.91
40.19	40.60	0.41	1,336.84	PXT	PCR	2.91
40.60	41.15	0.55	1,336.36	DIAB	DIAB	2.91
41.15	41.98	0.83	1,335.68	DIAB	DIAB	2.87
41.98	42.30	0.32	1,335.10	SHZO	SHZO	2.87
42.30	42.34	0.04	1,334.92	PCR	PCR	2.87

BHID	XSTART	YSTART	ZSTART	XEND	YEND	ZEND
UK33	-37,835.90	-48,270.70	1,377.24	-37,835.90	-48,270.70	1,218.07
FROM	**TO**	**LENGTH**	**Z**	**ROCKTYPE**	**UNIT**	**RD**
42.34	42.42	0.08	1,334.86	PXT	PCR	2.87
42.42	43.66	1.24	1,334.20	PXT	PCR	3.03
43.66	43.80	0.14	1,333.51	DIAB	DIAB	3.03
43.80	47.06	3.26	1,331.81	DIAB	DIAB	
47.06	65.05	17.99	1,321.19	DIAB	DIAB	
65.05	66.61	1.56	1,311.41	SHZO	SHZO	2.91
66.61	66.81	0.20	1,310.53	PXT	LrPXT	2.91
66.81	67.69	0.88	1,309.99	PXT	LrPXT	2.90
67.69	68.17	0.48	1,309.31	SERP	LrPXT	2.90
68.17	69.49	1.32	1,308.41	SERP	LrPXT	2.98
69.49	69.65	0.16	1,307.67	PXT	LrPXT	2.98
69.65	69.66	0.01	1,307.58	PXT	LrPXT	2.95
69.66	70.14	0.48	1,307.34	SERP	LrPXT	2.95
70.14	70.67	0.53	1,306.83	PXT	LrPXT	2.95
70.67	71.07	0.40	1,306.37	SERP	LrPXT	2.95
71.07	71.46	0.39	1,305.97	SERP	LrPXT	2.95
71.46	71.63	0.17	1,305.69	PRD	LrPXT	2.95
71.63	72.46	0.83	1,305.19	SERP	LrPXT	2.95
72.46	72.94	0.48	1,304.54	SERP	LrPXT	2.89
72.94	73.05	0.11	1,304.24	QCV	QCV	2.89
73.05	73.11	0.06	1,304.16	PXT	LrPXT	2.89
73.11	74.59	1.48	1,303.39	PXT	LrPXT	3.01
74.59	75.65	1.06	1,302.12	PXT	LrPXT	3.01
75.65	75.72	0.07	1,301.56	AMPH	XENO	3.01
75.72	75.90	0.18	1,301.43	PEGM	LrPXT	3.01
75.90	76.10	0.20	1,301.24	AMPH	XENO	3.01
76.10	76.21	0.11	1,301.08	AMPH	XENO	2.92
76.21	76.43	0.22	1,300.92	PEGM	LrPXT	2.92
76.43	76.70	0.27	1,300.68	PXT	LrPXT	2.92
76.70	76.95	0.25	1,300.42	PEGM	LrPXT	2.92
76.95	77.02	0.07	1,300.26	DOLM	XENO	2.92
77.02	77.48	0.46	1,299.99	PXT	LrPXT	2.92
77.48	77.64	0.16	1,299.68	DOLM	XENO	2.92
77.64	79.18	1.54	1,298.83	DOLM	XENO	3.00
79.18	80.65	1.47	1,297.32	DOLM	XENO	3.06
80.65	81.04	0.39	1,296.40	DOLM	XENO	3.04
81.04	81.18	0.14	1,296.13	PXT	LrPXT	3.04
81.18	82.32	1.14	1,295.49	DOLM	XENO	3.04
82.32	83.58	1.26	1,294.29	DOLM	XENO	2.79

BHID	XSTART	YSTART	ZSTART	XEND	YEND	ZEND
UK33	-37,835.90	-48,270.70	1,377.24	-37,835.90	-48,270.70	1,218.07
FROM	**TO**	**LENGTH**	**Z**	**ROCKTYPE**	**UNIT**	**RD**
83.58	83.75	0.17	1,293.57	PXT	LrPXT	2.79
83.75	84.95	1.20	1,292.89	PXT	LrPXT	2.90
84.95	84.97	0.02	1,292.28	PXT	LrPXT	
84.97	87.12	2.15	1,291.19	DIAB	DIAB	
87.12	87.13	0.01	1,290.11	DIAB	DIAB	3.13
87.13	88.80	1.67	1,289.28	PXT	LrPXT	3.13
88.80	89.17	0.37	1,288.26	PEGM	LrPXT	3.13
89.17	89.30	0.13	1,288.01	SHZO	SHZO	3.13
89.30	90.64	1.34	1,287.27	SHZO	SHZO	2.99
90.64	91.22	0.58	1,286.31	SHZO	SHZO	2.91
91.22	92.15	0.93	1,285.56	SHZO	SHZO	2.91
92.15	92.37	0.22	1,284.98	SCHI	TS	2.91
92.37	93.85	1.48	1,284.13	SCHI	TS	3.00
93.85	95.33	1.48	1,282.65	SCHI	TS	3.01
95.33	96.80	1.47	1,281.18	SCHI	TS	2.96
96.80	97.98	1.18	1,279.85	SCHI	TS	2.96
97.98	98.08	0.10	1,279.21	SCHI	TS	2.96
98.08	98.99	0.91	1,278.70	SCHI	TS	2.86
98.99	99.52	0.53	1,277.98	SCHI	TS	2.86
99.52	100.99	1.47	1,276.98	SCHI	TS	3.01
100.99	102.22	1.23	1,275.64	SCHI	TS	2.92
102.22	102.47	0.25	1,274.90	GAB	GAB	2.92
102.47	103.86	1.39	1,274.07	GAB	GAB	3.08
103.86	105.25	1.39	1,272.69	GAB	GAB	2.97
105.25	105.34	0.09	1,271.94	GAB	GAB	2.97
105.34	106.53	1.19	1,271.31	GAB	GAB	2.90
106.53	107.88	1.35	1,270.04	GAB	GAB	2.83
107.88	108.04	0.16	1,269.28	QTZ	QTZ	2.83
108.04	111.41	3.37	1,267.52	QTZ	QTZ	
111.41	113.46	2.05	1,264.81	DOLM	DOLM	
113.46	114.64	1.18	1,263.19	QTZ	QTZ	
114.64	115.29	0.65	1,262.28	DOLM	DOLM	
115.29	115.60	0.31	1,261.80	QTZ	QTZ	
115.60	116.00	0.40	1,261.44	DOLM	DOLM	
116.00	117.90	1.90	1,260.29	QTZ	QTZ	
117.90	125.68	7.78	1,255.45	DOLM	DOLM	
125.68	147.95	22.27	1,240.43	DIAB	DIAB	
147.95	148.39	0.44	1,229.07	DOLM	DOLM	
148.39	151.58	3.19	1,227.26	GRAN	PEGM	
151.58	154.46	2.88	1,224.22	QTZ	QTZ	
154.46	154.84	0.38	1,222.59	GRAN	PEGM	
154.84	155.09	0.25	1,222.28	QTZ	QTZ	
155.09	159.17	4.08	1,220.11	GRAN	GRAN	

List of key terms

1. Uitkomst Complex
2. Massive chromitite
3. Chromite mineral chemistry
4. Chromite crystal fracturing
5. Chromitite raft model
6. Chromitite deformation in conduit system
7. Chromitite profile of Nkomati mine.
8. Syn-magmatic deformation
9. Structural deformation of Massive Chromitite layer
10. Geomorphology of Massive Chromitite layer